DEVELOPMENT OF A PROTOTYPE SCANNER FOR PULSED ULTRASOUND COMPUTED TOMOGRAPHY

By

Sheila J. McFarland

B.Sc. (Hon. Physics), University of Regina, 1991
M.Sc. (Physics), University of British Columbia, 1994

A THESIS SUBMITTED IN PARTIAL FULFILLMENT OF THE
REQUIREMENTS FOR THE DEGREE OF
DOCTOR OF PHILOSOPHY

in

THE FACULTY OF GRADUATE STUDIES
DEPARTMENT OF PHYSICS AND ASTRONOMY

We accept this thesis as conforming
to the required standard

THE UNIVERSITY OF BRITISH COLUMBIA

December 2000

In presenting this thesis in partial fulfillment of the requirements for an advanced degree at the University of British Columbia, I agree that the Library shall make it freely available for reference and study. I further agree that permission for extensive copying of this thesis for scholarly purposes may be granted by the head of my department or by his or her representatives. It is understood that copying or publication of this thesis for financial gain shall not be allowed without my written permission.

Department of Physics and Astronomy
The University of British Columbia
6224 Agricultural Road
Vancouver, Canada
V6T 1Z1

Date:

December 20, 2000

Abstract

A prototype scanner for pulsed ultrasound computed tomography (UCT) has been built and tested with the aim of developing new imaging techniques that hold potential for the improved early detection of breast cancer. Two reconstruction algorithms were tested for their ability to produce quantitative 2D cross-sections of $\gamma_\kappa(\mathbf{r})$ and reflectivity, $R(\mathbf{r})$, where

$$\gamma_\kappa(\mathbf{r}) = \frac{\kappa(\mathbf{r}) - \kappa_0}{\kappa_0} \tag{0.1}$$

$$R(\mathbf{r}) = \gamma_\kappa(\mathbf{r}) - \gamma_\rho(\mathbf{r}) \tag{0.2}$$

and

$$\gamma_\rho(\mathbf{r}) = \frac{\rho(\mathbf{r}) - \rho_0}{\rho(\mathbf{r})} \tag{0.3}$$

$\kappa(\mathbf{r})$ and $\rho(\mathbf{r})$ are the compressibility and density throughout the image space, while κ_0 and ρ_0 describe water. γ_ρ is subsequently calculated from γ_κ and R. A Direct Fourier Method (DFM) that ignores attenuation was tested both as is and with the addition of an approximate attenuation correction based on the average distance ultrasound travels through tissue and water. An Algebraic Reconstruction Technique (ART) was also developed, which iteratively solves for γ_κ and R subject to rigorous attenuation correction.

In computer simulation, the DFM produced valid γ_κ and γ_ρ cross-sections only in the absence of attenuation and when $|\mathbf{r}| < 0.05|\mathbf{r}_j|$, where $\mathbf{r}$ and $\mathbf{r}_j$ are the position vectors of any scatter point and the source or detector, respectively. Points separately by 0.07 mm were resolved in simulation, and point amplitudes were reconstructed quantitatively to within $97 \pm 3\%$ and $95 \pm 4\%$ of their actual values for γ_κ and γ_ρ, respectively. Beyond $|\mathbf{r}| < 0.05|\mathbf{r}_j|$, Gaussian point-spread-functions (PSF's) were distorted into low amplitude halos. The approximate attenuation correction failed in simulation.

Experimentally, the DFM reconstructed images of a cylindrical tissue phantom with negative γ_κ and R and a 3 mm diameter. The resulting γ_κ and R cross-sections were primarily negative with an object diameter of 2.94 ± 0.06 mm and 1.94 ± 0.04 mm for

γ_κ and R, respectively. A valid γ_ρ could not be calculated due to the narrow R function. Experimentally, point-spread-functions were severely distorted by errors of only 1-2% in the measurement of $|\mathbf{r}_j|$.

In simulation, valid γ_κ and γ_ρ cross-sections were reconstructed with the ART for $|\mathbf{r}| < 0.3|\mathbf{r}_j|$ and in the presence of strong attenuation. Points separated by 0.05 mm were resolved in simulation, and point amplitudes were reconstructed quantitatively to within $100 \pm 14\%$ and $99 \pm 4\%$ of their actual values for γ_κ and γ_ρ, respectively. Strong attenuation was corrected to within an error of 0.2%. Convergence was not possible for images of more than 20×20 pixels due to ill-conditioning of the system. These theoretical results indicate, though, that the method holds promise given the application of conditioning algorithms.

Table of Contents

List of Figures

List of Tables

Acknowledgements

The completion of a Ph.D. thesis project is a multifaceted endeavor that is touched by many people. From providing technical support to offering encouragement, numerous individuals and organizations have influenced my work and are deserving of my thanks.

I would like to thank my supervisor, Dr. Calum MacAulay, for his technical advice and faith in my work. I feel that the experience of being his graduate student has shaped me into a confident professional capable of independent analysis and project management. My thanks goes out to Mr. Jerry Posakony for his technical support and encouragement. I would also like to thank Drs. Frank Podd and Inäki Schlaberg for providing me with their specialized line sources. My committee members, Drs. Alex Mackay, Branko Palcic, Doug Beder, and Greg Smith, also deserve thanks for their time and expert advice. In particular, I'd like to acknowledge Greg for his encouragement throughout the years. As well, I would like to thank our summer student Brock Wilson for doing a great job.

Moral support has been a crucial ingredient of my work, and for this I would like to thank my friends and extended family, my mother Edna, my father David, and my brother Jeff. In particular my mother's continual encouragement has been key in leading me to where I am today. I would like to thank my husband Mohammad Kermani, who provided a sounding board for me and encouraged me throughout the years.

I would like to acknowledge Dr. Jeff Young for making my years of teaching lab classes at UBC an enjoyable learning experience. I would also like to thank Ms. Frances Lasser for mentoring me in my entrepreneurial business assistantship in the Technology Development Office of the BC Cancer Agency.

This project has received the generous support of several organizations. I have been fortunate to be a Research Student of the National Cancer Institute of Canada supported with funds provided by the Terry Fox Run. Throughout my doctoral training, I was also supported by funds provided by the National Science and Engineering Research Council of Canada and the University of British Columbia. Additional funding for this project was kindly provided by both the British Columbia Science Council and the Canadian Breast Cancer Foundation. Travel funds for the presentations of results were provided by the BC Cancer Foundation, the National Cancer Institute of Canada, and the Ultrasonics International '99 Symposium.

GLOSSARY

Variables

$\mathbf{r}$, the positional vector corresponding to any scatter point
$\mathbf{r}_j$, the positional vector corresponding to either the source or the detector
$\mathbf{r}_s$, the positional vector corresponding to the source
$\mathbf{r}_d$, the positional vector corresponding to the detector
$\hat{\mathbf{n}}_j$, the unit vector corresponding to $\mathbf{r}_j$
$\hat{\mathbf{n}}_s$, the unit vector corresponding to $\mathbf{r}_s$
$\hat{\mathbf{n}}_d$, the unit vector corresponding to $\mathbf{r}_d$
$\hat{\mathbf{x}}$, unit vector along the x-axis
$\hat{\mathbf{y}}$, unit vector along the y-axis

(u, v), coordinates in the Fourier space of the image
τ, radii of the data circles in the Fourier space of an image
τ_{max}, the maximum distance from the origin of data in the Fourier domain of the image
τ_0, τ-dependent lowpass filter cutoff
τ_T, truncation limit in terms of τ
χ, the angles of the data rays in the Fourier space of an image
τ_{max}, the maximum radius of the data circles in the Fourier space of an image

r, radius, where applicable
t_s, time of flight of ultrasound from source to scatter point
t_d, time of flight of ultrasound from scatter point to detector
a, distance from the origin to either the source or detector
c, general term for the speed of sound
c_w, the speed of sound in water
c_t, the speed of sound in tissue
f, the frequency of sound
f_{Nyq}, the Nyquist frequency
f_D, the frequency at which ultrasound data is digitized
f_s, sampling frequency, equal to f_D
f_1, lower band limit frequency
f_2, upper band limit frequency
Ω_1, Ω_2, the angular frequency band limits of the incident field

$A(\omega)$, the frequency spectrum of the incident field
ω_0, central angular frequency of Ricker wavelet
f_0, central frequency of Ricker wavelet
λ, the wavelength of sound
ω, the angular frequency of sound $= 2\pi f$
$\tilde{k}$, the wave number of sound, which equals $\frac{1}{\lambda}$
k, the angular wave number of sound $= \frac{2\pi}{\lambda}$
n, index of refraction
v_c, amplitude of cosine component of narrow band signal
v_s, amplitude of sine component of narrow band signal

$p_0(\mathbf{r}, \omega)$, the incident insonifying field, as a function of position and ω
p_s, the scattered field with simplifying assumptions
pe_s, exact scattered field
$p(\mathbf{r}, t)$, the total ultrasound pressure field expressed a function of both position and time
$p(\mathbf{r}, \omega)$, the total ultrasound pressure field expressed a function of position and ω
H_0^1, the Hankel function of the first kind
Y_r, the Ricker wavelet
$g(\mathbf{r}|\mathbf{r}_j, k)$, 2D Green's function describing sound propagation as a function of $\mathbf{r}$ and k
$\tilde{g}$, the Green's function multiplied by attenuation terms
S, the $\mathbf{r}$ and k dependent term in the approximate 2D Green's function propagator
$\tilde{S}$, the function S multiplied by attenuation terms
α, multiplier term in the approximate 2D Green's function propagator
$\tilde{\alpha}$, incorrect α parameter from the paper by Blackledge *et al*
α and β, where applicable, coefficients in the approximate attenuation correction

$\psi_\theta(\tilde{\varphi}_s, k)$, projection data in the image Fourier space for a given source angle, $\tilde{\varphi}_s$
N_v, number of projections or views
κ_0, the compressibility of water
ρ_0, the density of water
$\kappa(\mathbf{r})$, the compressibility of the object being imaged, as a function of position
$\rho(\mathbf{r})$, the density of the object being imaged, as a function of position
$\gamma_\kappa(\mathbf{r})$, the compressibility gamma function
$\gamma_\rho(\mathbf{r})$, the density gamma function
I, the image being reconstructed

R, reflectivity function

Φ, multiplier term in front of γ_ρ in the image function

θ, the relative angle between the incident beam direction and the detector angle

φ_s, the angle of the source

φ_d, the angle of the detector

Φ_{phase}, Fourier phase angle

ξ, image normalization factor

PR, percentage ratio matrix

e, the error in an iterative technique

ATT_w, attenuation due to water

ATT_t, attenuation due to tissue

χ_t, coefficient in ATT_t

χ_w, coefficient in ATT_w

d_t, the distance that a particular ultrasound wave travels through tissue

d_w, the distance that a particular ultrasound wave travels through water

$\overline{d}_t$, the average distance that all ultrasound waves travel through tissue

$\overline{d}_w$, the average distance that all ultrasound waves travel through water

Z, acoustic impedance

$\mathrm{P}_\theta(\mathrm{t})$, projection data at some angle, θ

t, independent variable along the projection

$\mathrm{f}(x, y)$, tissue object function in general tomography experiment

β, received echo amplitude in reflection tomography

C_R, intensity reflection coefficient

M_d, mean of the power in the data

M_n, mean of the power in the noise signal

B, bulk modulus

V, volume

p, pressure

T_g, glass transition temperature

T_c, Curie temperature

V_p, dc poling voltage

q, the angle of incidence of a sound wave on a transducer face relative to the normal

ϕ, the irradiation angle in x-ray tomography

d, density of points in the Fourier domain of the image

Acronyms

ADC, analogue-to-digital converter
ART, algebraic reconstruction technique
BF, background field
CT, computed tomography
CW, continuous wave
DFT, Discrete Fourier Transform
DT, diffraction tomography
FOV, field of view
FFT, Fast Fourier Transform
FT, Fourier Transform
FWHM, full-width-half-maximum
HVL, half-value layer
IFT, Inverse Fourier Transform
LPF, lowpass filter
MRI, magnetic resonance imaging

PSF, point spread function
PZT, Lead-Zirconate-Titanate
RT, reflection tomography
SD, scatter data
SS, secondary scatter
SA, scattering amplitude
SA_{appr}, scattering amplitudes corrected for attenuation with the approximate approach
SA_B, scattering amplitudes not corrected for attenuation
SA_R, scattering amplitudes corrected rigorously through path tracing
SNR, signal-to-noise ratio
TOF, time of flight
TS, scatter off the tank
UCT, ultrasound computed tomography

UFR, unified frequency domain reconstruction

Definitions

Thermography

A breast thermogram is a pictorial representation of the infrared radiation of the skin over the breast, motivated by the fact that breast cancers can elevate the skin temperature of the affected breast.

MRI

MRI makes use of the magnetic properties of protons in hydrogen. The protons act like magnetic dipoles, which align with strong magnetic fields. Application of a radio frequency (RF) pulse destroys this alignment. Upon cessation of the RF pulse, the protons realign with the magnetic field and an RF signal is emitted, which is used to create the MR image.

Transillumination

Visualization of the translucency of the breast, obtained by transmission of infrared light through the tissue. Benign and malignant diseases can lead to changes in shades of colors and to distortions of vascular patterns.

Electrical Impedance Imaging

This form of imaging seeks to provide an image of the electrical impedance (resistance to the transmittance of faint electrical signals) of tissue.

Chapter 1
Introduction

1.1 Aim of this Work - Hypothesis

A prototype scanner for pulsed ultrasound computed tomography (UCT) has been built and tested with the aim of developing new imaging techniques that hold potential for the improved early detection of breast cancer. This waterbath based system incorporates two reconstruction algorithms based on the solution of the Chernov wave equation subject to the Born approximation. The algorithms attempt to reconstruct quantitative 2D cross-sections of compressibility and density for use in tissue characterization. The term quantitative indicates that the brightness of any given pixel is directly proportional to the value at that location of the tissue parameter in question. The first algorithm produces a reconstruction through the inversion of data in the 2D Fourier domain of the image (Direct Fourier Method introduced by Blackledge *et al*). The second algorithm is an algebraic reconstruction technique (ART) that produces images based on the iterative solution of a matrix system built upon knowledge of the scattered field and ultrasound propagation.

In order to be of potential use in the early detection of breast cancer, an imaging system must reconstruct quantitative images with resolution on the order of 2 mm [69]. This means that the system must be able to detect two separate point objects that are 2 mm apart. It was thus hypothesized in this thesis that the reconstruction algorithms incorporated in the pulsed UCT scanner could be demonstrated both in simulation and experimentally to have image resolution of at least 2 mm. It was hypothesized that the resultant γ_κ and γ_ρ images would indeed be quantitative. Furthermore, given the nonperiodic nature of pulsed UCT data, it was hypothesized that digital signal processing (DSP) techniques from the relatively young field of wavelet denoising could be applied to improve the data upon which the image reconstruction is based.

The overall aim of this thesis was to determine if indeed these hypotheses hold for the techniques and algorithms incorporated into the prototype pulsed UCT scanner. This thesis was furthermore a proof of concept study to identify the future development that is necessary for the creation of a second generation scanner that can be evaluated in a clinical setting.

It should be noted that image resolution is only one piece of the puzzle with respect to the evaluation of ultrasound scanners. A complete system development program, which is beyond the scope of this thesis, involves system evaluation in terms of potential lesion detectability, which is a complex issue affected by contrast, clutter and noise, as well as resolution. Noise refers to random processes that arise from thermal and electronic noise in the transducer and the electronics of the system. Clutter is also termed structural noise. This can take the form of either echoes from objects that are too small to be resolved by the system, which is termed speckle, or echoes from larger objects that are not of interest, such as vessel walls in the case of Doppler blood flow imaging and ribs in the case of breast imaging. Speckle imparts noise into the images, while echoes from larger structures can degrade image contrast if they are indistinguishable from the signals of interest. This thesis concentrated on evaluating image resolution capabilities under carefully controlled conditions in both simulation and experiment.

1.2 Thesis Highlights

This thesis outlines the study of two ultrasound computed tomography algorithms in a prototype UCT scanner. In addition, this work involved the study of methods for data interpolation, noise removal, and the iterative solution of linear systems, in support of the reconstruction algorithm development and testing. The prototype scanner employs pulsed ultrasound fields, which is a relatively novel approach both theoretically and experimentally. Fewer than five papers have been written to develop theoretical algorithms for pulsed UCT. With regard to experimental scanner development, only one other group appears to be working in pulsed UCT, and this group is currently exploring non-destructive evaluation (NDE) in industry [78].

This first part of this thesis focusses on extensive theoretical tests of the method by Blackledge *et al* for the reconstruction of 2D functions of density and compressibility for non-attenuating objects using pulsed UCT [10]. Specifically the functions reconstructed are

$$\begin{aligned} \gamma_\rho(\mathbf{r}) &= \frac{\rho(\mathbf{r}) - \rho_0}{\rho(\mathbf{r})} \\ \gamma_\kappa(\mathbf{r}) &= \frac{\kappa(\mathbf{r}) - \kappa_0}{\kappa_0} \end{aligned} \tag{1.1}$$

κ_0 and ρ_0 are the compressibility and density of the background fluid, which is generally water. Note that the $\gamma_\kappa(\mathbf{r})$ definition differs from that of $\gamma_\rho(\mathbf{r})$ in that the background parameter, rather than the tissue parameter, is the denominator. These particular gamma functions in turn result from the solution of the wave equation to be discussed in Chapter 2. In reality, γ_κ and the reflectivity function, $R = \gamma_\kappa - \gamma_\rho$, are reconstructed, and γ_ρ is calculated from these images. In simulation, the method by Blackledge *et al* was tested as is for non-attenuating objects. It was also tested for attenuating objects upon the addition of an approximate attenuation correction based on the average distance traveled by ultrasound through tissue and water in a given experiment. Preliminary experimental tests were also performed to determine the potential viability of the approach.

The second part of this thesis involves an attempt to develop a rigorous reconstruction algorithm that includes a correction for frequency-dependent attenuation, which is a major stumbling block in pulsed UCT. The algorithm developed includes what is herein called an "attenuated propagator," which is a function that describes the propagation of ultrasound in the presence of attenuation due to water and tissue. This propagator was incorporated into an algebraic reconstruction technique (ART) intended to determine $\gamma_\kappa(\mathbf{r})$ and $\gamma_\rho(\mathbf{r})$ of the object being investigated. The method was found to be very computationally intensive, as most ART routines are.

Regarding prototype system design and results, the following key results of simulations and experiments were obtained:

- In experimental tests, the method by Blackledge *et al* was dramatically effected by errors as low as 1-2% in the measurement of the distance from the source or detector to the origin, given by $|\mathbf{r}_j|$.
- The method by Blackledge *et al* was able to reconstruct a 3 mm wide tissue phantom with negative γ_κ and R. The resulting γ_κ and R cross-sections indicated object functions that were primarily negative. The FWHM of the γ_κ image was 2.94 ± 0.06 mm, while that for the R image was 1.94 ± 0.04 mm.
- Wavelet denoising with the Daubechies 9 and Daubechies 20 wavelet families offered no improvement of data compared to lowpass filtering.
- In simulation, the method by Blackledge *et al* produced narrow, Gaussian γ_κ and γ_ρ point-spread-functions (PSF's) for points in the absence of attenuation whose distance from the origin, $|\mathbf{r}|$, was less than 5% of $|\mathbf{r}_j|$. The maximum image resolution for this limited case was approximately 0.07 mm.
- This method unfortunately cannot produce proper PSF's for points with $\frac{|\mathbf{r}|}{|\mathbf{r}_j|} > 5\%$. It is also not possible to add a rigorous attenuating correction to this algorithm, and the approximate correction failed.
- In simulation, the algebraic reconstruction technique produced consistently shaped, narrow γ_κ and γ_ρ PSF's for points with varying $\frac{|\mathbf{r}|}{|\mathbf{r}_j|}$ (tested up to 30%) in both the absence and presence of attenuation. The maximum image resolution was approximately 0.05 mm.
- The ART is capable in simulation of rigorously correcting for attenuation such that images suffer a change in power of less than 0.15% when comparing results in the absence and presence of attenuation.
- The algebraic reconstruction technique has difficulty converging on an image solution for γ_κ and γ_ρ cross-sections of more than 20×20 pixels.

These results together with others outlined in Chapter 5 provide the basis for additional research discussed in Chapter 6, primarily in the refinement of iterative methods.

1.3 Organization of this Thesis

This thesis is composed of six chapters. The first chapter includes background information that describes the medical motivation behind this thesis. It also describes current techniques in ultrasound imaging. Computed tomography is explained in brief and the chapter concludes with an outline of developments in ultrasound tomography, together with the advantages and disadvantages of the different UCT methods.

Chapter 2 provides extensive theoretical background. The first part of the thesis explains the motivation behind the use of pulsed ultrasound and describes the physics model that is the basis behind both the method by Blackledge *et al* as well as the ART. The remainder of the chapter outlines pertinent details of the derivation of the algorithm by Blackledge *et al* and describes the effect of attenuation in the tissue-water system.

Chapter 3 provides details of the prototype scanner that was built for experimental UCT tests. The different sources and the hydrophone detector are described, along with the stepper motor apparatus that was designed to move the sources and hydrophone automatically in very small steps. Principles behind the design of the water tank are outlined. The chapter concludes with a description of the electronics chosen for the prototype scanner.

The fourth chapter describes various experimental methods that were incorporated into this work. The chapter begins with a development of the approximate attenuation correction as well as the ART with attenuated propagators. Chapter 4 continues with a discussion of necessary noise removal and digital signal processing (DSP) techniques based on both conventional Fourier methods as well as wavelet analysis. The chapter ends with a comparison of various data interpolation methods for potential use in the method by Blackledge *et al.*

Chapter 5 presents numerous results of γ_κ and γ_ρ image reconstruction using the algorithms outlined in this thesis. The method by Blackledge *et al* was extensively tested in computer simulation to determine its capabilities. Various situations were examined, including the presence or absence of frequency-dependent attenuation and dispersion and the presence or absence of noise. Both Fourier-based and wavelet-based denoising techniques were studied. A tissue phantom experiment was also performed using the method by Blackledge *et al* to gain additional understanding of its potential. Chapter 5 also includes several key preliminary studies of the ART in simulation. The image resolution and quantitative capabilities of the algorithm were studied. As well, tests were done to determine the ability of the algorithm to reconstruct points with varying locations and in both the absence and presence of attenuation.

Chapter 6 summarizes the findings of this thesis and discusses possibilities for future work. The thesis concludes with five appendices. The first appendix includes a detailed derivation of the Blackledge method, which augments both Chapter 2 as well as the outline contained in Reference [10]. Appendix B adds to this with a derivation of ∇S, an approximate term that is used in the mathematical description of ultrasound wave propagation. The third appendix derives a more rigorous expression for ∇S in both non-attenuating and attenuating media. Appendix D outlines phantom construction, and Appendix E discusses iterative algorithms for potential use in the algebraic reconstruction technique.

1.4 Medical Motivation

Breast cancer is a widespread disease that afflicts women worldwide. In a 1985 survey of 18 cancer types in 24 regions of the world, breast cancer was shown to be the most common malignancy in the women, accounting for 19.1% of all such cancers [67]. Today in Canada and the United States, breast cancer is the most common cancer in women and the second leading cause of cancer death among women [65, 63, 76]. Table 1.1 illustrates that tens of thousands of women in North America are afflicted with invasive breast cancer each year, and that thousands more die each year as a result. More than 1 in 10 women who live to age 80 will develop the disease, and more than 24% will die

Country	Estimated New Cases in 1999	Estimated Deaths in 1999
US	175000	43300
Canada	18700	5400

Table 1.1: The above data illustrate the statistics for breast cancer in North American women. Listed are the 1999 Canadian and US incidence and mortality estimates [1, 63].

as a result [1, 65, 63]. It is also the number one killer of North American women aged 35-55, resulting in the most lost years of life among this group [65, 63]. The incidence of breast cancer is expected to increase as the world population ages, with estimates of more than one million new cases worldwide per annum by the year 2000 [59]. It is of interest to note that although the disease is primarily a women's affliction, there are in fact approximately 1300 new cases of breast cancer among men annually in the US, and a further 400 deaths [5].

Most women who develop breast cancer have no risk factors to aid in early detection and treatment [63]. As such, the best approach towards controlling this disease is through the development of new technologies for improved early detection and diagnosis to allow for earlier treatment [31]. Detection is the ability to find suspicious breast features, while diagnosis is the ability to distinguish which features indicate malignancy. In recent years, early detection has proven key in increasing the survival rates of women diagnosed with breast cancer. Between 1950 and the late 1980's, the overall breast cancer mortality was relatively stable and over 40% [1]. However, since 1989 the death rate has decreased an average of 1.8% per year due to earlier detection and diagnosis and improved treatments [1]. Table 1.2 outlines the current age-related five-year survival rates for US women. It is alarming that the survival rate for women decreases as the age at cancer diagnosis increases. Researchers speculate the reason to be that younger women may have tumors that are more aggressive and less responsive to hormonal therapies. It is also alarming that regardless of age, the five-year survival rate is no better than 86%. However, as

Age (years)	Percentage of US Women (%)
< 45	81
45-64	85
> 65	86

Table 1.2: The above data illustrate the age-related five-year survival rates in the US for women diagnosed with breast cancer [1, 63].

more breast cancers are diagnosed at earlier stages, the death rates are expected to decline. As such, scientists and engineers continually work to develop new technologies for improved accuracy and reliability in breast cancer detection. The common goal is to develop systems that produce high resolution images of breast structural features as well as quantitative parameters that correlate to the pathological state of the tissue.

X-ray mammography is currently the only imaging technique routinely used in breast cancer screening. It has had much success in early breast cancer detection, and indeed has proven more useful than any other breast imaging technique to date. There is recent evidence that regular mammographic screening may reduce the chances of dying from breast cancer by 17% for women in their forties, and by 30% for women between the ages of 50 and 69. However, even though the field of mammography is continually advancing, the imaging technique continues to suffer from the difficulty of maximizing both test sensitivity and specificity. High sensitivity means that a test for a disease can identify nearly all afflicted patients, resulting in few false negative results. If the test also has high specificity, it is further able to properly exclude patients that do not have the disease; thus high specificity results in few false positive results.

There remains a significant rate of false-negatives and false-positives in x-ray mammography. With regard to sensitivity, several examples are quoted in the literature. For instance, approximately 25% of breast tumors in women in their forties evade detection by mammography [63]. There is also a high false-negative rate among woman less than age thirty-five [7, 61]. The poor sensitivity is mostly due to poor imaging of dense tissue by mammography and failure to recognize subtle early signs of breast abnormality [1, 63]. The statistics regarding specificity indicate significantly more problems. Screening mammography cannot yet provide a definite diagnosis, and every person with a positive screening test must undergo a biopsy to determine if in fact cancer exists. The biopsy is currently the "gold standard" in breast cancer diagnosis. However, studies have indicated that 68-87% of biopsies yield negative results [52]. Part of the problem is that mammograms poorly differentiate solid tumors from benign cysts, which occur in more than 50% of women [7, 61].

The high rate of unnecessary biopsies not only causes undue stress and discomfort for millions of women the world over, but it also presents a significant drain of health care dollars. To illustrate this point, consider the example of a country with 25 million women of the age at which screening is recommended. Assume that 50% of these women actually have an x-ray screening examination. If 5% of the mammograms performed annually are positive, breast lesions in an estimated 625 thousand women would require further evaluation each year. This example further assumes a low estimate that 50% of these women undergo biopsy. On average each procedure costs US$2000, which is calculated based on the costs of the conventional techniques of needle biopsy and surgical biopsy. The final estimated cost of biopsies annually would be US$625 million.

Efforts to improve the specificity and sensitivity of breast cancer screening and thus eliminate the biopsy of benign breast lesions have led to several technological developments. These include improved x-ray mammographic techniques and interpretation, thermography, transillumination, electrical impedance imaging, magnetic resonance imaging (MRI), conventional ultrasound, and 3D ultrasound. Brief descriptions of these methods can be found in the Glossary, and further information can be found in Reference [28]. Concurrent with this has also been the development of new micro-biopsy procedures such as fine needle aspiration and computer-directed cutting needle biopsy, also described in the Glossary. These technologies, however, still involve extensive use of hospital resources, as well as stress and discomfort to patients.

1.5 Ultrasound as an Imaging Probe

This thesis investigates the potential for a new ultrasound computed tomography method that employs pulsed ultrasound fields. Ultrasound imaging is a useful and non-invasive technique in which high frequency sound (1-10 MHz) is transmitted through the body. The first use of diagnostic ultrasound was reported in the 1940's by Dr. Karl Dussik, a psychiatrist who was at the hospital in Bad Ischl, Austria. He attempted to locate brain tumors by using two transducers, one to insonify the tissue and the other to detect the transmitted sound waves and hence measure the transmission of ultrasound through the head. Routine use of diagnostic ultrasound imaging began in the 1950's. It was during this time that academic interest began in the field of breast sonography. Notable studies were those by Wild, Neal and Reid, who used pulse-echo techniques to study benign and malignant breast diseases, and those by Howry, Bliss and Scott, who employed a 2 MHz compound scanning system to study the breast [41, 42, 84, 85, 86].

Currently ultrasound has many uses in medicine, with primary emphasis on obstetrics and women's healthcare (*in vitro* fertilization, guided breast biopsy, gynecology). Applications in obstetrics allow for the investigation of fetal development. Today nearly every fetus undergoes examination with ultrasound at least once. The uses of ultrasound in obstetrics range widely, from determining pregnancy date by baby size and detecting multiple fetuses, to detecting certain defects, such as those related to the heart. A major application of ultrasound in obstetrics is biometry, which is the measurement of various fetal dimensions.

Ultrasound imaging in gynecology has been made possible by the development of intravaginal imaging, which uses an endocavitary transducer probe. Applications in gynecology include the monitoring of the dynamics of follicle growth, endometrium development, and fibroid growth. Endocavitary probes are also used in other fields of medicine. For instance, intrarectal ultrasonography of the prostate is used to diagnose benign prosthetic hypertrophy and prostate malignancies. The combination of laparoscopic ultrasonography and laparoscopy also allows urologists and surgeons to perform direct biopsies more carefully under ultrasonographic guidance.

In cardiology, ultrasound is used for the real-time dynamic imaging of the movement of cardiac structures (heart valves and ventricular walls) during the cardiac cycle. It is possible to monitor arterial diameters and the displacement of arterial walls during the cardiac cycle, which ultimately provides tissue characterization information regarding arterial wall stiffness and elasticity.

Doppler imaging is an important application of ultrasound that is used for the non-invasive measurement of blood flow. The Doppler effect is a change in the wavelength of scattered ultrasound that is dependent upon the movement of scatterers relative to the transducer probe. The resulting change in wavelength is used to analyze blood flow. The most important recent development in Doppler ultrasound is the advent of color flow imaging which indicates flow direction as well as rate. Flows directed towards the probe are presented in shades of red, while those directed away from the probe are seen in shades of blue. Attempts have been made to develop transcranial Doppler for the imaging of brain arteries, but MRI remains superior for brain imaging.

Regarding health effects, there have been no reports linking ill effects with ultrasound exposures well below those used in ablation procedures. The peak intensity of the ultrasound field used for ablation is on the order of 1 kW/cm^2, whereas the field intensity used in imaging is generally on the order of 10 mW/cm^2. The official statement of the American Institute of Ultrasound in Medicine (AIUM), included in their statement on Safety in Training and Research that was approved March 1993, is that during the history of the use of clinical ultrasound there have been no confirmed reports of adverse biological effects on patients resulting from insonification with field intensities less than 100 mW/cm^2 [2]. Furthermore, the AIUM makes the additional statement that insonification

	Diagnostic Ultrasound	**X-rays**
wave type	longitudinal mechanical waves	electromagnetic waves
transmission media	elastic medium	none required
wavelength in tissue	$\sim 1.5\times10^{-3} - 7.5\times10^{-5})$ m	$\sim 3\times(10^{-9} - 10^{-11})$ m
resolution	$\sim 0.15 - 0.75$ mm	$\sim 100\,\mu$m
mode of generation	stressing the medium	accelerating electric charges
velocity in tissue	depends on the medium order of 1.5 mm/μs	depends on the medium order of $\sim \frac{1}{n}\,2.998\times10^{8}$ m/s n = index of refraction ($\sim$1.33)
similar waves	seismic, acoustic	radio, light, microwaves

Table 1.3: Differences between Ultrasound and X-rays.

in the low MHz frequency range for up to 500 seconds is safe at even higher intensities when the energy per unit area is less than 50 J/cm^2 [51]. For comparison, the ultrasound fields used in the experimental work presented in this thesis had a corresponding energy per unit area of 50 μJ/cm^2.

Ultrasound energy is very different from x-ray energy, as can be seen in Table 1.3. In particular, the wavelength of ultrasound is several orders of magnitude larger that than of the x-rays used in screening mammography. A consideration of wave theory alone indicates that the resolution is approximately 0.5λ, where λ is the wavelength of the ultrasound or x-rays. However, ultrasound imaging is limited to resolutions on the order of 0.15-0.75 mm due to scattering, refraction and attenuation. The most current technologies in digital x-ray mammography have a resolution limit on the order of 100 μm due to x-ray detector capabilities. However, although x-ray mammography can resolve much smaller objects than ultrasound, 0.15-0.75 mm resolution is sufficient and useful for the detection of early breast cancer [46, 69]. Indeed, it is difficult to biopsy questionable breast masses that are smaller than 2 mm in diameter [69]. Thus, although ultrasound imaging cannot image microscopic features such as calcifications, it still has the potential to find lesions at an early enough stage to be of use in breast cancer detection.

Ultrasound does have some advantages over x-ray mammography. In particular, mammography cannot distinguish cysts from other breast diseases, while ultrasound can do so with accuracy rates of better than 96% [7, 61]. Furthermore, quantitative ultrasound imaging, such as tomography, can provide not only structural/density information, as does mammography, but also information regarding tissue compressibility and angular scattering cross-section. Measurements of angular scattering cross-section, also termed directivity, indicate how much ultrasound is scattered into various directions from a particular region of tissue, which may be useful for tissue characterization. Knowledge of tissue compressibility in particular may be useful for the early detection of breast cancer. Palpation is routinely used for the detection of breast tumors close to the skin surface. Hence, compressibility imaging is a natural extension of the physical examination of palpable lesions. Palpation results are dependent upon the elastic properties of tissue, and the only imaging modality that makes use of elastic waves as a probe is ultrasound. Thus, ultrasound can be used to investigate compressibility, while imaging modalities that use ionizing radiation or magnetic fields cannot.

The use of ultrasound in screening programs is hampered by poor image resolution due to noise in the data and the complex physics of the tissue/sound interaction. However, given the resolution that can ultimately be achieved with continued research, it is certainly possible that ultrasound imaging, and in particular UCT, will be able to detect early cancers on the order of $\frac{1}{2}$ mm in diameter.

1.6 Some Basic Sound and Ultrasound Concepts

Sound is defined as a periodic disturbance in either the density of a fluid or in the elastic strain of a solid. The disturbance is generated by a vibrating object, and it results in molecular motion within the medium. Sound waves are longitudinal, which means that the molecular motion is in the same direction as the propagation of wave energy. This is in contrast to transverse waves, such as water waves, for which molecular motion is mainly perpendicular to the propagation of wave energy. Ultrasound is merely sound with a frequency, f, greater than 20 KHz, which is about the upper limit of human hearing. Often the amplitude of a sound wave throughout space is referred to as a field.

Sound can be described as either continuous wave (CW) or pulsed. CW simply means that the sound wave is made up of mostly one frequency. Hence the shape of the disturbance field is sinusoidal, as illustrated in Figure 1.1.A. In contrast, a pulse is a single, transient disturbance that travels through space. An example of a pulse is illustrated in Figure 1.1.B.

Sound waves have a wavelength, λ, and a speed, c, which are related through frequency by the equation

$$c = f\lambda \tag{1.2}$$

A sound wave can also be described by its wave number $\tilde{k}$, which is the number of complete wavelengths that can fit into a unit distance. This parameter is given by

$$\tilde{k} = \frac{1}{\lambda} \tag{1.3}$$

Alternatively, the angular wave number, k, is often referred to, where

$$k = \frac{2\pi}{\lambda} \tag{1.4}$$

The speed of sound, c, is dependent upon both the inertial property and the elastic property of the propagation medium. Specifically, the inertial property is density and the elastic property is the bulk modulus, B, and the speed of sound can be expressed as

$$c = \sqrt{\frac{B}{\rho}} \tag{1.5}$$

The bulk modulus is the parameter that describes the extent to which an element of the medium changes in volume, V, as the pressure, p, applied to that element is changed. The bulk modulus is given by

$$B = -\frac{\Delta p}{\Delta V/V} \tag{1.6}$$

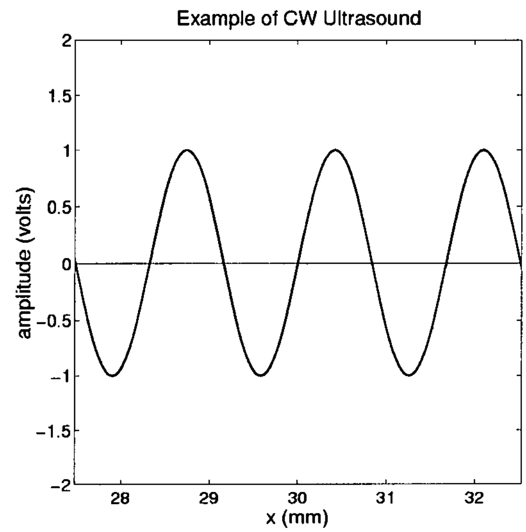

(A)

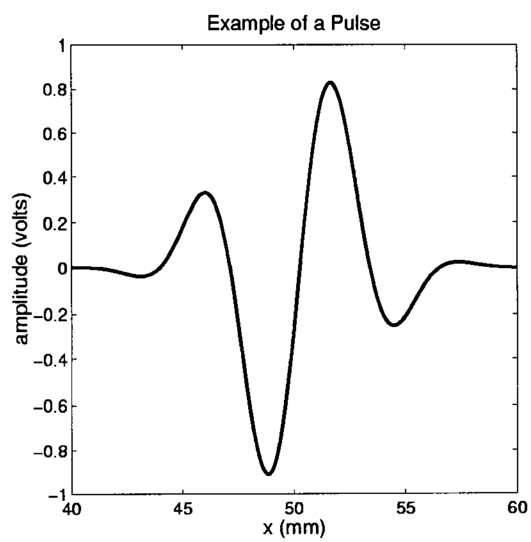

(B)

Figure 1.1: Figure A illustrates an example of continuous wave ultrasound, while Figure B shows an example of a pulse.

Material	**Speed of Sound (mm/μs)**
Air	0.33
Fat	1.46
Water (20°C)	1.48
Average Soft Tissue	1.54
Brain	1.51
Liver	1.56
Kidney	1.56
Blood	1.57
Muscle	1.57
Bone	4.1

Table 1.4: Speed of sound in some biological materials [43, 51].

Equation 1.5 makes intuitive sense. The elastic property determines the ability of the propagation medium to store potential energy. This is important because as the sound wave passes through the medium, potential energy is alternately stored and released as the medium undergoes rarefaction and compression. If the medium is able to store more potential energy, there will be a greater restoring force acting on its molecules, and the wave will travel faster. The inertial property determines the ability of the medium to store the kinetic energy of the sound wave. If a medium is more dense, there is more mass per unit volume. A given unit volume can therefore store more kinetic energy and have a lower velocity than a lighter unit volume in a less dense medium, resulting in a lower speed of sound. In this thesis, the compressibility is considered rather than the bulk modulus. This is simply the inverse of the bulk modulus, and hence the equation for c can alternatively be written as

$$c = \frac{1}{\sqrt{\kappa\rho}} \tag{1.7}$$

Table 1.4 illustrates the speed of sound in various media of different density and compressibility. Evidently, c varies by up to 8% throughout different soft tissues of the body.

The speed of sound is also dependent upon temperature and frequency. Evidently, as the temperature rises, the density decreases and the speed of sound increases. Temperature change is not a problem with conventional diagnostic ultrasound, since body temperature is at a nearly constant value. However, tissue is often immersed in a water bath for UCT imaging. The temperature of the water must be maintained and monitored to ensure the quality of image reconstruction. The dependence of sound speed upon frequency is termed dispersion. This is generally not of concern in the clinical imaging of soft tissue, since dispersion is less than 1% over the frequency range of 1-20 MHz [43]. However, pulsed UCT analyzes data in a complex mathematical process that magnifies the error which results if dispersion is not considered. This topic is discussed in detail in Section 5.3.6.

The acoustic speed in a medium together with its density defines the acoustic impedance, Z, which is given by

$$Z = \rho c \tag{1.8}$$

A change in acoustic impedance defines an interface, and ultrasound is reflected by interfaces with dimensions larger than the maximum wavelength in the source. The corresponding reflection coefficient, C_R, that describes the reflected ultrasound beam intensity is the following:

$$C_R = \left(\frac{Z_1 \cos(\theta_2) - Z_2 \cos(\theta_1)}{Z_1 \cos(\theta_2) + Z_2 \cos(\theta_1)}\right)^2 \tag{1.9}$$

where $\cos(\theta_1)$ and $\cos(\theta_2)$ are the angles of incidence and transmission relative to the normal vector of the interface. Evidently, larger differences in impedance result in more ultrasound reflection. As an example, consider water, average soft tissue, and bone, which have acoustic impedances of 1.48×10^{-6}, 1.63×10^{-6} and 7.8×10^{-6} $\frac{kg}{m^2 s}$, respectively [43]. The resulting intensity of the reflected ultrasound at a soft tissue/bone interface is 46% of the incident beam, while it is only 0.2% at an interface between soft tissue and water for normal incidence.

1.7 Current Use of Ultrasound in Breast Cancer Imaging

Due to physical constraints in most medical situations, it is often impossible to perform ultrasound image reconstruction with sound energy that is scattered in directions other than directly back into the source transducer (termed pulse-echo or backscattered sound energy). For example, in ultrasound cardiovascular imaging, signals that are not directly backscattered are generally immeasurable due to very large acoustic impedance discontinuities at tissue-bone and air-tissue interfaces that result in significant scatter back into the body, as well as due to attenuation losses [47]. As such, most medical ultrasound imaging is done with information obtained from reflected sound energy. Breast tissue, however, lends itself to investigation from all angles and tends to have similar acoustic properties throughout its boundaries with relatively small differences at tissue interfaces [47]. As such, breast cancer is the subject of research in novel imaging techniques such as ultrasound computed tomography. Commercially, however, the widespread availability of conventional ultrasound B-scanners has motivated the use of this imaging modality in breast imaging, primarily for guiding needle biopsies and for the differentiation of cysts from solid masses [33].

1.7.1 B-Scan Imaging

B-scan imaging is also referred to as pulse-echo imaging because only backscattered sound energy is used in the image reconstruction process. This type of imaging uses a simplified image reconstruction algorithm that is based on geometrical considerations only and which insonifies the tissue only at one angle for each image. This is in contrast to 3D ultrasound, which reconstructs an image from data collected at various angles, and ultrasound computed tomography, which again uses several view angles and also incorporates a detailed physics model of the sound-tissue interaction. Due to the simplified approach of B-scanning, the resulting images are generally incomplete and exhibit poor resolution [47]. For many years, however, this was the only type of ultrasound imaging that was commercially feasible. As such, B-scanners have been widely accepted in healthcare practice.

B-scan imaging does afford the flexibility to image a variety of tissues throughout the body. It is not necessary to gather information with transmitters and receivers positioned in a circle around the tissue. Rather, insonification and scatter detection are done from the same side as the instrument head is swept by the clinician, and a small beam of ultrasound insonifies the object. An image is formed by displaying the backscattered signal as a function of both beam direction and sound time-of-flight (TOF), or rather the time required for the sound energy to travel from the source, backscatter from the tissue and undergo detection. B-scan imaging provides qualitative tissue information and produces images that approximately delineate tissue interfaces. The patient is supine, and scans are recorded in different directions as the operator manually moves the ultrasound probe. Because only backscattered sound waves are recorded, image reconstruction is based on only a small portion of scattered sound. As such, the images generally suffer from distortions and poor resolution compared to x-ray mammography and MRI [43].

B-scan image reconstruction attempts to determine an approximation to the reflectivity function of the insonified object, which is defined by

$$R = \gamma_\kappa(\mathbf{r}) - \gamma_\rho(\mathbf{r}) \tag{1.10}$$

Thus, if the tissue compressibility and density change similarly in space, the image will show no change. Note that the reflectivity function and the reflection coefficient are two entirely different, yet related, entities. First of all, R refers to scatter, while C_R refers to reflection. Recall that reflection takes place when ultrasound insonifies acoustic impedance interfaces with dimensions greater than λ. When the interface dimensions are smaller than λ, scattering occurs. This redirected sound energy spreads out in all directions about point scatterers in the object. Sound energy that happens to travel back to the source location from throughout the tissue is a measure of the reflectivity function of the object[1]. Similarly, ultrasound that is reflected from a large interface is a measure of the reflection coefficient of the interface. Essentially, reflected ultrasound is a subset of the full complement of sound that is backscattered from all parts of the tissue. If one were to integrate the backscatter that arises due to R for all points along an interface curve only, C_R could then be extracted.

Due to significant support in industry for B-scanner development, the techniques have become very sophisticated over the years. Developments in transducer design, signal processing techniques and image analysis techniques have helped to raise conventional ultrasound scanning to what is generally a useful imaging modality. Furthermore, the extension of B-scanning to 3D imaging that has occurred in the past 5-7 years has vastly improved the images that are possible with reflection data. It is beyond the scope of this introduction to go into great detail regarding the theory behind B-scan imaging. Hence, only key elements will be discussed and the reader is referred to References [29] and [45] for further information.

A brief analysis of B-scan imaging is a useful introduction to wave mathematics and ultrasound principles. As an example, consider an ultrasound beam that is limited to a narrow region along a line within the object being imaged, as illustrated in Figure 1.2. To simplify the explanation, attenuation due to tissue is not being considered here. The tissue gives rise to spherically-expanding waves from scatter points within its boundaries. The insonification pulse is very short, and hence there is a direct relationship between when the reflected wave is detected and the distance, x, from which it originated in the object space.

Using simple wave mathematics, the incident pulse can be written as

$$\psi_i(x,y) = \begin{cases} p_t(t-\frac{x}{c}) & \text{for } y=0 \\ 0 & \text{elsewhere} \end{cases}$$

where p_t is the original pulse waveform and c is the average speed of sound in this exper-

[1]The relation between backscatter and R is mathematically derived in Section 2.2.2

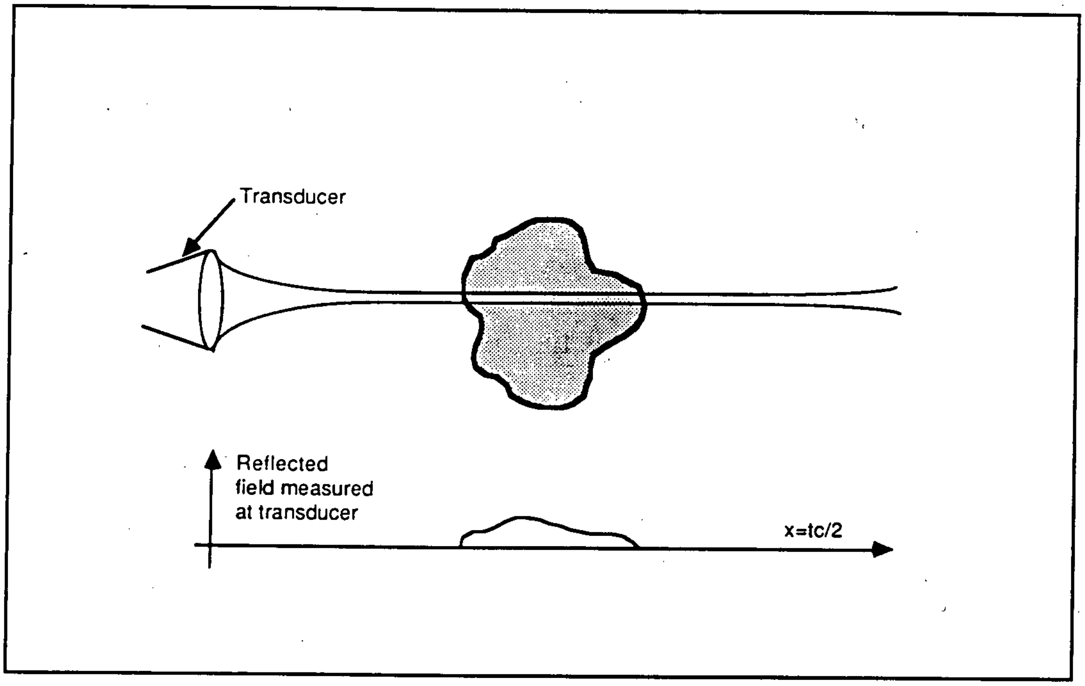

Figure 1.2: This schematic illustrates the process by which B-scan imaging is performed. The ultrasound beam is limited to a narrow region along a line, which is scanned across the tissue.

iment. This equation describes a pulse traveling along the x-axis, which is perpendicular to the transducer face. At an arbitrary point (x, y), some fraction of the incident field is scattered back to be detected by the transducer. The fraction of scatter is given by the reflectivity function, R, and the scatter field at the location $(x, y = 0)$ will be approximately given by

$$\psi(x, y = 0) = R(x, y = 0)p_t(t - \frac{x}{c}) \tag{1.11}$$

As this scatter field, ψ, travels back to the transducer, it will be reduced in amplitude due to spherical spreading of the beam. It also acquires a further time delay of $\frac{x}{c}$ to account for the additional travel time. Considering a 2D model of sound scatter, the energy in the field is decreased by a factor of $\frac{1}{x}$. Thus the field amplitude is decreased by a factor of $\frac{1}{\sqrt{x}}$, and the final detected scatter field that is reflected from the location $(x, y = 0)$ can be expressed as

$$\psi_s(\text{due to point x, y} = 0) = R(x, y = 0)\, p_t(t - 2\frac{x}{c})\frac{1}{\sqrt{x}} \tag{1.12}$$

This term is then integrated over all scatter points along the narrow beam line (the x-axis), resulting in a total scattered field at any time t of

$$\psi_s(t) = \int R(x, y = 0)\, p_t(t - 2\frac{x}{c})\,\frac{1}{\sqrt{x}}\,dx \tag{1.13}$$

Further reduction of mathematics is possible if the insonification pulse can be approximated by an impulse, or delta function. The total scattered field can then be approximated by

$$\psi_s(t) \;=\; \int R(x, y = 0)\,\delta(t - 2\frac{x}{c})\,\frac{1}{\sqrt{x}}\,dx \tag{1.14}$$

Making a change of variable given by $\tilde{x} = \frac{2x}{c}$ yields

$$\begin{aligned}\psi_s(t) &= \frac{c}{2}\int R(\frac{c\tilde{x}}{2}, y = 0)\,\delta(t - \tilde{x})\,\frac{1}{\sqrt{\frac{c\tilde{x}}{2}}}\,d\tilde{x} \\ &= \sqrt{\frac{c}{2t}}\,R(\frac{tc}{2},\, y = 0)\end{aligned} \tag{1.15}$$

Evidently, in the case of impulse insonification there is a direct relation between the scatter field that is detected at time t and the tissue reflectivity function, R, at distance $x = \frac{tc}{2}$. Substituting $t = \frac{2x}{c}$ yields an estimate of the reflectivity function given by

$$\tilde{R}(x, y = 0) = \sqrt{\frac{4x}{c^2}}\,\psi_s(\frac{2x}{c}) \tag{1.16}$$

Recalling that the ultrasound field employed in B-scan imaging is a narrow beam that travels along a line, it is evident by Equation 1.16 that each position of the transducer maps out an estimate of the reflectivity function along the corresponding beam line. By scanning the transducer across the object, a set of scan lines are built up to provide a picture of the total $\tilde{R}$. The resolution of the $\tilde{R}$ image is dependent upon both the time duration of the incident pulse (range resolution) and the width of the ultrasound beam (lateral resolution).

1.7.2 3D Ultrasound

The basis behind this imaging modality is that B-scan images at various angles are placed together in a coregistration process to yield an image of the approximate reflectivity function with higher resolution than in conventional B-scanning. In 3D ultrasound imaging, data are obtained by recording conventional 2D B-scans at various orientations, together with information about the position and orientation of the ultrasound scanning head for each corresponding scan. This general idea is illustrated in the schematic of Figure 1.3, which illustrates 3 such B-scans being recorded at different orientations. Each 2D B-scan is acquired in the typical fashion with smooth sweeps of the probe, to yield a relatively planar view of the tissue. Multiple sweeps are then compounded with knowledge of the position and orientation of the probe during each B-scan. A common coordinate system is maintained throughout the imaging process by connecting a transmitter to the ultrasound scanning head, which communicates the scan orientation to the ultrasound machine. Two examples of devices for this purpose are the Polhemus Fastrak™ and the Ascension Bird™ sensor. Using data from non-parallel scan planes, tissue volume reconstructions can be created with algorithms for fitting surfaces to incomplete noisy interfaces. The resolution that is obtainable with current systems is on the order of 0.2 mm. As is illustrated in the example in Figure 1.4, excellent images of tissue boundaries have been achieved via 3D ultrasound.

During the past 5-10 years, the success of 3D imaging in academic research has motivated several imaging technology companies to develop commercial systems. Currently, these companies include: ATL, ALOKA, General Electric, Kretz, Medison, Medison America, and Tomtec. However, although 3D ultrasound is gaining popularity for its clear

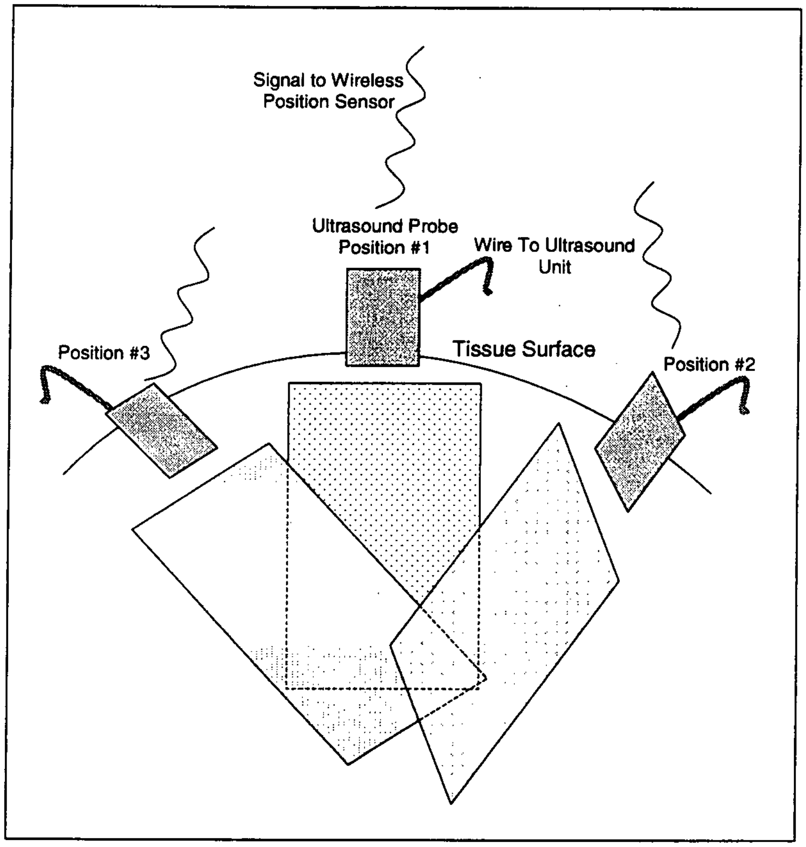

Figure 1.3: This schematic illustrates the general method of acquiring 3D ultrasound data.

pictures of gross tissue boundaries, it does not have the potential for use in quantitative imaging of tissue parameters such as density, compressibility, or scattering cross-section, all of which may be useful for early cancer detection. Rather, these backscatter images provide high resolution images of tissue reflectivity. Thus, 3D ultrasound cannot detect variations in density and compressibility when these parameters are changing similarly in space.

1.8 Computerized Tomographic Imaging

Tomography refers to the cross-sectional imaging of some physical parameter of an object using data that are collected by investigation of the object from various angles.

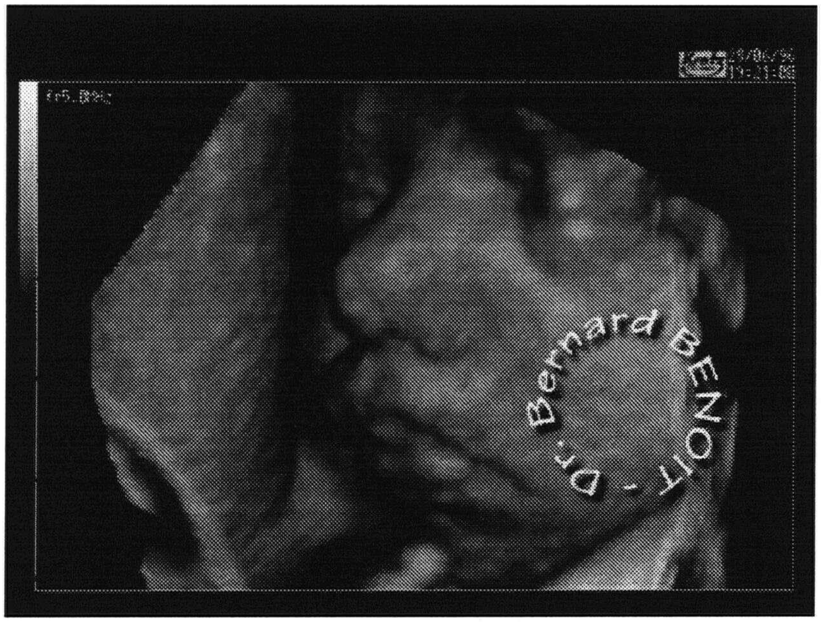

Figure 1.4: This figure illustrates an excellent example of a 3D image of fetus at 32 weeks. This work was done by Dr. Bernard Benoit [9]

In describing this type of imaging as cross-sectional, it is meant that 2D slices of a 3D object are reconstructed. Most medical imaging systems perform imaging in this way, and many build up a 3D view of the object by stacking consecutive 2D slices [4, 47]. Data that is collected at each angle about the object is termed a projection. The data are acquired via two means: either through illumination with a probing field or through detection of emissions from a radioisotope administered to the patient. In the former situation, the probing field can take many forms, such as acoustic energy (ultrasound), electromagnetic energy (microwaves), ionizing radiation (x-rays), and magnetic energy (magnetic resonance imaging). When a probing field is employed, the data can be collected either through reflection of the field from the object or transmission of the field through it. The latter is accompanied by scattering. The term computerized is used to describe this type of imaging because the reconstruction of the image is based on a mathematical algorithm that combines the information from various angles to yield an image of some parameter.

The method of reconstructing an object function from its projections was developed by Radon in 1917 [47]. However, use of the concept was minimal until the 1960's with the invention of the x-ray CT scanner by Hounsfield. The advent of sophisticated reconstruction algorithms for x-ray CT quickly yielded images that were highly accurate in the sense that morphological details were unambiguous and in excellent agreement with anatomical features. The success of x-ray CT motivated the development of CT methods in nuclear medicine, magnetic resonance, ultrasound and microwaves.

1.8.1 Diffracting Versus Nondiffracting Sources

X-ray CT, magnetic resonance imaging (MRI) and tomography with radioisotopes are all imaging modalities that employ nondiffracting energy sources. In other words, the probing or emitted energy travels in straight lines with very little scatter. The image reconstruction algorithms are based on models of straight line energy propagation. This is not the case with ultrasound and microwaves, which are classified as diffracting sources of energy. When an object is illuminated with a diffracting source, the energy waves are scattered in every direction from inhomogeneities that are much smaller than the wavelength of the waves. This is termed diffraction, and it must be incorporated into the model of tissue/energy interaction upon which the image reconstruction algorithms are based.

In experiments with nondiffracting sources, any given data point in a tomographic projection at a particular angle is equal to the integral of the object parameter in question along a line through the object. This type of imaging is also termed straight ray tomography. Examples of projections in straight ray tomography are illustrated in Figure 1.5. The parallel projection is the simplest in concept, and Figure 1.5 illustrates how two projections of this type are built up for a typical tissue object function, $f(x, y)$. The source is extended linearly, and the source field travels along the parallel arrow lines

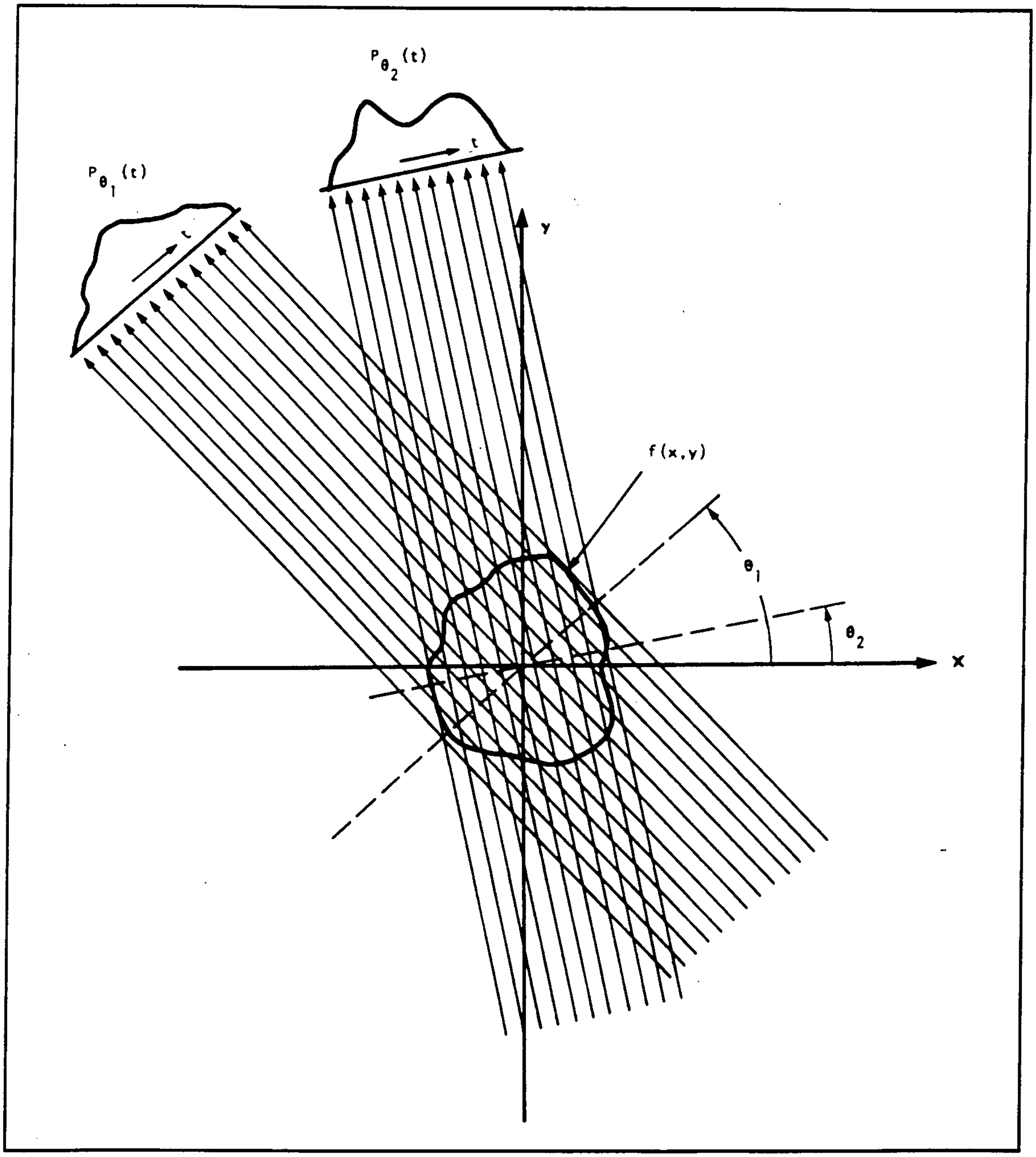

Figure 1.5: This figure illustrates how to construct two parallel tomographic projections for a nondiffracting source.

shown. The integrals are performed along these lines to produce the projection data $P_{\theta_1}(t)$ and $P_{\theta_2}(t)$ at angles θ_1 and θ_2, respectively. Similarly, other geometries can be used, such as fan beam, in which the source is a point instead of a linearly extended object.

This is not the case with diffracting sources such as ultrasound and microwaves. The probing energy field does not travel along rays, and image projections do not represent integrals of an object function along straight line paths. The projections in fact have an entirely different meaning, and the development of corresponding image reconstruction algorithms involves solving a wave equation, to be discussed in more detail in Section 2.2.1.

1.8.2 Ultrasound Computed Tomography

It is desirable to produce highly resolved and accurate quantitative images of tissue using ultrasound, in which one can assign a direct correspondence between the brightness of the image pixels and the value of a particular tissue parameter. Ultrasound computed tomography has the potential to provide such images, and as such has become a growing field of research. UCT involves the automated scanning of tissue at many different angles using a computer-controlled setup. Thus, the breast is well suited for UCT as it allows inspection from all angles when the patient is lying prone. Various tomographic methods look at different aspects of the interacting ultrasound, such as how much sound is reflected or scattered and in what direction. Depending on the type of tomography performed, this imaging modality can provide information such as the variation of sound speed throughout the tissue, the compressibility of the tissue, and the amount of sound absorbed or scattered by the tissue. The goal is to use this information to detect cancer in the breast.

At the very least, UCT systems could potentially provide an adjunct to x-ray mammography. Although the cost of building a system would not warrant its use simply in differentiating cysts from breast lesions, where conventional ultrasound scanners perform well, UCT could be of extensive use in tissue characterization for the early detection of breast cancer. This would have the effect of reducing the number of unnecessary and often disfiguring biopsies. Fewer women would have to wait to undergo a biopsy and to receive test results. The ultimate goal of UCT research, however, is the development of high resolution, noninvasive imaging systems for breast cancer screening in situations where x-ray mammography produces questionable results. Research by various investigators indicates that UCT has the potential to provide accurate tissue information that can be used for early breast cancer detection [22, 32, 35, 46, 53].

The Early Years

Ultrasound tomography was first applied experimentally by J.F. Greenleaf and his colleagues at the Mayo Clinic in the mid 1970's [37]. These first algorithms were adopted from transmission x-ray CT. Hence, straight paths with no scattering were assumed as a model for ultrasound propagation. However, since the wavelength of the sound used in UCT is roughly the same size as the diameters and spacing of the tissue structures that scatter the sound waves, diffraction effects are in fact significant. Thus, these initial algorithms produced images that could not be used to reliably detect tumors [35].

Reflection Tomography and Diffraction Tomography

These early attempts in the field indicated that tomography with a diffracting energy source requires an entirely different approach in terms of how the data projections are mathematically modeled. As such, new reconstruction algorithms were developed that included the solution of the wave equation, which was used to model sound propagation more rigorously. Two imaging modalities that arose from this work are known as diffraction tomography (DT) and reflection tomography (RT). Diffraction tomography is the term generally used to describe UCT algorithms that make use of sound that is scattered at angles other than 180°. Reflection tomography, on the other hand, is based only on backscattered ultrasound. Although this is similar to B-scan imaging, the modalities are in fact very different due to the inclusion of wave mathematics in the RT algorithm.

Reflection tomography is simple in terms of imaging geometry. It is not necessary to encircle the object being imaged with an annular array of transducers, since insonification and scatter detection are done on the same side with the same transducer. This can alternatively be viewed as a limitation since only a portion of the ultrasound is in fact reflected from tissue interfaces directly back to the ultrasound scanning head. The method thus neglects a large percentage of sound intensity on the order of 99% that is scattered into all other angles about the interface. Reflection tomography is also limited in terms of what information it can yield. Diffraction tomography aims at providing images of certain object parameters through the solution of different wave equations. Examples of such parameters are density, compressibility and refractive index, $n = \frac{c_0}{c(\mathbf{r})}$, where c_0 is the speed of sound in water and $c(\mathbf{r})$ is the spatially varying speed of sound in the region in question. The mathematics in reflection tomography reduce to an image of reflectivity only.

Much of reflection tomography theory has been developed by Norton and Linzer. Reference [66] presents detailed derivations of their reconstruction algorithms employing point sources. Algorithms employing planar sources can be found in Reference [47]. A key component to the RT algorithms is the use of broadband pulses, which have a short wavelength on the order of 1 mm. As will become evident, this allows for the measurement of line integrals through the object reflectivity function. These integrals are not necessarily taken along a straight path. Consider the example illustrated in Figure 1.6, in which a single point transducer operating in pulse-echo mode insonifies an object with spherically divergent pulses. The received echo amplitude, β, measured at time t, is the sum of all reflections from scatter points a distance of tc from the transducer, where c is the average speed of sound in the media that are being investigated. This

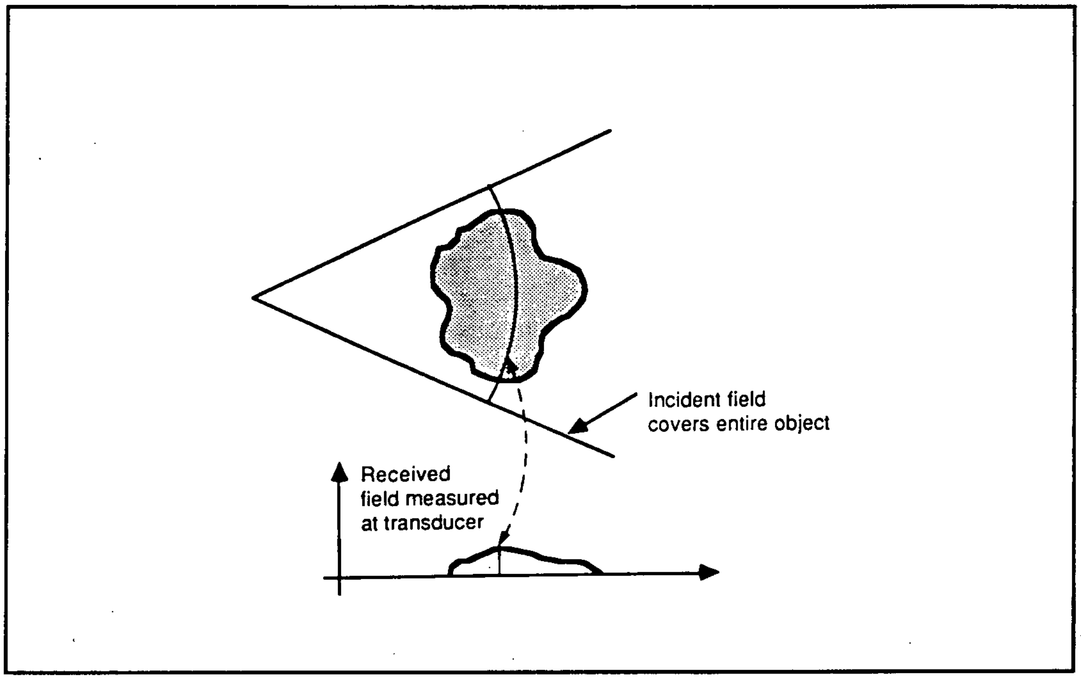

Figure 1.6: This figure illustrates the method of reflection tomography with point sources.

localization of scatter points is made possible by the short wavelength of the ultrasound pulses. The reflected signals that add up to create β are directly proportional to the reflectivity function at the corresponding scatter points. Hence, this type of tomography measures some function of R over circular arcs. In Figure 1.6, the measurement point with amplitude β is the sum of all reflection contributions over the arc in the incident ultrasound beam. It should be noted that there is of course some error inherent in this simple model due to variances in the speed of sound throughout the propagation media.

Diffraction tomography is more general than reflection tomography in that the ultrasound scatter recorded for image reconstruction is not limited to pulse-echo energy. Ultrasound propagation is again modeled with a wave equation. This type of imaging has been developed over the last 15 years by a number of groups [22, 30, 36, 53, 80]. The scattering process is analyzed in terms of the spatially dependent tissue density, $\rho(\mathbf{r})$, and compressibility, $\kappa(\mathbf{r})$. From this information, different mathematical techniques can be used to compute $\rho(\mathbf{r})$ and $\kappa(\mathbf{r})$ given knowledge of the sound waves scattered at many angles. Several groups have worked to develop various DT mathematical techniques, which are generally 2D approaches due to the complex nature of the physics involved [22, 36, 53, 80].

As will become evident in Section 2.2, the solution of the wave equation in diffraction tomography is a nonlinear problem. Consequently an exact analytical solution does not exist, and the search for a suitable approximate solution is a difficult task. There are two approaches to this problem in DT. The first involves the use of iterative techniques to solve the wave equation. However, such techniques are generally too computationally intensive for real-time imaging and have thus had limited success [11, 16, 17]. A second approach and far more common approach involves perturbation methods that assume tissue is a weak scatterer of sound [10, 21, 32, 46, 53, 80, 88]. Either the Born and Rytov approximations can be applied to simplify the mathematics and make the wave equation solvable. In the Born approximation, the interacting sound field is assumed to be equal to the incident field. In the Rytov approach, one assumes that the phase shift between the incident and scattered sound fields is very small. In short, the tissue is assumed to be a weak scatterer of sound, and the ultrasound field is not changed significantly by the scattering process. These techniques have the potential to provide useful results with little computation time, which is an important aspect of any clinically-viable imaging application.

The final key feature of both RT and DT algorithms is that ultrasound reflection or scatter data recorded at different angles yields a subset of data points in the Fourier space of the image that is being reconstructed. By taking data at more angles, the Fourier space is filled in until enough points are known to determine the corresponding image.

Algebraic Reconstruction Techniques

The algebraic reconstruction technique differs from the tomographic methods described thus far in that data from different projections are built up in the physical space of the image rather than in its Fourier space. A measure of the image is stored as a vector of unknowns, given by $\mathbf{x}$, and a measure of the scatter data is stored in another vector, given by $\mathbf{y}$. A model of the tissue-sound interaction physics is then used to devise a system of linear equations that relate $\mathbf{x}$ to $\mathbf{y}$. These equations comprise a set of simultaneous linear equations of the form

$$\mathbf{y} = \mathbf{A}\mathbf{x} \tag{1.17}$$

The elements of $\mathbf{x}$ are therefore unknown, and the aim is to devise a system with more equations than unknowns and then solve the system iteratively for $\mathbf{x}$. Evidently, the success of the method depends on two factors: first, how well the physics model describes reality, and second, how well the system converges iteratively on a valid $\mathbf{x}$.

Although this method is conceptually simpler than the Fourier space methods described previously, algebraic reconstruction techniques are generally too slow for use in most applications. However, it does appear to hold promise in cases where data from only a limited number of view angles are available. In experiments with small gelatin phantoms by Ladas and Devaney, the use of an ART was found to be superior to conventional diffraction tomography methods when data were acquired at only 26 angles, instead of an optimal 200 views [53].

Chapter 2
Theoretical Background

The development of a diffraction tomography algorithm requires several key steps. First, a source and detector of ultrasound must be chosen and the behavior of each must be well known and described by a model. These transducers must also be feasible to use in experimental work. Second, there must be a detailed understanding of the physics that describes how ultrasound propagates through tissue. This process is governed by a wave equation whose solution is nonlinear, thus adding to the difficulty of the model. Frequency dependent attenuation further complicates the problem. The third key step involves choosing assumptions that render the problem linear while maintaining the usefulness of the model in describing at least some subset of imaging situations. In the fourth step, the model of sound propagation is used to develop an image reconstruction algorithm that combines scatter data from different projections into an image of a specific tissue parameter.

In this thesis, the steps outlined have been taken to develop a prototype pulsed UCT system aimed at investigating the spatially varying density, $\rho(\mathbf{r})$, and compressibility, $\kappa(\mathbf{r})$, of both minimally attenuating and attenuating objects immersed in a background fluid, which is water. The algorithms yield images of the functions $\gamma_\rho(\mathbf{r})$ and $\gamma_\kappa(\mathbf{r})$, given by

$$\begin{aligned}\gamma_\rho(\mathbf{r}) &= \frac{\rho(\mathbf{r}) - \rho_0}{\rho(\mathbf{r})} \\ \gamma_\kappa(\mathbf{r}) &= \frac{\kappa(\mathbf{r}) - \kappa_0}{\kappa_0}\end{aligned} \tag{2.1}$$

where κ_0 and ρ_0 are the compressibility and density of the water. As was noted in Chapter 1, the denominator is spatially varying in the case of $\gamma_\rho(\mathbf{r})$ and constant in the $\gamma_\kappa(\mathbf{r})$

definition, and these particular functions result from the solution of the wave equation, to be discussed in Section 2.2.1. The basis for this work is the paper by Blackledge *et al* [10]. After some modifications, the algorithm cited in this paper was used to test pulsed UCT for minimally attenuating objects. The corresponding physics model was also the point of departure for the development of an algebraic reconstruction technique that includes a frequency dependent attenuation correction. The theory behind these image reconstruction algorithms is discussed in the following sections.

2.1 Nonplanar Sources and Pulsed Ultrasound

The theoretical basis for this thesis work assumes the use of individual line sources, while the majority of UCT methods to date have assumed that tissue is insonified with plane waves [21, 22, 32, 47, 48]. The use of planar sources is somewhat troublesome from a practical point of view because plane waves are difficult to create [32, 66]. A truly plane wave is emitted by an ideal plane wave transducer, which is flat in shape and large in extent compared to the object being insonified. Such a transducer does not exist to date, and hence the conventional method of creating a plane wave is through the use of an array of point sources. The transducers are excited by the same signal, and their individual spherical fields are superimposed to yield an approximation to a plane wave [47]. The characteristics of a plane wave detector are likewise approximated by summing all the signals that the point transducers see.

The lines sources used in this work emit pulsed ultrasound fields, and this choice was made after an extensive literature review. The use of pulsed ultrasound is a relatively novel approach in the field of computed tomography. To date, experimental UCT systems have employed continuous wave ultrasound only, and the vast majority of diffraction tomography algorithms also assume CW ultrasound [10, 32, 53, 80, 88]. However, the phase shift ambiguity problem associated with the use of continuous-wave ultrasound has limited the capabilities of these methods. In an imaging experiment, an ultrasound wave undergoes a phase shift due to propagation through regions with different acoustic impedances. In continuous wave UCT, the phase shift of the scattered field at any location in question is measured via quadrature detection [21, 32, 47, 53, 80]. This processing decomposes a narrowband signal, $v(t)$, with a center frequency of f_0 into the following sum:

$$v(t) = v_c(t)\ \cos(2\pi f_0 t) + v_s(t)\ \sin(2\pi f_0 t) \tag{2.2}$$

According to Fourier Theory, $v_c(t)$ and $v_s(t)$ are directly related to the real and imaginary parts of the Fourier Transform (FT) of v_c, from which the phase can in turn be calculated. This is compared to the phase of the insonifying wave, and the phase shift is determined for use in image reconstruction. However, the measured phase shift could be in error by a factor of 2π due to the 2π modulo periodic nature of the ultrasound wave. Hence there is an ambiguity in determining the phase shift, and image reconstruction is based on erroneous data. Furthermore, this error becomes increasingly large as the object being imaged increases in size. Hence, experimental work in continuous wave UCT has generally been limited to the investigation of objects that are on the order of 10 wavelengths in diameter (4-6 mm wide) [21, 32, 47, 53, 80]. The severity of the problem is illustrated in Reference [47], in which computer simulations concluded that cylinders immersed in water could be properly reconstructed only if the phase change across the object was less than 0.8π. Given a transducer operating frequency of 3 MHz and a change in the index of refraction of 20% relative to water, proper reconstructions are limited to objects that are less than 0.5 mm in radius [47]. Several phase-unwrapping techniques have been developed in an attempt to correct this problem, with limited success [47].

In contrast, pulsed ultrasound computed tomography insonifies objects with nonperiodic transient fields. Quadrature detection is not used to measure phase information. Rather, the transient scattered field is detected and Fourier Transformed. There is also always a reference point on the ultrasound pulse which can be used to determine any shifting that occurs upon propagation through an object. Comparison of the scatter Fourier spectrum with the incident field Fourier spectrum yields unambiguous phase information for use in image reconstruction.

Pulsed UCT also has other advantages over CW imaging. For instance, with transient fields one can simultaneously collect multifrequency data since a pulse is composed of a spectrum of frequencies within some particular band limit. Multifrequency data could yield more information about a tissue since a collection of sound waves with different frequencies interact simultaneously with the object. Also, the band limits generally include higher frequencies than the single frequency used in CW UCT. Higher frequencies can reconstruct smaller features on the order of $\lambda/2$, to within the physical limitations of the algorithms being used. Finally, both tissue compressibility and density can be determined with the methods for pulsed tomography used in this thesis, while CW UCT generally reconstructs only one specific parameter.

Despite these advantages, only a handful of groups have studied pulsed ultrasound computed tomography, and the focus has been theoretical rather than experimental. The major factor that has limited research in this field is frequency-dependent attenuation [68]. Data in any UCT experiment must be corrected in magnitude for the attenuation that occurs as the sound waves travel through tissue. The attenuation of a particular sound wave or portion thereof is in turn dependent upon both the total distance it travels through regions of different attenuation coefficient, particularly tissue, as well as the frequencies found in the sound wave. Evidently, for CW ultrasound, the correction process is simpler since the wave is composed of mostly one frequency. For pulsed UCT, a spectrum of frequencies is used; the attenuation coefficient therefore depends on the frequency region under analysis. This thesis includes two approaches towards solving this problem. One approach affords only an approximate correction that is based on the average distance that ultrasound travels through tissue and water, respectively in a given experiment. The second approach is more rigorous and includes attenuated propagators that describe the propagation of ultrasound from the source to detector via all possible scatter points with attenuation due to water and tissue included. These methods are outlined in detail in Sections 4.1 and 4.2, respectively.

2.2 Minimally Attenuating Objects

The method by Blackledge *et al* for reconstructing images of minimally attenuating objects was the starting point for the work involved in this thesis. This method for producing images of compressibility and density using pulsed UCT is classified as a direct Fourier method. That is, information in the Fourier domain of the image is built up from projections at various angles until the space is characterized sufficiently well to make inversion possible and yield an image. This requires the use of methods for interpolating data in Fourier space from a radial grid to a Cartesian grid, which is discussed in Section 4.6.

This section presents the highlights of the physics model development, while full details of the derivation can be found in Appendix A. The derivation makes reference to three key resources: the paper by Blackledge *et al* [10], the paper by Norton and Linzer [66], and Section 6.2 of the book by Morse and Ingard [62]. Minor errors were found in the work of Morse and Ingard, while several errors were found in the paper by Blackledge *et al*. The errors appear to be primarily typographical, since the final result is the same in both this thesis and the paper by Blackledge *et al*. To aid the reader in following the derivations, errors in the references have been noted.

2.2.1 The Physics Basis

In this reconstruction algorithm, the tissue being imaged is described by the Chernov Equation:

$$\nabla \cdot (\frac{1}{\rho(\mathbf{r})} \nabla p(\mathbf{r}, t)) = \kappa(\mathbf{r}) \frac{\partial^2}{\partial t^2} p(\mathbf{r}, t) \tag{2.3}$$

$p(\mathbf{r}, t)$ is the pressure field at any time, t, during the experiment and at any location, $\mathbf{r}$, within the image region [10, 62, 66]. Note that this equation is expressed incorrectly in the paper by Blackledge *et al*, with a negative sign on the right hand side. Since the 3D problem is difficult to solve, this theory considers 2D sound pressure fields only, which is a conventional approach in UCT [21, 32, 47, 53, 80]. Thus

$$\mathbf{r} = x\hat{\mathbf{x}} + y\hat{\mathbf{y}} \tag{2.4}$$

where $\hat{\mathbf{x}}$ and $\hat{\mathbf{y}}$ are unit vectors in the xy-plane. Equation 2.3 models tissue as a nonviscous, compressible fluid. Viscosity refers to a fluid's resistance to flow due to internal frictional forces. A more viscous fluid flows more slowly than a fluid with less viscosity due to increased internal friction. Although certain fluids in the body are considered viscous, such as lymph fluid, the most prevalent human biological fluids have relatively low viscosity in the healthy body. For instance, it is well known that blood generally has low viscosity, but can become more viscous in the presence of certain disorders such as leukemia Polycythemia vera [92]. Furthermore, the constituents of the human body have a high water content, ranging from 50-65% (women 50-60%, men 60-65%), and water has a low viscosity at the temperatures in the human body [55]. Hence, the modeling of soft tissue as a nonviscous fluid of spatially varying ρ and κ is a valid approach that has been applied by several groups [23, 32, 47, 66].

To both sides of Equation 2.3, the following term is added

$$\kappa_0 \frac{\partial^2}{\partial t^2} p(\mathbf{r}, t) - \frac{1}{\rho_0} \nabla^2 p(\mathbf{r}, t) \tag{2.5}$$

Note that the step cited here in the reference by Morse and Ingard is incorrect in that the time derivative includes a factor of ρ and thus has improper units. In Equation 2.5, the substitution $c_0 = (\kappa_0 \rho_0)^{-\frac{1}{2}}$ is made, where c_0 is the speed of sound in the background fluid, and the expression is further reduced to yield an equivalent wave equation given by:

$$\nabla^2 p(\mathbf{r}, t) - \frac{1}{c_0^2} \frac{\partial^2}{\partial t^2} p(\mathbf{r}, t) = \frac{\gamma_\kappa(\mathbf{r})}{c_0^2} \frac{\partial^2}{\partial t^2} p(\mathbf{r}, t) + \nabla \cdot (\gamma_\rho \nabla p(\mathbf{r}, t)) \tag{2.6}$$

In the paper by Blackledge *et al*, this equation is quoted incorrectly with a factor of -1 in the time derivative on the right hand side. Equation 2.6 is a time dependent wave equation with a forcing term that is a function of $\gamma_\kappa(\mathbf{r})$ and $\gamma_\rho(\mathbf{r})$. The Fourier Transform is then applied to both sides of this equation to yield

$$\nabla^2 p(\mathbf{r},\omega) + k^2 p(\mathbf{r},\omega) = -k^2\gamma_\kappa(\mathbf{r})p(\mathbf{r},\omega) + \nabla\cdot(\gamma_\rho(\mathbf{r})\nabla p(\mathbf{r},\omega)) \tag{2.7}$$

where $k = \omega/c_0$ is the angular wave number in the background fluid. Note that the expression quoted in the chapter by Morse and Ingard is incorrect in that the $\nabla\cdot(\gamma_\rho(\mathbf{r})\nabla p(\mathbf{r},\omega))$ term includes an extra negative sign. The solution to Equation 2.7 at any detector position $\mathbf{r} = \mathbf{r_d}$ is given by

$$\begin{aligned} p(\mathbf{r}_d,\omega) = p_0(\mathbf{r}_d,\omega) &+ k^2\int_{\Re^2} g(\mathbf{r}|\mathbf{r}_d,k)\gamma_\kappa(\mathbf{r})p(\mathbf{r},\omega)\mathrm{d}^2\mathbf{r} \\ &- \int_{\Re^2} g(\mathbf{r}|\mathbf{r}_d,k)\nabla\cdot(\gamma_\rho(\mathbf{r})\nabla p(\mathbf{r},\omega))\mathrm{d}^2\mathbf{r} \end{aligned} \tag{2.8}$$

Note that the signs preceding the two integrals in the paper by Blackledge *et al* are both opposite to what they should be. $p_0(\mathbf{r}_s,\omega)$ is the Fourier Transform of the incident ultrasound field at any detector position $\mathbf{r}_d$, and $g(\mathbf{r}|\mathbf{r_s},\mathbf{k})$ is the 2D Green's function that describes wave propagation in two dimensions in the background fluid. For outgoing waves, the 2D Green's function in the absence of attenuation has the form

$$g(\mathbf{r}|\mathbf{r}_d,k) = -\frac{i}{4}H_0^1(k|\mathbf{r}-\mathbf{r}_d|) \tag{2.9}$$

where H_0^1 is the Hankel function of the first kind. Note that the solution quoted in the reference by Blackledge *et al* is incorrect by a factor of -1, which results in the wrong pulse shape upon propagation of the incident field. The Green's function determines the phase of the frequency components in the ultrasound wave. Phase in Fourier space determines the propagation time (and by extension the propagation distance) in physical space, so consequently the Green's function provides information regarding how far the pulse has propagated. Since attenuation is not included, the Green's function does not change the shape of the ultrasound pulse. Note that the Green's function is symmetric with respect to the interchange of $\mathbf{r}$ and $\mathbf{r}_d$. Stated equivalently, the field value measured by a detector at position $\mathbf{r}_d$ due to a source located at $\mathbf{r}$ is the same as the value that would be measured if the positions of the source and detector were switched. This is termed the *Principle of Reciprocity.* In terms of variable notation, this principle dictates that $g(\mathbf{r}|\mathbf{r}_d, k) = g(\mathbf{r}_d|\mathbf{r}, k)$.

Equation 2.8 is nonlinear in that the functional form of the total field p is not only being solved for, but it is also found within the integral sign. Thus, it is not possible to determine an exact analytical solution to Equation 2.8. As discussed in Section 1.8.2, two approaches are possible here. The less common approach uses iterative techniques to solve the equation in a computationally intensive manner. The difficulties associated with this approach have motivated most researchers to follow the perturbative Born or Rytov approaches, in which weak scattering is assumed in order to render Equation 2.8 solvable [10, 21, 32, 46, 53, 80, 88]. For the initial prototype development included in this thesis, the Born approximation has been used. It is applied at this point to yield

$$\begin{aligned} p(\mathbf{r}_d, \omega) \quad = \quad & p_0(\mathbf{r}_d, \omega) + k^2 \int_{\Re^2} g(\mathbf{r}|\mathbf{r}_d, k)\gamma_\kappa(\mathbf{r})p_0(\mathbf{r}, \omega)\mathrm{d}^2\mathbf{r} - \\ & \int_{\Re^2} g(\mathbf{r}|\mathbf{r}_d, k)\nabla \cdot (\gamma_\rho(\mathbf{r})\nabla p_0(\mathbf{r}, \omega))\mathrm{d}^2\mathbf{r} \end{aligned} \tag{2.10}$$

Note again that the signs preceding the two integrals in the paper by Blackledge *et al* are both opposite to what they should be, which is the error carried over from Equation 2.8.

The algorithm also assumes that the insonifying pulse is created by a line source (recall the model is 2D), which is generally considered to be a field that is easily obtainable in the lab [10, 32]. The incident field at any given location, $\mathbf{r}$, due to a source with position vector, $\mathbf{r}_s$, is written

$$p_0(\mathbf{r}, \omega) = A(\omega)g(\mathbf{r}|\mathbf{r}_s, k) \tag{2.11}$$

where $A(\omega)$ is the amplitude spectrum of the incident pulse. Of particular note is that the insonifying field has zero phase at the source location. The phase of all frequency components in the source then evolves in a periodic fashion between 0 and 2π as the field propagates away from the source. The incident pulse is also assumed to be band limited from Ω_1 to Ω_2 (between frequencies f_1 and f_2). The source and detector are also assumed to be significantly far from any point of origin of ultrasound scatter, located at $\mathbf{r}$ in the image space. As such, the following relation holds for $\mathbf{r}_j$ equal to $\mathbf{r}_s$ or $\mathbf{r}_d$:

$$|k||\mathbf{r}-\mathbf{r_j}| \gg \mathbf{1} \tag{2.12}$$

for every angular wave number, k, for which

$$\frac{\Omega_1}{c_0} \leq |k| \leq \frac{\Omega_2}{c_0} \tag{2.13}$$

This means that the object is placed in the far field region of both the source and detector. Equation 2.12 essentially has the effect of imposing a highpass filter in the temporal frequency space of the ultrasound signals. These assumptions allow the exact Green's function to be expanded in terms of a simpler function given by

$$\begin{aligned} g(\mathbf{r}|\mathbf{r}_j, k) &\approx \alpha S \\ \alpha &= i\frac{\exp(3i\pi/4)}{2\sqrt{2\pi}} \\ S &= \frac{\exp(ik|\mathbf{r}-\mathbf{r_j}|)}{(k|\mathbf{r}-\mathbf{r_j}|)^{\frac{1}{2}}} \end{aligned} \tag{2.14}$$

Note that the value of α quoted in the paper by Blackledge *et al* is incorrect by a factor of i, resulting in the wrong phase information. Next an expression for ∇S is required, whose derivation is outlined in Appendix B. The result is

$$\begin{aligned} \nabla S &= ik\hat{\mathbf{n}}_j S, \text{ for } |k||\mathbf{r}-\mathbf{r_j}| \gg \mathbf{1} \\ \hat{\mathbf{n}}_j &= \frac{(\mathbf{r}-\mathbf{r}_j)}{|\mathbf{r}-\mathbf{r}_j|} \end{aligned} \tag{2.15}$$

Combining all the assumptions and simplifications yields an expression for Fourier Transform of the total ultrasound field, $p(\mathbf{r}_s, \mathbf{r}_0, \omega)$, at any detector point

$$\begin{aligned} p(\mathbf{r}_d, \mathbf{r}_s, \omega) &\approx \alpha A(\omega) S(k|\mathbf{r}_d-\mathbf{r}_s|) + \alpha^2 A(\omega) k^2 I \\ I &= \int_{\Re^2} S(k|\mathbf{r}-\mathbf{r}_d|)(\gamma_\kappa(\mathbf{r}) - (\hat{\mathbf{n}}_d \cdot \hat{\mathbf{n}}_s)\,\gamma_\rho(\mathbf{r}))S(k|\mathbf{r}-\mathbf{r}_s|)\mathrm{d}^2\mathbf{r} \end{aligned} \tag{2.16}$$

Note that in the paper by Blackledge *et al*, the source and detector location vectors (referred to as $\mathbf{r}_0$ and $\mathbf{r}_s$, respectively) have been accidentally flipped in the corresponding equation.

An expression for $\hat{\mathbf{n}}_d \cdot \hat{\mathbf{n}}_s$ must now be derived, which requires the definition of an imaging geometry. Figure 2.1 illustrates the experimental UCT setup in which a source transducer with position vector $\mathbf{r}_s$ insonifies an object located about the origin with a pulse that has an amplitude spectrum $A(t)$. The scattered field is detected by a second transducer with position vector $\mathbf{r}_d$. Both the source and detector are situated at a distance a from the origin, and at angles of φ_s and φ_d, respectively. Note that φ_s is always larger than φ_d. The unit vectors $\hat{\mathbf{n}}_s$ and $\hat{\mathbf{n}}_d$ can then be written as

$$\begin{aligned} \hat{\mathbf{n}}_s &= \hat{\mathbf{x}}\cos(\varphi_s) + \hat{\mathbf{y}}\sin(\varphi_s) \\ \hat{\mathbf{n}}_d &= \hat{\mathbf{x}}\cos(\varphi_d) + \hat{\mathbf{y}}\sin(\varphi_d) \end{aligned} \tag{2.17}$$

Furthermore, φ_s and φ_d are related by

$$\theta = \varphi_d - \varphi_s + \pi \tag{2.18}$$

which leads to

$$\hat{\mathbf{n}}_s \cdot \hat{\mathbf{n}}_d = -\cos(\theta) \tag{2.19}$$

Note that the paper by Blackledge *et al* quotes a value for this expression that is incorrect by a factor of -1. Substituting this expression for the dot product into Equation 2.16 results in

$$\begin{aligned} p(\mathbf{r}_d, \mathbf{r}_s, \omega) &\approx \alpha A(\omega) S(k|\mathbf{r}_d - \mathbf{r}_s|) + \alpha^2 A(\omega)\, k^2 I \\ I &= \int_{\Re^2} S(k|\mathbf{r} - \mathbf{r}_d|)(\gamma_\kappa(\mathbf{r}) + \cos(\theta)\,\gamma_\rho(\mathbf{r})) S(k|\mathbf{r} - \mathbf{r}_s|)\, \mathrm{d}^2\mathbf{r} \end{aligned} \tag{2.20}$$

The first term in Equation 2.20 corresponds to the propagation of the incident field from the source to the detector, while the second term represents the scatter term. Essentially the scatter term is the sum of contributions from all scatter points in the

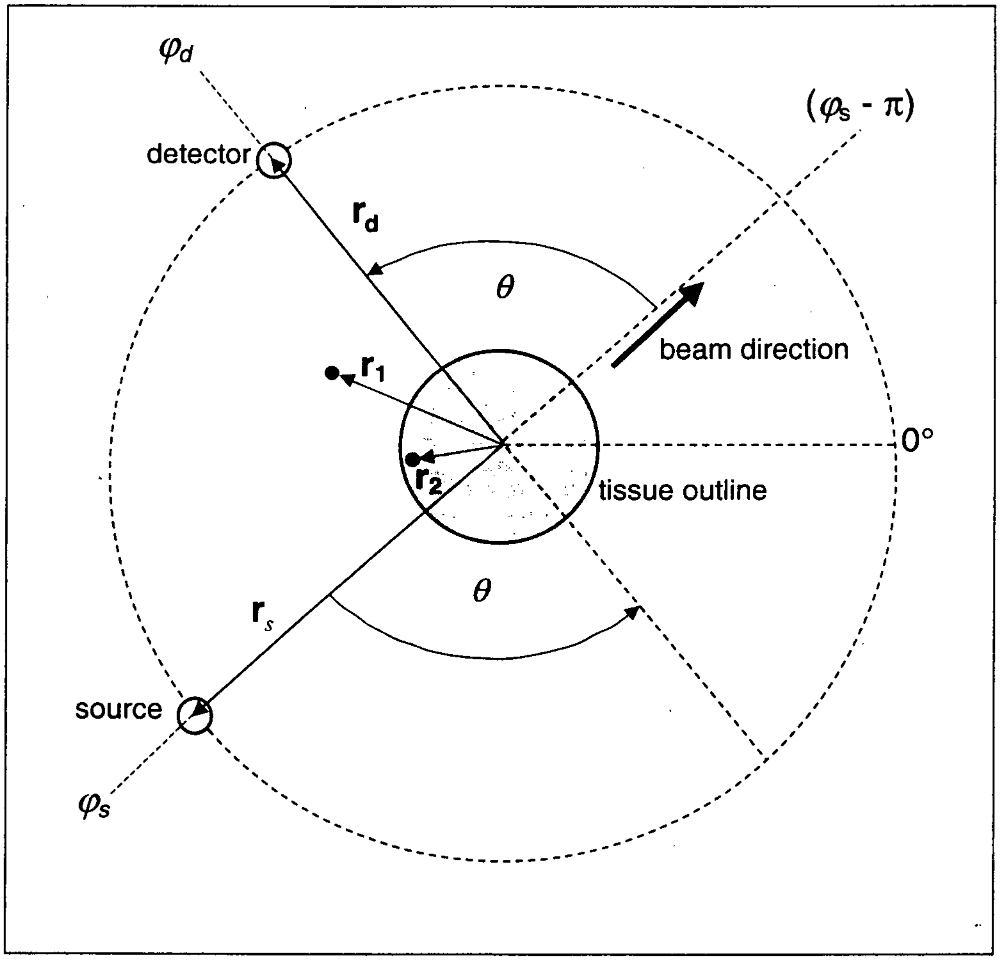

Figure 2.1: This schematic illustrates the UCT experiment geometry upon which the reconstruction algorithm is developed. Vectors $\mathbf{r}_1$ and $\mathbf{r}_2$ are two examples of $\mathbf{r}$, which is the location vector of scatter points within the image.

image space, each propagated first from the source to the scatter location and finally to the detector by the free space Green's function. Each scatter contribution is weighted by $(\gamma_\kappa(\mathbf{r}) + \cos(\theta)\gamma_\rho(\mathbf{r}))$. Use of the free space Green's function implies that second order scattering, in which the scatter contributions undergo additional scatter processes, is not considered. Also, attenuation is ignored in this model.

Equation 2.20 can be further simplified by once again applying the far field assumption, this time equivalently stated as

$$\frac{|\mathbf{r}|}{|\mathbf{r}_j|} \ll 1 \tag{2.21}$$

where again $\mathbf{r}_j$ is equal to $\mathbf{r}_s$ or $\mathbf{r}_d$. The analysis yields the following result:

$$S(k|\mathbf{r} - \mathbf{r}_j|) \approx \frac{\exp(ik(\hat{\mathbf{n}}_j \cdot \mathbf{r} + |\mathbf{r}_j|))}{k^{\frac{1}{2}}|\mathbf{r}_j|^{\frac{1}{2}}} \tag{2.22}$$

Note that this approximation results in a loss of phase information and ultimately is responsible for the relatively poor performance of the reconstruction algorithm. This will be discussed in more detail in Section 5.1.3. The application of 2.22 results in a final solution of

$$\begin{aligned} p(\mathbf{r}_d, \mathbf{r}_s, \omega) &\approx \alpha A(\omega)(S(k|\mathbf{r}_d - \mathbf{r}_s|) + \alpha J) \\ J &= k\frac{\exp(ik(|\mathbf{r}_d| + |\mathbf{r}_s|))}{(|\mathbf{r}_d||\mathbf{r}_s|)^{\frac{1}{2}}} \int_{\Re^2} \chi \\ \chi &= \exp(ik\hat{\mathbf{n}}_d \cdot \mathbf{r})(\gamma_\kappa(\mathbf{r}) + \cos(\theta)\gamma_\rho(\mathbf{r})) \exp(ik\hat{\mathbf{n}}_s \cdot \mathbf{r})\mathrm{d}^2\mathbf{r} \end{aligned} \tag{2.23}$$

2.2.2 The Reconstruction Algorithm

Substituting the expressions

$$\begin{aligned} \hat{\mathbf{n}}_d &= \hat{\mathbf{x}}\cos(\varphi_d) + \hat{\mathbf{y}}\sin(\varphi_d) \\ \hat{\mathbf{n}}_s &= \hat{\mathbf{x}}\cos(\varphi_s) + \hat{\mathbf{y}}\sin(\varphi_s) \end{aligned} \tag{2.24}$$

and

$$\begin{aligned} \mathbf{r}_d &= a\hat{\mathbf{n}}_d \\ \mathbf{r}_s &= a\hat{\mathbf{n}}_s \end{aligned} \tag{2.25}$$

into Equation 2.23 leads to an algorithm for reconstructing images of $\gamma_\rho(\mathbf{r})$ and $\gamma_\kappa(\mathbf{r})$. The analysis yields the following result for the Fourier Transform of the total ultrasound field detected at any point $\mathbf{r}_s$:

$$p(\mathbf{r}_d, \mathbf{r}_s, \omega) \approx \mathrm{F1} + \mathrm{F2} \times \psi_\theta(\varphi_s, k) \tag{2.26}$$

where

$$\begin{aligned} \mathrm{F1} &= \alpha\, A(\omega)\, \frac{\exp(2ika\, \cos(\frac{\theta}{2}))}{(2ika\, \cos(\frac{\theta}{2}))^{\frac{1}{2}}} \\ \mathrm{F2} &= \alpha^2\, A(\omega)\, k\, \frac{\exp(2ika)}{a} \\ \psi_\theta(\varphi_s, k) &= \int_{\Re^2} \exp(-i(ux + vy))(\gamma_\kappa(\mathbf{r}) + \cos(\theta)\gamma_\rho(\mathbf{r}))\, \mathrm{dx}\, \mathrm{dy} \end{aligned} \tag{2.27}$$

and

$$\begin{aligned} u &= -2k\, \sin(\frac{\theta}{2})\, \sin(\frac{\theta}{2} + \varphi_s)) \\ v &= 2k\, \sin(\frac{\theta}{2})\, \cos(\frac{\theta}{2} + \varphi_s) \end{aligned} \tag{2.28}$$

Note that the signs quoted for both u and v in the paper by Blackledge *et al* are opposite to what they should be. The first and second terms of Equation 2.26 correspond to the propagated incident and scattered fields, respectively. Equation 2.27 indicates that $\psi_\theta(\varphi_s, k)$ is the subset of points corresponding to data for angles θ and φ_s in the Fourier Transform space of the image, I, given by

$$I = \gamma_\kappa(\mathbf{r}) + \cos(\theta)\gamma_\rho(\mathbf{r}) \tag{2.29}$$

for a nonattenuating object.

Equations 2.26 through 2.28 provide the basis of an algorithm that reconstructs this image. For a given experiment, θ is fixed and as such the angle between the source and detector is fixed. This configuration is then stepped around the object being imaged so that the detector is placed at each angle in a set of φ_d values. A given φ_d corresponds to a different view at which data are collected. $\psi_\theta(\varphi_s, k)$ can be determined for each view by rearranging Equation 2.26 as follows:

$$\psi_\theta(\varphi_s, k) \approx \frac{p(\mathbf{r}_d, \mathbf{r}_s, \omega) - \mathrm{F1}}{\mathrm{F2}} \tag{2.30}$$

The incident field is measured at each angle φ_d with the object removed from the tank. Each resulting $\psi_\theta(\varphi_s, k)$ provides a subset of data in the Fourier Transform space of the image, I. Eventually enough data are collected to render inversion possible to yield the image.

Evidently, reconstruction with ultrasound data scattered at $\theta = 90^\circ$ yields an image of $\gamma_\kappa(\mathbf{r})$ alone since $\gamma_\rho(\mathbf{r})$ is weighted by $\cos(\theta)$. Reconstruction with backscatter data, for which $\theta = 180^\circ$, yields an image of the reflectivity function, which has been previously defined in Equation 1.10 as

$$R = \gamma_\kappa(\mathbf{r}) - \gamma_\rho(\mathbf{r}) \tag{2.31}$$

These two experiments allow $\gamma_\rho(\mathbf{r})$ to be solved for, completing the investigation of both $\gamma_\kappa(\mathbf{r})$ and $\gamma_\rho(\mathbf{r})$. Indeed, any two angles, θ_1 and θ_2, theoretically allow both gamma functions to be determined as follows:

$$\begin{aligned} I_1 &= \gamma_\kappa(\mathbf{r}) + \cos(\theta_1)\gamma_\rho(\mathbf{r}) \\ I_2 &= \gamma_\kappa(\mathbf{r}) + \cos(\theta_2)\gamma_\rho(\mathbf{r}) \end{aligned} \tag{2.32}$$

$$\begin{aligned} \gamma_\kappa(\mathbf{r}) &= \frac{1}{2}(I_1 + I_2 - \gamma_\rho(\mathbf{r})(\cos(\theta_1) - \cos(\theta_2))) \\ \gamma_\rho(\mathbf{r}) &= \frac{I_1 - I_2}{\cos(\theta_1) - \cos(\theta_2)} \end{aligned}$$

However, as will become evident in Section 2.2.7, the resolution of the images depends upon the value of θ.

To use the term coined by Blackledge *et al*, the reconstruction algorithm leads to a Diffraction Slice Theorem, which is illustrated in Figure 2.2. This theorem determines the Fourier space coordinates that correspond to data recorded for each source angle, φ_s,

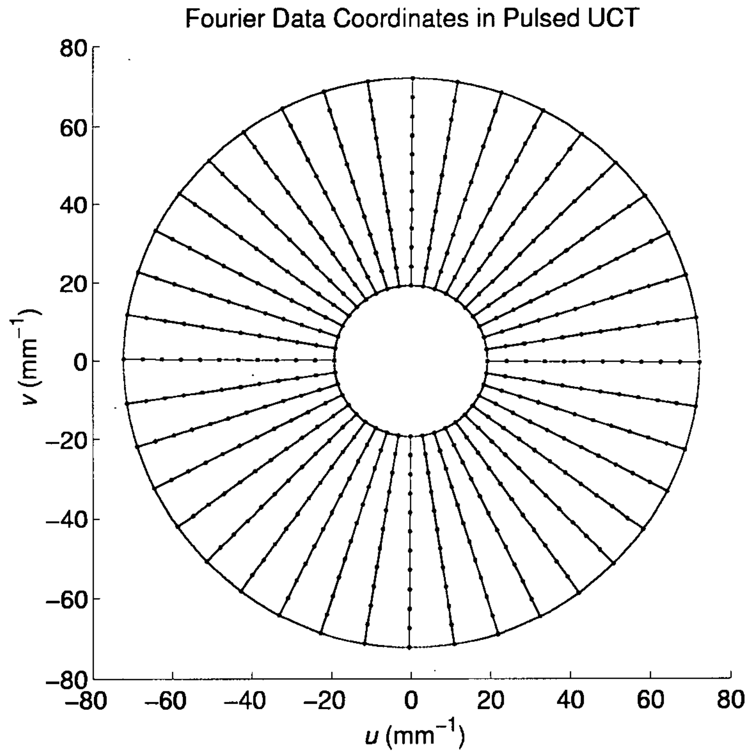

Figure 2.2: Illustration of the Diffraction Slice Theorem.

in an experiment with a constant θ. Equation 2.28 is a parametric expression of u and v in terms of φ_s and k, and it thus describes a geometric relationship between uv-space and $\varphi_s k$-space. For a given φ_s, varying k between the band limits of the pulse results in (u, v) coordinates that map out a linear slice in Fourier space. This slice passes through the origin at an angle

$$\chi = (\frac{\theta}{2} + \varphi_s) \tag{2.33}$$

relative to the u-axis. The length of each slice is

$$l = 2(\frac{\Omega_1}{c_0} - \frac{\Omega_2}{c_0}) \sin(\frac{\theta}{2}) \tag{2.34}$$

Thus, ultrasound scatter data corresponding to the same temporal angular wave number,

k and a different view angle, φ_s, is transformed into Fourier data on circles in the uv-space of the image. The radius of the corresponding circles is easily calculated from the expressions for u and v in Equation 2.28, to yield

$$\begin{aligned} \tau &= \sqrt{u^2+v^2} \\ &= 2k\sin(\frac{\theta}{2}) \end{aligned} \tag{2.35}$$

Alternatively, scatter data corresponding to the same view angle and increasing angular wave number are transformed into Fourier data on radial lines. As more views are recorded, a donut-shaped region of data is mapped out in the Fourier space of the image. Upon collecting enough data, inversion can yield the image $I = \gamma_\kappa(\mathbf{r}) + \cos(\theta)\gamma_\rho(\mathbf{r})$ given by Equation 2.29.

This reconstruction algorithm is consistent with that of continuous wave computed tomography, in which insonification at a particular view angle yields Fourier data on a semicircle that passes through the origin. As such, data corresponding to a particular frequency are transformed onto a circular arc in Fourier space. Examples of such projections are illustrated in Figure 2.3. Evidently, as the angular wave number increases, the radius of curvature of the arc decreases, which is also consistent with the theory outlined in this thesis. In the case of pulsed UCT, the circular paths corresponding to each frequency are in fact full circles rather than semicircles, and instead of passing through the origin, they are concentric about the origin.

The Diffraction Slice Theorem is also of interest due to its similarity to the Projection Slice Theorem from tomography with nondiffracting sources, such as x-ray CT. The latter theorem states that the Fourier Transform of a projection recorded at an angle ϕ maps a linear slice in the Fourier space of the corresponding image at the same angle ϕ [21, 47]. In the case of diffraction tomography, however, the angles in the physical and Fourier spaces are not equal. Furthermore, in straight-ray tomography, the Fourier space data are not subject to a low frequency cutoff. Another important difference between x-ray CT methods and this reconstruction algorithm is that the total angular range over which data

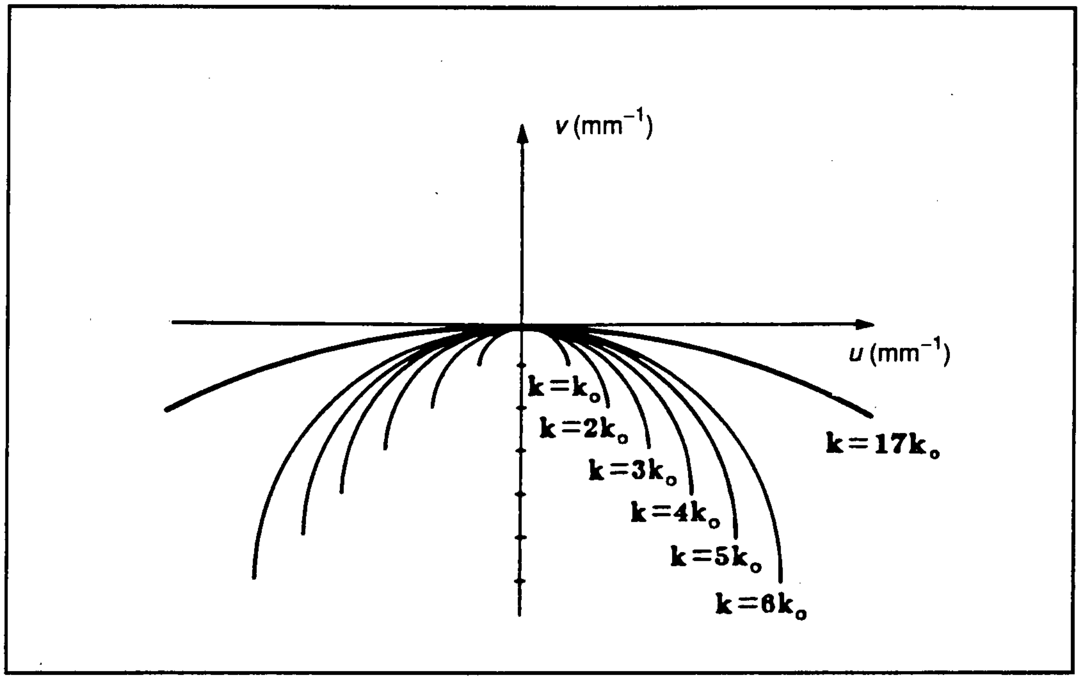

Figure 2.3: This figure illustrates examples of projections in CW ultrasound computed tomography. Ultrasound scatter recorded at a particular angle yields data in the image Fourier space that lie on semicircular arc that passes through the origin. The angular view determines the orientation of the arc and the radius of curvature is inversely proportional to the angular wave number.

must be recorded in the former may be restricted to 180° since the projection obtained is identical for irradiation at any angle, ϕ, and the corresponding angle, $\phi + 180°$ [47]. For pulsed UCT, this is only true of objects that possess two symmetrical hemispheres because the data recorded are based on TOF. This is illustrated with the example of a point object in Figure 2.4. Evidently, with the source and detector at 90° and 0°, respectively, the scattered ultrasound pulse will arrive earlier in the detected signal than if the source and detector are situated at 270° and 180° instead, due to the smaller sound travel paths involved.

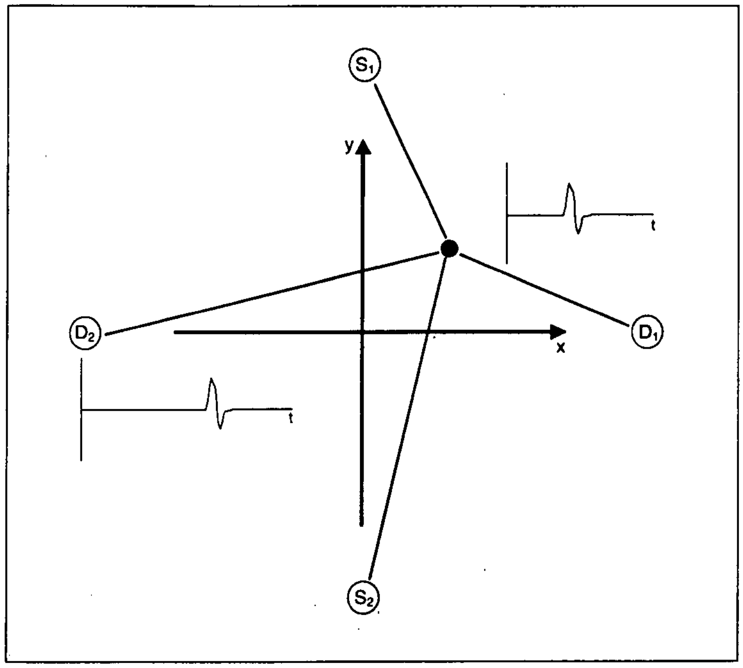

Figure 2.4: This plot illustrates that data recorded from opposite directions are not the same.

Equations 2.26 through 2.28 for transforming projection information into 2D Fourier space information are consistent with the required properties of real images. According to Fourier Theory, an image described by a real function $f(x, y)$ has a 2D Fourier Transform for which the following symmetry rule holds:

$$\mathrm{FT}(-u, -v) = \mathrm{FT}^{+}(u, v) \tag{2.36}$$

The 1D data, $\psi_\theta(\tilde{\varphi}_s, k)$, that are deposited on a given radial slice corresponding to a source angle of $\tilde{\varphi}_s$ is derived from Equation 2.26. This equation is dependent upon $p_\theta(\tilde{\varphi}_s, k)$, which is the Fourier Transform of a real signal and thus obeys the following

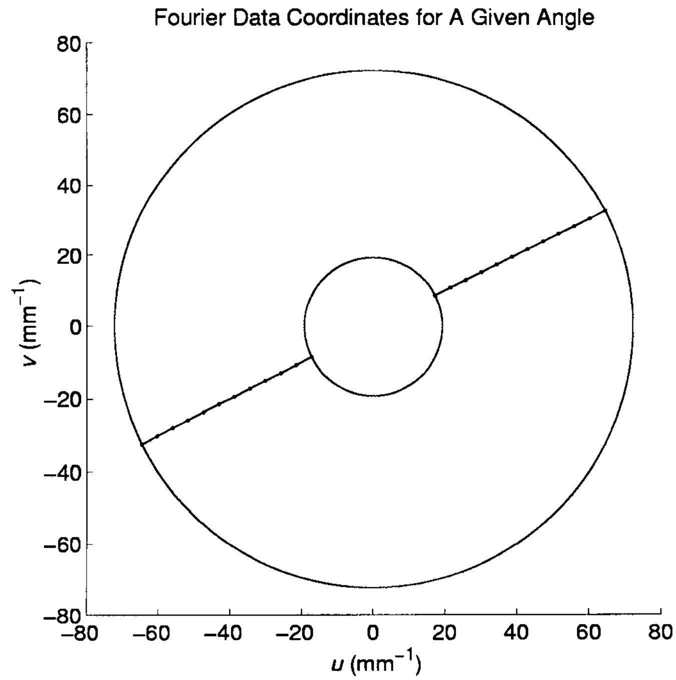

Figure 2.5: This plot illustrates the (u, v) coordinates of ψ_θ data along the radial slice corresponding to one source angle equal to $\tilde{\varphi}_s$.

symmetry in k-space:

$$p_\theta(\tilde{\varphi}_s, -k) = p_\theta^+(\tilde{\varphi}_s, k) \tag{2.37}$$

The final expression for $\psi_\theta(\tilde{\varphi}_s, k)$ also obeys the same symmetry rule and thus

$$\psi_\theta(\tilde{\varphi}_s, -k) = \psi_\theta^+(\tilde{\varphi}_s, k) \tag{2.38}$$

The corresponding (u, v) coordinates at which the $\psi_\theta(\tilde{\varphi}_s, k)$ data are placed in Fourier space are illustrated in Figure 2.5. Evidently, the 2D symmetry rule expressed in Equation 2.36 holds for these data. The result is the same for any $\tilde{\varphi}_s$, and therefore the reconstruction algorithm always derives Fourier data that corresponds to a real image.

2.2.3 Corrected Green's Function Propagator

The simplified approximation to the Green's function propagator quoted in the work by Blackledge *et al* has incorrect phase, which in turn yields incorrect ultrasound wave propagation. The following section illustrates the correction that was made to obtain an approximate Green's function for the description of ultrasound propagation in the near field of a pulsed source with a finite bandwidth [10].

Recall that the far field assumptions described by Equations 2.12 and 2.13 allow the exact Green's Function to be expanded in terms of a simpler function given by

$$g(\mathbf{r}|\mathbf{r}_j, k) \approx \alpha \frac{\exp(ik|\mathbf{r} - \mathbf{r_j}|)}{(k|\mathbf{r} - \mathbf{r_j}|)^{\frac{1}{2}}} \tag{2.39}$$

The α parameter is imaginary. Any error in α thus affects the phase of the wave components and adds error to the propagation distance of the pulse. The value of α quoted in [10] is

$$\tilde{\alpha} = \frac{\exp(3i\pi/4)}{2\sqrt{2\pi}} \tag{2.40}$$

However, this propagator does not describe the real and imaginary parts of the propagator properly, as illustrated in Figure 2.6. Rather, the correct value of α was found to be

$$\alpha = i\frac{\exp(3i\pi/4)}{2\sqrt{2\pi}} \tag{2.41}$$

As illustrated in Figure 2.7, the real and imaginary parts of the corrected approximation to the Green's function agree with the exact Green's function propagator. Examples are shown for propagation through distances of 20 and 100 mm.

2.2.4 Use of the Fast Fourier Transform

The paper by Blackledge *et al* suggests the use of the Finite Fourier Transform (Finite FT) in the reconstruction algorithm [10]. For a 1D discrete function of time made up of N time samples, this transform is given by

$$\mathrm{FT}(\omega) \quad = \quad \sum_{j=1}^{N} \exp(-i\omega t_j)\, f(t_j)\Delta t \tag{2.42}$$

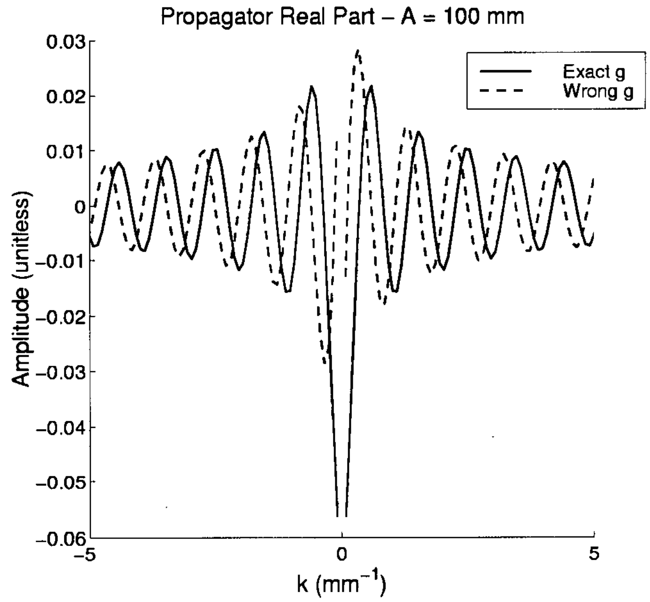

(A)

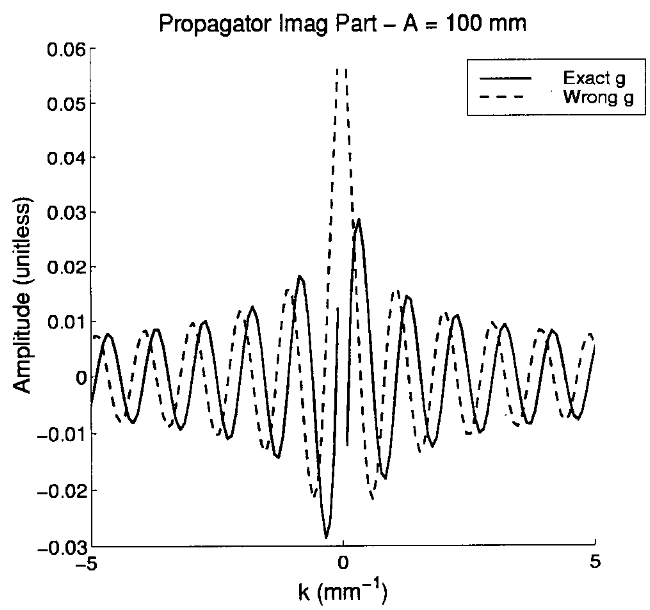

(B)

Figure 2.6: This figure illustrates the discrepancy between the exact free space Green's function propagator and the approximate one quoted in Blackledge *et al.* Figures A and B illustrate the real part and imaginary parts of these functions, respectively, for a propagation distance of 100 mm.

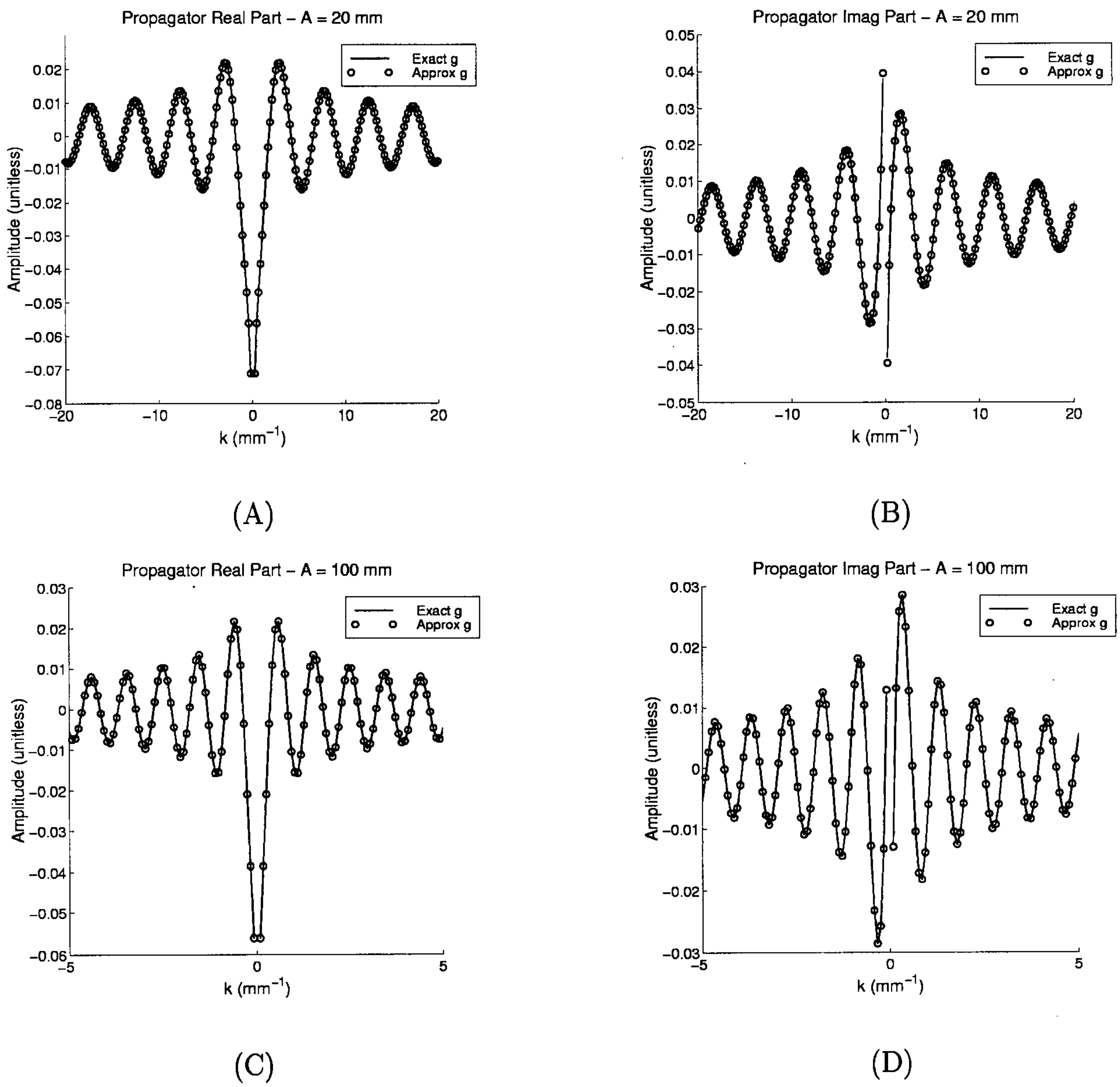

Figure 2.7: This figure compares the exact and approximate 2D propagators. Figures A and B illustrate the real and imaginary spectra for propagation through a distance of 20 mm, while Figures C and D illustrate the same for a distance of 100 mm. Evidently, there is good agreement between the exact form and the approximation.

$$f(t) = \sum_{j=1}^{N} \exp(i\omega_j t)\, \mathrm{FT}(\omega_j)\Delta\omega$$

Essentially the Finite FT is simply the discrete FT with limits on the summation. By extension, the Finite FT of a 2D function known at M and N discrete values of x and y, respectively, is given by

$$\begin{aligned} \mathrm{FT}(u,v) &= \sum_{j=1}^{M} \{\sum_{k=1}^{N} \exp(-i(ux_j + vy_k))\, f(x_j, y_k)\Delta x \Delta y\} \\ f(x,y) &= \sum_{j=1}^{M} \{\sum_{k=1}^{N} \exp(i(u_j x + v_k y))\, \mathrm{FT}(u_j, v_k)\Delta u \Delta v\} \end{aligned} \tag{2.43}$$

Equations 2.42 and 2.43 are Discrete Fourier Transforms (DFT's). The calculation of Fourier data by use of these equations is a very slow and inefficient process. A far better approach is to use the Fast Fourier Transform (FFT), which is the most computationally efficient implementation of the DFT. Furthermore, the FFT yields the same result as all other less efficient implementations of the DFT. In using the FFT to compute the Finite Fourier Transform, however, the result of the forward and inverse transforms must be multiplied by factors of $\Delta x \Delta y$ and $\Delta u \Delta v$, respectively, since these are not included in the FFT. Furthermore, there are various conventions for FFT formulas, such as multiplying or dividing by either 2π or the number of points in the FFT, depending on whether the inverse or forward transform is being computed. These must be taken into account when using a particular FFT instead of the Finite Fourier Transform in the reconstruction algorithm.

2.2.5 The Fourier Transform Sign Convention

The sign convention of the Fourier Transform used in wave propagation theory is opposite to that which is conventionally used in engineering and most of physics [62]. Generally the exponential functions in the forward and inverse 1D transforms are $\exp(-i\omega t)$ and $\exp(i\omega t)$, respectively. In wave propagation theory, however, the signs of the exponential arguments are opposite to this convention. In fact, if the wrong convention is used, a non-physical situation occurs when propagating a pulse to any location. Upon inverse transforming the propagated Fourier spectrum to obtain the time-dependent field that a detector would see at that location, a pulse with a negative time-of-flight results.

In order to apply this convention with a typical FFT routine, such as that available in the Matlab™ programming environment, the following transformation must be applied to the output of the forward 1D FFT:

$$\mathrm{FFT} = \mathrm{real}(\mathrm{FFT}) - \imath\, \mathrm{imag}(\mathrm{FFT}) \tag{2.44}$$

The frequencies corresponding to this output are calculated as per usual. In order to change the sign convention used in the inverse 1D transform, the output remains the same, while the corresponding time vector, $\tilde{t}$ is calculated as follows:

$$\tilde{t} = -t \tag{2.45}$$

where t is the original time vector calculated as per usual.

2.2.6 Behavior of the Exact Propagator

The behavior of the exact propagator was investigated to gain an understanding of the model. A simulation was performed in which the source was assumed to be a line transducer that produced a pulsed field with a Ricker wavelet time profile, which is defined by

$$\begin{aligned} Y_r &= \sqrt{\frac{\pi}{2}}\{u^2 - \frac{1}{2}\}\exp(-u^2) \\ u &= \frac{\omega_0 t}{2} = \pi f_0 t \end{aligned} \tag{2.46}$$

In Equation 2.46, time t ranges over both negative and positive values, with the simulation experiment starting at $t = 0$. Also, f_0 is the peak frequency of the wavelet. Ricker wavelets with ω_0 equal to 6.0, 7.5 or 20 MHz have pulse lengths[1] in water at 20°C of

[1]Here pulse length is defined as the distance between points on the pulse where the amplitude is reduced to $\leq 0.1\%$ of the pulse maximum.

approximately 3.2, 2.6, and 1.0 mm. The pulse shape at $t = 0$ for $\omega_0 = 7.5$ MHz is illustrated in Figure 2.8.A, while the real part of the corresponding Fourier spectrum is illustrated in Figure 2.8.B. Note that since the incident pulse is centered over $t = 0$, the imaginary Fourier spectrum is zero. Figure 2.9 illustrates the pulse shape as it is propagated through increasing distances. An important feature to note is that the propagated pulse is unphysically larger than the incident pulse for propagation distances less than $\sim 2 \times 10^{-2}$ mm. This is due to the bad behavior of the propagator with small distances, in the form of a lack of frequency-dependent oscillations. A second feature to note is that the pulse height decreases with distance, which is expected due to the nearly $|\mathbf{r} - \mathbf{r}_j|^{-\frac{1}{2}}$ dependence of the Hankel function. The last interesting feature is the change in pulse shape from symmetrical to asymmetrical. This results from the nearly $k^{-\frac{1}{2}}$ dependence of the Hankel function.

2.2.7 Theoretical Resolution

When determining the image resolution that is possible with the algorithm by Blackledge *et al*, the Nyquist Theorem must be considered because image reconstruction is dependent upon data that have been discretely sampled in Fourier space. The Nyquist Theorem states that when a function $f(m)$ is sampled at intervals of Δm, data in the Fourier domain can be determined for frequencies up to a maximum of

$$f_{Nyq} = \frac{1}{2\Delta m} \tag{2.47}$$

where f_{Nyq} is known as the Nyquist frequency. Alternatively, this also means that if data in Fourier space are known for frequencies $f \leq f_{Nyq}$, then the maximum resolution in physical space is

$$\Delta m = \frac{1}{2\, f_{Nyq}} \tag{2.48}$$

Furthermore, these equations preclude that the Nyquist frequency is one half the frequency at which $f(m)$ is sampled. In 2D and 3D systems, each dimension is analyzed separately in this manner.

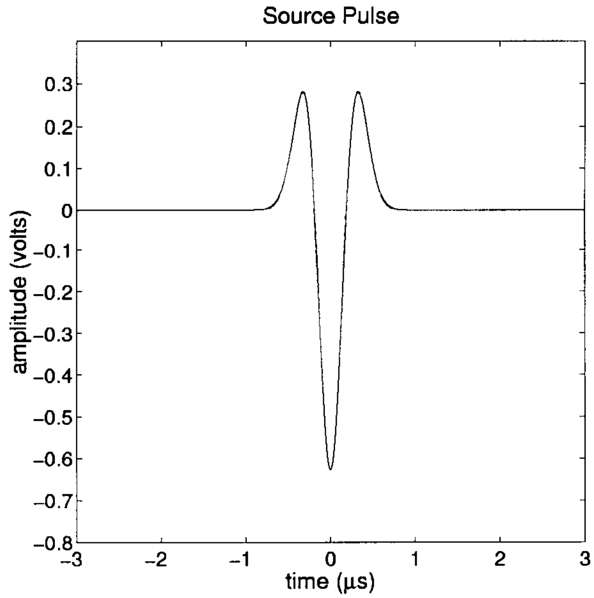

(A)

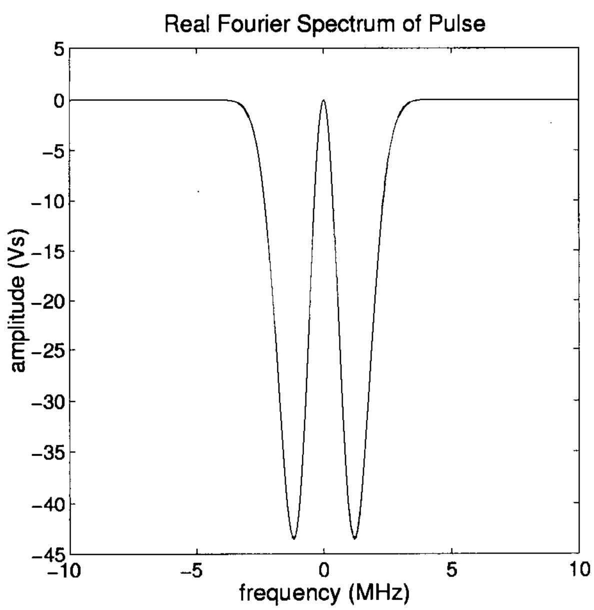

(B)

Figure 2.8: This figure illustrates the incident pulsed field used in various computer simulations. Figure A shows the time profile, while Figure B illustrates the real part of the Fourier spectrum of the source.

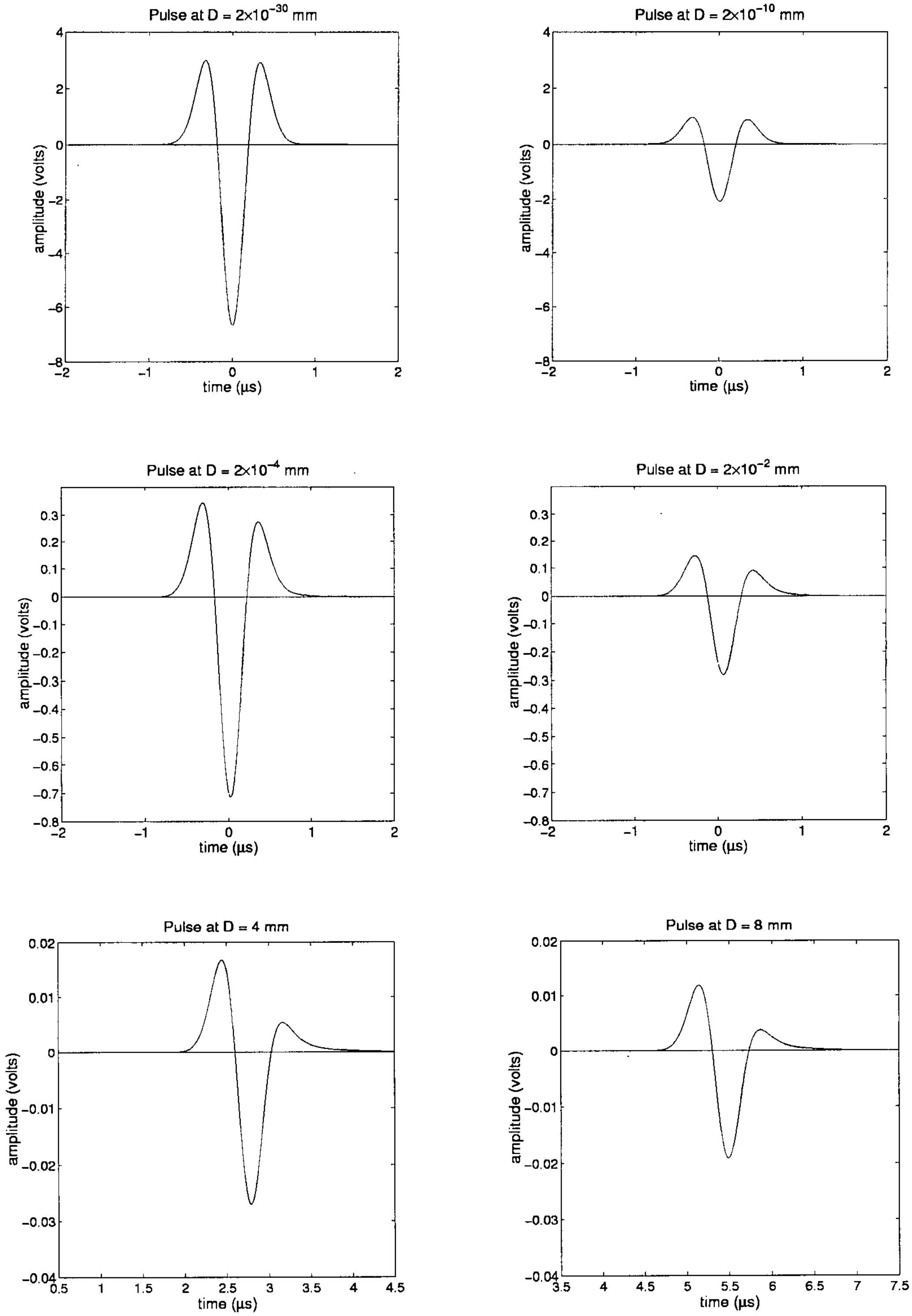

Figure 2.9: This figure illustrates the pulse as it is propagated by the 2D Green's function.

According to these relations, the image resolution that is theoretically possible for minimally attenuating objects can be determined. Consider an experiment in which ultrasound scatter data are recorded at several angles, φ_d, with the relative angle between the source and detector remaining constant at θ. The scattered field is detected by a transducer whose output signal is digitally sampled at a frequency of f_D. According to the Nyquist Theorem, the Nyquist frequency of these data is $f_{Nyq} = \frac{1}{2}f_D$. Furthermore, the maximum angular wave number considered in the reconstruction algorithm can be calculated as

$$k_{max} = \frac{2\pi f_{Nyq}}{c} \tag{2.49}$$

where c is the speed of sound in the background medium. Recalling Equation 2.35 for the radii of data rings in uv-space, the maximum radius that is possible is given by

$$\tau_{max} = 2k_{max}\sin(\frac{\theta}{2}) \tag{2.50}$$

By extension, both u_{max} and v_{max} are equal to τ_{max}; as such, the analysis will be identical for both the x and y dimensions. u is the angular wave number along the first dimension in 2D Fourier space, and it is equal to $2\pi f_x$, where f_x refers to spatial sampling frequency along the x-axis. Combining Equations 2.49 and 2.50, it is evident that the Fourier data of the image are known for select f_x values up to and including

$$\begin{aligned}(f_x)_{max} &= \frac{1}{\pi}\,k_{max}\,\sin(\frac{\theta}{2}) \\ &= \frac{1}{\pi}\,\frac{2\pi f_{Nyq}}{c}\,\sin(\frac{\theta}{2})\end{aligned} \tag{2.51}$$

Again according to the Nyquist Theorem, Δx can be calculated to be

$$\begin{aligned}\Delta x &= \frac{1}{2\,(f_x)_{max}} \\ &= \frac{c}{4f_{Nyq}\sin(\frac{\theta}{2})}\end{aligned} \tag{2.52}$$

The result is identical for the y dimension. Hence, the maximum image resolution along both the x and y directions is inversely proportional upon both $\sin(\frac{\theta}{2})$ and the Nyquist frequency of the digitized scatter signal.

f_{Nyq} (MHz)	Δx for $\theta = 90^{\circ}$ (mm)	Δx for $\theta = 180^{\circ}$ (mm)
1	0.52	0.37
2	0.26	0.19
4	0.13	0.093
8	0.065	0.046

Table 2.1: The above data illustrate sample image resolutions based on the theoretical calculations for minimally attenuating objects.

To gain some understanding of the magnitude of these values, consider an experiment in which scatter is digitized at 20 MHz. The corresponding f_{Nyq} is 10 MHz. The resulting Δx values for $c = 1.48$ mm/μs and θ equal to 90° and 180° are 0.052 mm and 0.037 mm, respectively. Results for different upper band limits scale up or down with the value of f_{Nyq}, as illustrated in Table 2.1. These values suggest that excellent image resolution is theoretically possible. However, this level of performance is not realistically attainable for tissues due to the application of the Born approximation and the far field assumptions in the development of the reconstruction algorithm, which was the approach taken to render the mathematics of the tissue/ultrasound system solvable.

The results quoted assume that all available Fourier data are used in the image reconstruction process. However, in order to apply the Fast Fourier Transform, the data must be interpolated onto a square grid in Fourier space, which reduces the image resolution by a factor of $\sqrt{2}$. The reason for this is illustrated in Figure 2.10. Without resorting to extrapolation into the unknown space beyond the largest Fourier data circle defined by radius τ_{max}, the interpolation grid is limited to a width of

$$\frac{1}{\sqrt{2}}\tau_{max} \tag{2.53}$$

As such, $(f_x)_{max}$ is decreased by a factor of $\sqrt{2}$, while Δx increases by the same factor to 0.074 mm and 0.052 mm for θ equal to 90° and 180°, respectively. Again, the results are identical for Δy.

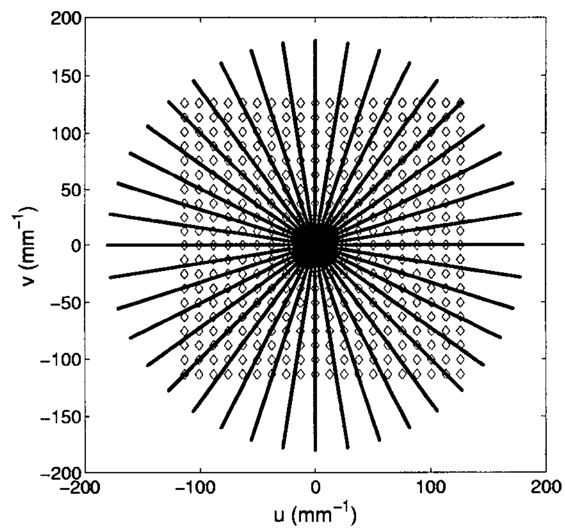

Figure 2.10: This figure illustrates how the extent of uv-space is reduced by the interpolation of data from a radial grid to a square grid. The lines represent the radially-situated data, while the diamonds represent the data situated on the corresponding square grid.

2.2.8 Interpolation to a Square Grid

If an interpolation in Fourier space is performed, the spacing of the square grid should be compatible with the spacing of the original radially situated data. As such, this spacing should not be less than the largest distance between any two adjacent points in the original Fourier data. Since the data are on a radial grid, this distance corresponds to the maximum of either the radial spacing or the spacing along the data circle with the largest radius, τ_{max}.

In order to calculate the radial spacing, $\Delta\tau$, consider again the sample experiment described in Section 2.2.7. The digitized ultrasound scatter signal is Fourier Transformed. If there are N sample points in the digitized signal, then according to Fourier Theory the transform will provide discrete data at frequencies of

$$f = i\,\frac{2f_{Nyq}}{N}, \text{ where } i = -\frac{N}{2}, -(\frac{N}{2}-1), ..., 0, ..., (\frac{N}{2}-1) \tag{2.54}$$

Therefore,

$$\Delta f = \frac{2f_{Nyq}}{N} \tag{2.55}$$

and

$$\Delta k = \frac{4\pi f_{Nyq}}{cN} \tag{2.56}$$

According to the expression for τ given by Equation 2.35, the corresponding radial spacing in uv-space is

$$\begin{aligned} \Delta\tau &= 2\Delta k \sin(\frac{\theta}{2}) \\ &= \frac{8\pi f_{Nyq}}{cN} \sin(\frac{\theta}{2}) \end{aligned} \tag{2.57}$$

The calculation of the spacing along the largest data circle is much more straightforward. By simple geometry, the arc length between points on this circle is given by $\tau_{max}\,\Delta\varphi_d$, where

$$\Delta\varphi_d = \frac{2\pi}{N_v} \tag{2.58}$$

N_v is the number of view angles at which projections are recorded, and $\Delta\varphi_d$ is expressed in radians. Substituting for τ_{max} and k_{max} using Equations 2.50 and 2.49 yields the following result for the spacing along the largest Fourier data circle:

$$\Delta\text{arc} = \frac{8\pi^2 f_{Nyq}\sin(\frac{\theta}{2})}{N_v c} \tag{2.59}$$

The final result for the interpolation grid spacing is then equal to the maximum of $\Delta\tau$ and Δarc. The ratio of the two spacings is

$$\frac{\Delta\text{arc}}{\Delta\tau} = \frac{\pi N}{N_v} \tag{2.60}$$

so the arc length spacing is the limiting parameter until $N_v > \pi N$, which is unlikely.

Revisiting the experiment described in Section 2.2.7, it is further assumed that the transducers are a typical distance of d = 150 mm from the center of the tank. Recall that the frequency spectrum of the incident field is assumed to be negligible beyond

f_{Nyq} = 10 MHz, the speed of sound is c = 1.48 mm/μs and the sampling frequency is f_D = 60 MHz. The average TOF of ultrasound scatter is then approximately $2d/c$ = 203μs. The corresponding number of time points, N, in the scatter signal at 60 MHz sampling is 12180. The radial spacing according to Equation 2.57 is then 0.0099 mm^{-1} and 0.014mm^{-1} for θ equal to 90° and 180°, respectively. If the number of views is assumed to be 400, the arc spacing is a factor of 95 times larger with values of 0.94 mm^{-1} and 1.33 mm^{-1}, respectively. Hence, the interpolation grid spacing in this example is limited by the value of Δarc.

This analysis leads to an interesting result. According to Equations 2.50 and 2.53, for this example τ_{max} = 42 mm^{-1} and 60 mm^{-1} for θ equal to 90° and 180°, respectively. With the Fourier grid spacings calculated above, the corresponding grid size is 45 × 45 for both values of θ. Recalling that Δx and Δy are equal to 0.074 mm and 0.052 mm for θ values of 90° and 180°, respectively, the resulting images will be only 3.3 mm and 2.3 mm wide. The width is proportional to the number of view angles, and some values are summarized for θ = 90° in Table 2.2. The reconstruction algorithm

N_v	f_{Nyq} **(MHz)**	**Grid Size**	**Image Size (mm)**
200	10	22 × 22	1.6
400	10	45 × 45	3.3
800	10	90 × 90	6.7
1600	10	180 × 180	13.3
3200	10	360 × 360	26.6
3200	5	360 × 360	37.7
6400	5	720 × 720	75.3
800	3	90 × 90	15.7
3200	3	360 × 360	62.8

Table 2.2: The above data illustrate example image sizes for two values of f_{Nyq} and various N_v.

evidently zooms in on a portion of the object to potentially yield useful information. By moving the center of the UCT system to another part of the object, a different close-

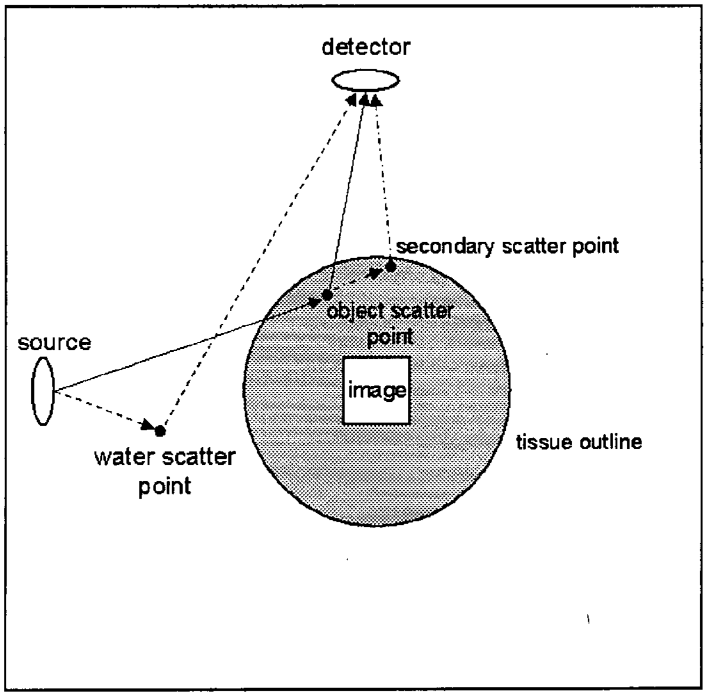

Figure 2.11: This plot illustrates the sources of scatter from points outside the image space that are ignored when the image size is very small.

up picture would result. However, there exists a source of error that increases as the image size decreases in proportion to the total object size. As illustrated in Figure 2.11, there is additional ultrasound scatter in the system that is not considered in the image reconstruction process. A significant amount of scatter originates from areas of the object that lie outside the image space but which are still insonified by the incident field. A portion of scatter also originates from the surrounding water. Although this source of error exists even when the image space spreads beyond the object perimeter, the effect is more pronounced when all scatter points in water are ignored. Second order scattering is neglected throughout the object and water regardless of the image size. Within the framework of the original method by Blackledge *et al*, the problem of neglected first order scatter can be alleviated by either reducing f_{Nyq} or increasing N_v. Alternatively, one can attempt to reduce the interpolation grid spacing to much less than the spacing between adjacent points on the radial grid. Results of this exercise are presented in Section 5.3.4.

The discussion thus far has assumed that f_{Nyq} is not more than 10 MHz. However, data sampling rates are in fact generally much higher than 20 MHz in practice. According to the Nyquist Theorem, the reconstruction of data from discrete time samples is possible only if the sampling rate is at least $2f_{BW}$, where f_{BW} is the band limit of the data [56]. Accurate reconstructions require a sampling rate that is a higher multiple of f_{BW}. As such, data that are band limited at 10 MHz will be sampled at ~60 MHz to boost accuracy. However, this results in a Nyquist frequency of 30 MHz and, by Equation 2.52, corresponding values of Δx equal to 0.017 mm and 0.012 mm for θ of 90° and 180°, respectively. This precludes that 2000×2000 pixels would be required to reconstruct an image that is a square of only 17 mm × 17 mm. This alone is an unmanageable size in terms of the interpolation from the radial grid and the subsequent inverse FFT. For instance, interpolating from a radial grid of only 100 views and 2000 radial points to a Cartesian grid of 800×800 was found to take more than 24 hours within the Matlab™ programming environment.

2.2.9 A Note on Lowpass Filtering and Truncation

Recall from Section 2.2.1 that the ultrasound source is band limited from f_1 to f_2, outside of which its corresponding Fourier data are negligible and characterized by noise. As such, a lowpass filter (LPF) should be applied to the source and the scatter data, as per the discussion to follow in Section 4.3.1. In this thesis, a conventional Butterworth lowpass filter was used. However, although this filtering has the effect of improving the look of the data, it is rendered ineffective in Equation 2.30 of the reconstruction algorithm. Here the filtered scatter Fourier data are divided on a frequency-by-frequency basis by the filtered source spectrum, and since Butterworth filtering and division are both linear operations, the filtering effect is removed. Therefore, the data processing must be done in the 2D Fourier space of the image instead, after the division of the data by the source spectrum.

This analysis illustrates that any desired lowpass filtering must be performed along each ray of data in the Fourier domain of the image. Figures 2.12.A and 2.12.B illustrate this concept. The first figure illustrates the linear transformation from scatter data, $p_s(\mathbf{r}_d, \mathbf{r}_s, \omega)$, for a given view to a radial line of data, $\psi_\theta(\varphi_s, k)$, in the Fourier domain of the image[2]. This was discussed in Section 2.2.2. This ray of data is a discrete function of radius, τ, in uv-space. The second figure illustrates that a f-dependent LPF for the scatter data can be similarly transformed into a τ-dependent LPF for the radial data. This equivalent filter can then operate on each radial line of data in the image Fourier domain, resulting in the desired lowpass filtering. f and τ are related by Equation 2.35, and therefore the cutoff τ_0 can be calculated from the cutoff f_0 by $\tau_0 = \frac{4\pi f_0}{c_0}\sin(\frac{\theta}{2})$. f_0 is determined by the spectrum of the source and scatter data, as per usual. Since the f-dependent and τ-dependent lowpass filters are equivalent, they are discussed interchangeably throughout this thesis.

By this discussion it is evident that f_2 has a corresponding limit τ_2 in the Fourier domain of the image, and the lowpass filtering operation will effectively null data beyond a radius of τ_2 in uv-space. Information is, however, embodied in the fact that Fourier data beyond τ_2 are negligible, and these data could potentially enhance the FFT inversion process that generates an image. However, retaining all the data result in significantly more processing. For example, if the Nyquist frequency is 3 times larger than f_2, then τ_{max} is also 3 times larger than the band limit τ_2, and 8 times more data are processed if all data are retained. This requires significant computing power, particularly with

[2]Recall the definition of ψ in Equation 2.26

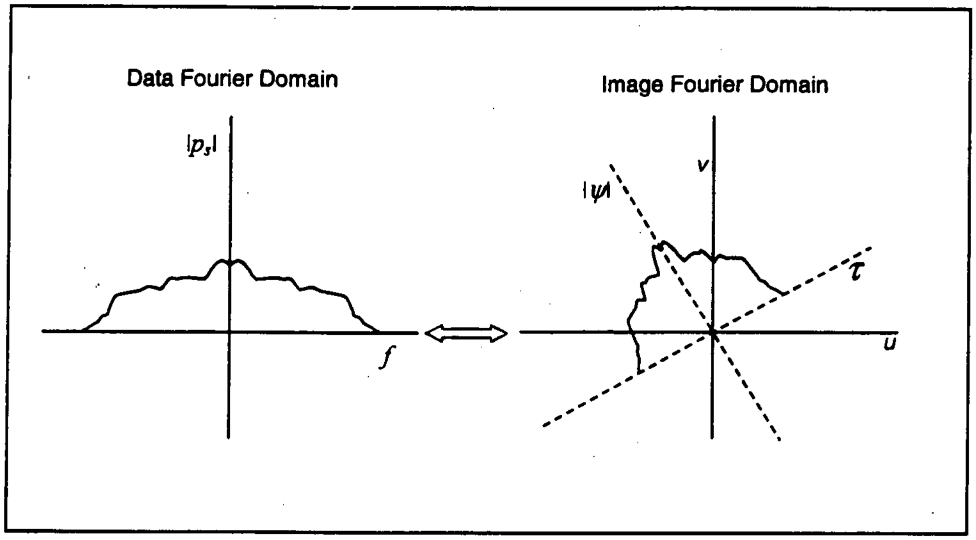

(A)

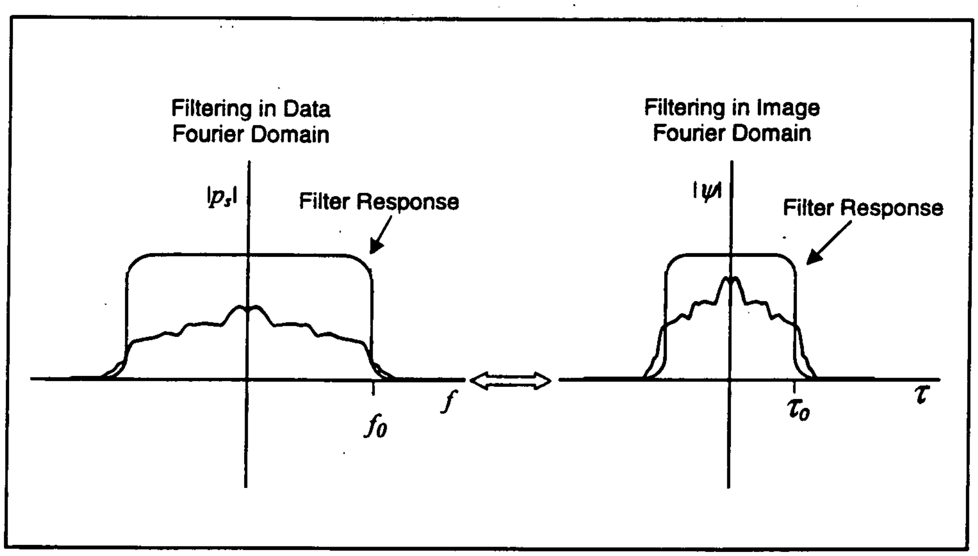

(B)

Figure 2.12: Figure A illustrates the transformation from scatter Fourier data to a radial line of data in the Fourier domain of the image. Figure B illustrates the equivalence of lowpass filtering in the Fourier domain of the data and along radial lines in the Fourier domain of the image.

respect to the interpolation in Fourier space. In addition, it was indicated in Section 2.2.8 that if all Fourier data are retained, the reconstruction of images with practical total widths is not possible given current computing power in the prototype scanner. An alternative is to truncate most of the Fourier data that correspond to spatial frequencies beyond the τ_2 region. This reduces the Nyquist frequency and increases Δx for a more viable reconstruction routine. In testing the reconstruction algorithm in simulation, the truncation and non-truncation methods were compared in Section 5.3.1.

2.3 Process Behind the Reconstruction of Each View

This section analyzes what is represented by the data recorded at each angle. Recall that the detector records a voltage trace that is directly proportional to the ultrasound field reaching it as a function of time. The reconstruction algorithm subsequently determines from what locations in space this sound energy scattered; it does this by analyzing time-of-flight information. Figure 2.13 illustrates the concept of TOF through a sketch of cylindrical pulse propagation and the detection of scatter from points immersed in water. At any time t_s after the excitation of the source, the ultrasound field in water is spread out along a fuzzy arc of the same width as the pulse and a distance $t_s \cdot c_w$ away from the source. Scatter is shown originating at Point A along this arc, which is a distance $d_{A \rightarrow det}$ away from the detector. Hence, this scatter signal requires a time of $t_d = d_{A \rightarrow det}/c_w$ to travel to the detector. The total TOF is therefore $t_s + t_d$ for scatter originating from Point A. However, this analysis leads to the conclusion that scatter originating along arcs through the tissue have the same TOF. Figure B illustrates a nearly linear arc of points that all result in scatter with the same TOF equal to $t_s + t_d$. As such, each digitized time point of data with a given TOF could have originated from a set of scatter points on a corresponding curve of constant travel time, called an isochrone.

To determine the shape of the isochrones, it is useful to first determine the shape of lines of equal scatter path length, with is the distance ultrasound travels in going from

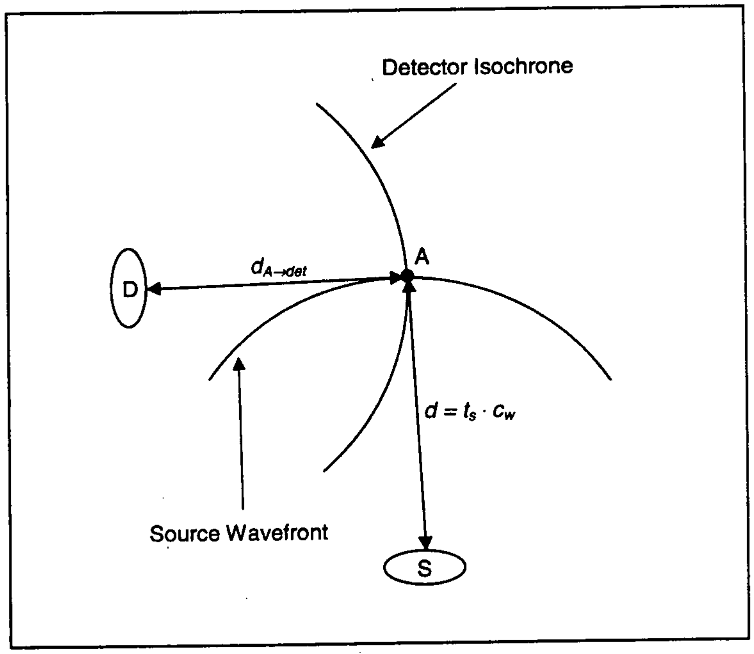

(A)

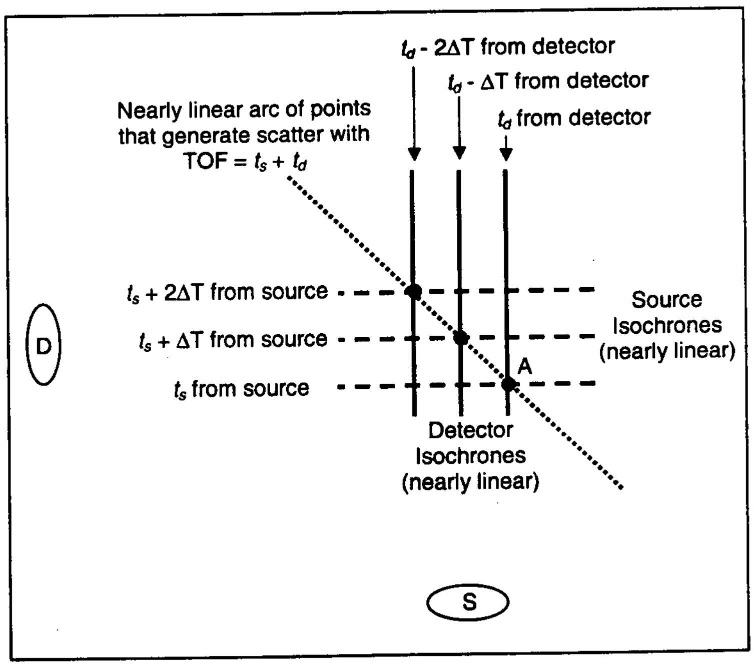

(B)

Figure 2.13: Figure A illustrates the distance that an ultrasound wave travels in water before it is detected after scattering from an arbitrary point labelled A. Figure B illustrates the locations of other points that result in scatter signals with the same TOF as scatter that originates from Point A.

the source to a scatter point and finally to the detector. One could compose this line on paper by connecting a string of a given length to two pins representing the source and detector. By pulling the string taut with a pen while drawing a curve, the result would be a curve of equal path length. Mathematically, this is an ellipse by definition with the source and detector located at the focii. By extension, the center of the ellipse is situated at the middle of the line joining the source and detector.

If the speed of sound varies little or not at all along all paths from the source or detector to every location on the ellipse, then the curve evidently also corresponds to an isochrone. If the speed of sound varies along different paths, as is true in the physical world, then the isochrone will not be a perfect ellipse. This situation is mathematically complex and does not appear to be analyzed to date in the UCT literature.

To illustrate the elliptical isochrones, consider an example in a Cartesian coordinate system that has been both shifted and rotated such that the ellipse center is at the origin and the focii are on the x-axis. The focii must be located at the source and detector positions, $\mathbf{r}_s$ and $\mathbf{r}_d$. This necessitates that the total distance from the source to any point (x, y) on the ellipse to the detector is a constant, C. Mathematically this can be stated as

$$C = \{(x - r_{sx})^2 + (y - r_{sy})^2\}^{-\frac{1}{2}} + \{(x - r_{dx})^2 + (y - r_{dy})^2\}^{-\frac{1}{2}} \tag{2.61}$$

Also the equation of the ellipse is

$$1 = (\frac{x}{a})^2 + (\frac{y}{b})^2 \tag{2.62}$$

Equations 2.61 and 2.62 are difficult to solve for simultaneously, but this can be done numerically by cycling through different values of a and b until C is constant for all (x, y) on the ellipse. Figure 2.14 illustrates the partial curves of several isochrones for a typical source and detector geometry, with $\mathbf{r}_s$ = (0, −100) mm and $\mathbf{r}_d$ = (−100, 0) mm. Note that the curves are nearly linear, particularly where they cross the perpendicular bisector of the line joining the source and detector.

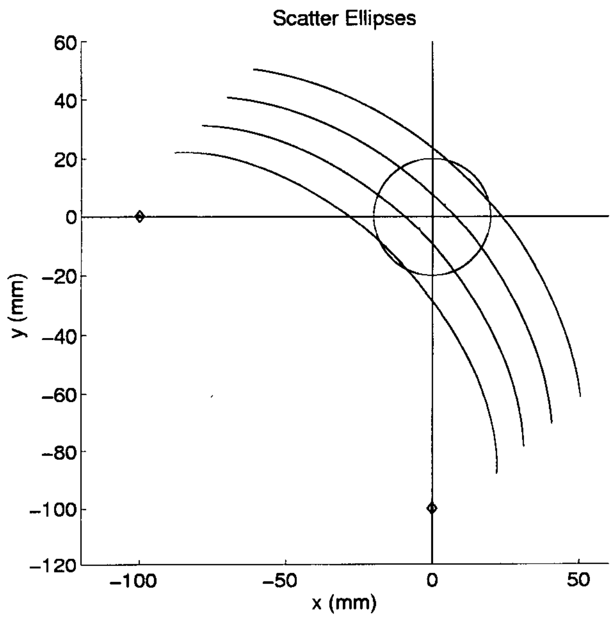

Figure 2.14: This figure illustrates the partial curves of several isochrones for a typical source and detector geometry, with $\mathbf{r}_s = (0, -100)$ mm and $\mathbf{r}_d = (-100, 0)$ mm. The circle represents the object that is being insonified. Note that the curves are nearly linear inside the object.

Essentially there is one such isochrone for every digitized time point in the detected ultrasound field. If the imaging algorithm could reconstruct the data exactly without any simplifying approximations, it would take the detected ultrasound contained in each time point at a particular view angle and spread it evenly over its corresponding elliptical isochrone. Sequential data points for a given view would yield sequential elliptical curves in the image space. Analysis of all data points for a given view would thus build up a partial image that consists of these curves.

This analysis of the single view reconstruction raises two points. The first is that the imaging system has no resolution in the lateral dimension (at 90° to the perpendicular bisector of the line joining the source and detector) since it cannot distinguish any two points on a given isochrone. Each view extracts information in the axial dimension only (along the perpendicular bisector of the line joining the source and detector). This is why numerous views must be combined to build up an accurate image, with each view defining the image along one direction. As data are collected at more views, the image space is defined along more directions, which is the basic idea behind computed tomography.

The second point to note is that in fact the reconstruction algorithm is based on several simplifying approximations which effectively "warp" the nearly linear (inside the insonified object) elliptical isochrones into straight lines that are parallel to the line joining the source and detector. This is evident in that each view yields a radial line of data in the 2D Fourier domain of the image. Radial lines of data provide spatial information in the image only along that line, as is illustrated by the example in Figure 2.15. Figure A plots the Fourier data for one representative view, while the image corresponding to these data is plotted in Figure B. Note that Fourier data are shown in a zoom view, and that the 2D function contains only zeros beyond the viewing region up to u and $v = 0.5$ mm^{-1}. More will be said on this warping of the isochrones in Section 5.3 of the Results Chapter.

2.4 Discussion of Attenuation Effects

Attenuation has a significant effect on the imaging process and a correction for it must be applied in order to obtain accurate and highly resolved images of attenuating media such as breast tissue. In order to achieve these images, a correction for attenuation due to tissue and water should be included in the reconstruction process. Both forms of attenuation are dependent upon two parameters that vary in any given insonification experiment. The first parameter is the angular wave number, or alternatively frequency, of the ultrasound field. When using pulsed fields, the source Fourier spectrum spans a range of frequencies, and attenuation increases with frequency. The second parameter is distance. Energy in the ultrasound field is absorbed by the propagation medium, and the greater the distance of travel, the more energy is absorbed. Attenuation results in a

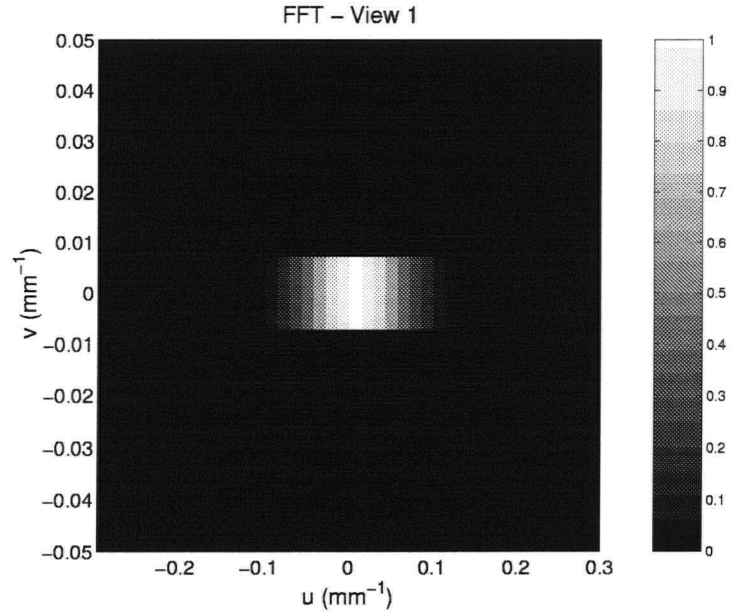

(A)

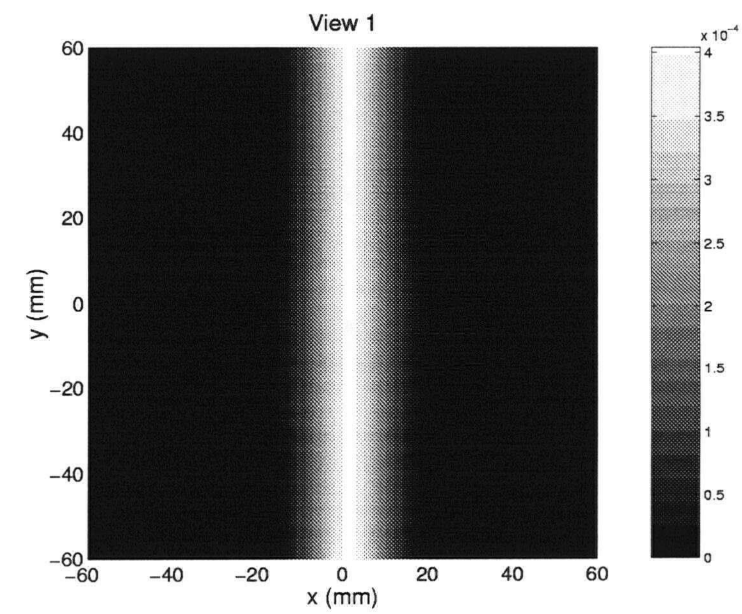

(B)

Figure 2.15: Figure A plots the Fourier data for one representative view, while the image corresponding to these data is plotted in Figure B.

reduction of ultrasound field amplitude at every point in the pulse.

Attenuation in tissue varies depending on composition. However, breast tissue falls under the category of soft tissue and is thus generally considered to have one average attenuation coefficient. This coefficient is a well-known empirical value, given by

$$1\frac{\mathrm{db}}{\mathrm{MHz}\cdot\mathrm{cm}} \tag{2.63}$$

which is quoted in numerous sources [43, 51, 87]. Given that frequency is $f = kc_t/2\pi$, where c_t is the average speed of sound in soft tissue, Equation 2.63 can be used to derive an expression for the attenuated ultrasound field amplitude in tissue, which is given by

$$\begin{aligned} A_t &= A_0\mathrm{ATT}_t(d_t, k) \\ \mathrm{ATT}_t(d_t, k) &= 10^{-\chi_t d_t k} \\ \chi_t &= \frac{-0.1c_t}{40\pi\,\mathrm{MHz}\cdot\mathrm{mm}} \end{aligned} \tag{2.64}$$

Here A_0 is the initial field amplitude, k is the angular wave number of the ultrasound in units of mm^{-1}, and c_t is equal to 1.54 mm/μs. d_t is the distance in millimeters that the ultrasound field travels through tissue.

The attenuation coefficient for water is quite different and is quoted in Reference [87] as

$$0.00022\frac{\mathrm{db}}{\mathrm{mm}\cdot\mathrm{MHz}^2} \tag{2.65}$$

Note that this expression is again based on empirical results. It can be easily derived through an analysis of the frequency dependence of half-value layer for water, which is the path length that reduces the intensity of the ultrasound beam to half of its original value. Substituting $f = kc_0/2\pi$, the following relation emerges that predicts the attenuated amplitude of the ultrasound field in water as a function of d_w and wave number:

$$\begin{aligned} A_w &= A_0\mathrm{ATT}_w(d_w, k) \\ \mathrm{ATT}_w(d_w, k) &= 10^{-\chi_w d_w k^2} \\ \chi_w &= \frac{-0.00022c_0^2}{80\pi^2\,\mathrm{MHz}^2\cdot\mathrm{mm}} \end{aligned} \tag{2.66}$$

Frequency (MHz)	d_w**(mm)**	**Amplitude Attenuation (%)**
1	50	0.13
4	50	2.0
10	50	11.9
1	100	0.25
4	100	3.9
10	100	22.4
1	150	0.38
4	150	5.9
10	150	31.6

Table 2.3: The above data are values of amplitude attenuation for ultrasound fields of different frequencies travelling through various distances of water.

where c_0, d_w, and k are measured in units of mm/μs, mm, and mm^{-1}, respectively. Reductions in ultrasound field amplitude as predicted by this relation are tabulated in Table 2.3 for various frequencies and values of d_w.

The attenuation coefficient in water is evidently dependent upon the square of frequency while that in tissue appears to be linear with frequency. It is important to keep in mind however, that the value quoted for tissue is only an average. In reality, the attenuation coefficient for tissue varies depending upon the type of tissue. For instance, that for muscle and tumour cells is actually dependent upon $f^{1.1}$, while that for fatty tissue is dependent upon $f^{1.5}$. The power that frequency is raised to varies due to tissue properties such as density, stiffness and viscosity [87]. Although very little is currently understood about the mechanisms of ultrasound attenuation, the expressions for the attenuation coefficients have been explained to some extent by finite element analysis [87]. This essentially models the ultrasound propagation medium as an extensive system of damped, coupled oscillators. The type of damping applied in the analysis falls into three main categories:

- Stiffness-proportional damping - dependent upon element stiffness (= Area $\times$ Elastic Modulus) and dependent upon f^2.

- Mass-proportional damping - dependent upon element mass and independent of frequency.
- Viscoelastic damping - dependent upon element fluid viscosity, and the corresponding attenuation can depend on frequency raised to any power from 0 to 2.

Through finite element analysis, it has been determined that attenuation in water is exactly described by stiffness-proportional damping, while attenuation in tissue appears to be modelled primarily by viscoelastic damping [87].

Chapter 3
Apparatus

The UCT prototype scanner design is shown in Figure 3.1. The scanner design includes a Plexiglas^{TM} water bath. The tissue being imaged is immersed in water because ultrasound is highly attenuated by air. The water couples the transducers to the object, thus allowing most of the ultrasound energy to travel freely into the object. The water bath houses two transducers, one to insonify the object and the other to detect scattered ultrasound. The transducers are supported by spindles that are individually rotated to allow for full circular motion of the source and detector around the tissue. It would be ideal to use an array of transducers that can each transmit and detect ultrasound as directed by the data acquisition system. However, the cost would be several times greater and is not warranted at the prototype stage. The two-transducer setup only adds to the data collection time and does not limit the experiments that can be performed. Prototypes of similar design have been used successfully by other groups, and they permit a large range of experiments to be performed [10, 32, 53, 80, 88].

The source is controlled by a pulser-receiver module that applies a negative voltage spike to the leads of the transducer. Several different pulsed transducers were employed in the course of the prototype development in order to test the system. These included concave and convex cylindrical transducers, a focussed commercial source, and a line source, all of which are described in Section 3.1. The detector transducer is a spot-poled reflector type hydrophone, which is discussed in Section 3.2. It converts the mechanical energy in the detected ultrasound field into a voltage signal. This signal is then input into an electronics setup composed of a preamplifier, the receiver (amplifier) portion of the pulser-receiver, and an analogue-to-digital converter (ADC). The ADC digitizes

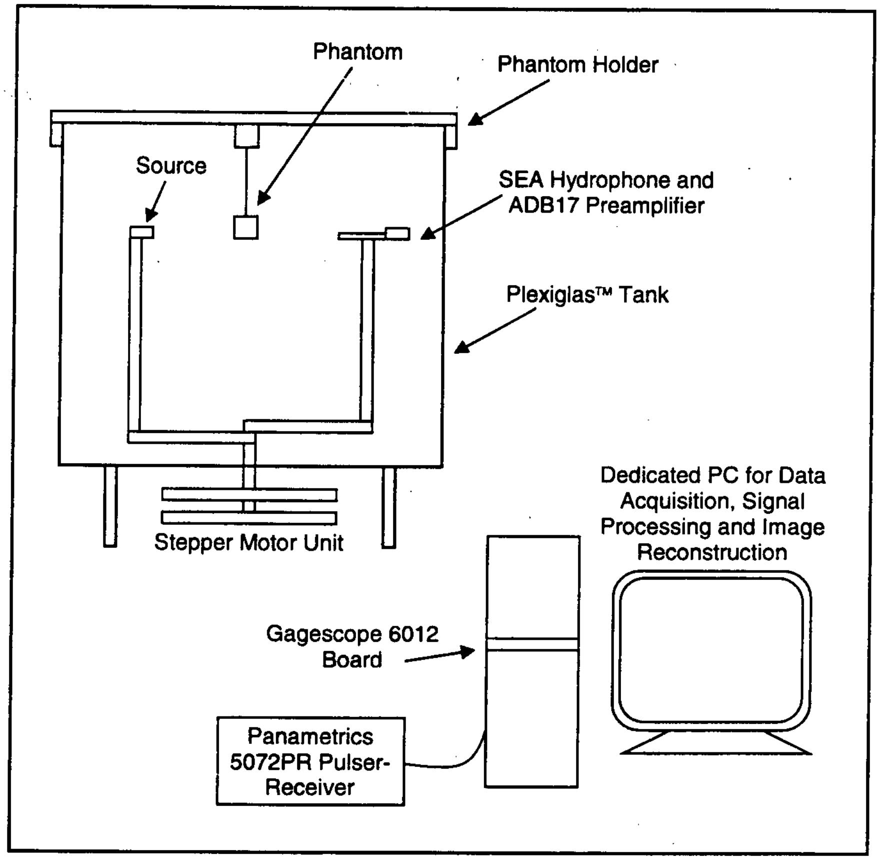

Figure 3.1: Schematic of the prototype pulsed UCT scanner.

the amplified voltage signal to enable subsequent digital signal processing and image reconstruction. The ADC is a board that sits inside a 400 MHz Pentium II PC with 192 MB of RAM, which controls the entire scanner setup. This computer performs sound wave generation, signal acquisition, signal processing, and image reconstruction. All data acquisition and data analysis software has been written in the Matlab™ programming environment.

3.1 THE SOURCES

Recall that the reconstruction method by Blackledge *et al* assumes the incident pulsed ultrasound field has the form of

$$p_0(\mathbf{r}, \omega) = A(\omega) g(\mathbf{r}|\mathbf{r}_s, \omega) \tag{3.1}$$

where $g(\mathbf{r}|\mathbf{r}_s, \omega)$ is the 2D Green's function propagator and $A(\omega)$ is the amplitude spectrum of the source. As such, the ideal source for use with this imaging technique has zero phase at its location, $\mathbf{r}_s$, and its field spreads out cylindrically from this point in 2D. Attempts were therefore made to physically generate this source field through the use of several different transducers. The first attempts made use of cylindrical sources that produced a pulsed field that was laterally uniform over an angle of $\pm 30^\circ$. The pulse had a wavelength of approximately 2 mm. Two of these sources were kindly produced by Mr. Jerry Posakony, a world expert in transducer technology who was formerly the manager of the Automation and Measurement Sciences Department at Batelle Pacific Northwestern Laboratories. These sources are not identical in that one has a convex face that produces a diverging field with a focal point behind the transducer face, while the other has a concave face that produces a field that converges at a focal point in front of the transducer. Unfortunately, both sources became corroded after a few experiments. This resulted in significant ringing that destroyed the concave source data signal. In the convex source the corrosion completely broke the connection to the piezoelectric element. Piezo Systems, Inc., of Cambridge, quoted US\$1K-2K to reproduce the convex source, so it was decided at this time to pursue the experimental work with other available sources. Two pulsed line sources were kindly provided by Drs. Frank Podd and Inäki Schlaberg, who are with the University of Leeds Process Tomography Unit which develops time-of-flight tomography methods for non-destructive evaluation. As described in Reference [78], these transducers each have an active element with dimensions 0.5×10 mm. The emission angle is approximately $\pm 35^\circ$, and the field strength within this region falls off with distance. However, these custom-made sources are incorporated into a specialized array in their current application. When used in the prototype UCT scanner, the soldered leads of the single transducer were in contact with water, which caused significant ringing and signal noise when backscatter mode was used. In addition, the sidescatter signal from these transducers was quite small and submersed in significant noise. The application of electronic sealant to the leads unfortunately did not alleviate this problem sufficiently to allow for use of these sources in the scanner. However, it was possible to detect a signal 3-5 cm directly in front of the line source for use in an additional test of the source model embodied in the reconstruction algorithm by Blackledge *et al.* The results of this are presented in Section 5.6.3.

Due to the above mentioned difficulties, the only source that was available for experimental use was a Panametrics V326 transducer with a 5.0 MHz center frequency and 0.375 inch diameter flat and circular active element. Unlike the cylindrical source assumed in the reconstruction algorithm, this source produces a field with a strong main lobe on axis and weak side lobes. The side lobes were not of concern in the experimental work because only objects with small diameters less than 4 mm were investigated. The field was foccussed at $\sim$ 25 mm. The near field was not investigated, nor were objects placed in this region for insonification, due to the erratic nature of the field according to transducer theory. Beyond the focus, the field strength decreased with distance due to beam spreading. The field had a full-width-half-maximum of roughly 10 ± 2 mm between the distances of 30 and 60 mm measured axially from the transducer face. The incorporation of this source into the reconstruction algorithm is discussed in Section 5.6.2, and the corresponding experimental results are presented in Section 5.6.3.

3.2 The Hydrophone

The hydrophone in the prototype scanner, which is illustrated in Figure 3.2, is a Model SPRH-B-0500 spot-poled reflector type device that was built by Speciality Engineering

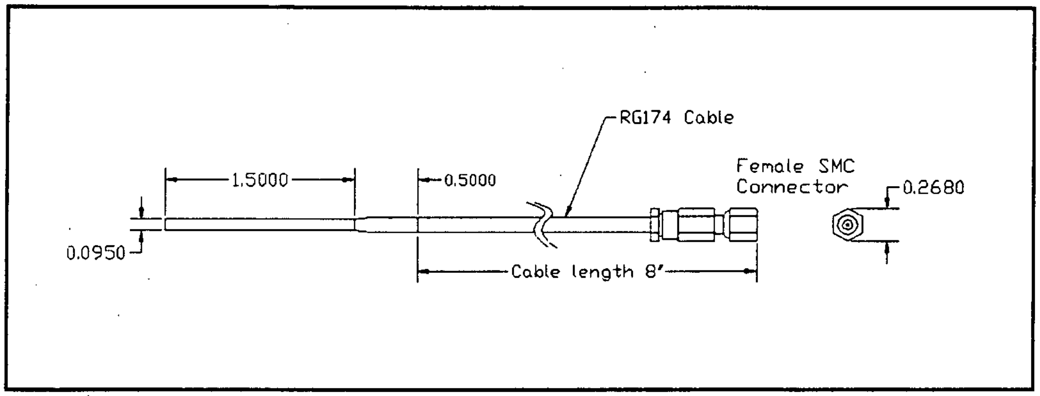

Figure 3.2: This figure illustrates the general design of the SPRH-B-α hydrophones (Copyright Speciality Engineering Associates). The width of the active element, α, is determined by the spot-poling process. All units are in inches.

Associates (SEA). This device outputs a voltage that is directly proportional to the pressure applied to it by an acoustic field, which is a characteristic termed piezoelectricity. The active element of the hydrophone is a disc that is 0.003 inch thick and made of the specialized ceramic known as Lead-Zirconate-Titanate (PZT). PZT is very versatile in that its physical, chemical and piezoelectric characteristics can be tailored to specific applications. It is also chemically inert. The ceramic disk is encased in a flat stainless-steel tip that is approximately 0.095 inches in diameter, which is in turn covered with a thin coating of a polymer called parylene to protect against corrosion due to water. The term "reflector type" in the name of the hydrophone model refers to the transducer design in which a ceramic element is backed by a material with a high acoustic impedance, which facilitates high sensitivity together with fast voltage rise times (ie: rapid reaction to the acoustic field) [8].

When a PZT ceramic is manufactured, the many dipolar molecules that make up its composition are not aligned. Without dipole alignment, the ceramic cannot exhibit piezoelectric properties and thus cannot detect acoustic fields. "Poling" is the process

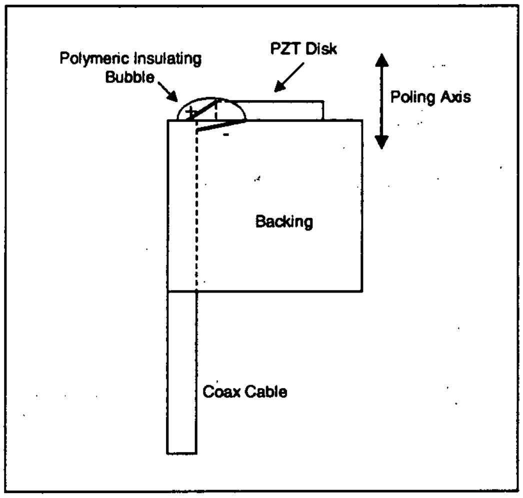

Figure 3.3: This figure is a closeup of the hydrophone tip. It illustrates the PZT disc and its backing, as well as the coax cable that carries the poling electrodes.

of permanently aligning the dipoles by applying a large electrical potential across the ceramic. "Spot-poling" is a special process in which the activated region of the ceramic can be limited to a tiny spot that is determined by the size of the electrodes that apply the electric field to the transducer. In the scanner hydrophone, this spot size is 500 microns. A small active area is desirable because the hydrophone will then have a wider field of view.

Figure 3.3 is a closeup view of the hydrophone tip that clearly shows the PZT disc and its backing, as well as the coax cable that carries the poling electrodes. The positive and negative electrodes are connected to the front (outside the hydrophone) and back (inside the hydrophone) sides of the PZT disc, respectively. In the poling process, the PZT disc and backing are placed in a dielectric oil bath, which is then heated to above the PZT glass transition temperature, T_g, but below the Curie temperature T_c. A dc poling voltage, V_p, is then applied across the electrodes. With the field still on, the temperature is slowly lowered to below T_g, and the field is subsequently removed. The applied electrical field is usually on the order of several kV/mm. After the poling process, the poling electrodes are used to transmit the piezoelectric voltage that results from acoustic field detection. The dimension between the poling electrodes is called the poling axis, and the piezoelectric dipoles are aligned with this axis.

After the PZT active element has been poled, its dimensions will change whenever it is insonified by an acoustic pressure field. Fields that compress the element along its poling axis (and therefore expand it along the perpendicular axis) will cause the hydrophone to output a voltage with opposite polarity compared to V_p. Fields that compress the element perpendicular to its poling axis (and therefore expand it along the poling axis) will result in voltage output that has the same polarity as compared to V_p. The induced voltage is directly proportional to the amount of compression/expansion to within the operating limits of the hydrophone.

For UCT experiments using pulses, it is desirable to have a hydrophone with a relatively flat response over the frequency band width of the source, which generally spans 100 KHz to 10 MHz. In other words, the hydrophone should output a similar voltage for a given amount of acoustic deformation at its face with little dependence upon frequency in the region of interest. If a detector response is not flat, then a frequency dependent correction must be applied to the spectrum of its output signal in order to determine the proper spectrum of the measured ultrasound field. The correction in turn introduces error into the data. SEA builds hydrophones with a relatively flat response by mounting the piezo-ceramic disk on a backing that has a matched or higher acoustic impedance, followed by termination into a high electrical impedance. A stainless steel backing was used in the hydrophone for the UCT scanner.

Figure 3.4 illustrates the frequency response of the hydrophone, as calibrated by the manufacturer. The response is relatively flat until around 10 MHz, which is the first region in which the ceramic disk exhibits a resonance. This resonance occurs when the wavelength of the longitudinal motion set up in the ceramic is equal to twice the thickness of the ceramic disk [73]. After 10 MHz, sound energy is rapidly dissipated

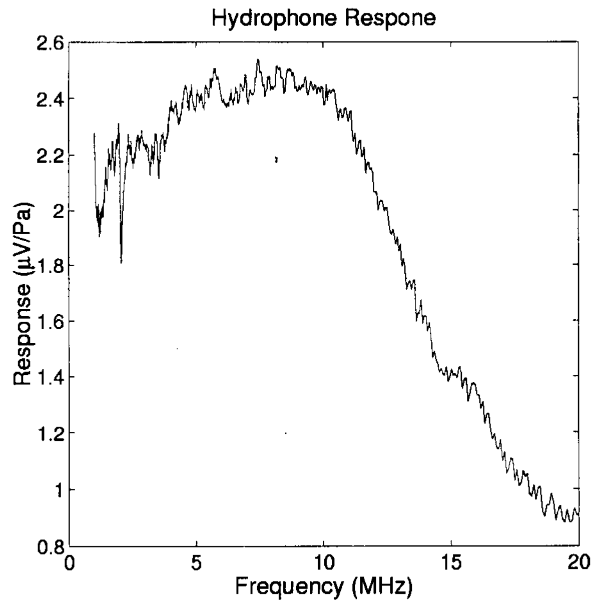

Figure 3.4: This figure illustrates the frequency response of the SPRH-B-0500 hydrophone, as calibrated by the manufacturer.

through resonant losses in the ceramic. Below 10 MHz, a small dip of about -2 db is evident at 1.5 and 2.5 MHz. The manufacturer explains that this is due to radial resonances in the steel backing of the hydrophone [73].

A description of the hydrophone angular response requires application of the Acoustical Reciprocity Theorem, which states that the receiving characteristics of a transducer acting as a detector are identical to its transmitting characteristics while acting as a source [50]. Stated another way, the directivity function of an ultrasound source as a function of direction and frequency is identical to the sensitivity of that same transducer when it is operated as a detector. Directivity simply refers to the amount of ultrasound that is radiated in any given direction about a transducer. Returning to the discussion of the hydrophone, the hydrophone inventor suggests that its angular response can be loosely described as the combination of the free baffle and rigid baffle models [73]. A free baffle is essentially a membrane stretched across a cylinder. The directivity function of this type of transducer is directly proportional to $\cos(q)$, where q is the angle of incidence of the sound wave on the baffle relative to the normal [50]. On the other hand, a rigid baffle is essentially a piston transducer, and it has a directivity function that is proportional to the following angular function [50]:

$$D \propto \frac{2\,J_1(ka\,\sin(q))}{ka\,\sin(q)} \tag{3.2}$$

J_1 is the Bessel function of the first kind. The directivity function described by Equation 3.2 has a main amplitude lobe between the first two null values and side lobes beyond these values. This pattern results from constructive and destructive interference between sound waves that are generated by different regions of the transducer face. With actual piston transducers, the ultrasound field produced does not fall to zero but instead reaches some minimum value. If the hydrophone in the prototype scanner were operated as a source of ultrasound, its directivity function would be proportional to a function given by the combination of the two models [73]:

$$\frac{2\,\cos(q)\,J_1(ka\,\sin(q))}{ka\,\sin(q)} \tag{3.3}$$

By the Reciprocity Theorem, the receiving characteristics of the hydrophone are identical to the directivity function, resulting in a theoretical sensitivity described by the expression above. Figure 3.5.A illustrates the theoretical angular response for a frequency of 5.05 MHz (wave number of 21.5 mm^{-1} in water at 20°C). The corresponding experimental response was measured for a narrow frequency band of 5.0-5.1 MHz, and this result is plotted Figure 3.5.B. Note that both the theoretical and experimental plots illustrate a relative angular response, since Figure 3.5.A plots Equation 3.3 and the experimental waveform was amplified before processing. Evidently, there is good agreement between experiment and theory. The experimental response drops by no more than 75% of its maximum over an angle of ±9.5°. Thus, if the hydrophone were situated 200 mm away from an object, it could view objects with diameters of up to 65 mm with very little drop in response over the extent of the object due to angle.

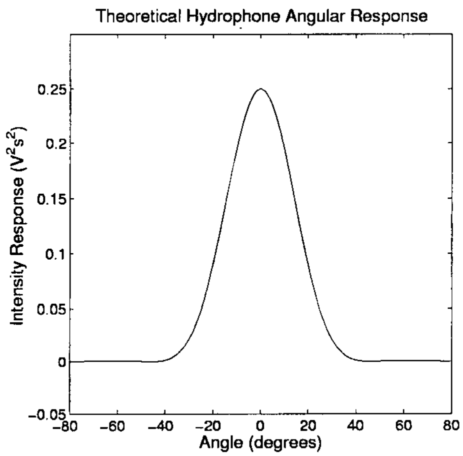

(A)

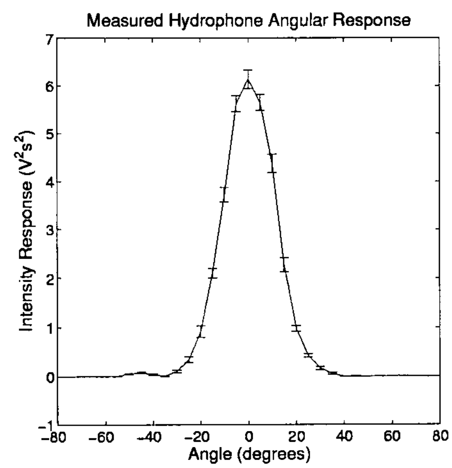

(B)

Figure 3.5: This Figure illustrates characteristics of the SEA 0.5 mm diameter hydrophone used in the prototype UCT scanner. Figure A illustrates the theoretical angular response for a frequency of 5.05 MHz (wave number of 21.5 mm^{-1} in water at 20°C), while the corresponding measured response for the narrow frequency band of 5.0-5.1 MHz is plotted in Figure B.

3.3 Stepper Motor Apparatus

It is desirable for a pulsed UCT scanner to be capable of sampling a scattered ultrasound field at points that are very close together. Recall from Section 2.2.8 that image size is directly proportional to the number of views, N_v, and therefore inversely proportional to the arc spacing between field sample points on the detector ring. Furthermore, Table 2.2 illustrated that values of $N_v \geq 6400$ are necessary for image widths that are comparable to the sizes of tissues that are imaged. Recall that if the image width is much smaller than the tissue size, there is a source of error due to the significant amount of scatter that originates from tissue areas outside the image space but which is ignored in the image reconstruction process. For a typical source and detector distance of 200 mm and $N_v = 6400$, the arc spacing between consecutive placements of the source-detector configuration is only 0.196 mm.

Note that fine transducer stepping is also a requirement in continuous wave UCT, but for a different reason. In this situation, image resolution is dependent upon how finely in space the scattered field is sampled while the source is kept stationary. If a typical 5 MHz source is used, its wavelength in water at 20°C is $\lambda = 0.296$ mm, and the maximum possible image resolution is $0.5\lambda = 0.148$ mm [32]. In order to potentially achieve this resolution, the detector must record the scattered field at successive locations that are no more than 0.5λ apart [32]. Given a typical detector distance of 200 mm, this would necessitate the recording of at least 8500 views. By extension, image resolution of approximately 1 mm would necessitate the recording of 1260 views.

The design of the prototype UCT scanner thus incorporated a mechanism that was aimed at allowing the movement of both the source and detector transducers in very small angular steps. Desired specifications were set at:

- 8000 steps over 360° (step size $\sim$ 2.7 minutes of an arc)
- error of $\pm 5\%$ in each step ($\sim \pm 8$ seconds of an arc)

The suitability of gear mechanisms was initially studied. Expert consultation from a custom gear house was sought, which was backed up by information in References [26] and [27] by Darle Dudley, who is a leader in the field of gear design. It was determined that step sizes and accuracies on this order are generally beyond the realm of even most sophisticated, custom-made worm gears. This is primarily due to the fact that gear motion involves the sliding of pinion teeth against gear teeth. Therefore, clearance must be left to allow for lubrication, and this space limits the stepping accuracy. Custom-made precision gears have tooth position accuracies of about $\Delta x = 0.0003$ inches [72]. A typical gear setup for the scanner would have been a 17-tooth pinion combined with a 187-tooth gear that has a diameter of 3.896 inches. Each component would have a tooth position error of Δx for a combined error of $2\Delta x$. Given a detector and source distance of 200 mm, this would translate to an error in the transducer positioning of approximately 0.062 mm. Unfortunately, this error is 32% of the desired step size at 200 mm for pulsed UCT.

It was suggested that the best option was to incorporate a traction drive into the scanner. The apparatus, which is illustrated in Figure 3.6, consists of a small capstan and large drive ring that interact via friction between their smooth surfaces. Hence, they are also referred to as friction drives. Traction drives are used where low power and highly accurate positioning is required. The unit was designed to position the transducers in steps of 0.05^o over a full 360^o with good accuracy on the order of $\pm 10 - 15\%$. The 25 mm diameter capstan is connected to the stepper motor shaft, and it fits snugly against the 250 mm diameter drive ring. The motor moves the capstan, which turns the drive ring through frictional force. The drive ring is connected to a spindle inside the tank that holds a transducer. There are two transducers in the prototype system, so there are two drive ring/capstan pairs in the traction drive. The connections between the drive rings and the transducer spindles pass through the tank by way of a bushing mechanism with two concentric pieces, one for each drive ring. Although the concentric bushing

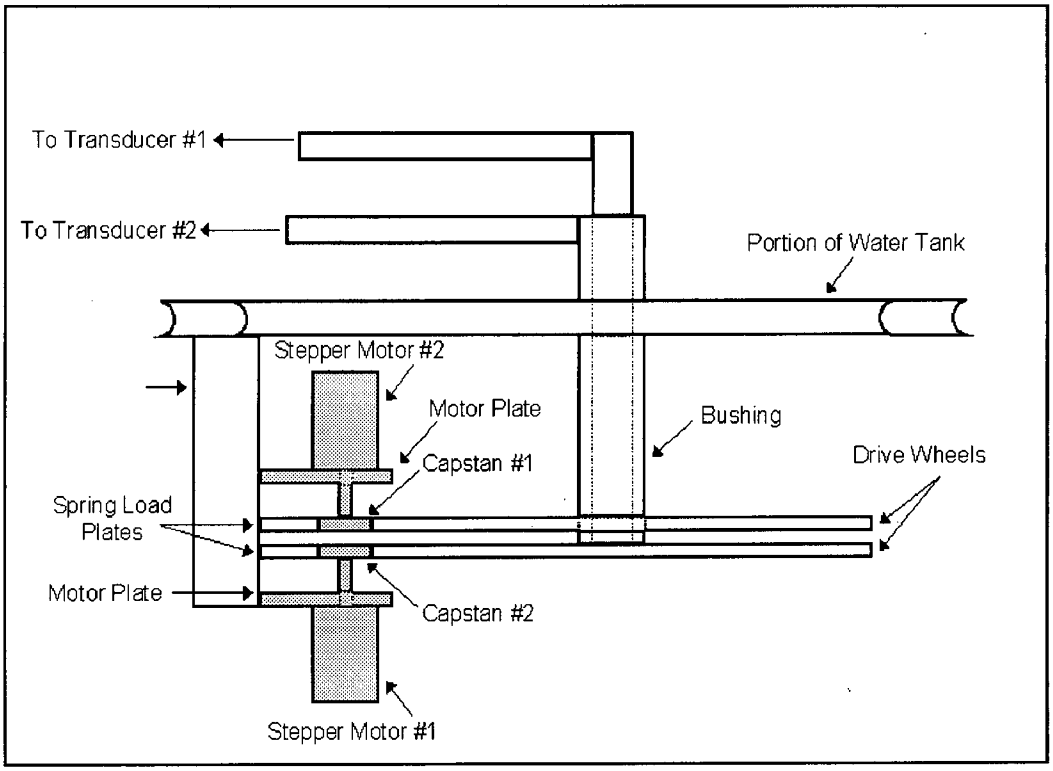

Figure 3.6: This figure illustrates the traction drive in the prototype UCT scanner.

mechanism has been used in other experimental UCT scanners, traction drives have not been used previously in ultrasound tomography [32]. However, these drives are common in precision positioning systems for large telescopes, such as those at the W.M. Keck Observatory in Hawaii and at the Kitt Peak National Observatory in Arizona [90, 91]. Traction drives are used to enable precision movement in robotics. The interested reader is referred to Reference [89] for a list of related publications.

Before the traction drive could be implemented, extensive calculations were required to determine if the system would theoretically work. In brief, the main limitation is that there must be sufficient frictional force at the contact zone of the capstan and drive ring surfaces in order to transmit motion to the drive ring. The frictional force, in turn, depends on both the coefficient of friction in the contact zone as well as the normal force applied to the drive ring by loading of the capstan. However, if the normal force is too large, the metal surfaces of the drive ring and capstan will experience plastic deformation, which leads to slippage of the traction drive. The study thus involves the analysis of rolling contact between two elastic solid cylinders, which is governed by the Hertz Theory of elastic contact.

The key references used for the contact problem were Landau and Lifshitz [54], and the books by Darl Dudley [26, 27]. The final result of the calculations indicated that a steel capstan combined with a steel drive ring would provide more than sufficient frictional force without plastic deformation. However, a major problem in the design of the drive was unfortunately discovered upon incorporating the traction drive into the UCT scanner. Recall that the drive rings are connected to the spindles through a concentric bushing mechanism. The outer drive ring is very easy to move and in fact can be rotated by the traction drive. In contrast, the inner drive ring is subject to substantial friction inside the bushing, which has increased over time due to corrosion inside the bushing. The force required to overcome this friction is significantly greater than what the current traction drive can provide. Given the costly nature of a new stepper motor apparatus, it was decided that a proof of concept study of the reconstruction algorithms would be conducted before additional funding is allocated towards improving the drive. As such, it was decided to use cylindrical phantoms for the majority of tests. For these, the scattered field can be recorded for a few representative angles, and these data can then be copied for as many views as desired. This approach has been used by other UCT researchers with useful results [32]. In the case of imaging experiments with noncylindrical phantoms, the required number of views can be kept to a minimum by restricting the object size to a few mm. The drive rings can then be clamped together at a relative angle of θ, and data can be recorded for each view by manually rotating the apparatus. The error in positioning the source and detector that is associated with this method is estimated to be $\pm 11\%$. This error is relatively large due primarily to the accuracy with which the apparatus can be positioned manually.

It should be noted that an attempt was made at holding the transducers stationary while rotating the phantom. A phantom holder was designed and carefully machined with the intent of accurately rotating the phantom with a stepper motor. However, the accuracy with which this apparatus held the phantom on center was not sufficient for use with this tomography method. Section 5.6.3 describes the large effect on image reconstruction that results from small errors in the measurement of the distance from the origin to the source or detector. The phantom holder did not maintain enough accuracy in this distance to be of use.

Because the traction drive ultimately did not operate as expected, the calculations involved in the Hertz Contact Problem have not been included in this thesis for purposes of brevity. Any parties interested in the mathematics involved are referred to Citations [26, 27, 54]. The author of this thesis may be contacted for further information.

3.4 Water Tank Design

The water bath was designed to ensure that reflections from the tank walls are easily separated from data through TOF analysis. A simulation of first-order ultrasound scattering in the absence of refraction was performed, in which a cylindrical tissue 60 mm in radius was insonified by a pulsed line source that was band limited from 1 to 10 MHz. An analysis was done of sound waves in the following four categories, which are illustrated in Figure 3.7:

- **Scatter Data (SD)** - Waves that were scattered from tissue and then detected by the hydrophone without further interaction.

- **Secondary Scatter (SS)** - Waves that were scattered from tissue, followed by reflection off the tank and subsequent detection.

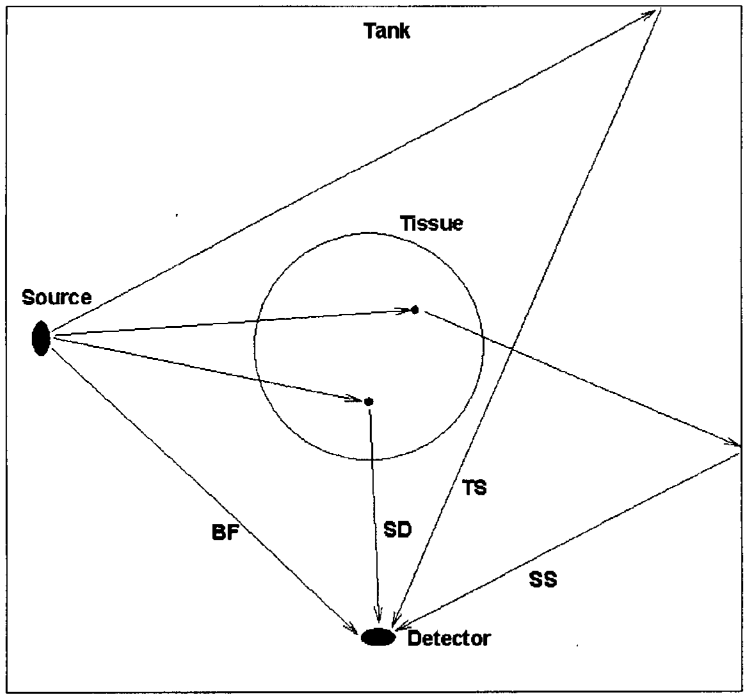

Figure 3.7: This schematic illustrates the four categories of detected sound that were considered in the simulation of scatter (scatter data (SD), secondary scatter (SS), tank scatter (TS), and background field (BF)). The source transmits a cylindrical wave, some portions of which follow the dashed arrows shown. Additional arrows indicate example paths along which these wave portions scatter.

- **Tank Scatter (TS)** - Waves that missed the tissue, but which were detected after scattering off the walls of the tank.
- **Background Field (BF)** - Waves that missed the tissue and reached the detector without scattering from any structures.

The simulated source transmits a cylindrical wave, and in the absence of refraction, selected portions of its field follow the arrows shown radiating from the transducer. Additional arrows in Figure 3.7 illustrate selected paths along which these field portions scatter. The analysis involved generating 1000 source field portions at random angles about the line transducer and tracing their paths as the field scattered in tissue or off the tank walls. Each scatter location was modelled as a cylindrical scatterer, which generates a scatter wave equally in all directions. The times-of-flight corresponding to all possible travel paths in the four scatter categories were calculated and histogrammed.

In doing this analysis, the frequency dependent field-of-view (FOV) of the hydrophone was considered. A transducer is said to have a FOV $= \pm\eta^{o}$ at a certain frequency, f, if it can detect an ultrasound field characterized by f when the corresponding wave fronts are incident upon its face at angles up to η to the normal. Recall from Section 3.2 that the hydrophone is modelled as the combination of a free and rigid baffle, with a sensitivity that is described by Equation 3.3. The nulls of this expression are determined by the directivity function of the rigid baffle, or piston transducer. The nulls defining the main lobe lie at an angle of $\pm\eta$, where

$$\sin(\eta) = \frac{0.61\lambda}{a} \tag{3.4}$$

and a is the radius of the transducer. Most of the ultrasound energy detected by a piston transducer is contained in the main lobe, and the FOV is therefore typically defined as this angle. In the TOF analysis to determine tank size, sound waves with a given wavelength λ were rejected if the corresponding angle of incidence at the hydrophone was greater than $\pm\eta$.

Through TOF analysis, it is evident that the background field is not an issue in an imaging experiment. At $\theta = 180^{o}$, there is no background field at the detector location because a backscatter signal is being recorded. At $\theta = 90^{o}$, the background field arrives at the detector well before the scatter. With the source and detector located a typical distance of 200 mm from the origin, the background field arrives at the detector with a TOF $= \sim 190$ μs. The first scatter signals for tissues with radii on the order of 5-7 cm, on the other hand, arrive with a TOF $= \sim 214 - 227$ μs due to the increased distance the sound waves travel on the path from the source to the object and then to the detector.

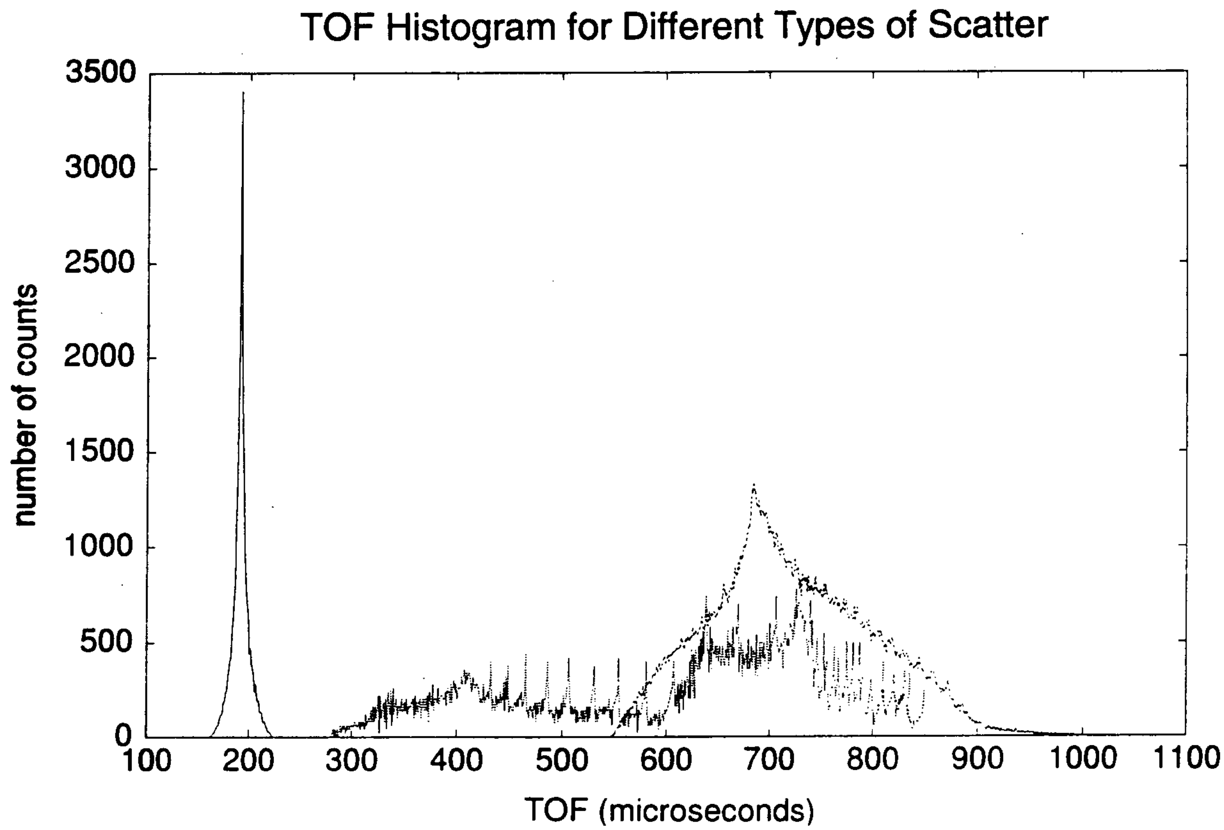

Figure 3.8: This figure illustrates the TOF histogram of scatter data (solid line - TOF = 160-220μs), tank scatter (dotted line - TOF = 290-850μs) and secondary scatter (dashed line - TOF = 550-1000μs) for a typical situation in which the tank was 70 cm wide, $|\mathbf{r}_s| = 12.4$ cm, $|\mathbf{r}_d| = 15.7$ cm, and the relative angle between the source and detector ranged from $0^\circ - 90^\circ$. The tissue radius was 4 cm.

In the simulation, tissues with radii varying from 3 to 7 cm were studied, together with typical source and detector distances between 12 and 20 cm. Since the type of UCT to be explored had not yet been decided when the tank was designed, the relative angle between the source and detector was allowed to vary between +90° and -90°, which covers both imaging setups for the methods presented in this thesis. With respect to TOF, scatter data arrive first due to the smaller sound path lengths involved, followed by tank scatter and then secondary scatter. Figure 3.8 illustrates a typical TOF histogram of scatter data, tank scatter and secondary scatter for a simulation in which the tank size was 70 cm $\times$ 70 cm, $|\mathbf{r}_s|$ was 12.4 cm, $|\mathbf{r}_d|$ was 15.7 cm, and the relative angle between the source and detector was varied between 0^o and 90^o. The tissue radius was 4 cm.

A tank of width 70 cm was found to be optimal in terms of practical use and separation of data from tank scatter by TOF analysis. With the broad range of source/detector distances and tissue sizes studied, the last data signal arrived at least 40 μs earlier than the first tank scatter signal. Secondary scatter generally arrived at the hydrophone about 400 μs after the scatter data were detected. Evidently the tank has a reverberation time, given by the time required for all scatter off the walls to be absorbed and die down in amplitude to the noise level of the amplifier. The tank was found to have a reverberation time of approximately 1150 microseconds, allowing for a new ultrasound pulse to be transmitted for data-acquisition rates up to 800 Hz.

3.5 The Electronics

3.5.1 The Pulser-Receiver

The UCT scanner includes a Panametrics model 5072PR pulser-receiver that is designed for use in thickness gauging, flaw detection, medical research, and materials characterization. The pulser section of the unit produces an electrical pulse that excites the piezoelectric source transducer to produce an ultrasound pulse. The excitation pulse is a negative impulse with an amplitude on the order of -100 V. The impulse amplitude can be varied by selecting the pulse energy to be 13, 26, 42 or 104 μJoules. The output impedance can be set at 8 specific values in the range of 15-500 Ohms, including 50 Ohms. The pulse rise time is $\sim$ 5 ns at 50 Ohms output and minimum pulse energy. The unit has an External Trigger connection and a Sync Out signal.

3.5.2 Components Beyond The Hydrophone

Upon detection by the hydrophone, the ultrasound field signal is converted to a voltage signal, which is then input into an electronic setup composed of three units:

- A Model ADB17 Specialty Engineering Associates preamplifier.
- Receiver section of the 5072PR Panametrics pulser-receiver.
- A Gagescope 6012 analogue-to-digital converter.

The preamp is necessary because the hydrophone construction includes a high impedance RG174 output cable, which attenuates voltage signals significantly. This cable is thus only 20 cm long, and it is connected to the preamplifier, which has a gain that is typically 17 db into 50 ohms or 20 db into a high impedence. The preamp output is also connected to a low impedence coax cable, which can transmit voltage signals for long distances. The preamp has a high input impedance that facilitates good sensitivity as well as wide band width. It consists of a low noise, three-stage discrete transistor amplifier. The first stage is an FET for high impedance, and the final stage is an emitter follower for driving 50 ohms at frequencies up to 25 MHz. As illustrated in Figure 3.9, the gain varies from only 17.3 to 16.8 db between 1 and 10 MHz. The preamplifier is waterproofed by the manufacturer.

Following preamplification, the signal enters the Panametrics pulser-receiver, which can apply a gain of -59 to +59 db. According to the manufacturer, this unit has a linear response within the range of $\pm$ 1 volt. Furthermore, from 0.1 to 20 MHz, the receiver amplifier gain is flat to within 2 db. Gain curves for the 40 and 50 db amplifier settings are shown in Figure 3.10.

The final component of the data acquisition system is the Gagescope 6012 ADC board with 12 bit operation and 1 MB of memory. This unit digitizes the voltage signal from the transducer so that the information can be input to algorithms for digital signal processing and image reconstruction. When the Gagescope 6012 is set to its lowest input range of $\pm$100 mV, the smallest voltage that can be detected is $\pm$0.05 mV. By extension, successive memory values represent an additional voltage of $\sim$ 0.05 mV, and the error associated with each location is therefore $\sim$ 0.025 mV. When the pulser-receiver is set at a

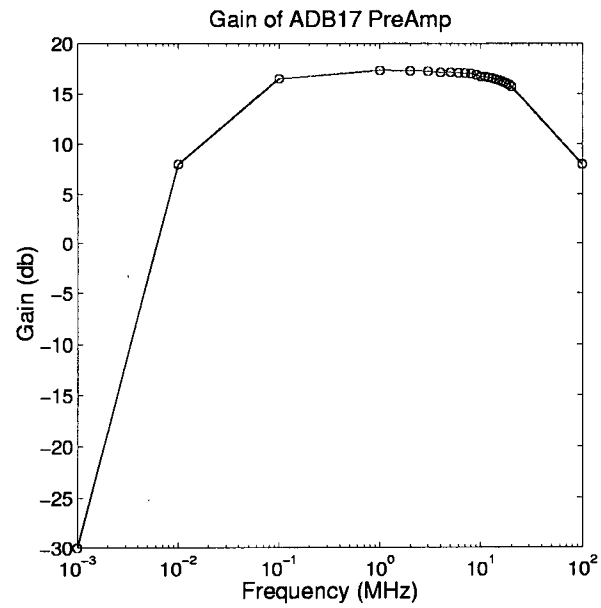

(A)

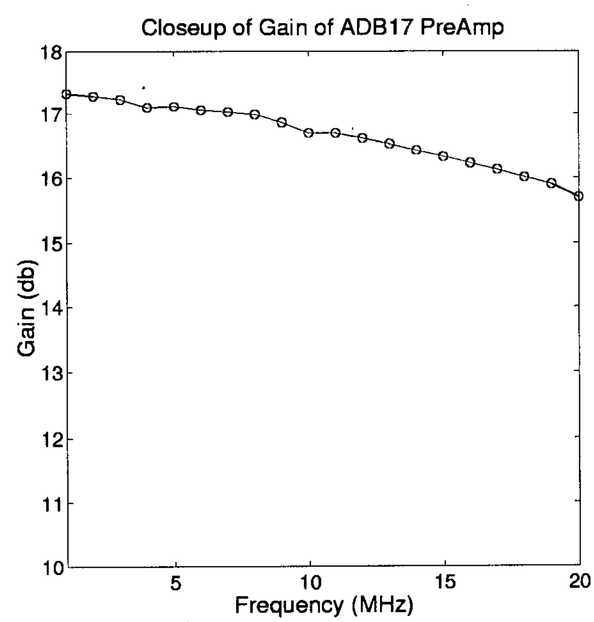

(B)

Figure 3.9: Figures A and B illustrate a broad view and a closeup, respectively, of the frequency response of the Speciality Engineering Associates ADB17 preamplifier. The gain is very flat and varies from only 17.3 to 16.8 db between 1 and 10 MHz.

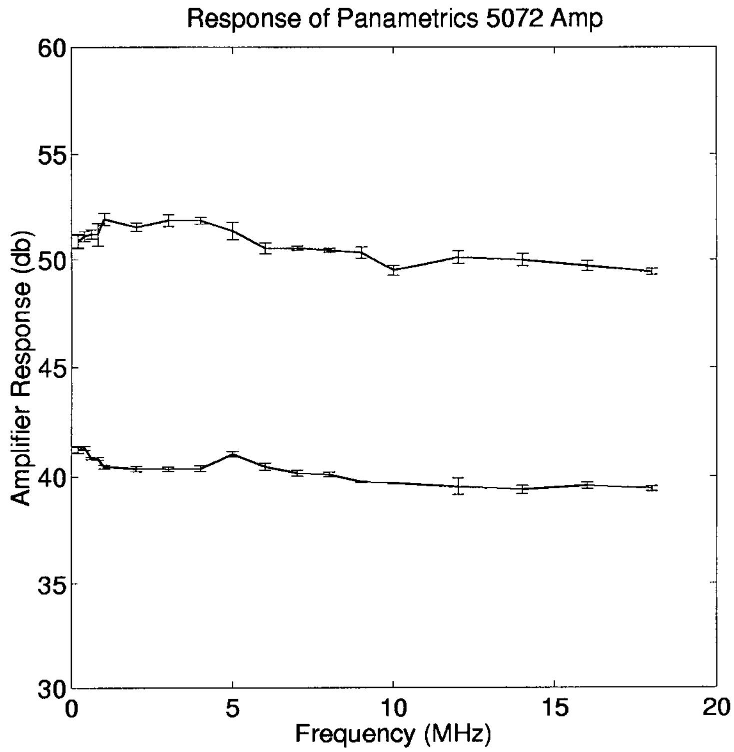

Figure 3.10: Illustration of the frequency response of the amplifier portion of the Panametrics 5072 pulser-receiver for the amplifier settings of 40db and 50db. The response is flat to within 2 db from 0.1-20 MHz.

gain of 40 db, the average magnitude of the points in a typical digitized ultrasound signal is on the order of 30 mV. Thus the percentage error in the signal voltage measurements is very low and on the order of $\pm 0.1\%$. The Gagescope 6012 has an External Trigger input that is fed by the Sync Out signal of the Panametrics pulser-receiver. Hence, time zero is defined as the moment when the pulser excites the source transducer with a voltage impulse, and the ADC board begins recording the hydrophone output from this time onward.

Chapter 4
Experimental Methods

It was necessary for several experimental methods to be incorporated into the prototype UCT scanner. An approximate correction for frequency dependent attenuation was developed in an attempt to obtain "first order" corrected images. A novel imaging algorithm was also developed, which is based on an algebraic reconstruction technique that includes the concept of an attenuated propagator. This is similar to the Green's function propagator, with the exception that factors are added that describe attenuation due to water and tissue. In addition, a preliminary study was done of conventional DSP methods for noise reduction. Finally, a study was done to compare several methods of interpolating Fourier data from a radial grid to a square grid. The method that imparted the least error was incorporated into the image reconstruction algorithms. The experimental methods studied or developed in this thesis are discussed in detail in the following sections.

4.1 Approximate Correction for Attenuation

An approximate attenuation correction was studied in an attempt to extend the method of Blackledge *et al.* For each new imaging experiment, a corresponding attenuation factor can be calculated that is dependent upon ultrasound wave number, k, the average distance ultrasound travels through tissue, $\overline{d}_t$, and the average distance that the waves travel through water, $\overline{d}_w$. Like the original reconstruction method, the approximate attenuation correction assumes that only first order scattering occurs.

The correction method requires knowledge of an approximate tissue outline, which can be obtained from a simple backscatter image based upon TOF analysis. The tissue can be insonified at several view angles by a source that emits a pulse with a short length and narrow width. Some fraction of the pulse will be reflected directly back to the transducer, which can be used to detect the backscatter signal. The TOF is simply

$$t = \frac{2\Delta d}{c_w} \tag{4.1}$$

where Δd is the distance between the transducer face and the tissue surface that lies directly in front of it. The transducer position is known for each angle, and therefore the tissue perimeter can be built up from the composite pieces determined from each view between 0° and 360°.

As described in Section 2.4, attenuation due to both water and tissue is dependent upon the distance that an ultrasound wave travels in each medium and the angular wave number being considered. If it is known for certain that a particular scatter signal travelled through exactly D_t mm of tissue and D_w mm of water, then the detected signal can be Fourier Transformed to yield the function $\mathrm{FT}_d(k)$, and an attenuation correction coefficient, Q, can be applied to each Fourier component to yield new components $\mathrm{FT}_c(k)$ given by

$$\begin{aligned} \mathrm{FT}_c(k) &= \mathrm{FT}_d(k)\, Q \\ Q &= \mathrm{ATT}_t^{-1}(D_t, k)\, \mathrm{ATT}_w^{-1}(D_w, k) \end{aligned} \tag{4.2}$$

where ATT_t and ATT_w are defined by equations 2.64 and 2.66, respectively. However, the cylindrical source formalism embodied in the method by Blackledge *et al* makes it impossible to know d_t and d_w exactly, even for small time windows of the scatter signal. The analysis in Section 2.3 illustrated that pulses scattering from different points along elliptical isochrones through the image space have the same time-of-flight. As such, even a single point in the detected ultrasound signal can have scatter subsignals that each travelled along paths with vastly different d_t and d_w. Thus it is generally quite difficult to correct for frequency and path-dependent attenuation.

It was hypothesized that an approximate attenuation correction could be developed by reducing the independent parameters to only frequency through the adoption of a single d_t and d_w for all regions of the tissue. Fourier data that are approximately corrected, $\mathrm{FT}_{appr}(k)$, could then be calculated from the original detected signal components, $\mathrm{FT}_d(k)$, in the approach of Blackledge *et al.* The process involves the application of an approximate correction coefficient, Q_{appr} that is the inverse of a rough attenuation coefficient, C, as shown in the following:

$$\begin{aligned} \mathrm{FT}_{appr}(k) &= \mathrm{FT}_d(k)\, Q_{appr} = \mathrm{FT}_d(k)\, \frac{1}{C} \\ C &= \mathrm{ATT}_t(d_t = \alpha \bar{d}_t, k) \times \mathrm{ATT}_w(d_w = \beta \bar{d}_w, k) \\ &= 10^{-\chi_t\,(\alpha \bar{d}_t)\,k} \times 10^{-\chi_w\,(\beta \bar{d}_w)\,k^2} \end{aligned} \tag{4.3}$$

Recall that χ_t and χ_w are defined according to Equations 2.64 and 2.66 in Section 2.4. The parameters α and β were introduced in order to allow some degree of flexibility in developing a reasonably good approximate attenuation correction. An attempt was furthermore made to chose good values of α and β through the following analysis.

The approximate correction was developed via a computer simulation of first order scattering in a 2D system in the absence of refraction. The source was assumed to be cylindrical, and it radiated a short wave train (a few cycles of CW ultrasound) of a given frequency, f, in all 2D directions about the transducer. Scatter from 200 random points in three 2D cylindrical tissues with radii of 30, 40 and 50 mm, respectively, was analyzed for a multitude of frequencies between 1 and 10 MHz. Assuming the tissue to be cylindrical was considered to be a reasonable approach since the breast would approximate a cylinder in the waterbath setting. The majority of the breast tissue would be situated within a cylindrical cross-section, and hence most attenuation would occur within this cylinder. A first order scatter event was defined as a unit fraction of a sound wave of a given frequency radiating from the source, traversing the tissue, scattering from a point and reaching the detector. The amplitudes of the scattered unit waves are termed scatter amplitudes (SA's), and these were attenuated in simulation due to both water and tissue.

The scatter amplitude for each event was then corrected with two approaches. First, an approximate correction was applied to the detected scatter amplitudes, SA_d, as per Equation 4.3 to yield SA_{appr}:

$$\mathrm{SA}_{appr} = \mathrm{SA}_d \, Q_{appr} \tag{4.4}$$

Secondly, a more accurate correction coefficient, Q_R, was determined based on tracing wave paths from the source to the detector via each scatter point in the absence of refraction. A far more accurate d_t and d_w was thus obtained for each of the 200 first order scatter events. This yielded a rigorously corrected scatter amplitude, SA_R, for each scatter event, given by:

$$\begin{aligned} \mathrm{SA}_R &= \mathrm{SA}_d \, Q_R \\ Q_R &= \mathrm{ATT}_t^{-1}(d_t, k)\, \mathrm{ATT}_w^{-1}(d_w, k) \end{aligned} \tag{4.5}$$

where k corresponded to the wave train in the event under consideration. SA_{appr} and SA_d were then compared to the more accurate SA_R. Percentage errors were calculated for each scatter event as follows:

$$\epsilon = \frac{|\mathrm{X} - \mathrm{SA}_R|}{|\mathrm{SA}_R|} \times 100\% \tag{4.6}$$

where X was either SA_{appr} or SA_B.

Via the simulation, values of α and β were determined which minimized the error in the scattering amplitudes. These variables were the only experimental parameters, and all remaining terms in Equation 4.3 follow from the empirical formulas for attenuation in tissue and water given by Equations 2.64 and 2.66. The simulation indicated that the SA error was minimized for all tissue examples only when $\alpha = 1.5$. Stated another way, the approximate attenuation correction performed best when the assumed distance of propagation through tissue was $1.5\overline{d}_t$ for every scatter point within the tissue. In contrast, the optimal value of β varied directly and nonlinearly with tissue radius. The

Range of ϵ for SA_B (%)	**% of Scatter Events with ϵ in Range**
0-50	6.2
50-100	4.0
100-500	4.4
500-1000	3.7
1000-50000	34.7
50000-100000	8.3
> 100000	38.7

Table 4.1: The above data illustrate the error in scattering amplitude with no attenuation correction applied. Each SA corresponds to a different scattering point and ultrasound frequency.

best β values for the three tissue radii of 30, 40 and 50 mm were determined to be 1.9, 3.0 and 5.0, respectively. Different values of β resulted in a few SA error values that were greater than 100%. It is not surprising that the $\overline{d}_w$ multiplier is generally quite large. The attenuation due to water is 1-2 orders of magnitude less than that due to tissue, and thus the water term in the correction is essentially acting a fine-tuning mechanism.

The $\overline{d}_w$ multiplier was found to dictate the percentage of SA errors that were greater than 100%. For instance, multipliers of 3 and 2.5 together with a tissue radius of 40 mm resulted in 0% and 0.15% of the SA errors being greater than 100%, respectively. The multiplier in front of $\overline{d}_t$ affected the relative percentages of SA errors in the ranges of $0 - 50\%$ and $50 - 100\%$. The results of an example simulation for a tissue radius of 40 mm are presented in Figure 4.1, where ϵ is plotted for SA_{appr}. On this graph, one curve as a function of frequency is plotted for each of the scatter points. Table 4.1 presents values of ϵ for SA_B given the same scattering tissue. The approximate correction had a positive effect on the scatter amplitude errors. SA_{appr} values for 100% of the scatter events had less than 100% error when compared to the rigorously corrected SA's. In the case of no attenuation correction, SA_B for 89.8% of the scatter events had greater than 100% error compared to SA_R. Furthermore, SA_B values for 38.7% of the scatter events

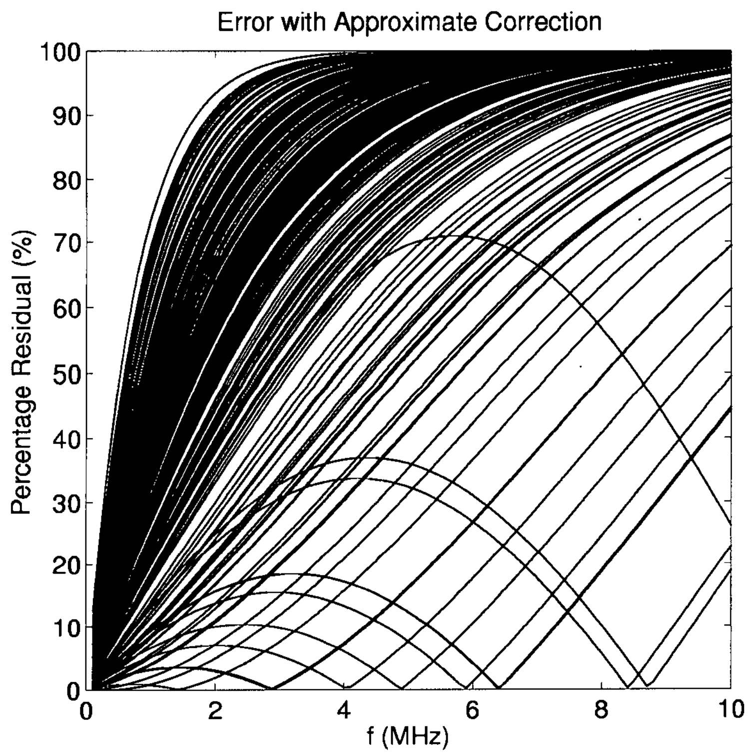

Figure 4.1: This graph illustrates the percentage errors in scatter amplitude that result after the application of the approximate attenuation correction described by Equation 4.3. One curve as a function of frequency is plotted for every scatter point.

had greater than $10^5\,\%$ error. Evidently, the approximate attenuation correction yields input data for image reconstruction that has much less error than with no correction at all.

4.2 ART with Attenuated Propagators

According to Equation 2.10 in Section 2.2.1, the scattered ultrasound field in two dimensions can be written as

$$\begin{aligned} p_s(\mathbf{r}_d, \mathbf{r}_s, \omega) &= p(\mathbf{r}_d, \mathbf{r}_s, \omega) - p_0(\mathbf{r}_d, \mathbf{r}_s, \omega) \\ &= A(\omega)\, k^2 \int_{\Re^2} g(\mathbf{r}|\mathbf{r}_d, k)\gamma_\kappa(\mathbf{r})g(\mathbf{r}|\mathbf{r}_s, k)\mathrm{d}^2\mathbf{r} - \end{aligned} \tag{4.7}$$

$$A(\omega) \int_{\Re^2} g(\mathbf{r}|\mathbf{r}_d, k) \nabla \cdot (\gamma_\rho(\mathbf{r}) \nabla g(\mathbf{r}|\mathbf{r}_s, k)) \mathrm{d}^2\mathbf{r}$$

after the application of the Born approximation and the introduction of a pulsed line source. Recall that the propagator, $g(\mathbf{r}|\mathbf{r}_j, k)$, describes both the reduction in field amplitude due to geometrical spreading, as well as the phase change due to ultrasound propagation from $\mathbf{r}$ to $\mathbf{r}_j$. It has the form

$$g(\mathbf{r}|\mathbf{r}_j, k) = -\frac{i}{4} H_0^1(k|\mathbf{r} - \mathbf{r}_j|) \tag{4.8}$$

where H_0^1 is the Hankel function of the first kind [81]. Equation 4.7 is a suitable starting point for the development of an algebraic reconstruction technique in which frequency dependent attenuation can be included. The resulting algorithm has the potential to reconstruct $\gamma_\rho(\mathbf{r})$ and $\gamma_\kappa(\mathbf{r})$ for attenuating objects.

4.2.1 The Attenuated Propagator

If the distances the ultrasound wave travels through water and tissue are known to be $d_w(\mathbf{r}, \mathbf{r}_j)$ and $d_t(\mathbf{r}, \mathbf{r}_j)$, respectively, terms describing attenuation due to tissue and water along the path from $\mathbf{r}$ to $\mathbf{r}_j$ can be expressed as

$$\begin{aligned} \mathrm{ATT}_t &= 10^{-\chi_t d_t k} \\ \mathrm{ATT}_w &= 10^{-\chi_w d_w k^2} \end{aligned} \tag{4.9}$$

Recall that these expressions follow from Equations 2.64 and 2.66 in Section 2.4. The original propagator in Equation 4.8 can be transformed into an attenuated propagator of the form

$$\tilde{g}(\mathbf{r}|\mathbf{r}_j, k) = \mathrm{ATT}_w(d_w(\mathbf{r}, \mathbf{r}_j), k)\, \mathrm{ATT}_t(d_t(\mathbf{r}, \mathbf{r}_j), k)\, g(\mathbf{r}|\mathbf{r}_j, k) \tag{4.10}$$

Recall that in the nonattenuating case, the assumptions of far field imaging and use of a band limited source enables the Green's function to be expanded as

$$g(\mathbf{r}|\mathbf{r}_j, k) = \alpha S \tag{4.11}$$

$$\begin{aligned} S &= \frac{\exp(ik|\mathbf{r}-\mathbf{r_j}|)}{(k|\mathbf{r}-\mathbf{r_j}|)^{\frac{1}{2}}} \\ \alpha &= i\frac{\exp(3i\pi/4)}{2\sqrt{2\pi}} \end{aligned}$$

Equation 4.11 can therefore be transformed into an approximate attenuated propagator of the form

$$\begin{aligned} \tilde{g}(\mathbf{r}|\mathbf{r}_j,k) &= \alpha\tilde{S}(k|\mathbf{r}-\mathbf{r}_j|) \\ \tilde{S}(k|\mathbf{r}-\mathbf{r}_j|) &= \mathrm{ATT}_w(d_w(\mathbf{r},\mathbf{r}_j),k)\,\mathrm{ATT}_t(d_t(\mathbf{r},\mathbf{r}_j),k)\,S(k|\mathbf{r}-\mathbf{r}_j|) \end{aligned} \tag{4.12}$$

4.2.2 p_s in Presence of Attenuation

The expressions for $\tilde{g}$ and $\tilde{S}$ can be substituted into Equation 4.7 to derive an expression for the spatially varying p_s in the presence of frequency dependent attenuation. Using the simplified notation that $\tilde{S}_{\mathbf{r}_j} = \tilde{S}(k|\mathbf{r}-\mathbf{r}_j|)$, the expression for the scattered field is

$$p_s(\mathbf{r}_d,\mathbf{r}_s,\omega) = A(\omega)\,\alpha^2\int_{\Re^2}\tilde{S}_{\mathbf{r}_d}\{k^2\,\gamma_\kappa(\mathbf{r})\tilde{S}_{\mathbf{r}_s} - \nabla\cdot(\gamma_\rho(\mathbf{r})\nabla\tilde{S}_{\mathbf{r}_s})\}\,\mathrm{d}^2\mathbf{r} \tag{4.13}$$

All that remains is the derivation of an expression for $\nabla\tilde{S}_{\mathbf{r}_j}$.

The derivation of $\nabla\tilde{S}$ follows steps similar to those in the derivation of S in Appendix B, with the exception that terms due to attenuation in water and tissue are included. This exercise yields a new result that does not appear to have been previously cited. First the operation of ∇ on $\tilde{S}$ is expanded to yield

$$\nabla\tilde{S} = \nabla S\,\mathrm{ATT}_w\,\mathrm{ATT}_t + \mathrm{T1} + \mathrm{T2} \tag{4.14}$$

$$\begin{aligned} \mathrm{T1} &= S\,\nabla\{\mathrm{ATT}_w\}\,\mathrm{ATT}_t \\ \mathrm{T2} &= S\,\mathrm{ATT}_w\,\nabla\{\mathrm{ATT}_t\} \end{aligned} \tag{4.15}$$

From the **C.R.C. Standard Mathematical Tables**, $\nabla(10^u)$ can be written

$$\nabla(10^u) = \frac{\partial(10^u)}{\partial u}\nabla u = 10^u\,\ln(10)\,\nabla u \tag{4.16}$$

Thus,

$$\begin{aligned}\nabla \mathrm{ATT}_w &= \nabla\{10^{-\chi_w d_w k^2}\} \\ &= \mathrm{ATT}_w \cdot \ln(10) \cdot \nabla(-\chi_w\, d_w\, k^2) \\ &= -\chi_w\, k^2\, \mathrm{ATT}_w \ln(10) \nabla d_w\end{aligned} \tag{4.17}$$

Similarly, the expression for $\nabla \mathrm{ATT}_t$ is

$$\begin{aligned}\nabla \mathrm{ATT}_t &= \nabla\{10^{-\chi_t d_t k}\} \\ &= -\chi_t\, k\, \mathrm{ATT}_t \ln(10) \nabla d_t\end{aligned} \tag{4.18}$$

Substituting these expressions for T1 and T2 into Equation 4.14 and recalling that

$$\nabla S = ik\hat{\mathbf{n}}_j S \tag{4.19}$$

yields

$$\begin{aligned}\nabla \tilde{S} &= S\, \mathrm{ATT}_w \mathrm{ATT}_t\, \{ik\hat{\mathbf{n}}_j - k\ln(10)(\chi_w\, k \nabla d_w - \chi_t\, \nabla d_t)\} \\ &= S\, \mathrm{ATT}_w \mathrm{ATT}_t\, \{ik\hat{\mathbf{n}}_j - \mathrm{T3}\}\end{aligned} \tag{4.20}$$

Evidently, if it can be shown that $\mathrm{T3} \ll ik\hat{\mathbf{n}}_j$, then the attenuated propagator will simply reduce to the original propagator multiplied by the attenuation coefficients in water and tissue.

Term T3 can be expanded as follows:

$$\begin{aligned}\mathrm{T3} &= k\ln(10)(\chi_w\, k\nabla d_w - \chi_t\, \nabla d_t) \\ &= k\ln(10)\{\frac{-0.00022 c_w^2}{80\pi^2\,\mathrm{MHz}^2 \cdot \mathrm{mm}}\, k\nabla d_w - \frac{-0.1 c_t}{40\pi\,\mathrm{MHz}\cdot\mathrm{mm}}\, \nabla d_t\} \\ &= k^2 \nabla d_w\, 1.4053 \times 10^{-6}\mathrm{mm} + k\nabla d_t\, 1.2255 \times 10^{-3}\end{aligned} \tag{4.21}$$

where c_w and c_t are 1.48 mm/μs and 1.54 mm/μs, respectively. Note that T3 has the same units as the $ik\hat{\mathbf{n}}_j$ term of $\nabla\tilde{S}$, as required. $d_w(\mathbf{r}, \mathbf{r}_j)$ and $d_t(\mathbf{r}, \mathbf{r}_j)$ are functions that are not known analytically but which must be determined numerically given $\mathbf{r}$ and

$\mathbf{r}_j$. To a first order approximation, in which refraction is not considered, $d_w(\mathbf{r}, \mathbf{r}_j)$ and $d_t(\mathbf{r}, \mathbf{r}_j)$ are simply the distances travelled through water and tissue, respectively, along the straight-line path joining $\mathbf{r}$ and $\mathbf{r}_j$. Calculation of these distances involves determining numerically if in fact the straight-line path intersects tissue, and where these intersection points lie.

In this thesis, this analysis was performed via a computer simulation that tracked the ultrasound paths. A 2D function of $d_w(\mathbf{r}, \mathbf{r}_j)$ and $d_t(\mathbf{r}, \mathbf{r}_j)$ was thus calculated numerically throughout sample image spaces, and from this, $\nabla d_w(\mathbf{r}, \mathbf{r}_j)$ and $|\nabla d_t(\mathbf{r}, \mathbf{r}_j)|$ was also determined numerically. Results for $\mathbf{r}_s = (150, 0)$ mm, $\mathbf{r}_d = (0, 150)$ mm, $\theta = 90°$, and tissue radius equal to 40 mm are presented in Figure 4.2. Figures A and B of this composite illustrate the 2D d_t and d_w functions, respectively, while Figure C and D illustrate the $|\nabla d_t|$ and $|\nabla d_w|$ functions. Note that these graphs are intuitively correct since one expects the largest gradients to lie along the edges of the tissue "shadow" lines. Regardless of the values of θ, $\mathbf{r}_j$ and tissue radius, the range of minimum and maximum values for $\frac{\partial d_w}{\partial x}$, $\frac{\partial d_w}{\partial y}$, $\frac{\partial d_t}{\partial x}$, and $\frac{\partial d_t}{\partial y}$ always fell in the range of -11 to +11. As can be seen in Figure 4.2, the maxima and minima occur in regions where ultrasound paths just begin to enter the tissue. Most value of the partial derivatives are in fact much smaller, with average values of $\frac{\partial d_w}{\partial x}$, $\frac{\partial d_w}{\partial y}$, $\frac{\partial d_t}{\partial x}$, and $\frac{\partial d_t}{\partial y}$ lying in the range of 0.5 to 1.3. Note that all values quoted are unitless by definition since d_t and d_w have units of length.

Upon substituting $\nabla d_w = \nabla d_w <\approx= 10(\hat{\mathbf{x}} + \hat{\mathbf{y}})$ into Equation 4.21, T3 reduces to

$$\mathrm{T3} \quad <\approx \quad \{k^2\, 1.4053 \times 10^{-5}\,\mathrm{mm} + 1.2255 \times 10^{-2}\, k\}(\hat{\mathbf{x}} + \hat{\mathbf{y}}) \tag{4.22}$$

Returning to Equation 4.20

$$\begin{aligned} \nabla \tilde{S} \quad \approx \quad & S\, \mathrm{ATT}_w \mathrm{ATT}_t \times \\ & \{ik\hat{\mathbf{n}}_j - (k^2\, 1.4053 \times 10^{-5}\,\mathrm{mm} + 1.2255 \times 10^{-2}\, k)(\hat{\mathbf{x}} + \hat{\mathbf{y}})\} \end{aligned} \tag{4.23}$$

Given that $|k| < 42\mathrm{mm}^{-1}$ for a typical imaging experiment, the term in $(\hat{\mathbf{x}} + \hat{\mathbf{y}})$ is much smaller in magnitude than the imaginary component in the above expression. As such,

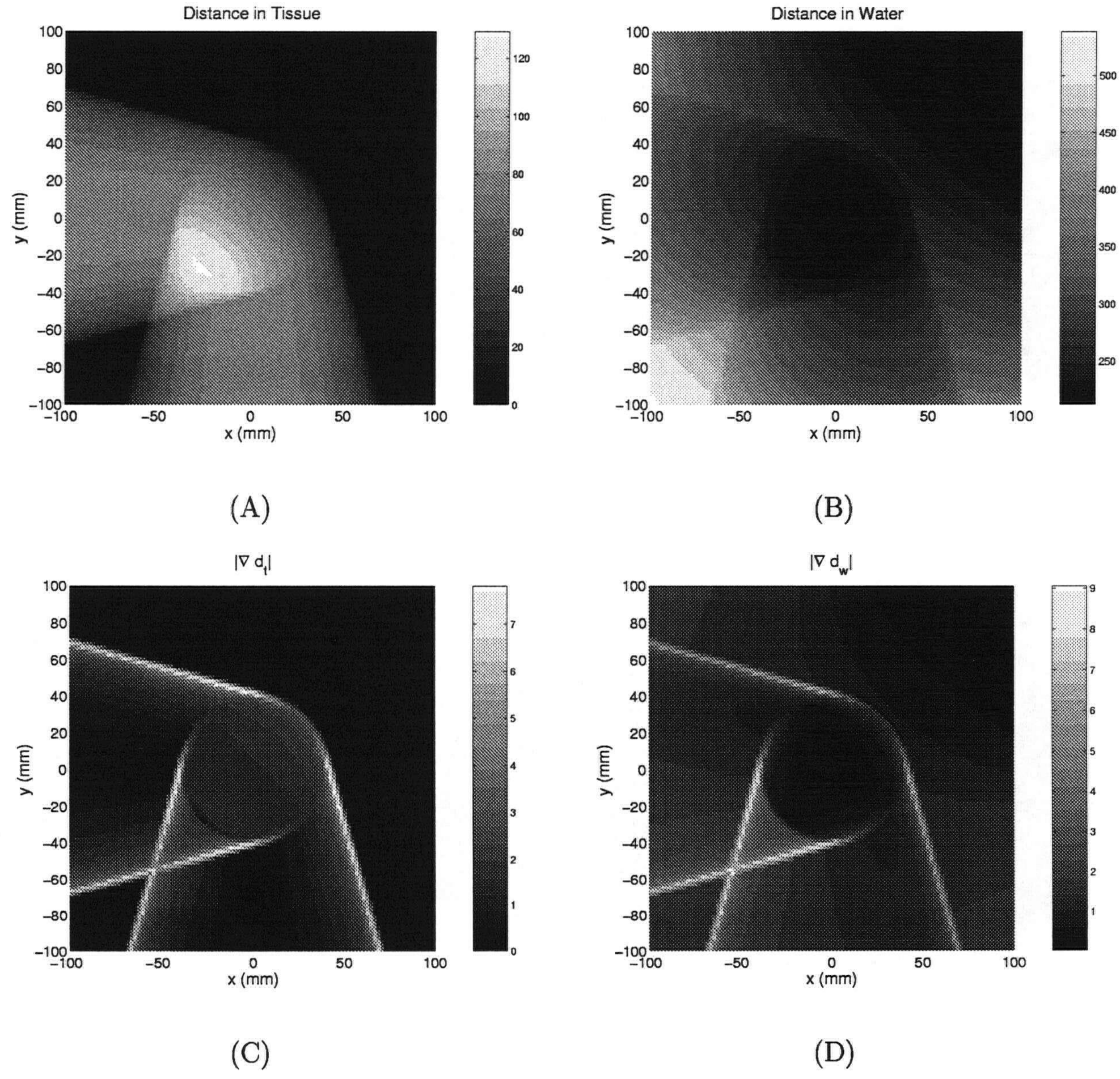

Figure 4.2: This figure illustrates the 2D functions of d_t (A), d_w (B), $|\nabla d_t|$ (C) and $|\nabla d_w|$ (D) for a particular simulation in which $\mathbf{r}_s = (150, 0)$ mm, $\mathbf{r}_d = (0, 150)$ mm, $\theta = 90°$, and the tissue radius was 40 mm.

it follows that

$$\begin{aligned} \nabla\tilde{S} &\approx \mathrm{ATT}_w\mathrm{ATT}_t\, ik\hat{\mathbf{n}}_j S \\ &\approx \mathrm{ATT}_w\mathrm{ATT}_t \nabla S \end{aligned} \tag{4.24}$$

This yields the interesting result that the gradient of the attenuated propagator is approximately equal to the original propagator in the absence of attenuation multiplied by the attenuation coefficients. However, it is important to note that this assumption implies that $\nabla\tilde{S}_{\mathbf{r}_j}$ does not impart a phase shift when operating on an ultrasound field. However, the expression for $\nabla\tilde{S}$ must be examined in the context of Equation 4.13 to ensure that the term in $(\hat{\mathbf{x}}+\hat{\mathbf{y}})$ remains negligible after all mathematical processing is complete. The approximation is addressed in more detail in Section 5.1.1. Results of a computer simulation analysis verifying the validity of this assumption are presented in Section 5.1.2.

Substituting $\tilde{g}$ for g, $\tilde{S}$ for S, and $\nabla\tilde{S}$ for ∇S in Equation 4.7 allows an expression for the spatially varying p_s in the presence of attenuation to be derived. The mathematical reduction proceeds as with no attenuation, as outlined in Equations A.23 through A.38 in Appendix A. The result is

$$p_s(\mathbf{r}_d,\mathbf{r}_s,\omega) = \alpha^2 A(\omega)\, k^2 \int_{\Re^2} \tilde{S}_{\mathbf{r}_d}\left(\gamma_\kappa(\mathbf{r}) + \cos(\theta)\gamma_\rho(\mathbf{r})\right)\tilde{S}_{\mathbf{r}_s}\, \mathrm{d}^2\mathbf{r} \tag{4.25}$$

which is similar to the result in the absence of attenuation, aside from the inclusion of the attenuated propagator, $\tilde{S}$. This expression can be made additionally accurate by substituting the exact attenuated propagator, $\tilde{g}(\mathbf{r}|\mathbf{r}_j,k)$, in the place of $\alpha\tilde{S}_{\mathbf{r}_j}$ to arrive at

$$p_s(\mathbf{r}_d,\mathbf{r}_s,\omega) = A(\omega)\, k^2 \int_{\Re^2} \tilde{g}(\mathbf{r}|\mathbf{r}_d,k)\left(\gamma_\kappa(\mathbf{r}) + \cos(\theta)\gamma_\rho(\mathbf{r})\right)\tilde{g}(\mathbf{r}|\mathbf{r}_s,k)\, \mathrm{d}^2\mathbf{r} \tag{4.26}$$

4.2.3 Derivation of the ART

Although Equation 4.26 looks similar to the equation for the scattered ultrasound field from Chapter 2, it can not be reduced to the reconstruction algorithm by Blackledge

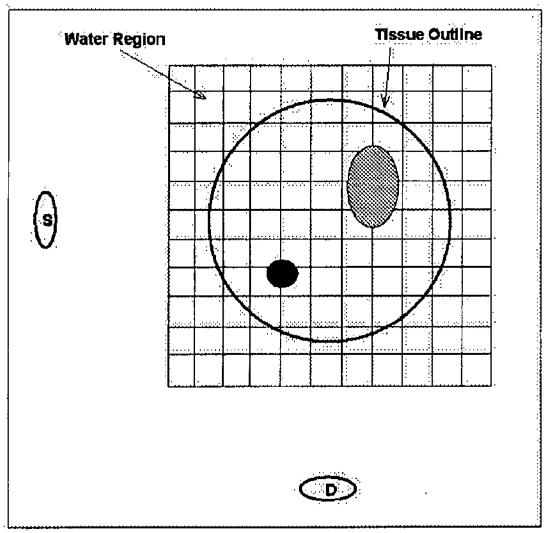

Figure 4.3: This figure illustrates the grid of pixels that is superimposed upon the image space for the purposes of ART development.

et al due to the presence of the nonanalytical functions $d_w(\mathbf{r}, \mathbf{r}_j)$ and $d_t(\mathbf{r}, \mathbf{r}_j)$. Instead, an Algebraic Reconstruction Technique can be derived from it. In developing the ART, a discrete coordinate system is first introduced as illustrated in Figure 4.3 by superimposing a square grid of pixels on an image space that includes the object being imaged as well as a small perimeter of background pixels. The grid size is M×N, and each cell has a location defined by $\mathbf{r}_{ij}$. The grid represents a 2D image with elements defined by $I_{ij} = \gamma_\kappa(\mathbf{r}_{ij}) + \cos(\theta)\gamma_\rho(\mathbf{r}_{ij})$. It is assumed that the grid size is small enough such that the image is relatively constant throughout each pixel. As described in Section 4.1, knowledge of the object outline can be obtained from a backscatter image taken with a narrow beam source. Each cell is then labelled either within or outside the object, and this information is mathematically represented in a spatial extent map. This map shall henceforth be termed an indicator function, Υ, after the work of Kaveh and Soumekh regarding the frequency domain interpolation problem [49]. Please note, however, that the work cited is unrelated to the current analysis. The indicator function has the simple form

$$\Upsilon_{ij}(x_i, y_j) = \begin{cases} 1, & (x_i, y_j) \in \text{imaged object} \\ 0, & \text{elsewhere} \end{cases}$$

An attenuated propagator, $\tilde{S}_{ij}$, can be calculated for each pixel in the image. Equation 4.26 can then be discretized as follows:

$$p_s(\mathbf{r}_d, \mathbf{r}_s, \omega) = A(\omega)k^2 \sum_{i=1}^{\mathrm{M}} \sum_{j=1}^{\mathrm{N}} \tilde{g}(\mathbf{r}_{ij}|\mathbf{r}_s, k)\, I_{ij}\, \tilde{g}(\mathbf{r}_{ij}|\mathbf{r}_d, k)\, \Delta x \Delta y \tag{4.27}$$

An alternative way of storing the grid and its associated variables is in the form of vectors. The grid is then stored as a vector of length L, and each cell has a location stored in the vector $\mathbf{r}_i$. The grid represents an image that is stored as a vector with elements defined by $I_i = \gamma_\kappa(\mathbf{r}_i) + \cos(\theta)\gamma_\rho(\mathbf{r}_i)$, and each pixel of the image has a corresponding attenuated propagator, $\tilde{S}_i$. The indicator function is also redefined as a vector given by

$$\Upsilon_j(\mathbf{r}_j) = \begin{cases} 1, & \mathbf{r}_j \in \text{imaged object} \\ 0, & \text{elsewhere} \end{cases}$$

Since the input data are converted to a digital signal by an ADC, the wave numbers are in fact also discretized into N_k different values spanning both positive and negative k-space. Corresponding to these are N_k angular frequencies, ω_i. Using the notation

$$\begin{aligned} \tilde{g}^i_j &= \tilde{g}(\mathbf{r}_j|\mathbf{r}_s, k_i)\, \tilde{g}(\mathbf{r}_j|\mathbf{r}_d, k_i) \\ b_i &= p_s(\mathbf{r}_d, \mathbf{r}_s, k_i) \\ A_i &= A(\omega_i) = A(k_i) \end{aligned} \tag{4.28}$$

the summation in Equation 4.27 can be rewritten as

$$\begin{aligned} b_i &= A_i k_i^2 \sum_{j=1}^{L} \tilde{g}(\mathbf{r}_j|\mathbf{r}_s, k_i)\, I_j\, \tilde{g}(\mathbf{r}_j|\mathbf{r}_d, k_i)\, \Delta x \Delta y \\ &= A_i k_i^2 \sum_{j=1}^{L} \tilde{g}_j^i I_j\, \Delta x \Delta y \end{aligned} \tag{4.29}$$

N_k such equations for the full set of angular wave numbers can be placed together in the following matrix equation:

$$\mathbf{b} = \mathbf{TI} \tag{4.30}$$

which becomes the following when expanded fully:

$$\begin{bmatrix} b_1 \\ b_2 \\ . \\ . \\ b_{N_K} \end{bmatrix} = \begin{bmatrix} A_1 k_1^2\, \tilde{g}_1^1 & A_1 k_1^2\, \tilde{g}_2^1 & .\ . & A_1 k_1^2\, \tilde{g}_L^1 \\ A_2 k_2^2\, \tilde{g}_1^2 & A_2 k_2^2\, \tilde{g}_2^2 & .\ . & A_2 k_2^2\, \tilde{g}_L^2 \\ . & . & .\ . & . \\ . & . & .\ . & . \\ A_{N_K} k_{N_K}^2\, \tilde{g}_1^{N_K} & A_{N_K} k_{N_K}^2\, \tilde{g}_2^{N_K} & .\ . & A_{N_K} k_{N_K}^2\, \tilde{g}_L^{N_K} \end{bmatrix} \begin{bmatrix} I_1 \\ I_2 \\ . \\ . \\ I_L \end{bmatrix} \Delta x \Delta y \tag{4.31}$$

The vector f is readily available since it is measured during a UCT experiment. The $\tilde{g}_i^j$ functions can be calculated to a first order approximation in the absence of refraction by tracing the straight-line paths that ultrasound waves travel through the tank and determining where the paths intersect tissue. Therefore, the matrix system in Equation 4.31 can be solved iteratively to determine the image stored in the vector I. Knowledge of f at any one angle provides only a subset of the final image. These subsets must each be solved for iteratively and then combined together to yield a final image. The advantage of this approach is two-fold. First, data can theoretically be corrected for frequency dependent attenuation. Second, the exact propagator is employed, which should theoretically result in a more accurate reconstruction in comparison to the method by Blackledge *et al.*

4.2.4 Iterative Solution

The main difficulty with this method is that the matrix system is very large. For instance, there are 10000 unknowns in an image of 100×100 pixels. Techniques do exist to readily solve sparse systems with on the order of 10^6 unknowns, which is 100 times larger than the system at hand. However, the attenuated propagator matrix is generally not sparse. As an example, with 10 MHz sampling, a tissue radius of 80 mm, and the source and detector located 200 mm from the origin, the elements of A range from 1 to 0.009, with 99% of the values being greater than 0.01.

The feasibility of this method has been evaluated in initial tests in this thesis. In doing so, two iterative techniques were implemented: the conjugate gradient method and the Jacobi iterative technique. The formulas for both are outlined in Appendix E. It is noted that in order to obtain convergence, the formulas were modified from their classical forms to include the application of a boundary condition that arises from the definitions of $\gamma_\rho(\mathbf{r})$ and $\gamma_\kappa(\mathbf{r})$ and from the fact that the image extends past the tissue boundary. Under this condition, it was assumed that the image was sufficiently larger in width than the object such that the pixels in the first and last row and column corresponded to water. As such, these pixels could be assigned image values of zero. Without including the boundary condition in the solution, the iterative methods either converge on invalid solutions or do not converge at all. Results of the feasibility study are presented in Section 5.7.

4.3 Necessary Noise Removal

In the prototype scanner, the detected ultrasound signals are digitized and noise is subsequently removed through digital signal processing (DSP) methods. Ultrasound signals are generally quite weak in amplitude because attenuation reduces the sound field amplitude by $\sim 11-68\%$ over the frequency range of 1-10 MHz for each centimeter that it travels through tissue [43, 51]. This becomes problematic when the amplitude of the recorded data is on the order of the background noise in the ultrasound signals. Several sources of noise are apparent in any experiment. For instance, there is noise inherent in the speaker and microphone electronics and also due to vibrations in the surroundings. Noise also results from the electronic circuitry of the computer in which the ADC board is housed. An additional source of unwanted signals is evident in backscatter imaging, in which minute signals from air bubbles in the water make up part of the background noise. This source of noise can be overcome, however, if a degassing procedure is introduced into the system. Lastly, signals from tissue include not only the sound reflected or scattered from tumor boundaries and tissue interfaces, but speckle noise caused by sound scattered from many small structures within the tissue that are too small to be resolved by the imaging system. All these sources of noise degrade the data that is input to the reconstruction algorithms.

The rapid development of more powerful and economical computers has facilitated the use of real-time digital signal processing to improve the data before it is input into a reconstruction algorithm. As with all quantitative imaging methods, the quality of the image is limited by the quality of the reconstruction input data. Digital filters can be used to remove the noise, but care must be taken not to destroy useful information.

4.3.1 Analysis of Noise in the Signal

Several sources were used in the testing of the prototype scanner. However, upon averaging at least 200 different signals recorded at the same location using the same source, the noise in the resulting average signal has similar, although not identical, features regardless of the transducer used. As such, only two examples will be provided in this section. Figures 4.4.A and 4.4.B illustrate typical ultrasound signals after they have been amplified by the SEA preamplifier and Panametrics receiver and digitized by the Gagescope 6012. In Figure A, ultrasound was backscattered from a 3 mm wide aluminum rod that was insonified with the concave source. In Figure B, ultrasound from the

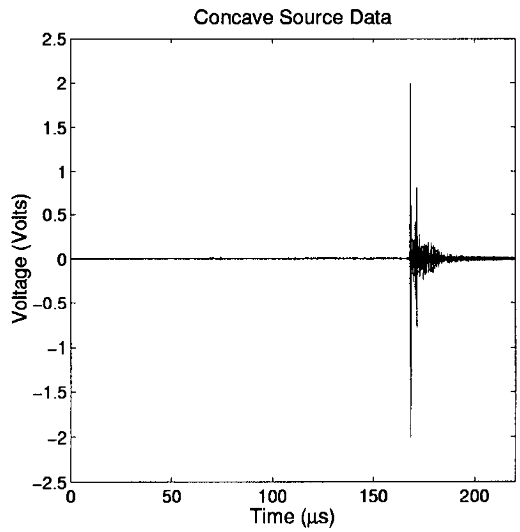

(A)

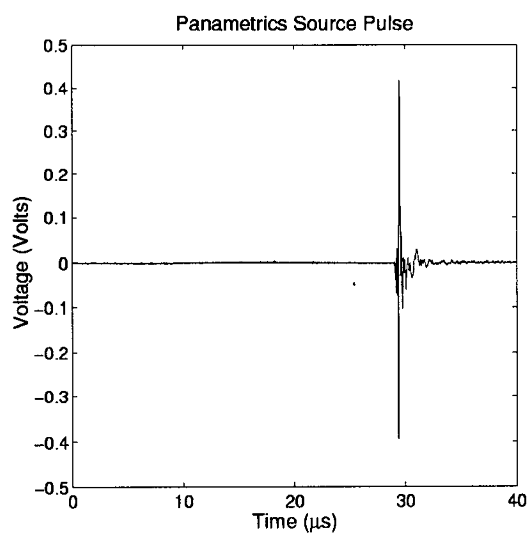

(B)

Figure 4.4: Figures A and B illustrate two examples of signal time profiles. In Figure A, ultrasound was backscattered from a 3 mm wide aluminum rod after insonification by the concave source. In Figure B, ultrasound from the Panametrics source was detected after transmission through water.

Panametrics source was detected after transmission through water. To reduce noise, 200 and 300 signals were averaged together in the backscatter and transmission examples, respectively. In addition, the source ringing that occurs in the first 9 μs was removed by substituting the voltage points in this region with those in the next 9 μs. A dc offset equal to the average signal amplitude has been subtracted from each example.

It was assumed that the noise is generally constant in time throughout the detected ultrasound signal. In other words, the noise detected before the arrival time of the first scatter data were assumed to be similar to that which underlies the data. Hence, to create noise vectors for analysis, points were extracted from between 0-150 μs and 0-25 μs for the backscatter and transmission signals, respectively. The region of data for each example was estimated to lie from 168-192 μs and 29-33 μs for the backscatter and transmission signals, respectively. The data regions for the concave and Panametrics sources were found to have spectra that were band limited by approximately 10 and 20 MHz, respectively. With the data and noise vectors, signal-to-noise ratios (SNR's) were calculated. Several formulas for SNR are used throughout research and engineering, and a standard one is applied in this work, given by:

$$\mathrm{SNR} = 10\log_{10}(\frac{M_d}{M_n}) \tag{4.32}$$

where M_d is the mean of the power in the data region, and M_n is the mean of the power in the noise. The SNR in the unprocessed signals were 26 and 27 db for the backscatter and transmission examples, respectively. The corresponding Fourier spectra of the noise vectors are illustrated in Figure 4.5. Both noise spectra are relatively flat throughout the frequency range, with a few exceptions. There are high frequency spikes at $\sim \pm 20$ MHz and $\sim \pm 25$ MHz for the concave and Panametrics source, respectively, and both signals exhibit a very low frequency peak spread between $\sim \pm 0.2$ MHz. The high frequency peaks are likely related to noise in the circuitry of the individual sources. Note that the spectrum of the backscatter signal includes significant components in the range of -6 and 6 MHz, which overlaps with the data spectrum. This was likely due to backscatter from

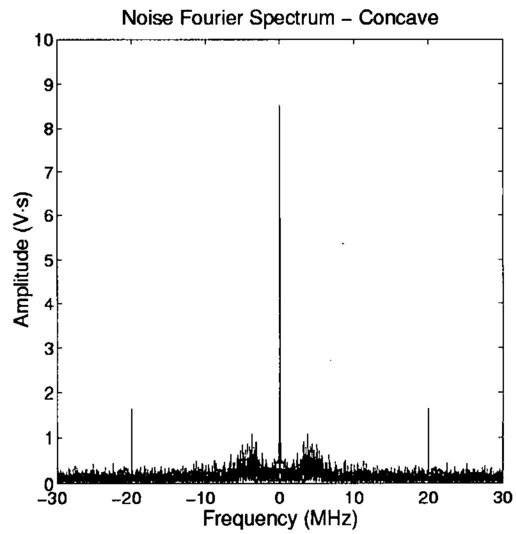

(A)

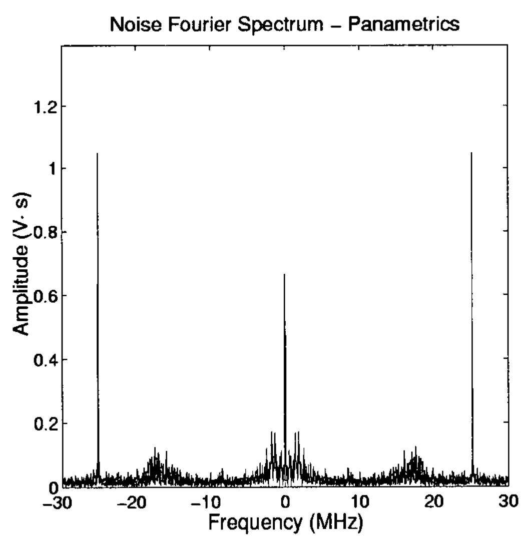

(B)

Figure 4.5: Figures A and B the Fourier spectra of noise in typical backscatter and transmission signals, respectively. The backscatter signal corresponds to the concave source, while the transmission signal corresponds to the Panametrics source.

air bubbles that were floating between the source and the aluminum rod. This can be overcome in the second generation system if a degassing procedure is introduced. Also of note are the higher Fourier amplitudes between 10 and 20 MHz in the noise spectrum of the transmission signal. The source of this has not been identified, although it is suggested that it may be either electrical noise or acoustic noise in the form of harmonics [71].

The unfiltered noise amplitude has been histogrammed for each example, and the results are presented in Figure 4.6. The sparse nature of the histograms is due to the digital sampling of the signal combined with the low level nature of the noise. The histograms indicate that the amplitudes in both noise vectors have a somewhat Gaussian distribution that is not quite zero-mean.

4.4 Conventional Denoising Techniques

All the sources used in this thesis work are band limited. The concave and Panametrics sources in particular have upper frequency limits of approximately 10 and 12 MHz. Beyond these limits, the information contained in the signal does not contain valid data. As such, to avoid reconstructing noise rather than data, conventional filtering techniques can be applied to denoise the data. The most common of these is the lowpass filter, which gradually zeros data beyond a certain frequency. In the prototype UCT scanner, a lowpass Butterworth filter was applied to the signals, with an amplitude response of

$$G(f) = \frac{1}{\sqrt{1 + (\frac{f}{f_0})^{2n}}} \tag{4.33}$$

In the above equation, n is the order of the filter and f_0 is the frequency at which the filter response is -3 db. Generally n was chosen to be 20 to facilitate a relatively sharp frequency cutoff.

A 20th order lowpass filter with $f_0 = 10$ MHz for the concave source and $f_0 = 12$ MHz for the Panametrics source was applied to the respective noisy signals. The filtered

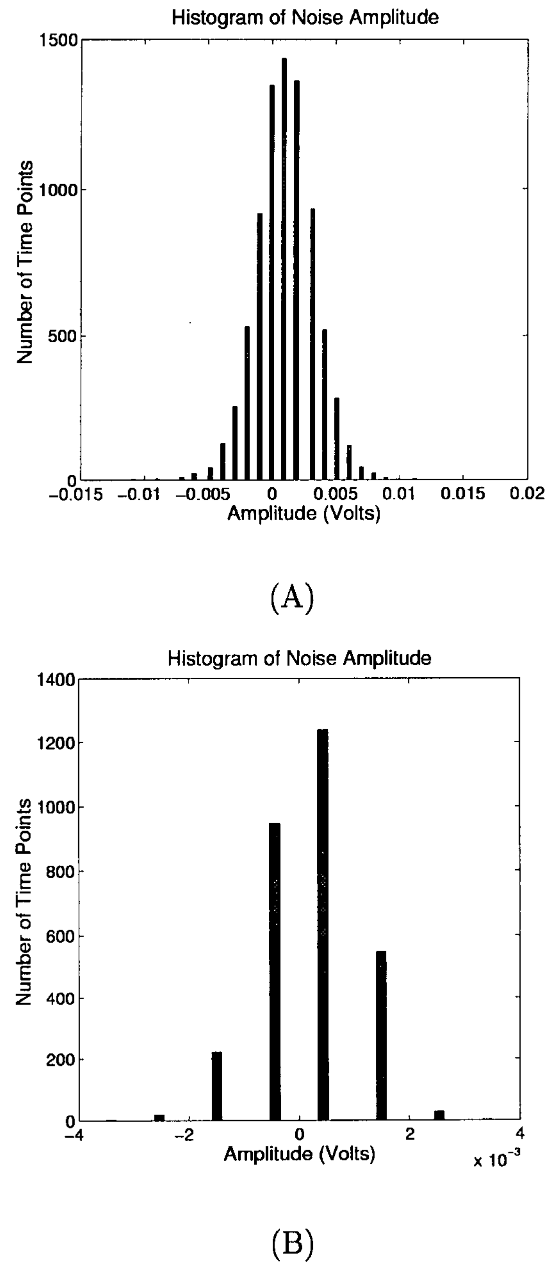

Figure 4.6: Figures A and B illustrate the amplitude histograms of noise in typical backscatter and transmission signals, respectively. The backscatter signal corresponds to the concave source, while the transmission signal corresponds to the Panametrics source.

Fourier data were then inverse transformed and the data and noise vectors were again extracted from the resulting signal. Lowpass filtering afforded a 3 db SNR increase in each example. The amplitude histograms of the noise in the filtered signals are illustrated in Figures 4.7.A and 4.7.B. Evidently, the noise in the backscatter signal is still quite Gaussian, although it is not zero-mean. The noise in the filtered transmission signal no longer has Gaussian statistics. The problem lies in the low frequency noise components with $f < 0.3$ MHz, which is an effect that can be seen in some UCT data. To alleviate this problem the transmission signal was further filtered with a Butterworth highpass filter (HPF), which has the following amplitude response:

$$G(f) = \frac{1}{\sqrt{1 + (\frac{f_0}{f})^{2n}}} \tag{4.34}$$

Again, n is the order of the filter and f_0 is the frequency at which the filter response is -3 db. $n = 20$ was chosen for the transmission signal to facilitate a relatively sharp frequency rise. Upon inverse transforming and extracting the noise, the noise amplitudes were histogrammed, as illustrated in Figure 4.8.A. The concave source backscatter signal was also filtered with the HPF and the residual noise statistics are illustrated in Figure 4.8.B. The residual noise in both cases is now zero-mean Gaussian. These examples indicate that the noise characteristics vary slightly from source to source. Additional analyses indicated that the characteristics also vary slightly from experiment to experiment.

Although Butterworth filtering is a firm beginning in terms of noise removal, Section 5.5 will illustrate that it does not yield data that are accurate enough for UCT image reconstruction. In order to further improve the data, two approaches have been studied in this thesis work. One approach involved wavelet denoising, which is discussed in the following Section. The other approach involved the application of a moving average filter, which again falls under the category of conventional filtering methods. The moving average filter is presently the most commonly used technique for removing noise that lies within data band limits. This is a smoothing technique that has been in use for a number of decades. The filter is easy to implement and understand, and it is also optimal for

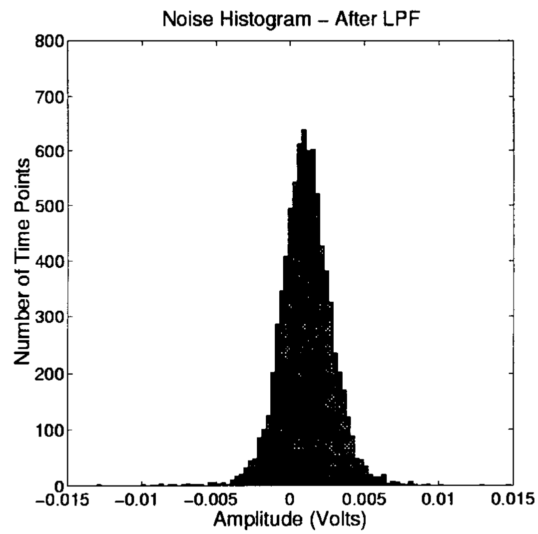

(A)

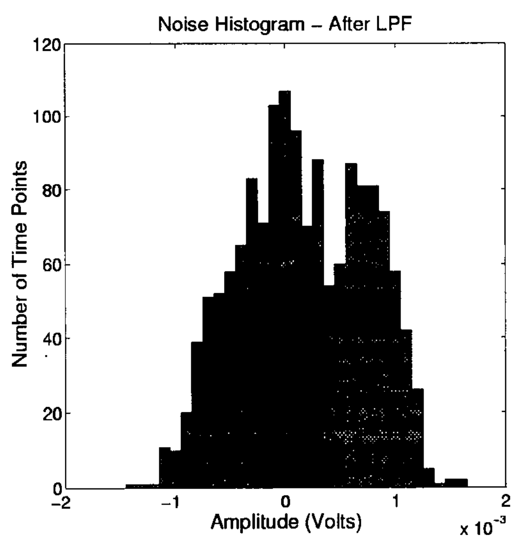

(B)

Figure 4.7: This figure illustrates the amplitude histograms of the noise in the backscatter (A) and transmission (B) signals after the application of a Butterworth LPF of order 20.

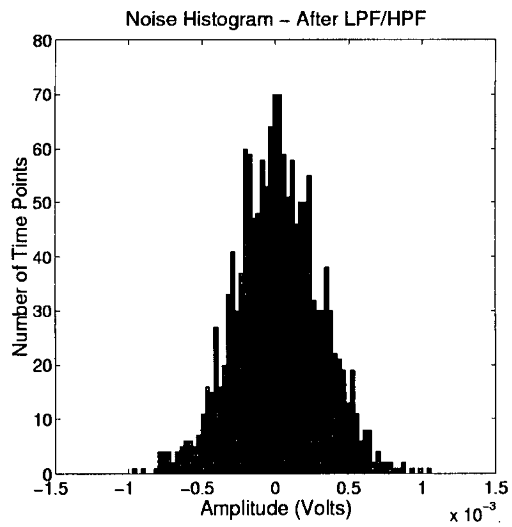

(A)

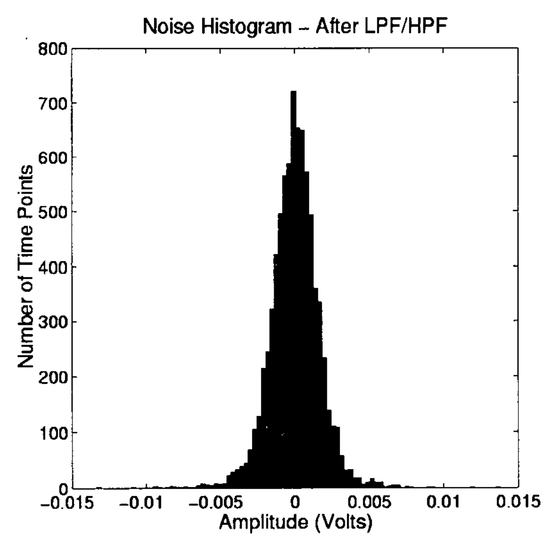

(B)

Figure 4.8: These figures illustrate the amplitude histograms of the noise in the Panametrics source transmission signal (A) and the concave source backscatter signal (B) after the application of a Butterworth HPF of order 20, in addition to a previous application of an order 20 Butterworth LPF.

reducing white noise while retaining a sharp step response. Hence, it is a useful filter for denoising time domain transient signals such as that found in pulsed UCT data [79]. Implementation of the moving average filter begins with choosing a window width that is an odd integer, m. The width indicates the number of points that are averaged together in each operation. When the filter operates on a datum, the window is centered over the point and all data in the window are averaged. The center datum is then replaced with the result. The window moves through the data until each point has been replaced with an average. Points near the beginning and end of the data vector are handled in the same manner, except that only 1 to $(m-1)$ points can be included in the averages. As the window size is increased, the smoothing or denoising effect is enhanced.

Figure 4.9 illustrates the effect of the moving average filter. The top figure illustrates the unfiltered spectrum of the data region in the Panametrics source example from Section 4.3. The bottom figure illustrates the spectrum after it has been processed with a 5-point moving average filter. The advantage is that noise is indeed removed, but the disadvantage is that the features of the data are substantially changed.

4.5 Wavelet Theory

Wavelets are mathematical functions that are used as basis functions in wavelet theory, just as sinusoidal functions are the basis functions in Fourier theory. Figure 4.10 illustrates four examples of commonly used wavelets, namely Symlet 6, Symlet 8, Daubechies 9 and Coiflet 5. Although wavelets can represent functions of any variable, in this work they are used in the time domain. As such, time will generally be referred to in the following discussion. Wavelets and Fourier basis functions are similar in that they are both localized in frequency. The main differences between the two types of basis functions are that wavelets are of compact support (localized in space) and they are scale-varying, whereas Fourier basis functions are not [34]. The support of a time domain function is defined as the interval in continuous time outside of which the function is zero, and com-

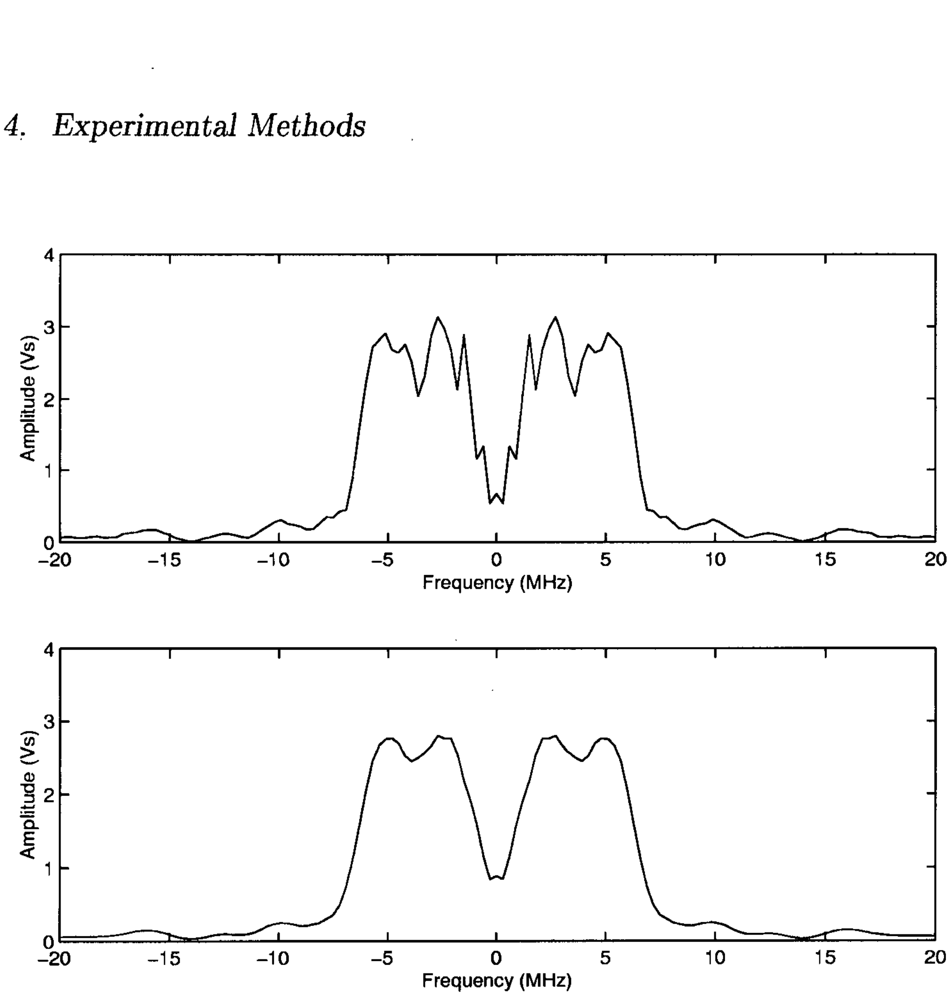

Figure 4.9: These figures provide an example of moving average filtering. The top figure illustrates the unfiltered spectrum of the data region in the Panametrics source example from Section 4.3. The bottom figure illustrates the spectrum after it has been processed with a 5-point moving average filter.

pact support means that this interval is finite. Basis functions that are not scale-varying, such as sines and cosines, are used to represent a particular function over its entire time interval. Scale-varying functions, such as wavelets, represent functions only over intervals of varying temporal width and location [34]. For instance, if a function is defined over the domain from 0 to 1, it can be analyzed at different scales. At the largest scale it can be analyzed over two successive intervals: (0, 1/2) and (1/2, 1). It can alternatively be viewed at a slightly finer scale over four successive intervals: (0, 1/4), (1/4, 1/2), (1/2, 3/4) and (3/4, 1). And so on. Wavelets of different scale are used to represent the function over the intervals of different scale.

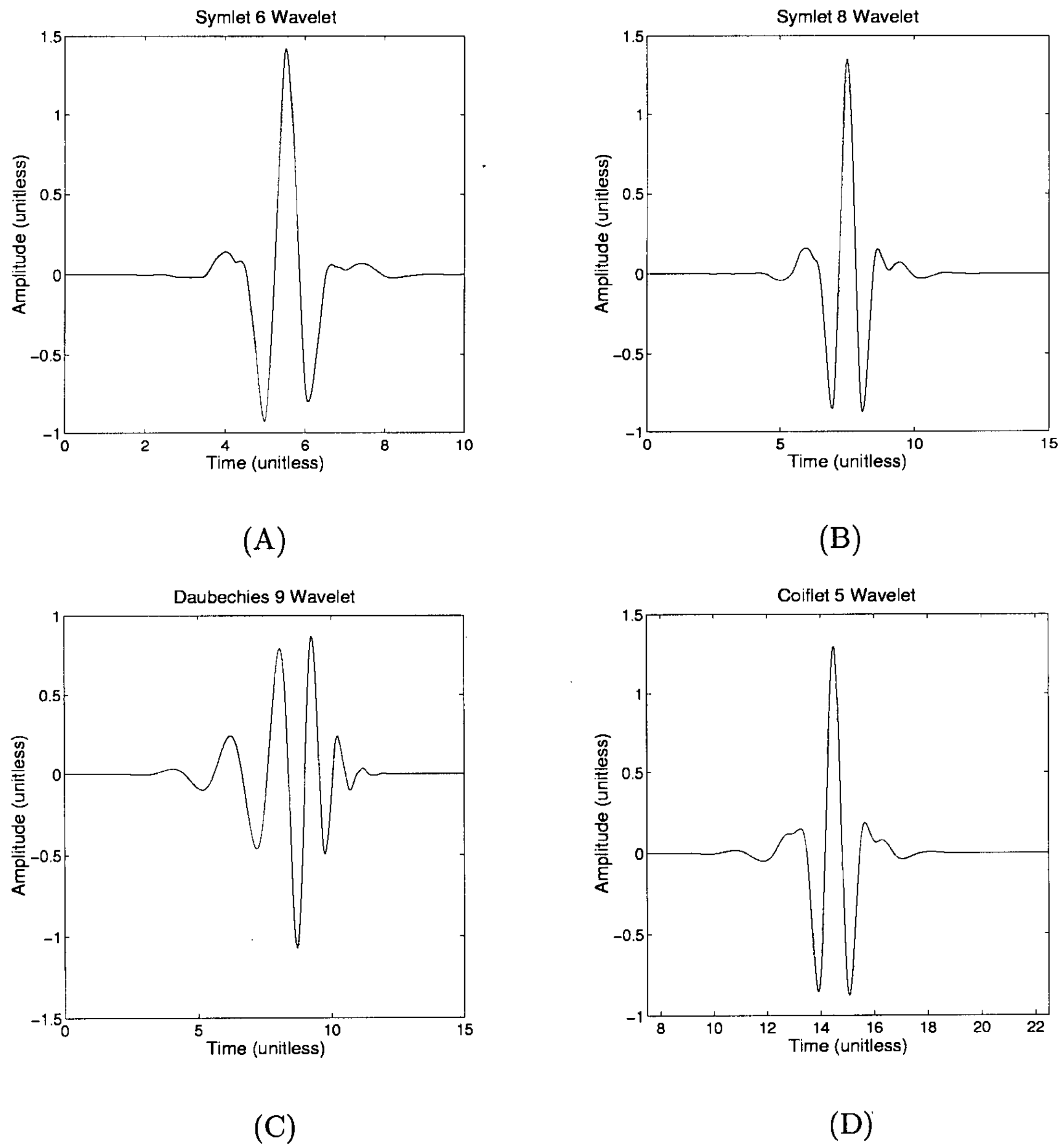

Figure 4.10: This figure illustrates some well-known wavelet functions. A) Symlet 6 B) Symlet 8 C) Daubechies 9 D) Coiflet 5.

The idea of scale-varying basis functions was formed in the 1930's but it was not until after 1985 that wavelets came into being with the work of Stephane Mallat and Ingrid Daubechies. Since then, wavelet analysis techniques have been widely developed in various fields that include astronomy, geophysics, acoustics, nuclear engineering, electrical engineering, neurophysiology, music, magnetic resonance imaging, optics, radar, and pure mathematics. The techniques are used in a variety of problems, from signal processing and the solving of partial differential equations to image compression and speech discrimination [34, 57].

Fourier analysis is generally better for data that are continuous in nature. Pulsed UCT data, however, are transient in nature. In other words, the data are not sinusoidal and the corresponding pulses exist for a short time only. It thus follows that pulsed UCT data may be well-suited to mathematical representation by wavelets, provided a suitable family of wavelet functions can be determined.

4.5.1 Wavelet Analysis and the Wavelet Transform

In wavelet analysis, a particular family of wavelets is chosen to represent the function at hand. The members of the family, which define an orthogonal basis, are generated through dilations and translations of the "mother wavelet," which is also known as the "analyzing wavelet" [18, 34]. The rescaling is performed by a scaling function, and for the discrete wavelet transform used in this thesis, the rescaling is always in powers of two. The translations always place wavelet family members of the same scale in an end to end fashion with no overlap. Wavelet analysis then processes the function at the different scales or resolutions, and forms a representation of the function that is the linear superposition of the scaled and translated family members. This is the wavelet transform, and it is similar to the FFT only in that it is a linear operation. The major difference between the two transforms is the scale-varying nature of the wavelet transform. At larger scales, wavelets of larger support are used in the analysis, and gross features are analyzed. At small scales, wavelets of small support are used, and fine details are analyzed. As such, the wavelet transform is a multi-resolution operation, and it is better at processing signals with sharp, transient features than Fourier analysis [34, 57].

In wavelet analysis, the short basis functions are of high frequency and small support (therefore wide bandwidth) and are used to isolate signal discontinuities. The low frequency long basis functions are of large support (therefore narrow bandwidth) and are used to perform detailed frequency analysis. In practice, this multi-resolution analysis is embodied in the operation of two filters. One is a smoothing filter (like a moving average filter), and the other picks out the details of the data. Together they are termed a quadrature mirror filter pair [34].

Wavelets are classified by their number of vanishing moments, n, and it is this number that is included in the wavelet name. A wavelet has n vanishing moments if and only if its scaling function can generate polynomials of degree $\leq n$ [57]. In addition, the Fourier Transform of the wavelet is n continuously differentiable if the wavelet has n vanishing moments [57].

4.5.2 Process of Wavelet Denoising

One of the many applications of wavelet analysis is the removal of noise from signals, which is a relatively new practice that has already shown promise in the processing of electromyographic signals [77]. In computer simulations, there has been success in using wavelet analysis to detect acoustic signals in noise without a prior estimate of what the signals look like [15]. When the mother wavelet and by extension all the basis functions in the corresponding wavelet family mimic the shape of the data, wavelet analysis techniques can be used to extract the data from the noise. As already discussed, the wavelet transform essentially filters data in two complementary operations, one which smoothes data and looks at gross features and the another which brings out details [34]. The result is a set of coefficients at each scale or resolution that indicates how to represent the data at that resolution as the linear superposition of the corresponding scale-dependent wavelets. This is similar to the coefficients that are calculated in the Fourier transform, which indicate how to represent the data as the linear superposition of the sinusoidal basis functions.

Given that the mother wavelet has features in common with the data, only a few coefficients will be significant and many can be reduced or removed by thresholding. The remaining coefficients can be used in an inverse wavelet transform to reconstruct the data. The result is a cleaner signal that still exhibits important features of the data. In particular, sharp features are not smoothed in choppy signals by wavelet denoising, which is not the case with conventional filtering methods. These wavelet denoising techniques have been developed by Donoho *et al*, and they are included in the Matlab™ programming environment [24, 25, 60]. These methods are particularly efficient in the removal of Gaussian white noise [24, 25, 60].

The "wden" function in the Matlab™ programming environment performs the denoising of a 1D signal, **x**, using wavelets [60]. This function incorporates work developed over the years by Donohoe and his associates. To use this function one must first specify whether "soft" or "hard" thresholding is to be performed. Hard thresholding is a crude technique that simply sets to zero all the wavelet coefficients below a certain threshold. Soft thresholding, which is more mathematically complex, gradually reduces the wavelet coefficients towards zero if they are below a certain value (this is also referred to as "shrinkage" in the literature). The "wden" function takes as input a threshold selection rule for denoising through the selective reduction of wavelet coefficients. The selection rules can be any of the following:

- **rigrsure** - thresholding using Stein's Unbiased Risk Estimate
- **minimaxi** - minimax thresholding
- **sqtwolog** - threshold is $\propto \sqrt{2 \log_{10}(\text{length}(\mathbf{x}))}$
- **heursure** - a heuristic variant of the "rigrsure" and "sqtwolog" methods

Stein's Unbiased Estimate of Risk, which is used in the "rigrsure" method, involves the computation of a quadratic loss function that attempts to estimate the risk involved in choosing a particular threshold value [3, 60]. The risk is that valid data are removed by the thresholding procedure. Risk estimates are computed for various thresholds, and the threshold that minimizes the risk is chosen. One threshold is computed for the entire wavelet transform data set, and the selection is thus based on the entire data set [3, 60]. "Minimaxi" threshold selection is based on the Minimax Principle. This type of filtering minimizes the "worst-case" data estimation error under the assumption that there is no prior knowledge of the noise statistics [60]. This is in contrast to the well known Kalman filter, which assumes that the noise properties are known and minimizes the "average" data estimation error. The "sqtwolog" method is a variant of the "minimaxi" method. It uses the thresholding in the latter method multiplied by $\sqrt{2\ \log_{10}(\text{length}(\mathbf{x}))}$ [60]. Finally, the "heursure" method is simply an automated combination of "rigrsure" and "sqtwolog" that is heuristic, or based on trial and error. If the SNR is very small, "rigrsure" thresholding will compute a noisy signal. If this situation is detected and "heursure" is chosen, Matlab$^{\text{TM}}$ will automatically switch to "sqtwolog" thresholding [60].

All the threshold selection rules are based on the noise model that $\mathbf{x}(\mathbf{t}) = f(t) + e(t)$, where $e(t)$ and $f(t)$ are the time dependent Gaussian white noise vector and signal vector, respectively (option "one" input to "wden") [60]. Non-Gaussian and/or non-nonwhite noise are handled by multiplicative rescaling of the wavelet transform output. If the noise model is white but not Gaussian, the noise characteristics and amplitude are based on a single estimation using the first level coefficients (option "sln" input to "wden"). If the noise is both non-white and non-Gaussian, an estimate of the noise is performed at each resolution level (option "mln" input to "wden").

The wavelet denoising routine calls the function "wdec," which performs the 1D wavelet decomposition of the data using the specific wavelet family chosen. The analysis can proceed to a scale in which the viewing window includes a minimum of two data points, and recall that the scales are increased by factors of two. Thus, the wavelet decomposition can potentially proceed to L levels, where the length of the signal is 2^L. Signals with lengths that are not powers of 2 are first padded with zeros. At each level, denoising is performed based on the chosen parameters. The inverse transform is then performed at each level to yield several denoised representations of the original input.

4.5.3 Types of Wavelets Used

There are literally a myriad of wavelet families that could be chosen for the denoising of data. Standard wavelets, such as the Daubechies or the Symlet, can be used, and one can also define wavelet families that are custom adapted to a given set of data. Each wavelet family corresponds to a new filter, and hence a thorough analysis of wavelet filtering techniques is beyond the scope of this thesis. Preliminary work has been done, however, to gain some idea of the potential usefulness of wavelet analysis for denoising pulsed UCT data. In this preliminary study, mother wavelets from the Symlet and Daubechies groups were studied. Members within the corresponding families are both orthogonal and biorthogonal [60]. There are only a few Symlet wavelets, which can be of integer order n equal to 2 through 8, where n is the number of vanishing moments. There are many more Daubechies wavelets, which can have an order equal to any positive integer. Symlets have the most symmetry of all the wavelets, while Daubechies have very little symmetry [60].

A smooth, continuous mother wavelet is required to ensure that the wavelet analysis will not introduce discontinuities into the data [24, 25]. More smoothness is generally implied by more vanishing moments (higher order n) [57]. As such, the study used the relatively smooth Symlet 8 and Daubechies 9 mother wavelets, which were illustrated in Figure 4.10. In addition, these wavelets exhibit features that mimic pulsed ultrasound data. Results of the wavelet denoising study, and a comparison with use of the moving average filter, are presented in Section 5.5.

4.6 Interpolation Methods Necessary for Use of FFT

The algorithm used to obtain images of minimally attenuating objects is a Fourier reconstruction method. Essentially, scatter data recorded at each angle about the tissue yield a subset of points in the Fourier space of the image. These points are situated on a radial grid in Fourier space, and must be interpolated to a Cartesian grid in order to do the inverse FFT to obtain the image. The interpolation of FFT data from the radial grid to a Cartesian grid is a somewhat difficult procedure that results in image reconstruction errors.

An idea of the effect of interpolation errors on image reconstruction was obtained through the following computer simulation. A sample image of 100×100 pixels was input to a FFT operation to obtain error-free Fourier data. The image was of a simple cylinder with a Gaussian cross-section. Errors were then added to the Fourier data, and the inverse FFT was performed on the substandard data. The locations of the radial and Cartesian grid points were assumed to be well known and free of error. It was assumed that the error in the interpolated data would increase in direct proportion with the decrease in the density of radial data upon which the computation is based. The sign of the error was generated randomly. The density of radial grid points can be calculated as follows, with reference to Figure 4.11. Here a small subset of points in the Fourier Transform of an image is shown, with data situated on a radial grid. There are $N_{\varphi_s} = 4$ source angles. The grid is thus defined by N_{φ_s} spokes and by circles in Fourier space at discrete radii, τ. The first and second circles are shown with radii τ_1 and τ_2. The number of points in the ring defined by circles with radii $\tau_1 - \delta$ and $\tau_2 + \delta$ is simply $2N_{\varphi_s}$, and the area of this ring is $\approx \pi(\tau_2^2 - \tau_1^2)$. The density of points in the first ring is therefore

$$d = \frac{2N_{\varphi_s}}{\pi(\tau_2^2 - \tau_1^2)} \tag{4.35}$$

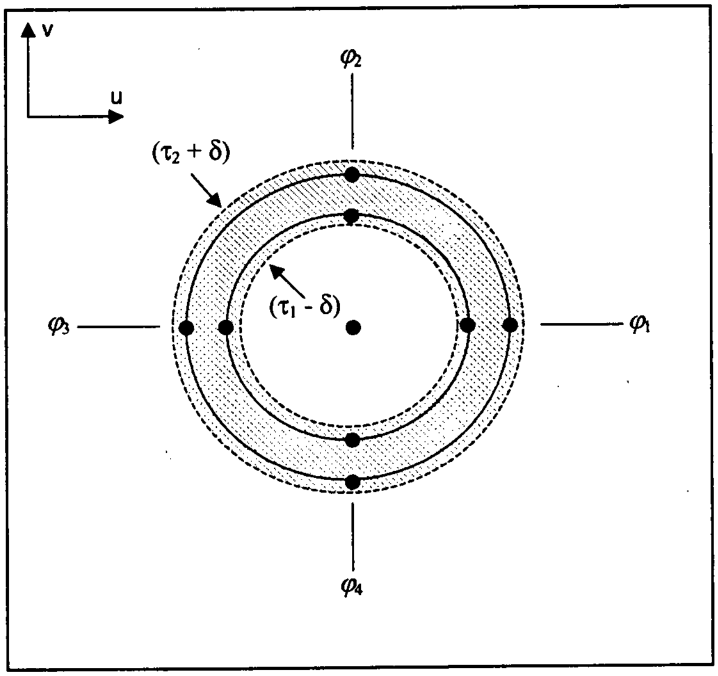

Figure 4.11: This schematic illustrates the radial grid point density in image Fourier space.

By extension, the density of points in the Nth ring is

$$d = \frac{2N_{\varphi_s}}{\pi(\tau_{N+1}^2 - \tau_N^2)} \tag{4.36}$$

Recall that N_{φ_s} data points are superimposed at the origin of uv-space. Since all these data are used in the calculation of the center point, the density of data inside the 0th "ring" is thus

$$d = \frac{2N_{\varphi_s}}{\pi\tau_1^2} \tag{4.37}$$

For a typical image with 200 N_{φ_s} and $\tau \leq 80$ mm^{-1}, the functions d and $1/d$ are plotted versus τ in Figures 4.12.A and 4.12.B. The error is assumed to be proportional to $1/d$ and is thus linearly dependent upon radial distance from the origin in Fourier space.

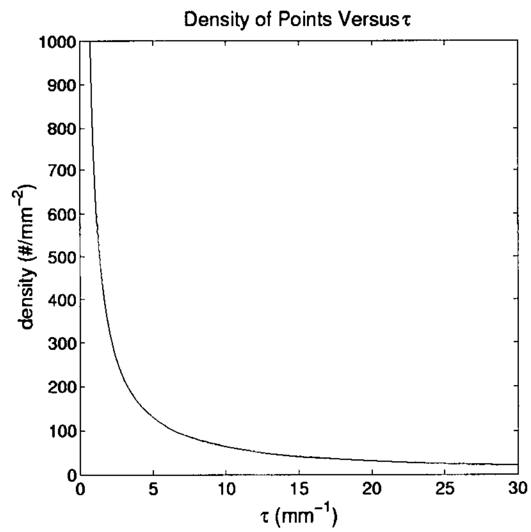

(A)

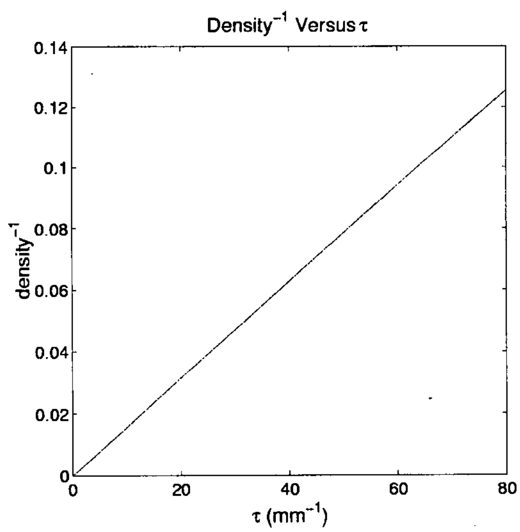

(B)

Figure 4.12: Figures A and B illustrate the radial grid point density as a function of the wave number τ, and the inverse of this function, respectively.

Figure 4.13 presents the results of a simulation in which errors were added to the Fourier data of an image. These errors were applied linearly with radial distance in Fourier space, with a minimum of 0% at the origin to a maximum of 20% at the largest distances. Figures 4.13.A and 4.13.B illustrate the original noise-free image and the corresponding Fourier Transform after adding noise, while Figures 4.13.C and 4.13.D illustrate the resulting noisy image with its corresponding residual image, respectively. Evidently, the interpolation errors have little effect on the image.

In studying this problem, two general approaches were taken. The first involved the use of Matlab™ interpolation methods that fall under the category of conventional numerical analysis. The second involved the use of a specialized interpolation routine known as the Unified Frequency-Domain Reconstruction (UFR), which was developed by Kaveh and Soumekh [49]. These methods are explained and compared in the following sections.

4.6.1 Matlab™ Interpolation

The routine "griddata" in the Matlab™ programming environment was evaluated as a means of interpolating Fourier data from the radial grid to the square grid necessary for the application of the inverse FFT. The points that "griddata" interpolates to usually lie on a square grid, which is where the routine gets its name.

The underlying methods to choose from in "griddata" are:

- linear - Triangle-based linear interpolation
- cubic - Triangle-based cubic spline interpolation
- nearest - Nearest neighbour interpolation

The cubic spline interpolation is a common piecewise polynomial approximation. It produces a smooth surface with no discontinuities. In this method, the data are approximated by the fitting of cubic polynomials between each successive pair of nodes. This

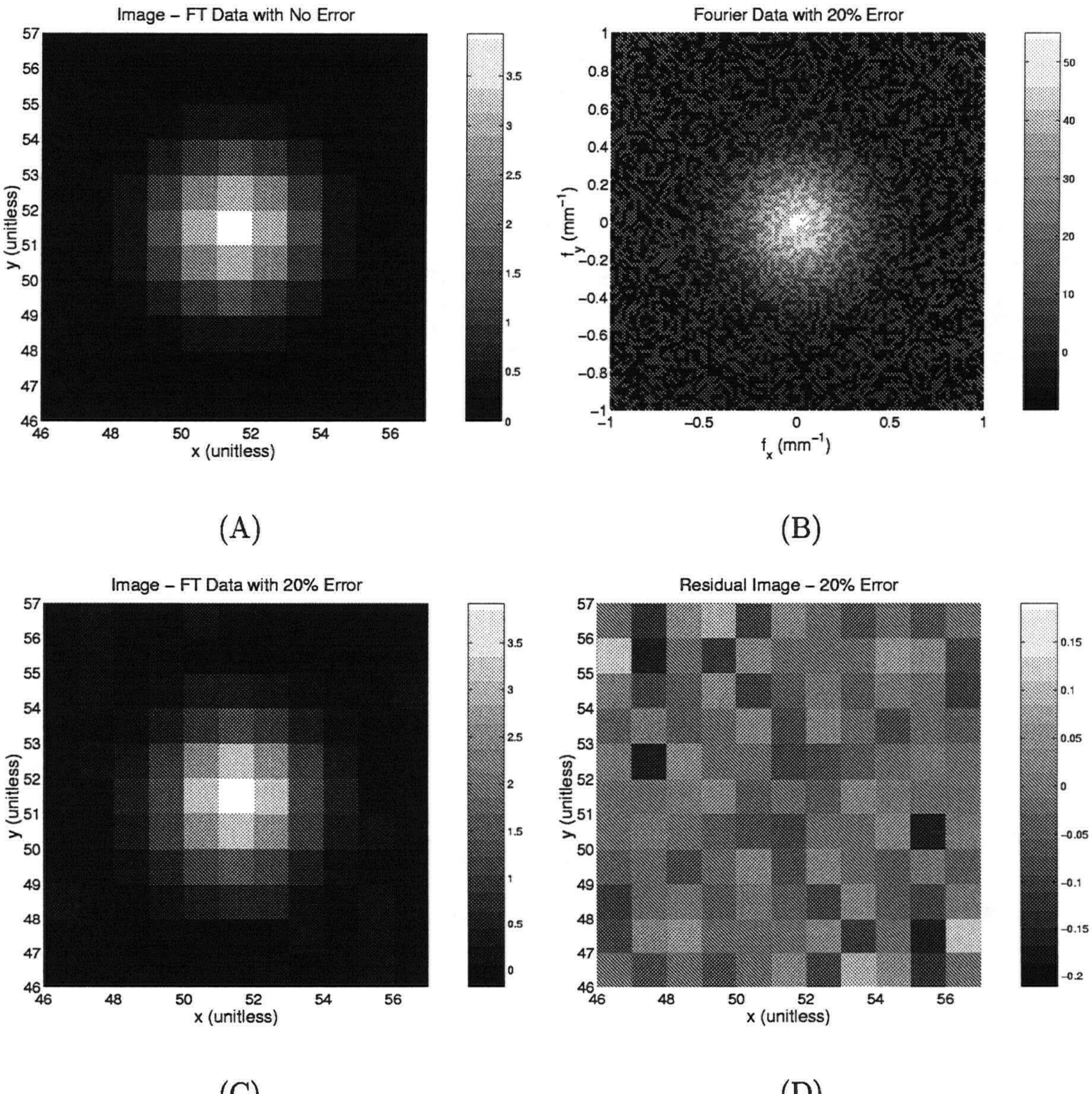

Figure 4.13: Figures A illustrates the original noise-free image and its Fourier Transform after noise has been added. Figures B and C illustrate the resulting noisy image with its corresponding residual image, respectively.

method ensures that both the interpolating function as well as its first and second derivatives are continuously differentiable over the region of interest. The derivatives of the interpolant do not, however, agree with those of the original function, even at the data nodes. Linear interpolation assumes a piecewise linear function can be constructed between any two neighbouring data points. Evidently, since polynomials are not involved, the method is simpler than the cubic spline interpolation. The interpolated surface is continuous, but it has discontinuities in the 1st derivative. The nearest neighbour interpolation simply assigns to a grid point the value of the nearest node. Evidently, this is a rudimentary method with very little computation. The nearest neighbour produces a surface that is not smooth.

4.6.2 Unified Frequency-Domain Image Reconstruction

A second approach to the frequency domain interpolation problem is the Unified Frequency-Domain Reconstruction. This method interpolates data in the frequency domain pursuant to the assumption that the image is of finite support (spatially limited). The spatial limitation is embodied in an indicator function, i, where

$$i(x,y) = \begin{cases} 1, & (x,y) \in \text{imaged object} \\ 0, & \text{elsewhere} \end{cases}$$

The indicator function has a Fourier Transform denoted by $I(u,v)$. If the object is a circle of radius r, then the FT of the indicator function is

$$I(u,v) = \frac{J_1(r\sqrt{u^2+v^2})}{r\sqrt{u^2+v^2}} \tag{4.38}$$

where J_1 is the Bessel function of the first kind of order 1. The UFR method begins with knowledge of the Fourier Transform, $F(u,v)$, of an unknown 2D function, $f(x,y)$, that is expressed in terms of Cartesian coordinates. f can be written as

$$f(x,y) = i(x,y)\, f(x,y) \tag{4.39}$$

Taking the Fourier Transform of both sides and applying the Convolution Theorem yields

$$\begin{aligned} F(u,v) &= \mathrm{FFT}(i(x,y)\,f(x,y)) \\ &= I(u,v) * F(u,v) \end{aligned} \tag{4.40}$$

The definition of convolution results in

$$F(u,v) = \int\int I(u-u', v-v')\,F(u',v')\,du'\,dv' \tag{4.41}$$

Also, measured data for $F(u',v')$ are only known at certain points on a non-Cartesian grid, which can be defined in terms of a transformation, T, as follows:

$$\begin{bmatrix} u' \\ v' \end{bmatrix} = T(\chi,\tau) = \begin{bmatrix} T_1(\chi,\tau) \\ T_2(\chi,\tau) \end{bmatrix} \tag{4.42}$$

In this project,

$$T(\chi,\tau) = \begin{bmatrix} \cos(\chi) & \sin(\chi) \\ \sin(\chi) & \cos(\chi) \end{bmatrix} \begin{bmatrix} \tau \\ 0 \end{bmatrix} \tag{4.43}$$

for $0 \leq \chi \leq 2\pi$ and $0 \leq \tau \leq \tau_{max}$. The transformation can be of any general form, however. The Jacobian for this particular transformation is therefore

$$J(u',v',\chi,\tau) = \begin{vmatrix} \frac{\partial u'}{\partial \chi} & \frac{\partial u'}{\partial \tau} \\ \frac{\partial v'}{\partial \chi} & \frac{\partial v'}{\partial \tau} \end{vmatrix} = \begin{vmatrix} \cos(\chi) & -\tau\cos(\chi) \\ \sin(\chi) & \tau\cos(\chi) \end{vmatrix} = \tau \tag{4.44}$$

Changing variables form u' and v' to χ and τ in Equation 4.41 yields the following result:

$$F(u,v) = \int\int I(u-T_1, v-T_2)\,F(T_1,T_2)\tau\,d\chi\,d\tau \tag{4.45}$$

Equation 4.45 can be discretized, in keeping with the data that are available, to arrive at

$$F(u,v) = \sum_{\mathrm{all}\tau}\sum_{\mathrm{all}\chi} I(u-T_1, v-T_2)\,F(T_1,T_2)\tau\,\Delta\chi\,\Delta\tau \tag{4.46}$$

Equation 4.46 can now be used to calculate a Fourier Transform datum at any (u, v) pair based on the known values of data at the points defined by χ and τ.

4.6.3 Sinc-based Interpolation

A sinc-based interpolation method for direct Fourier reconstruction has been developed by Stark [82]. Although this is considered to be an important addition to the field of Fourier-based reconstruction, Kaveh and Soumekh claim that the UFR approach performs better than the sinc-based approach [49]. Furthermore, the approach is highly intensive computationally, making its incorporation into a viable imaging system very difficult [70].

4.6.4 Comparison of the Interpolation Methods

A Gaussian object characterized by an FFT with radially-situated points was interpolated using the various methods described. Figure 4.14.A illustrates the profile along the u-axis in the original data. In this profile, there are 400 discrete radial points, and in the data to be interpolated, there were 200 such profiles at equally spaced angles. These data were interpolated to a Cartesian grid of size 50×50 points to yield a 2D function, f_{interp}. The distance from the origin was calculated for each Cartesian point, and the corresponding Gaussian amplitude was calculated to determine the expected FFT value at each point, given by f. This was compared to the interpolated FFT value, and an error term in the form of a squared residual was calculated as follows:

$$\text{residual}^2 = |f_{interp} - f|^2 \tag{4.47}$$

The error distributions for all three MATLAB™ interpolation methods as well as the UFR method are plotted in Figure 4.14.B. This plot shows the percentage of Cartesian grid points for which the residual^2 was less than some value ϵ, where ϵ is on the x-axis. Comparing the data for all four methods, it is evident that the MATLAB™ methods

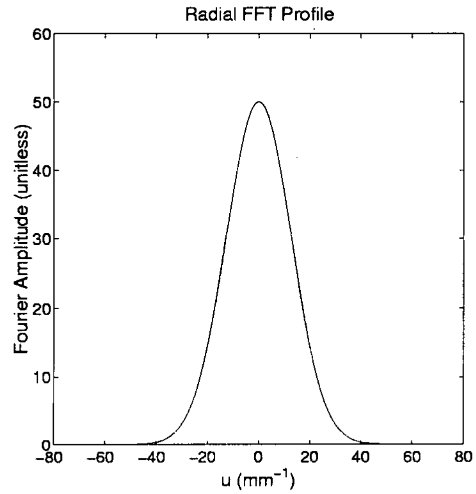

(A)

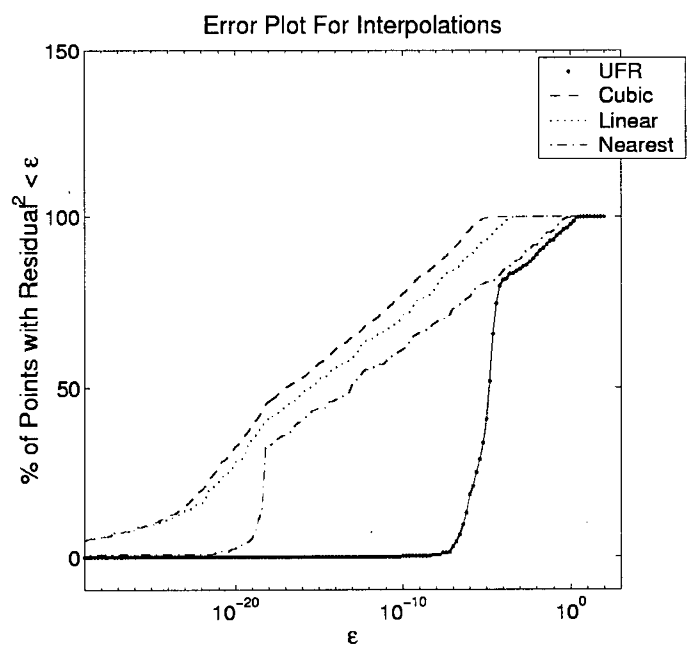

(B)

Figure 4.14: A Gaussian object defined by a radial grid was interpolated using the various methods. Figure A illustrates the profile along the u-axis in the original data. In this profile, there are 400 discrete radial points, and in the data to be interpolated, there were 200 such profiles at equally spaced angles. Figure B plots the percentage of Cartesian grid points for which the residual^2 was less than some value ϵ, where ϵ is on the x-axis. Shown are the results for the MATLAB^{TM} interpolation methods and the UFR method.

are superior to the UFR method. The best method is the MATLAB^{TM} cubic spline interpolation, for which only 4.0% of the points had a residual$^2 > 10^{-6}$. The second best method is the MATLAB^{TM} linear interpolation, for which only 6.9% of the points had a residual$^2 > 10^{-5}$.

Chapter 5
Results

In the course of this research, extensive theoretical tests as well as a key tissue phantom experiment were performed to determine the capabilities of both the method by Blackledge *et al* (Direct Fourier Method), with and without the approximate attenuation correction, as well as the algebraic reconstruction technique with attenuated propagators. The theoretical tests were accomplished via computer simulations of scattering, while the experimental work involved the construction of a phantom and the subsequent collection and reconstruction of data from a waterbath setting. In analyzing the behavior of the reconstruction algorithms, point-spread-functions (PSF's) were investigated. This involved the simulated scattering of ultrasound from one or more infinitesimal points. The image reconstruction process in turn produced a Gaussian-shaped PSF, rather than an infinitesimal spike. The width of the PSF is of interest in evaluating the reconstruction algorithms. The PSF can be described by its full width at half its maximum amplitude (full-width-half-max, ie: FWHM). The FWHM, in turn, is a measure of the image resolution of the reconstruction algorithm.

Various results are presented in the following sections, and key points are outlined here as follows:

- In the algorithm derivations, the simplification ($\nabla S_{\mathbf{r}_j} \approx ik\hat{\mathbf{n}}_j S_{\mathbf{r}_j}$) has no discernible effect when imaging objects with κ/ρ values in the range of human tissue.
- The simplification ($\nabla \tilde{S}_{\mathbf{r}_j} \approx ik\hat{\mathbf{n}}_j \tilde{S}_{\mathbf{r}_j}$) (case of attenuation) has no discernible effect when imaging objects with κ/ρ values in the range of human tissue.
- Dispersion results in the incorrect calculation of scatter TOF's by up to 0.5 μs, as well as the incorrect determination of pulse shape.
- The cylindrical source model describes line sources accurately to within only 3-5%.

The Direct Fourier Method yielded the following results in computer simulations:

- The simplification $(S_{\mathbf{r}_j} \approx \exp(ik(\hat{\mathbf{n}}_j \cdot \mathbf{r} + |\mathbf{r}_j|))/\sqrt{k|\mathbf{r}_j|})$ results in a miscalculation of scatter TOF's by up to 2 μs.

- The TOF error due to both this assumption and the isochrone warping discussed in Section 2.3 results in distorted, halo-shaped PSF's with reduced amplitudes.

- The TOF error worsens as $|\mathbf{r}|/a$ increases, where a is the distance from the origin to the source or detector, and $\mathbf{r}$ is the position vector of any scatter point.

- Dispersion distorts PSF's into low amplitude halos. If the dependence of acoustic speed upon frequency can be determined, images can be corrected reasonably well.

- Valid γ_ρ and γ_κ cross-sections can be generated only in limited cases for which $|\mathbf{r}| < 0.05a$ and in which there is no attenuation.

- For these limited cases, the algorithm exhibits image resolution of ~ 0.07 mm

- For these limited cases, the algorithm reconstructed point amplitudes quantitatively to within $97 \pm 3\%$ and $95 \pm 4\%$ of their actual values for γ_κ and γ_ρ, respectively.

- Beyond $|\mathbf{r}| < 0.05a$, PSF's become distorted into low amplitude halos.

- Images improve directly with the number of views when $\mathbf{r} \neq$ the origin.

- The approximate correction using $\overline{d}_t$ and $\overline{d}_w$ failed.

Using the Direct Fourier Method, a key experiment was done in which an agar-graphite cylindrical tissue phantom was imaged. The following results were obtained for the phantom, which had a negative γ_κ and R and a diameter of 3 mm:

- The resulting γ_κ and R cross-sections were primarily negative. The FWHM values were 2.94 ± 0.06 mm and 1.94 ± 0.04 for γ_κ and R, respectively.

- A valid γ_ρ image could not be calculated due to very narrow PSF for R.

- PSF's were severely distorted by errors of only 1-2% in the measurement of a.

The following results were determined via computer simulations of the ART:

- Valid γ_ρ and γ_κ cross-sections were generated with the ART for relatively large values of $|\mathbf{r}|$ (tested up to $|\mathbf{r}| = 0.3a$) and in the presence of strong attenuation.

- For these cases, the ART exhibits image resolution of ~ 0.05 mm.

- For these cases, the ART reconstructed point amplitudes quantitatively to within $100 \pm 14\%$ and $99 \pm 4\%$ of their actual values for γ_κ and γ_ρ, respectively.
- Strong attenuation can be corrected to within 0.2%.
- The ART has difficulty converging for images of more than 20×20 pixels (~ 10 mm $\times$ 10 mm) due to ill-conditioning of the propagator matrix.

Finally, this work lead to the following key results regarding noise filtering:

- In simulation, wavelet denoised data required smoothing to remove residual choppiness, resulting in an image improvement of only 10% over data that was only smoothed.
- In experiment, wavelet denoising with the Daubechies 9 and Daubechies 20 wavelet families offered no improvement of data compared to lowpass filtering.

Details of these and other results are presented in the sections to follow.

5.1 Effect of Various Assumptions

From time to time in the derivation of the image reconstruction algorithms, simplifying assumptions have been applied to render the mathematics tractable. In this section, the effect of three major assumptions will be presented.

5.1.1 The Assumption that $\nabla S_{\mathbf{r}_j} \approx ik\hat{\mathbf{n}}_j S_{\mathbf{r}_j}$

This assumption was applied in the derivation of the method by Blackledge *et al.* In Appendix B it was shown that

$$\nabla S_{\mathbf{r}_j} = \hat{\mathbf{n}}_j \{ik - \frac{1}{2}\frac{1}{|\mathbf{r} - \mathbf{r}_j|}\} S_{\mathbf{r}_j} \tag{5.1}$$

after which the real term was dropped due to its small magnitude relative to the imaginary term. This procedure is cited in the work by Blackledge *et al* as well as Norton and Linzer [10, 66]. However, this implies that $\nabla S_{\mathbf{r}_j}$ does not impart a phase shift when it operates on an ultrasound field. Hence, the assumption holds more meaning than if the terms being compared in magnitude were either both real or both imaginary. In addition, $\nabla S_{\mathbf{r}_j}$ is further operated on in the remainder of the reconstruction algorithm derivation. Hence, it is good judgement to verify that indeed the final effect of the dropped term remains negligible.

Appendix C outlines the derivation of an expression for the scattered field, p_s, when Equation 5.1 is used. To reiterate, the result is

$$\begin{aligned} p_s(\mathbf{r}_d, \mathbf{r}_s, \omega) &= \alpha^2 A(\omega)\, k^2 \times \\ & \int_{\Re^2} S(k|\mathbf{r} - \mathbf{r}_s|)\, (\gamma_\kappa(\mathbf{r}) + \Phi\gamma_\rho(\mathbf{r}))\, S(k|\mathbf{r} - \mathbf{r}_d|)\, \mathrm{d}^2\mathbf{r} \end{aligned} \tag{5.2}$$

where

$$\Phi = \cos(\theta)(1 + \frac{0.01428i}{k}\mathrm{mm}^{-1} - \frac{1}{k^2}\, 0.00714^2\mathrm{mm}^{-2}) \tag{5.3}$$

Recall that this expression is being compared to the one based on the approximate $\nabla S_{\mathbf{r}_j}$, in which Φ is simply equal to $\cos(\theta)$.

In order to determine the effect of using the approximate $\nabla S_{\mathbf{r}_j}$, a computer simulation was performed in which a pulsed ultrasound field was scattered from a very small point with compressibility $\gamma_{\kappa 1}$ and density $\gamma_{\rho 1}$. The point was located at $\mathbf{r}$ = (0, 0), and it was assumed to be a square of width dx. The magnitude of dx was assumed to be determined by the Nyquist frequency in the data. As discussed in Section 2.1, when a transient ultrasound field insonifies a region, the maximum spatial resolution that is possible from the data is $\lambda_{Nyq}/2$, which is one half the wavelength of the Nyquist frequency in the system being investigated. The grid on which the discrete scatter points lie in a computer simulation must then have a spacing, dx, of at most $\lambda_{Nyq}/2$ in order to closely approximate a "continuous" object relative to the wavelengths in the ultrasound field. Each individual scatter point then has a square element of area associated with it, with dimensions dx$\times$dx, from which ultrasound is assumed to scatter. The study at hand considers only one such scatter point with a square element of area of width $\lambda_{Nyq}/2$.

The small scatter point was assumed to be immersed in a nonattenuating fluid. Since for all intents and purposes the ultrasound in simulation traveled through only a uniform liquid with a speed of sound equal to that of water, refraction was not an issue due to the lack of acoustic impedance interfaces. The grid spacing was thus equal to $\frac{c_w}{2 f_{Nyq}}$. The source and detector transducers were located a distance of $a = 100$ mm from the origin, with a relative angle of θ between the beam direction and the detector angle. The coordinates of the source were fixed at $\mathbf{r}_s = (0, -a)$. The insonifying field was simulated from a line source that produced a Ricker wavelet defined as in Equation 2.46 by

$$\begin{aligned} Y_r &= \sqrt{\frac{\pi}{2}}\{u^2 - \frac{1}{2}\} \exp(-u^2) \\ u &= \frac{\omega_0 t}{2} = \pi f_0 t \end{aligned} \tag{5.4}$$

In Equation 5.4, recall that time t ranges over both negative and positive values, with the simulation experiment starting at $t = 0$. Also, f_0 is the peak frequency of the wavelet. Figure 2.8 in Section 2.2.6 illustrated the time profile and the Fourier spectrum of a Ricker wavelet with $\omega_0 = 7.5$ MHz, which has a corresponding pulse length of ~ 2.6 mm.

Using the 2D approach, Equation 5.2 can be transformed to a summation over scatter points. Since only one point was considered in this computer simulation, the resulting expression for the detected scatter field, p_s, is simply

$$p_s(\mathbf{r}_d, \mathbf{r}_s, \omega) = \alpha^2 A(\omega)\, k^2\, S(k|\mathbf{r} - \mathbf{r}_s|)\, (\gamma_{\kappa 1} + \Phi\gamma_{\rho 1})\, S(k|\mathbf{r} - \mathbf{r}_d|)\, \mathrm{dx}\,\mathrm{dy} \tag{5.5}$$

$$= \alpha^2 A(\omega)\, k^2\, S(ka)\, (\gamma_{\kappa 1} + \Phi\gamma_{\rho 1})\, S(ka)\, \mathrm{dx}^2 \tag{5.6}$$

Note that dy has been replaced with dx since the element of area is square. The above expression can be further improved by substituting the exact propagator $g(\mathbf{r}|\mathbf{r}_j, k)$ for the approximate one given by $\alpha S(k|\mathbf{r} - \mathbf{r}_j|)$. This results in

$$p_s(\mathbf{r}_d, \mathbf{r}_s, \omega) = A(\omega)\, k^2\, g(\mathbf{r}|\mathbf{r}_s, k)\, (\gamma_{\kappa 1} + \Phi\gamma_{\rho 1})\, g(\mathbf{r}|\mathbf{r}_d, k)\, \mathrm{dx}^2 \tag{5.7}$$

Recalling from Section 2.2.1 that the 2D Green's function is

$$g(\mathbf{r}|\mathbf{r}_j, k) = -\frac{i}{4} H_0^1(k|\mathbf{r} - \mathbf{r}_j|) \tag{5.8}$$

yields the following expression for the exact scattered field from the small point:

$$\begin{aligned} pe_s(\mathbf{r}_d, \mathbf{r}_s, \omega) &= -\frac{1}{16} A(\omega)\, k^2\, H_0^1(ka)\, (\gamma_{\kappa 1} + \Phi \gamma_{\rho 1})\, H_0^1(ka)\, \mathrm{dx}^2 \\ &= -\frac{1}{16} A(\omega)\, k^2\, H_0^1(ka)\, H_0^1(ka)\, \mathrm{dx}^2 \times \{\gamma_{\kappa 1} + \cos(\theta)\gamma_{\rho 1} + \\ &\qquad \cos(\theta)\, (\frac{0.01428i}{k} \mathrm{mm}^{-1} - \frac{1}{k^2}\, 0.00714^2 \mathrm{mm}^{-2})\gamma_{\rho 1}\} \end{aligned} \tag{5.9}$$

In contrast, the reconstruction algorithm assumes that the point produces a scatter field given by the approximate expression

$$p_s(\mathbf{r}_d, \mathbf{r}_s, \omega) = \alpha^2 A(\omega)\, k^2\, S(ka)\, S(ka)\, \mathrm{dx}^2\, (\gamma_{\kappa 1} + \cos(\theta)\gamma_{\rho 1}) \tag{5.10}$$

The fields described by Equations 5.9 and 5.10 were compared in the computer simulation to determine the effect of the simplifying assumptions. The first point to note is that the approximate field is nearly identical to the exact field when $\theta = 90^{\circ}$. This results because $\Phi = 0$ at this value of θ and also because αS is an excellent approximation to the exact Green's function propagator, as discussed in Section 2.2.6. As such, compressibility image reconstruction based on detected side scatter can potentially give good results with the original method of Blackledge *et al.* The second point to note is that the error term in p_s, which is

$$\epsilon = \cos(\theta)\, (\frac{0.01428i}{k} \mathrm{mm}^{-1} - \frac{1}{k^2}\, 0.00714^2 \mathrm{mm}^{-2})\gamma_{\rho 1} \tag{5.11}$$

has the largest magnitude in both backscatter and transmission experiments, in which $|\cos(\theta)| = 1$. Thus, backscatter imaging was investigated in this simulation as the worst case scenario regarding error in the model. Furthermore, the error term increases in magnitude directly with the value of $|\gamma_{\rho 1}|$. A value of $|\gamma_{\rho 1}| = 0.2$ is considered relatively large for soft tissue, which has densities similar to that of water [10, 43]. As such, $\gamma_{\rho 1}$ was kept less than or equal to this value. Lastly, within the case of backscatter imaging, the effect of the error term is evidently largest when ϵ increases in magnitude relative to the $(\gamma_{\kappa 1} + \cos(\frac{\pi}{2})\gamma_{\rho 1})$ term. It was therefore expected that the error in the ultrasound field would grow infinitely large when $\gamma_{\kappa 1}$ is equal to $\gamma_{\rho 1}$.

The computer simulation investigated the error in p_s for three values of $\gamma_{\rho 1}$, equal to $\{0.05, 0.1, 0.2\}$, and $-0.2 < \gamma_{\kappa 1} < 0.2$. Since tissue is also similar to water in its compressibility characteristics, this range generally covers most situations likely to be found in practical imaging situations [10, 43]. For every $(\gamma_{\kappa 1}, \gamma_{\rho 1})$ pair, the Fourier data pe_s and p_s were computed, together with the residual Fourier spectrum,

$$p_r = pe_s - p_s \tag{5.12}$$

A measure of the error in the Fourier data was obtained by computing the ratio of the sum of the power in p_r relative to that in pe_s, given by:

$$\mathrm{Q}_1 = \frac{\Sigma|p_r|^2}{\Sigma|pe_s|^2} \times 100\% \tag{5.13}$$

The denominator of Q_1 goes to zero when $\gamma_{\kappa 1}$ is equal to $\gamma_{\rho 1}$. As such, measures of error regarding the change in Fourier amplitude and phase were also calculated. The amplitude and phase of the residual field, p_r, is simply the change in Fourier amplitude and phase that results from the application of the simplifying assumption that $\nabla S_{\mathbf{r}_j} \approx ik\hat{\mathbf{n}}_j S_{\mathbf{r}_j}$. Therefore, the amplitude of p_r was summed over frequency to yield Q_2 as follows:

$$\mathrm{Q}_2 = \Sigma|p_r| \tag{5.14}$$

As well, the phase angle for each frequency was calculated by

$$\Phi_{phase}(f) = \tan^{-1}\left(\frac{\mathrm{imag}(p_r(f))}{\mathrm{real}(p_r(f))}\right) \tag{5.15}$$

and the absolute value of Φ_{phase} was summed over frequency to yield Q_3 as follows:

$$\mathrm{Q}_3 = \Sigma|\Phi_{phase}| \tag{5.16}$$

The simulation work indicated that these measures of error depend only on $\frac{\gamma_{\kappa 1}}{\gamma_{\rho 1}}$ and not on the specific values of the two parameters. Results for Q_1, Q_2 and Q_3 are illustrated in Figure 5.1, and Table 5.1 outlines some representative points in the Q_1 plot. Evidently, as expected the error in the model is worst and in fact increases towards infinity as $\gamma_{\kappa 1}$

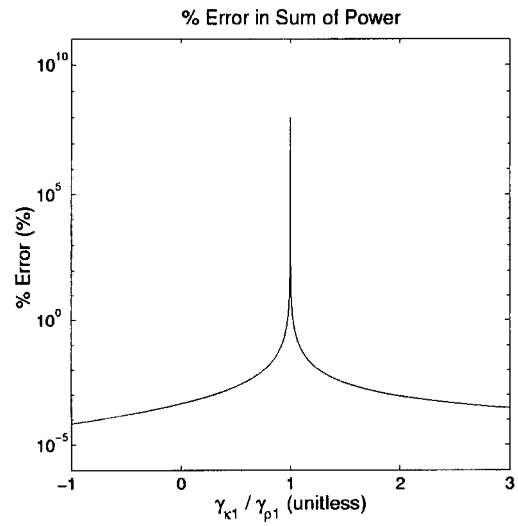

(A)

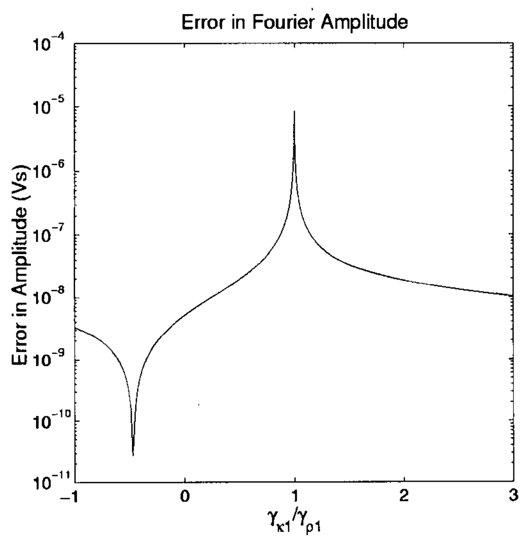

(B)

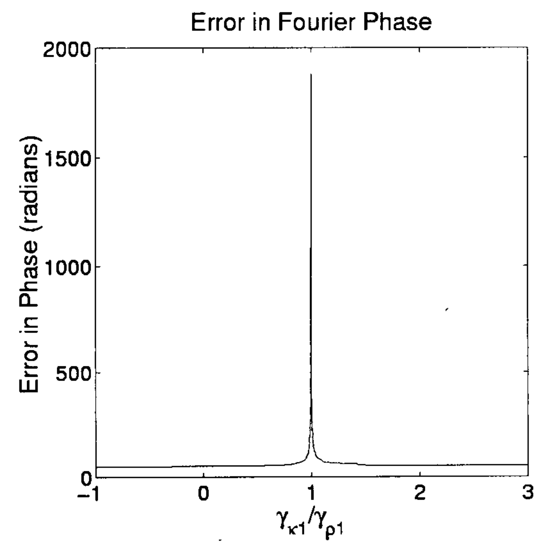

(C)

Figure 5.1: Figure A illustrates Q_1 as a function of $\frac{\gamma_{\kappa 1}}{\gamma_{\rho 1}}$ in the case of no attenuation. Evidently, the Q_1 error increases towards infinity as $\gamma_{\kappa 1}$ approaches $\gamma_{\rho 1}$. Figures B and C illustrate Q_2 and Q_3, respectively, as a function of $\frac{\gamma_{\kappa 1}}{\gamma_{\rho 1}}$.

$\frac{\gamma_{\kappa 1}}{\gamma_{\rho 1}}$ **(unitless)**	Q_1 (%)	$\frac{\gamma_{\kappa 1}}{\gamma_{\rho 1}}$ **(unitless)**	Q_1 (%)
-1.0	6.7×10^{-5}	3	2.9×10^{-4}
-0.5	1.5×10^{-4}	2.5	4.5×10^{-4}
0.0	4.4×10^{-4}	2	8.7×10^{-4}
0.5	2.2×10^{-3}	1.5	3.0×10^{-3}
0.95	0.24	1.05	0.26
0.995	24	1.005	24

Table 5.1: The above data illustrate representative points in the graph of Q_1 versus $\frac{\gamma_{\kappa 1}}{\gamma_{\rho 1}}$ in the case of no attenuation.

approaches $\gamma_{\rho 1}$. However, except for values of $\frac{\gamma_{\kappa 1}}{\gamma_{\rho 1}}$ in the range of 0.95-1.05, the total Q_1 error is still less than 0.26%. As such, image reconstruction based on the Fourier data should theoretically provide valid results up to this point. Fortunately, γ_κ and γ_ρ for soft tissue generally have opposite sign, as illustrated with some representative values in Table 5.2. This results in a Q_1 error of less than 2×10^{-4}% for Fourier data, according to Table 5.1.

Tissue Type	γ_κ	γ_ρ	$\frac{\gamma_\kappa}{\gamma_\rho}$
average soft tissue	-0.1286	0.0566	-0.44
liver	-0.1398	0.0566	-0.40
muscle	-0.1875	0.0741	-0.38
fat	0.0810	-0.0504	-0.62

Table 5.2: The above data illustrate γ_ρ and γ_κ values for some representative soft tissues.

5.1.2 The Assumption that $\nabla\tilde{S}_{\mathbf{r}_j} \approx ik\hat{\mathbf{n}}_j\tilde{S}_{\mathbf{r}_j}$

The computer simulation results presented in the previous section are valid for situations in which attenuation can be ignored. However, this is not generally the case in tissue imaging and as such the same analysis must be done for the attenuated propagator, $\tilde{S}_{\mathbf{r}_j}$, in order to test the effect on the model of the assumption that $\nabla\tilde{S}_{\mathbf{r}_j} \approx ik\hat{\mathbf{n}}_j\tilde{S}_{\mathbf{r}_j}$. This assumption was applied in the derivation of the ART that is aimed at the reconstruction of γ_κ and γ_ρ for attenuating objects.

In Section 4.2.2, it was shown that

$$\nabla \tilde{S}_{\mathbf{r}_j} \approx \tilde{S}_{\mathbf{r}_j}\{ik\hat{\mathbf{n}}_j - \mathrm{T3}\} \tag{5.17}$$

where

$$\begin{aligned} \mathrm{T3} &= (k^2\, 1.4053 \times 10^{-5}\,\mathrm{mm} + 1.2255 \times 10^{-2}\, k)(\hat{\mathbf{x}} + \hat{\mathbf{y}}) \\ &= (Bk^2 + Ck)(\hat{\mathbf{x}} + \hat{\mathbf{y}}) \end{aligned} \tag{5.18}$$

The term in term in $(\hat{\mathbf{x}} + \hat{\mathbf{y}})$ was then dropped because it is 3 orders of magnitude less than the imaginary component in the above expression. Therefore, it was assumed that

$$\nabla \tilde{S}_{\mathbf{r}_j} \approx ik\hat{\mathbf{n}}_j \tilde{S}_{\mathbf{r}_j} \tag{5.19}$$

As in the case of no attenuation, this implies that $\nabla \tilde{S}_{\mathbf{r}_j}$ does not result in a phase shift when it operates on an ultrasound field. Hence, this assumption also has more meaning than if the terms being compared were either both real or both imaginary. Like $\nabla S_{\mathbf{r}_j}$, the expression for $\nabla \tilde{S}_{\mathbf{r}_j}$ is further operated on during the remaining derivation of the reconstruction algorithm. Hence, it is necessary to verify that the final effect of the dropped term is in fact negligible.

Appendix C outlines the derivation of an expression for the scattered field with attenuation included, p_s, when Equation 5.17 is used. To reiterate, the result is

$$\begin{aligned} p_s(\mathbf{r}_d, \mathbf{r}_s, \omega) &= \alpha^2 A(\omega)\, k^2 \times \\ &\int_{\Re^2} \tilde{S}(k|\mathbf{r} - \mathbf{r}_s|)\, (\gamma_\kappa(\mathbf{r}) + \Phi\gamma_\rho(\mathbf{r}))\, \tilde{S}(k|\mathbf{r} - \mathbf{r}_d|)\, \mathrm{d}^2\mathbf{r} \end{aligned} \tag{5.20}$$

where

$$\begin{aligned} \Phi &= \cos(\theta) + \frac{1}{k^2}(Bk^2 + Ck)^2|\hat{\mathbf{x}} + \hat{\mathbf{y}}|^2 \\ &\quad - \frac{i}{k}\,(Bk^2 + Ck)\,\{\cos(\varphi_s) + \cos(\varphi_d) + \sin(\varphi_s) + \sin(\varphi_d)\} \end{aligned} \tag{5.21}$$

Recall that this expression is being compared to the equation for p_s based on the approximate $\nabla\tilde{S}_{\mathbf{r}_j}$, in which Φ simply equals $\cos(\theta)$.

In this computer simulation, it was again assumed that the same pulsed ultrasound field was scattered from a point identical in nature to that described in Section 5.1.1, with one exception. The point was assumed to be situated in a circular cross-section of tissue with radius equal to $0.2a$ and with its center at the origin. The coordinates of the source were again fixed at $\mathbf{r}_s = (0, -a)$, where $a = 100$ mm. The tissue was assumed to be immersed in water, and refraction at the water/tissue interface was ignored. With this geometrical setup, the scattered ultrasound detected in simulation for any view always traveled through a distance of d_w and d_t in water and tissue, respectively.

In the identical manner as outlined in Section 5.1.1, the nearly exact scattered field in the presence of attenuation from this small point was derived. The only difference in the derivation is that attenuation factors precede the propagators, and Φ has a different form. The result is as follows:

$$\begin{aligned} pe_s(\mathbf{r}_d, \mathbf{r}_s, \omega) &= -\frac{1}{16} A(\omega)\, k^2\, \mathrm{ATT}_w \mathrm{ATT}_t\, H_0^1(ka) \times \\ &\qquad (\gamma_{\kappa 1} + \Phi\gamma_{\rho 1})\, \mathrm{ATT}_w \mathrm{ATT}_t\, H_0^1(ka)\, \mathrm{dx}^2 \end{aligned} \tag{5.22}$$

ATT_w and ATT_t are defined as in Equations 2.64 and 2.66 to be

$$\begin{aligned} \mathrm{ATT}_t(d_t, k) &= 10^{-\chi_t d_t k} \\ \mathrm{ATT}_w(d_w, k) &= 10^{-\chi_w d_w k^2} \end{aligned} \tag{5.23}$$

where

$$\begin{aligned} \chi_t &= \frac{-0.1 c_t}{40\pi\, \mathrm{MHz} \cdot \mathrm{mm}} \\ \chi_w &= \frac{-0.00022 c_w^2}{80\pi^2\, \mathrm{MHz}^2 \cdot \mathrm{mm}} \end{aligned} \tag{5.24}$$

In contrast, the reconstruction algorithm assumes that the point produces a scattered field given by the approximate expression

$$p_s(\mathbf{r}_d, \mathbf{r}_s, \omega) = \alpha^2 A(\omega)\, k^2\, \mathrm{ATT}_w \mathrm{ATT}_t\, S(ka) \times \tag{5.25}$$

$$\mathrm{ATT}_w \mathrm{ATT}_t\, S(ka)\, \mathrm{dx}^2\, (\gamma_{\kappa 1} + \cos(\theta)\gamma_{\rho 1})$$

Evidently Φ is very different in the case of attenuation in that it is dependent upon k, φ_s and φ_d, in addition to θ.

Analysis indicates that the imaginary part of Φ, which accounts for the majority of the error in the model, is zero for all frequencies and for all combinations of φ_s and φ_d in the case of backscatter imaging. Furthermore, given that $|k| < 42\,\mathrm{mm}^{-1}$ for a typical imaging experiment, the real part of Φ is always equal to $\cos(\theta)$ to at least 4 significant figures. Hence, for backscatter imaging, pe_s is exactly equal to p_s. The model was found to be most in error for transmission imaging, in which $\theta = 0^\circ$. However, $\theta = 90^\circ$ was studied instead because it corresponds to compressibility imaging, which is a focus of this thesis. The value of the imaginary part of Φ was calculated for $k = 1\ \mathrm{mm}^{-1}$ and $\theta = 90^\circ$ for the full range of φ_d and φ_s. This indicated that the error in the model was equal and opposite in magnitude for $(\varphi_d, \varphi_s) = (0^\circ, 90^\circ)$ and $(180^\circ, 270^\circ)$ due to the sinusoidal trigonometric term in Equation 5.21. Both sets of angles were studied.

Again the error in p_s was studied for $\gamma_{\rho 1}$ equal to $\{0.05, 0.1, 0.2\}$ and $-0.2 < \gamma_{\kappa 1} < 0.2$ by computing the functions Q_1, Q_2 and Q_3 defined in Equations 5.13 through 5.16. As in the case of no attenuation, the simulation indicated that these quantities depend only on $\frac{\gamma_{\kappa 1}}{\gamma_{\rho 1}}$ and not on the values of the individual parameters. However, the inclusion of attenuation shifts the Q_1 and Q_2 graphs when d_t changes in magnitude relative to d_w. Results for Q_1, Q_2 and Q_3 are illustrated in Figures 5.2 and 5.3, and Table 5.3 outlines some representative Q_1 points plotted in Figure 5.2.A. The Q_1 error increases towards infinity as $|\frac{\gamma_{\kappa 1}}{\gamma_{\rho 1}}|$ approaches zero, which is as expected. However, up to a value of $|\frac{\gamma_{\kappa 1}}{\gamma_{\rho 1}}|$ = 0.1, the Q_1 error is still less than 0.9%. As such, γ_κ imaging should theoretically provide valid results up to this point. Referring again to Table 5.2, it is evident that $|\frac{\gamma_{\kappa 1}}{\gamma_{\rho 1}}|$ is generally less than 0.35, which precludes a Q_1 error of less than 0.14% according to Figure 5.2. Note that Q_1 is a nearly symmetric function of $|\frac{\gamma_{\kappa 1}}{\gamma_{\rho 1}}|$ for $d_t = 0.3a$, and that the graph deviates increasingly from symmetry about 0 with decreasing d_t.

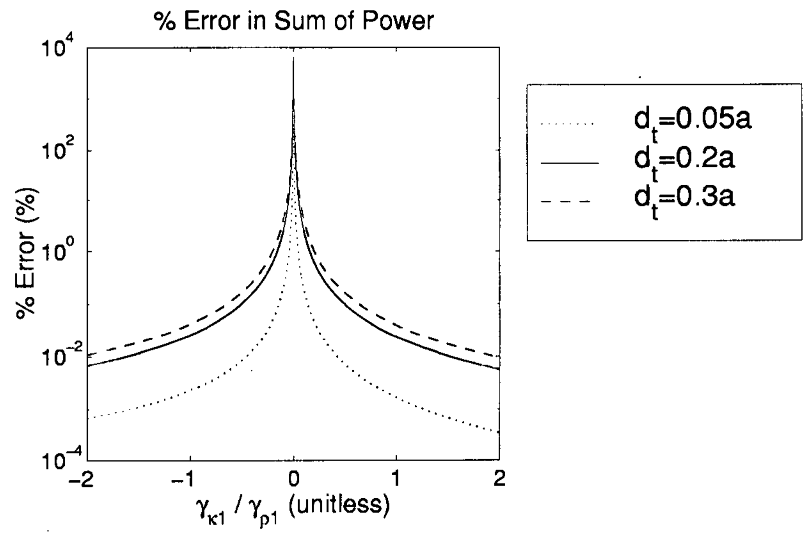

(A)

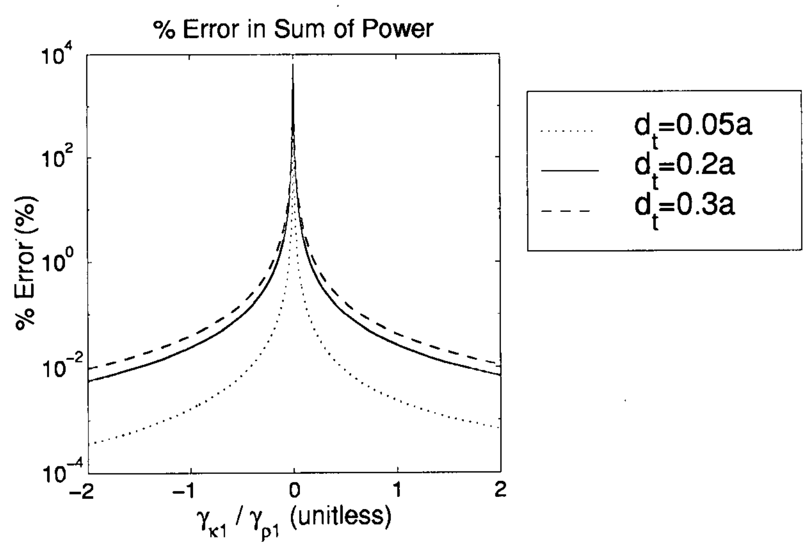

(B)

Figure 5.2: The above figures illustrate Q_1 as a function of $\frac{\gamma_{\kappa 1}}{\gamma_{\rho 1}}$ for the case in which attenuation is considered. Figures A and B plot the results for $(\varphi_d, \varphi_s) = (0^o, 90^o)$ and $(180^o, 270^o)$, respectively. Evidently, the corresponding graphs for the two angle sets are mirror images, and the Q_1 error increases towards infinity as $\frac{\gamma_{\kappa 1}}{\gamma_{\rho 1}}$ approaches zero.

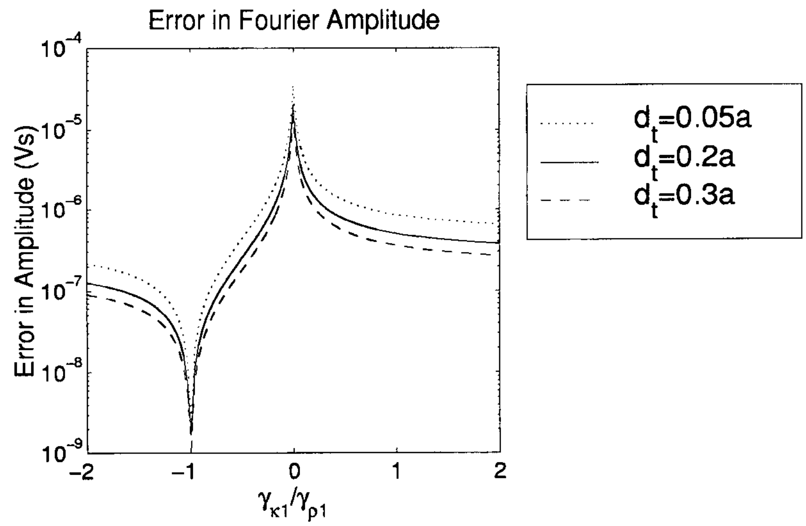

(A)

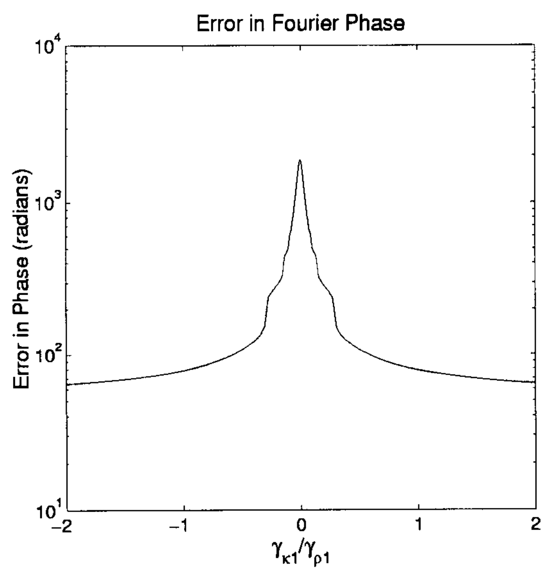

(B)

Figure 5.3: Figures A and B illustrate Q_2 and Q_3 as a function of $\frac{\gamma_{\kappa 1}}{\gamma_{\rho 1}}$ for the case in which attenuation is considered. These figures represent the results for both $(\varphi_d, \varphi_s) = (0°, 90°)$ and $(180°, 270°)$, since the corresponding errors in each case are identical by virtue of the sum of absolute values. Furthermore, the phase error graphs are identical regardless of the value of d_t.

$\frac{\gamma_{\kappa 1}}{\gamma_{\rho 1}}$ **(unitless)**	Q_1 (%), $d_t = 0.2a$	Q_1 (%), $d_t = 0.3a$
-2.0	2.7×10^{-3}	4.6×10^{-3}
-1	1.2×10^{-2}	1.9×10^{-2}
-0.38	8.3×10^{-2}	1.4×10^{-1}
-0.15	5.1×10^{-1}	8.9×10^{-2}
-0.01	1.2×10^{2}	2.0×10^{2}
-0.0025	2.0×10^{3}	3.2×10^{3}
0.0025	2.0×10^{3}	3.2×10^{3}
0.01	1.2×10^{2}	2.0×10^{2}
0.15	5.5×10^{-1}	9.0×10^{-1}
0.38	8.7×10^{-2}	1.4×10^{-1}
1	1.2×10^{-2}	2.0×10^{-2}
2	3.5×10^{-3}	5.5×10^{-3}

Table 5.3: The above data illustrate representative points in the graph of Q_1 versus $\frac{\gamma_{\rho 1}}{\gamma_{\rho 1}}$ with attenuation considered (Figure 5.2.A.

5.1.3 The Effect of Use of an Approximate $S_{\mathbf{r}_j}$

Recall that in Section 2.2.1 the original function $S_{\mathbf{r}_j}$ used in the approximation to the Green's function propagator was substituted with a simpler expression, given by

$$S_{\mathbf{r}_j} \approx \frac{\exp(ik(\hat{\mathbf{n}}_j \cdot \mathbf{r} + |\mathbf{r}_j|))}{k^{\frac{1}{2}}|\mathbf{r}_j|^{\frac{1}{2}}} \tag{5.26}$$

This resulted from the application of the far field assumption stated in expression 2.21. It was noted that this approximation results in a loss of phase information and ultimately is responsible for the relatively poor performance of the reconstruction algorithm. To obtain an idea of the magnitude of this effect, a computer simulation was performed in which the source and detector were situated at (0, -a) and (-a, 0), respectively, with a = 60 mm. The Ricker wavelet used in the simulations described in Section 5.1.1 was scattered from several points situated with $|\mathbf{r}|$ = 10 mm. Propagation of the pulsed ultrasound was calculated using both the exact and approximate $S_{\mathbf{r}_j}$. The pulses corresponding to the exact and approximate $S_{\mathbf{r}_j}$ are shown in Figures 5.4.B through 5.4.D with solid and dotted lines, respectively. Evidently, the pulse shape is largely preserved, but the pulse

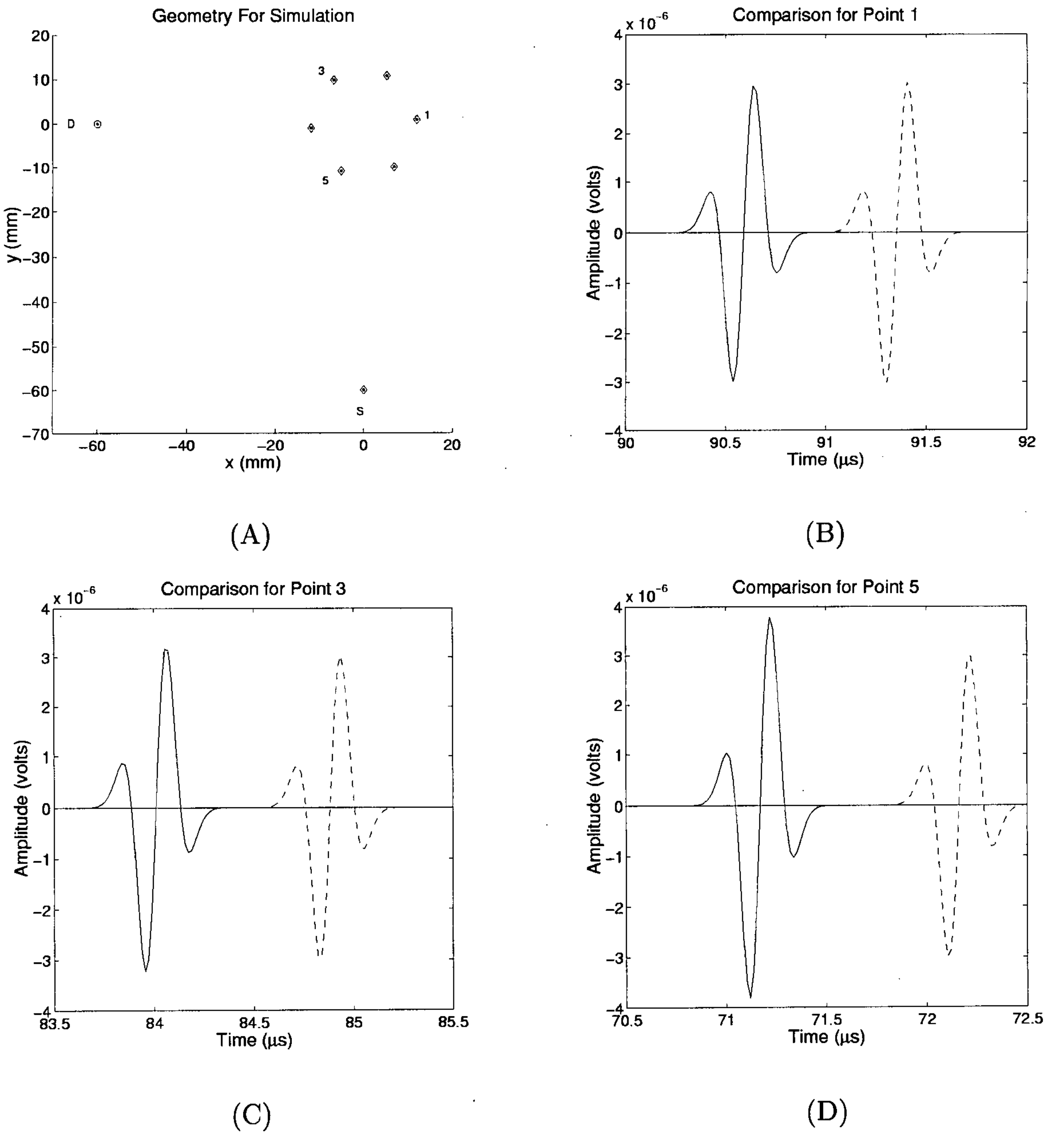

Figure 5.4: Figure A illustrates the experimental geometry in the computer simulation used to test the effect of the approximate $S_{\mathbf{r}_j}$. Scatter propagated from points 1, 3 and 5, all with $\mathbf{r} = 10$ mm, are illustrated assuming use of both the exact $S_{\mathbf{r}_j}$ (solid line) and the approximate $S_{\mathbf{r}_j}$ (dotted line).

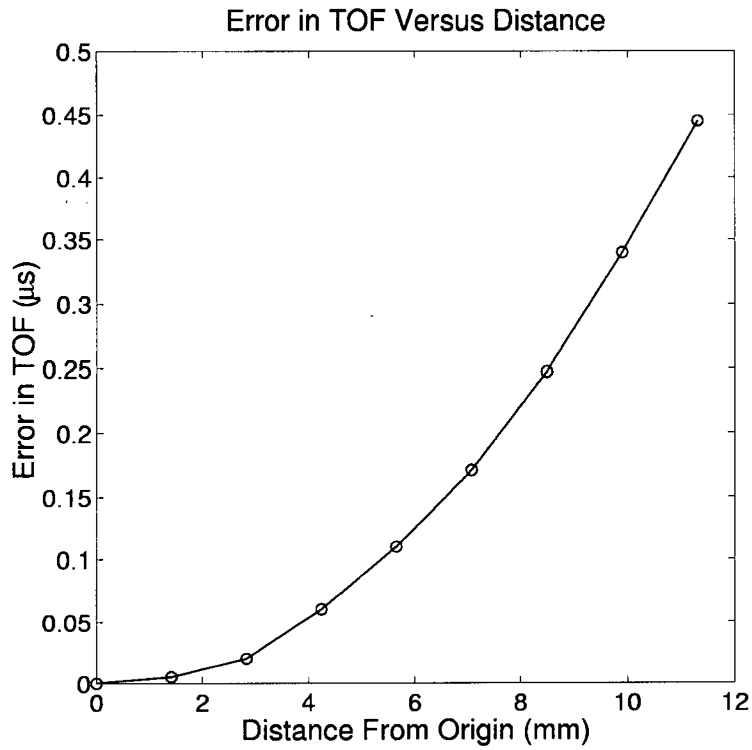

Figure 5.5: This figure plots the error in TOF for scatter points that lie along the diagonal in the 4th quadrant of the Cartesian grid. Evidently, the error increases non-linearly as the distance from the origin increases.

height is reduced in error in some cases. Also, the time-of-flight is always overestimated with use of the approximate $S_{\mathbf{r}_j}$. The maximum error in the TOF is 1μs for the simulation shown.

Computer simulations indicate that the error in the TOF is always on the order of 0-2 μs, being 0 μs for points at the origin and worsening as the value of $|\mathbf{r}|/a$ increases. To illustrate this, Figure 5.5 plots the TOF error given $\mathbf{r}_s = (0, -100)$, $\mathbf{r}_d = (-100, 0)$, and scatter points at $\mathbf{r} = (d, -d)$ mm, where d equals integers between 0 and 8. Evidently, the error in the time-of-flight increases non-linearly as the distance from the origin increases.

Furthermore, the error becomes as large as 7 μs when d is equal to 30 mm. As such, if smaller objects can be imaged or the source and detector can be placed further from the object, the reconstruction of γ_κ and γ_ρ will improve. However, this is generally not possible. The source must be close enough to the object such that the ultrasound field intensity is sufficient to generate detectable scatter upon insonification of the object. In addition, the detector sensitivity drops off at large distances and as such must be kept within 10-15 cm of the object. Hence, the TOF error is an effect that cannot be removed by geometry considerations alone.

Section 2.3 discussed the image reconstruction process that occurs with the analysis of data from each view. Figure 5.6.A sketches a closeup of an example elliptical isochrone that is "warped" into a line by the image reconstruction routine. As is illustrated, a point on the original isochrone is thus misplaced further away from the source and detector in this process. This in turn corresponds to an overestimation of the TOF of the scatter from the point shown. As such, the "warping" of the isochrones is due at least in part to the use of the approximate $S_{\mathbf{r}_j}$, which incorrectly overestimates time-of-flight. The error in TOF based on purely geometrical considerations is plotted in Figure 5.6.B. Here, the distance from the origin is measured along the incorrect linear isochrone passing through the origin with $\mathbf{r}_s = (0, -100)$ mm and $\mathbf{r}_d = (-100, 0)$ mm. The error in the TOF is calculated from the linear displacement that was experienced during the "warping" procedure by a point situated at the corresponding distance from the origin along the linear isochrone. Evidently, the TOF errors are significant and moreover are larger than the errors due to the use of the approximate $S_{\mathbf{r}_j}$, which accounts only in part for the "warping". This warping is a significant drawback of the reconstruction algorithm by Blackledge *et al.*

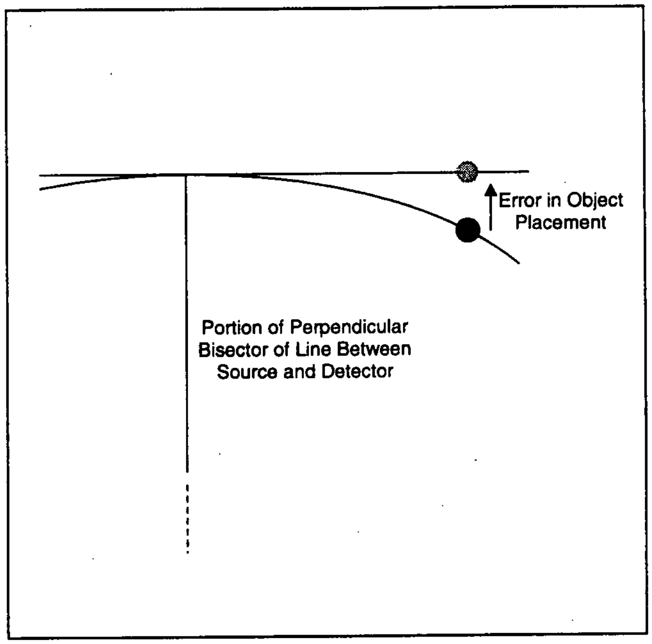

(A)

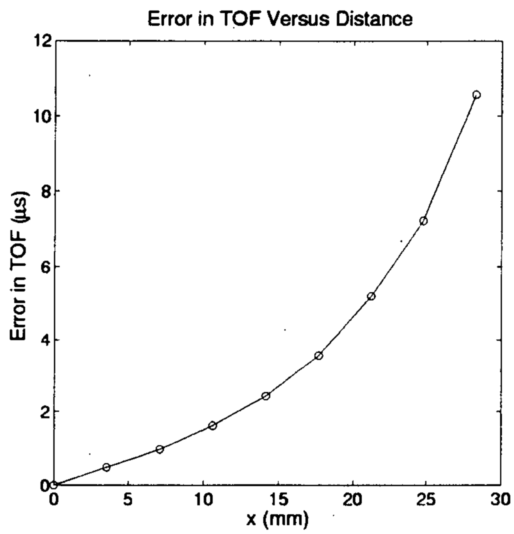

(B)

Figure 5.6: Figure A illustrates the misplacement of an example point when an isochrone is "warped" from an ellipse to a line. Figure B illustrates the error in TOF that will be associated with points along a linear isochrone through the origin as a result of the "warping" process.

5.2 General Notes Regarding the Computer Simulations

5.2.1 Simulation of Object and Scatter

Both the method by Blackledge *et al* and the algebraic reconstruction technique were extensively tested through computer simulation. As described in Section 5.1, ultrasound was scattered in simulation from objects made of one or more discrete points on a Cartesian grid. Each point had associated with it a square element of area with a width of dx. Recall from Section 5.1 that dx can be at most $\lambda_{Nyq}/2$, where λ_{Nyq} is the wavelength in water (20°C) corresponding to the Nyquist frequency of the data that are being simulated. The object was immersed in water, and a two dimensional model of scattering was used. For purposes of simplicity, refraction was not considered, and attenuation was incorporated in only a few simulations as noted. The source and detector were situated at a distance of $|\mathbf{r}_s| = a$ and $|\mathbf{r}_d| = a$ from the origin. The time dependence of the pulsed ultrasound field was described by the Ricker wavelet, given in Equation 5.4, with ω_0 equal to 20 MHz, unless otherwise noted. As such, the pulse length was $\sim$ 1.0 mm.

Returning to the assumption that $\Phi \approx \cos(\theta)$ and summing scatter contributions from all N discrete points in the object situated at locations $\mathbf{r}_i$, respectively, yields from Equation 5.7 the following expression for the non-attenuated scattered field

$$\begin{aligned} p_s(\mathbf{r}_d, \mathbf{r}_s, \omega) &= -\sum_{i=1}^{N} \frac{1}{16} A(\omega) \times \\ & k^2\, H_0^1(k|\mathbf{r}_i - \mathbf{r}_s|)\, (\gamma_\kappa(\mathbf{r}_i) + \cos(\theta)\gamma_\rho(\mathbf{r}_i))\, H_0^1(k|\mathbf{r}_i - \mathbf{r}_d|)\, \mathrm{dx}^2 \end{aligned} \tag{5.27}$$

The field was calculated according to Equation 5.27 for each view about the object. p_s was then generally input to the reconstruction algorithm without any further processing. However, in a few simulations as noted in the following sections, the field was further operated on to impart attenuation or dispersion effects. Attenuation was studied for both the method by Blackledge *et al* and the ART. However, since only preliminary studies were performed with the ART, the study of dispersion was limited to the former method only.

5.2.2 Points Regarding Analysis

In analyzing the behavior of the reconstruction algorithms, PSF's were investigated by scattering ultrasound in simulation from an isolated grid point at some known location. The point has an associated square element of area with particular values of γ_κ and γ_ρ and dimensions of dx×dx. As already indicated, image reconstruction spreads this tiny point out into a generally Gaussian shape called the PSF. The FWHM of the PSF is a measure of the image resolution of the reconstruction algorithm. As discussed in Section 5.1.1, the resolution should be on the order of $\lambda_{Nyq}/2$. Consequently, in water the FWHM of the point-spread-function given f_{Nyq} equal to 10 MHz should be approximately 0.074 mm; the expected FWHM's for other values of f_{Nyq} scale inversely with frequency. Also of interest is the amplitude of a point-spread-function for a given reconstruction relative to the actual value of the point in the original image. The results in the sections to follow illustrate that the reconstructions must always be normalized in order to reproduce a γ_κ or γ_ρ cross-section that exhibits amplitudes similar to the original object. Furthermore, the normalization factors for γ_κ, γ_ρ and R are not necessarily equal.

The "percentage ratio matrix" and the "power sum residual" are two other measures of performance that were used in the following sections. Often γ_κ and γ_ρ cross-sections were produced for objects composed of an M×N grid of points, with the purpose of determining the quantitative capabilities of the imaging algorithm. Following normalization of the reconstructed image, I, the amplitudes of the M×N corresponding point-spread-functions were placed in an array, Λ, and compared point-by-point with the amplitudes, Λ_0, in the original object, I_0. This comparison is herein referred to as the "percentage ratio matrix" of I relative to I_0, and its elements are defined by:

$$PR_{ij} = \frac{\Lambda_{ij}}{(\Lambda_0)_{ij}},\ i = 1, ..., \mathrm{M},\ j = 1, ..., \mathrm{N} \tag{5.28}$$

When two different reconstructions, I_1 and I_2, of the same object must be compared, the similarity between the two images can be measured in terms of a power sum residual.

First a residual image, I_r, is computed by

$$I_r = I_1 - I_2 \tag{5.29}$$

The ratio of the sum of the power in I_r relative to that in I_1 is then computed by

$$Q = \frac{\Sigma |I_r|^2}{\Sigma |I_1|^2} \times 100\% \tag{5.30}$$

In this thesis, Q is termed the "power sum residual."

It will become evident from the following results that the reconstructed image, I, is not an exact scaled version of the original object, I_0, for either the method by Blackledge *et al* or the ART. As such, it is necessary to choose a physical location, (x_N, y_N), at which the corresponding γ_κ or γ_ρ amplitudes in both I and I_0 are extracted for comparison to create a normalization factor, ξ. (x_N, y_N) was chosen to be the origin. The motivating factor was that this point experiences the most accurate reconstruction via the method by Blackledge *et al* as a result of the various approximations based on the far field assumption, such as that discussed in Section 5.1.3. As such, the reconstructed image was normalized by a factor of

$$\xi = \frac{I(0,0)}{I_0(0,0)} \tag{5.31}$$

This convention for choosing ξ was retained in tests of the algebraic reconstruction technique for lack of a better rule and to facilitate the comparison of the two methods.

5.2.3 Discussion of Applied Filtering

Reference is made to lowpass filtering throughout the following sections. First of all, this always refers to Butterworth filtering. Secondly, when the simulation was to test the algebraic reconstruction technique, the source and scatter data Fourier spectra are each filtered and an image is iteratively solved for. This is not the case, however, when the simulation was to test the method by Blackledge *et al*. Recall from Section 2.2.9 that lowpass filters applied to the source and data spectra are rendered ineffective by mathematical operations in this reconstruction algorithm. Instead, the lowpass filtering must be performed along each ray of data in the Fourier domain of the image as described in Section 2.2.9. A lowpass filter with a particular cutoff, f_0, that is designed for the frequency dependent scatter data must be transformed into an equivalent LPF for the τ-dependent radial data, where $\tau = \sqrt{u^2 + v^2}$ is the position along the ray in the Fourier domain of the image. This equivalent filter has a cutoff of

$$\tau_0 = \frac{4\pi f_0}{c_0} \sin(\frac{\theta}{2}) \tag{5.32}$$

where θ is the angle between the incident beam direction and the detector position vector, $\mathbf{r}_d$, and c_0 is the speed of sound in water at 20°C.

θ is equal to 90° and 180° for γ_κ and reflectivity imaging, respectively. Therefore, the cutoff value of τ for γ_κ imaging, given by $(\tau_0)_{\gamma_\kappa}$, is smaller by a factor of $\frac{1}{\sqrt{2}}$ when compared to the cutoff for reflectivity imaging, given by $(\tau_0)_R$. Often the Fourier data are not only filtered, but they may additionally be truncated at some frequency, f_T, that is greater than or equal to the band limit frequency, f_2, of the source. By extension, then, the corresponding τ truncation limits, $(\tau_T)_{\gamma_\kappa}$ and $(\tau_T)_R$, also differ by a factor of $\frac{1}{\sqrt{2}}$. An increase in the maximum value of τ means there is an increase in the maximum spatial frequencies, u_{max} and v_{max}, of the data. According to the discussion in Section 2.2.7, this in turn decreases both the image width and pixel spacing. In order to be able to subtract R from γ_κ to obtain γ_ρ, it is best to reconstruct the two images such that they have the same coordinates, thus circumventing the need to interpolate R at new (x, y) coordinates. $(\tau_T)_{\gamma_\kappa}$ and $(\tau_T)_R$ must therefore be made equal, and care must be taken to ensure that the corresponding γ_κ and R truncation frequencies, $(f_T)_{\gamma_\kappa}$ and $(f_T)_R$, do not lie in a region of valid data.

The following sections present results for simulations of the method by Blackledge *et al* in which the ultrasound source was a Ricker wavelet with ω_0 equal to either 20 MHz or 6 MHz. The source with $\omega_0 = 20$ MHz has a Fourier spectrum amplitude that drops to less than 0.7% beyond $f = 9.0$ MHz and only 0.0006% of the source power spectrum lies beyond this frequency. As such, a LPF with $f_0 = 9.0$ MHz was often applied in this thesis as the optimal filter for these data. After filtering, only 0.0002% of the power spectrum lies beyond 9.0 MHz, so the upper band limit, f_2, is considered to be this frequency. The expected image resolution is equal to $\lambda_{f_2}/2$, which is 0.08 mm in water at 20°C. For good measure, when data truncation was applied to these data, f_T was set at 11.3 MHz or higher. To experiment with lower frequency reconstructions, sometimes a much more limiting lowpass filter with $f_0 = 2.6$ MHz was applied to the simulated data for the source with $\omega_0 = 20$ MHz. After filtering, only 0.0001% of the power spectrum lies beyond 3.5 MHz, so the upper band limit, f_2, was set to this frequency. The corresponding expected image resolution in water at 20°C is 0.21 mm. For good measure, when data truncation was applied to these data, f_T was set 4.0 MHz or higher.

The source with $\omega_0 = 6$ MHz has a Fourier spectrum amplitude that drops to less than 0.7% beyond $f = 2.7$ MHz, and only 0.0008% of the source power spectrum lies beyond this frequency. As such, a LPF with $f_0 = 2.7$ MHz was often applied in this thesis as the optimal filter for these data. After filtering, only 0.0009% of the power spectrum lies beyond 2.7 MHz, so the upper band limit, f_2, was considered to be this frequency. The expected image resolution was then $\lambda_{f_2}/2$, and in water at 20°C this is 0.27 mm. For good measure, when data truncation was applied to these data, f_T was set at 3.4 MHz or higher.

5.3 Tests of the Method by Blackledge *et al* in Computer Simulation

Various simulations were performed to test the method by Blackledge *et al.* In the following sections, generally only image profiles and percentage ratio matrices are presented since these are more illustrative of key features than the corresponding images. The full-width-half-maxima of the point-spread-functions were measured along both the x and y axes, and these values were always found to be equal. In all simulations γ_κ was obtained from side scatter imaging, and γ_ρ was obtained by reconstructing the reflectivity through backscatter imaging and subtracting this from γ_κ. For the sake of brevity, results for either γ_κ or γ_ρ imaging, but generally not both, are presented since the same patterns were seen in this type of reconstruction. Also, the results did not depend upon the actual values of γ_κ and γ_ρ. This was expected by virtue of the linear nature of the Fourier transform.

The simulation of scatter from discrete elements of area means that the amplitude of p_s is inversely dependent upon the sampling frequency, f_s. An image based on p_s will also be inversely dependent upon f_s for two reasons: first, there are no factors in the reconstruction algorithm to cancel this dependency, and second, the IFFT is a linear transformation. As an example, data with $f_{s1} = 60$ MHz have a corresponding element of area equal to

$$\begin{aligned} A_1 &= \{\frac{1}{2}\frac{c_0}{f_{s1}}\}^2 \\ &= 6.08 \times 10^{-4}\,\mathrm{mm}^2 \end{aligned} \tag{5.33}$$

Data with $f_{s2} = 30$ MHz has a corresponding element of area equal to

$$\begin{aligned} A_2 &= \{\frac{1}{2}\frac{c_0}{f_{s2}}\}^2 \\ &= 2.43 \times 10^{-3}\,\mathrm{mm}^2 \end{aligned} \tag{5.34}$$

which is also equal to

$$A_2 = A_1 \times (\frac{f_{s1}}{f_{s2}})^2 \tag{5.35}$$

The two corresponding images will also exhibit this ratio of amplitudes due to the linear nature of the IFFT. As such, two images with different sampling frequencies must be normalized to some common sampling frequency in order to be properly compared. This approach has been made note of in the following sections where it was applied.

In the various tests of the method by Blackledge *et al*, it was observed that under certain circumstances the reconstructed image, I, was approximately a scaled version of the original object, I_0. For instance, this was the case when the following conditions held:

- Scatter point locations were close to the origin.
- Ricker wavelet had ω_0 equal to 20 MHz.
- Sampling frequency was greater than 70 MHz.
- No truncation of Fourier data.
- Lowpass filter with $f_0 = 2.6$ MHz was applied.
- The number of views, N_v, was ≥ 50.

As discussed in Section 5.2, the expected image resolution is 0.21 mm given the value of ω_0 and the LPF choice. An example of reconstructions that satisfy the conditions outlined above is illustrated in Figures 5.7.A and 5.7.B, in which the sampling rate was 75 MHz and N_v was 50. The scattering object in simulation consisted of 9 isolated points spaced 1.5 mm apart on a square grid. The γ_κ and γ_ρ values of the points in the scattering object were equal to

$$\gamma_\kappa = \gamma_{\kappa 0}\begin{bmatrix} 1 & 2 & 3 \\ 1 & 2 & 3 \\ 1 & 2 & 3 \end{bmatrix} \qquad \gamma_\rho = \gamma_{\rho 0}\begin{bmatrix} 1 & 2 & 3 \\ 1 & 2 & 3 \\ 1 & 2 & 3 \end{bmatrix} \tag{5.36}$$

where $\gamma_{\kappa 0}$ and $\gamma_{\kappa 0}$ were equal to 0.04 and 0.0909, respectively. The normalization factor, ξ, was found to be dependent upon the previously mentioned parameters as well as the overall number of points in the Cartesian grid in Fourier space. The percentage ratio matrices comparing the normalized reconstruction, I, to the original object I_0 for γ_κ and γ_ρ imaging, respectively, where

$$PR_{\gamma_\kappa} = \begin{bmatrix} 98.1 & 96.9 & 92.0 \\ 99.4 & 100.0 & 95.9 \\ 97.9 & 96.6 & 91.8 \end{bmatrix} \qquad PR_{\gamma_\rho} = \begin{bmatrix} 91.7 & 97.2 & 90.7 \\ 100.7 & 100.0 & 96.1 \\ 91.7 & 97.2 & 90.7 \end{bmatrix} \tag{5.37}$$

There is evidently excellent agreement between the expected and reconstructed values. The average over all entries in PR_{γ_κ} and PR_{γ_ρ} were $97 \pm 3\%$ and $95 \pm 4\%$, respectively,

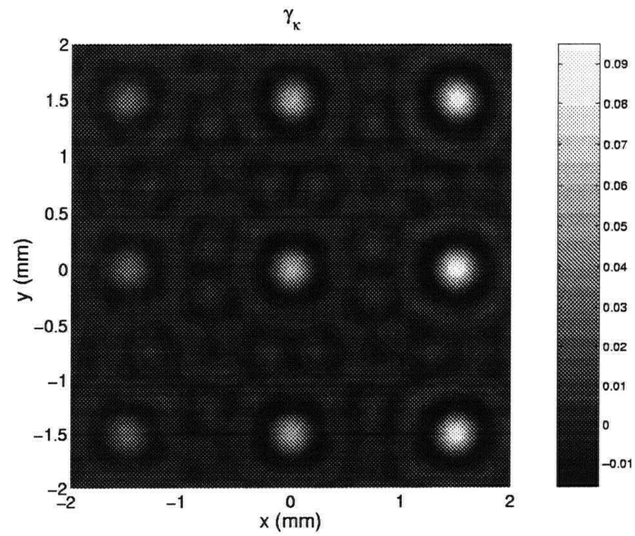

(A)

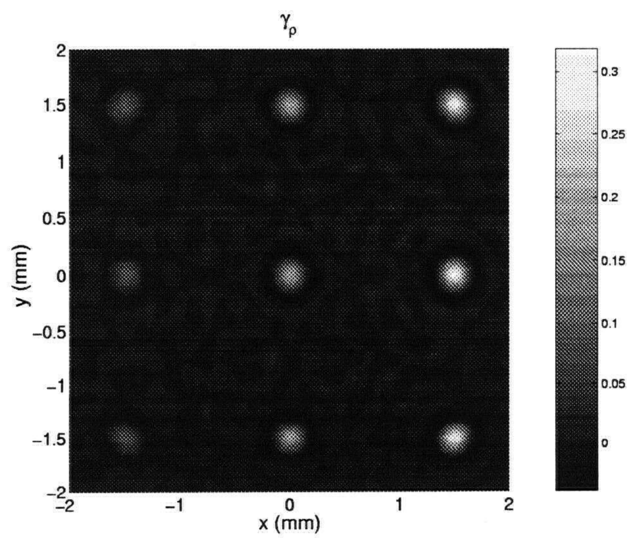

(B)

Figure 5.7: Figures A and B illustrate example reconstructions in which the resulting images are nearly scale copies of the original image.

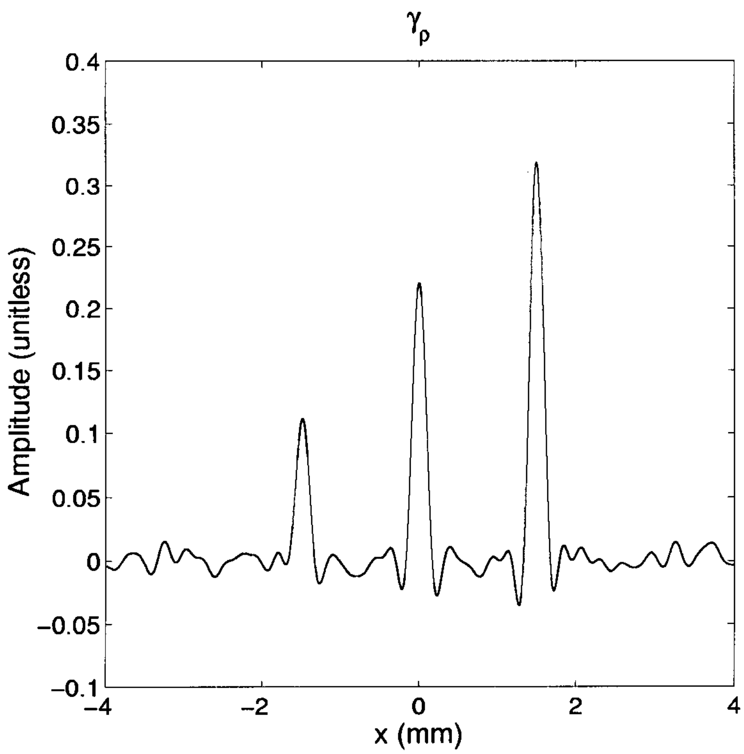

Figure 5.8: This figure illustrates the profile of γ_ρ along the x-axis.

indicating a relatively quantitative reconstruction algorithm for this object. Note, however, that some points in the reconstructions are not cylindrically symmetric, particularly in the γ_ρ image, due to the effect of scatterer location discussed in Section 5.3.2.

Figure 5.8 illustrates the profile of the reconstructed γ_ρ along the x-axis. The features of this profile are typical of all other profiles along the x and y axes in the γ_κ and γ_ρ images. Note that the value of the background pixels oscillates in the range of -0.011 to 0.008 and -0.03 to 0.02 for the γ_κ and γ_ρ images, respectively. The average FWHM of all the points in the γ_κ and γ_ρ images is 0.244 ± 0.004 mm and 0.192 ± 0.002 mm, respectively. Since the image resolution is expected to be 0.21 mm, the FWHM for γ_ρ is excellent in that it falls below this value, and the FWHM for γ_κ varies from theory by $\sim 16\%$.

5.3.1 The Effect of Filtering and Data Truncation

As discussed in Sections 2.2.8 and 2.2.7, the interpolation to a square grid necessitates a reduction of the data Nyquist frequency in order to increase the pixel size of the resulting image and ensure the reconstruction is practically computable. This can be accomplished either through sampling data at a higher frequency and subsequently truncating the data in frequency space, or by reducing the sampling frequency at the outset. These options in combination with different lowpass filter cutoffs were studied in simulation for γ_κ reconstruction. Together with use of a simulated Ricker wavelet source with ω_0 equal to 20 MHz, the following combinations of data processing approaches were investigated:

- **Case 1** - Apply LPF with $f_0 = 2.6$ MHz to data sampled at $f = 20$ MHz, with no need to truncate data.
- **Case 2** - Apply LPF with $f_0 = 9.0$ MHz to data sampled at $f = 20$ MHz, with no need to truncate data.
- **Case 3** - Apply LPF with $f_0 = 2.6$ MHz to data sampled at $f > 20$ MHz and truncate data at 11.3 MHz.
- **Case 4** - Apply LPF with $f_0 = 9.0$ MHz to data sampled at $f > 20$ MHz and truncate data at 11.3 MHz.

To test the relative performance of these options, the grid used in the simulations in Section 5.3, again with $\gamma_\kappa = 0.04$, was reconstructed subject to the above itemized circumstances. For Cases 1 and 2, the data were sampled at 20 MHz, whereas the sampling frequency was 75 MHz for the other two tests. There was always 100 views and a Ricker wavelet with ω_0 equal to 20 MHz was used. Upon normalization relative to the center point, the percentage ratio matrices of I relative to I_0 for Cases 1 through 4 were the following:

$$PR_1 = \begin{bmatrix} 93.3 & 96.9 & 93.9 \\ 96.0 & 100.0 & 97.2 \\ 93.3 & 96.9 & 93.9 \end{bmatrix} \qquad PR_2 = \begin{bmatrix} 42.4 & 59.7 & 43.9 \\ 55.9 & 100.0 & 61.0 \\ 42.4 & 59.6 & 43.9 \end{bmatrix} \tag{5.38}$$

$$PR_3 = \begin{bmatrix} 76.6 & 80.8 & 78.2 \\ 80.8 & 100.0 & 80.8 \\ 76.6 & 80.8 & 78.2 \end{bmatrix} \qquad PR_4 = \begin{bmatrix} 61.9 & 82.3 & 63.1 \\ 81.4 & 100.0 & 82.0 \\ 61.9 & 82.3 & 63.1 \end{bmatrix}$$

Evidently, the application of a lowpass filter with $f_0 = 2.6$ MHz with either truncated (Case 3) or non-truncated data (Case 1) yield the best results. However, the application of a LPF with $f_0 = 2.6$ MHz to data that have been sampled at 20 MHz (thus no need to truncate data) is best and affords a percentage ratio improvement of 16-22% throughout the image relative to Case 3 with a higher sampling frequency and truncation of data. Figures 5.9.A and 5.9.B illustrate the reconstructed γ_κ profiles along the x-axis for Case 1 and Case 3. Note that, for comparison purposes, the Case 1 image has been normalized to a sampling frequency of 75 MHz. Recall that this normalization was discussed in Section 5.3, and that it involves multiplying the image by a factor of $(\frac{20}{75})^2$.

Analysis of all the profiles indicates that the FWHM values for the peaks in Case 3 are not consistent, ranging from 0.206 mm at the center to 0.278 mm elsewhere. As discussed in Section 5.3, this is in comparison to the expected value of 0.21 mm given that a lowpass filter with $f_0 = 2.6$ MHz was applied. The FWHM values of all peaks in Case 1 had an average value of 0.271 ± 0.005 mm, which is off from the expected value by $\sim 29\%$.

5.3.2 The Effect of Scatterer Location

Given a particular source and detector distance equal to $|\mathbf{r}_j|$, computer simulations indicate that the reconstructed PSF for both γ_κ and γ_ρ imaging exhibits more error in

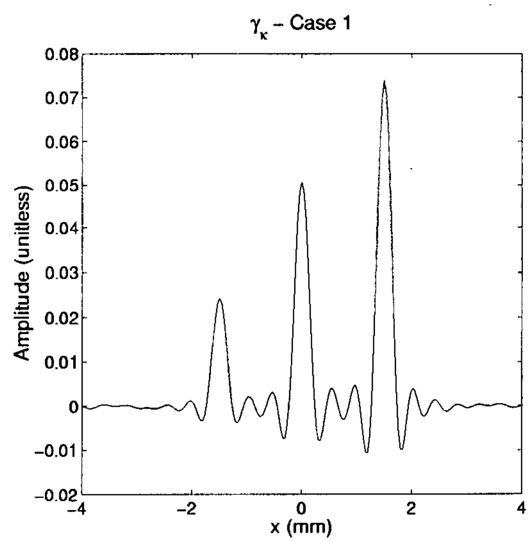

(A)

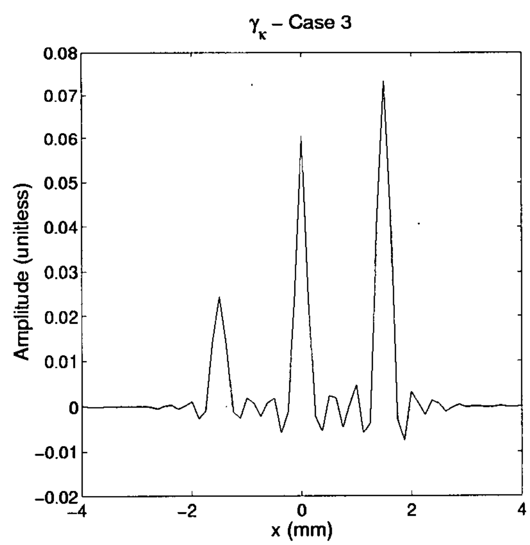

(B)

Figure 5.9: Figures A and B illustrate the reconstructed γ_κ profiles along the x-axis for Cases 1 and 3, respectively. Recall that the Fourier data for Case 3 has been truncated at a frequency of 3.4 MHz, while that for Case 1 has not been truncated and hence spans the range of 0-20 MHz.

terms of amplitude and lack of Gaussian shape as the location of the scatterer moves further from the origin. Also, for a given scatterer located at $\mathbf{r}$, the error in the PSF increases as $\frac{|\mathbf{r}|}{|\mathbf{r}_j|}$ increases. This is not surprising due to the approximations that were applied in the derivation of the reconstruction algorithm by Blackledge *et al.* Figure 5.10.A illustrates the γ_κ reconstruction for a point located at $(5, 5)$ mm, while Figures 5.10.B and 5.10.C illustrate the γ_κ reconstruction and corresponding x-axis profile for a point located at $(0, 0)$ mm, both with γ_κ equal to 0.04.

In both reconstructions, there were 100 views, the sampling frequency was 67.5 MHz, Fourier data were lowpass filtered with $f_0 = 9$ MHz, and data were truncated beyond 11.3 MHz to boost the image pixel size. The point at the origin has a uniform Gaussian-like PSF with an amplitude of $\sim 4.25 \times 10^{-3}$, while that at (5,5) mm has a hollow oval-shaped PSF with a maximum amplitude of only 5% that of the center point. The expected image resolution is 0.08 mm. The FWHM of the origin point is ~0.07 mm, which falls below the expected value. The ring of the point at (5,5) mm has large dimensions of approximately 0.4 mm $\times$ 0.8 mm. The halo effect in the shape of the PSF is expected from the TOF errors discussed in Section 5.1.3. For each view, scatter is being reconstructed further away from the source and detector than it should be, and the effect is the creation of a ring upon reconstruction of all views. The ring has a much lower amplitude than the point reconstruction should have in part because sound energy is being spread out over a larger area, as opposed to being concentrated into a point. However, most of the energy is being spread out along rays throughout the image that can be seen emanating from the scatterer location. This halo effect is a significant result that seriously limits the capabilities of this reconstruction algorithm. It will become evident, however, in the following section that this effect can be alleviated by the collection of data at a large number of views.

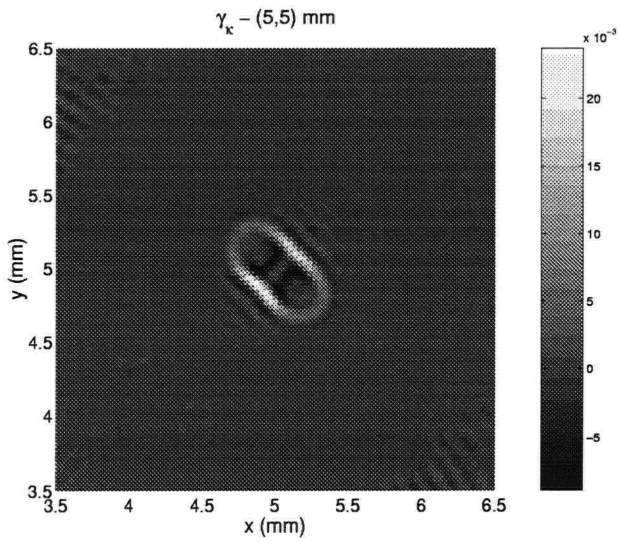

(A)

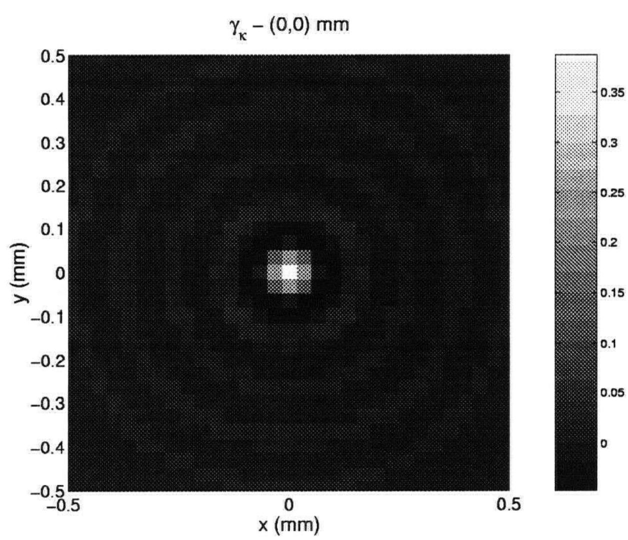

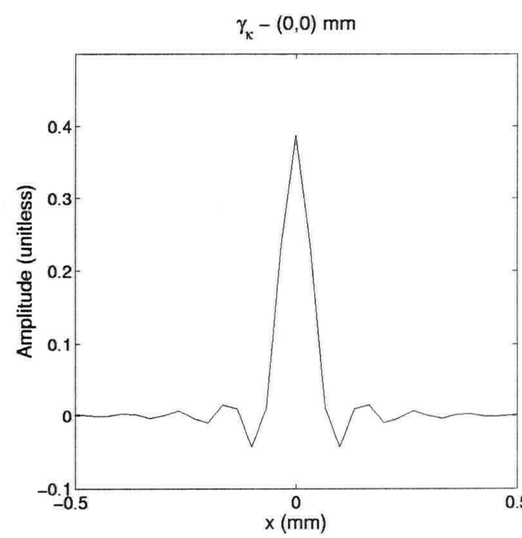

(B) (C)

Figure 5.10: This figure illustrates the effect of scatterer location on the reconstruction of γ_κ points. Figure A illustrates the result for a point located at (5,5) mm, while Figures B and C present the image and x-axis profile results for a point at (0,0) mm.

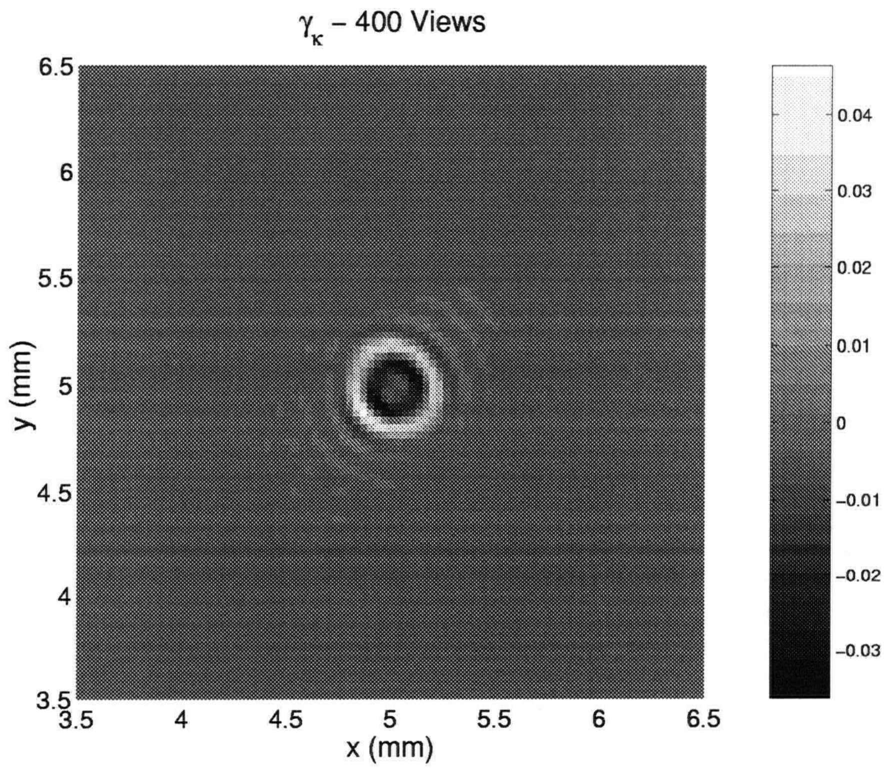

Figure 5.11: This figure illustrates the effect of the number of views on the reconstruction of γ_κ for a point located at (5,5) mm given 400 views of data. This is in comparison with Figure 5.10.A, which illustrates the same reconstruction with 100 views of data.

5.3.3 The Effect of the Number of Views

Section 2.3 described how each view at which data are recorded yields information along one direction through the image space. As the number of views increases, the object thus becomes more well-defined and the reconstructed image looks better. This effect can be seen in Figure 5.11 in which a point at (5, 5) mm with γ_κ equal to 0.04 is reconstructed with 400 views of data. The sampling frequency was 67.5 MHz, Fourier data were lowpass filtered at 9.0 MHz, and data in Fourier space were truncated at 11.3 MHz to boost the pixel size. Comparing this reconstruction to that in Figure 5.10.A, which was based on only 100 views of data, the effect of increasing N_v is dramatic. The halo becomes more tightly bound and cylindrically symmetric, and the amplitude of the PSF increases by a factor of 2.5. However, the maximum γ_κ amplitude is still only 12% of that for the point at (0,0) mm, due to the effect of scatterer location discussed in Section 5.3.2.

The change in maximum pixel amplitude in the previous example appears to result due to the misplaced location of reconstructed sound energy discussed in the previous section. This effect is not seen for a point at the origin, for which sound energy is not misplaced in the reconstructed image. The number of views was also set to 400, and γ_κ was again reconstructed for a point located at (0,0) mm with γ_κ equal to 0.04. The result was nearly identical to that for 100 views, shown in Figures 5.10.B and 5.10.C, and as such is not illustrated here. The power sum residual comparing the two images was negligible at 0.001%. Given that sound energy is being reconstructed in the proper location, it makes intuitive sense that the image amplitude does not depend upon the number of views. An increase in N_v simply defines the Fourier data of the image along additional radial lines. This does not increase the intensity in the Fourier domain of the image, but simply makes the space better defined. Due to the linear nature of the Fourier Transform, then, the intensity in the image does not increase either.

5.3.4 The Effect of Cartesian Grid Size in Fourier Space

The method by Blackledge *et al* has at its heart an interpolation from a radial grid to a Cartesian grid in the Fourier domain of the image, after which the data are operated on by the inverse FFT to yield an image. The pixel size in the x and y dimensions in the reconstructed image is inversely dependent upon the maximum values of u and v in the radial grid in Fourier space. The pixel size is thus obviously constant regardless of the fineness of the Cartesian Fourier grid. However, as more points are added to the Cartesian grid along the u and v dimensions, more points are added to the reconstructed image along the x and y dimensions, respectively.

As discussed in Section 2.2.7, the spacing of points in the Fourier domain should technically be not less than the largest distance between any two points on the radial grid. This is termed the optimal grid spacing. However, achieving the optimal grid spacing leads to some data requirements that are difficult to satisfy at the development stage. For instance, in order to reconstruct a square image of only 75 mm with an insonifying source that has a cutoff frequency of 5 MHz, there must be 6400 views of data. The corresponding optimal Cartesian Fourier grid has 720×720 points. Interpolating from a radial grid with 6400 rays to a Cartesian grid of this size is out of the question at the development stage however. The Matlab^{TM} interpolation is highly intensive in terms of memory and CPU time when performed inside the Matlab^{TM} workspace. For instance, the processing required for a typical simulation with 100 views of data and a 800×800 grid can take well over 24 hours to complete due to the interpolation. In a future version of the prototype system, the interpolation processing could likely be embedded in a dedicated electronics unit that would be orders of magnitude faster.

Due to these limitations, in this thesis work the spacing in the Cartesian Fourier space grid has generally been selected to be less than the optimal value. This choice has led to quite satisfactory results. To illustrate, Figures 5.12.A and 5.12.B present the results of a γ_κ image reconstruction for a point at the origin with γ_κ equal to 0.04 in which the number of pixels was optimal at 100×100 (A) and in which it was increased to 400×400 (B). In both reconstructions, the sampling frequency was 67.5 MHz, the number of views was 50, and data in Fourier space were not truncated. Evidently, there is excellent agreement between the two images, and it is thus not expected that the Cartesian grid size is an important factor in the image reconstruction. Upon interpolating the 400×400 image to a 100×100 grid, the power sum residual comparing the two images was negligible at 0.06%.

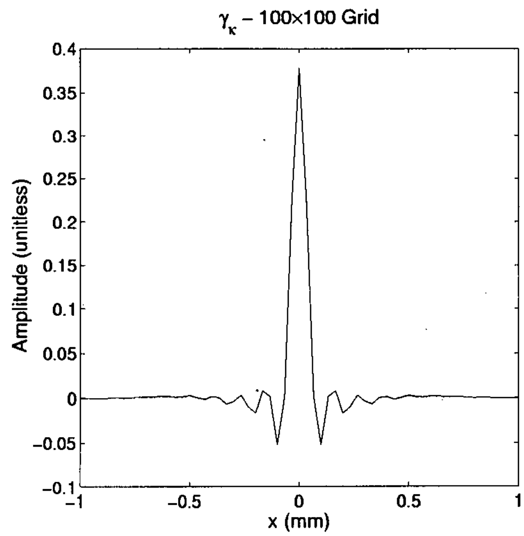

(A)

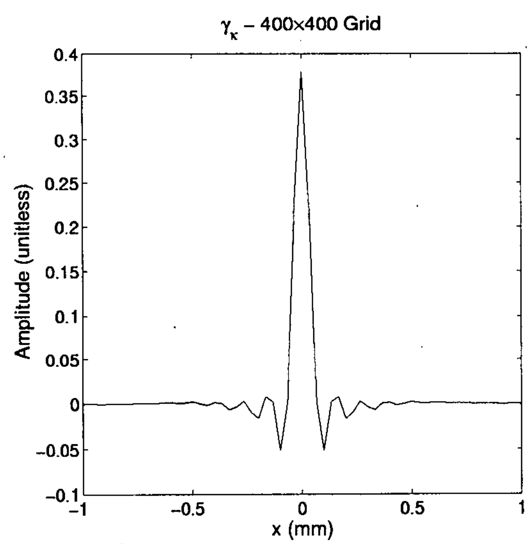

(B)

Figure 5.12: Figures A and B illustrate the reconstruction of γ_κ with Cartesian grid sizes in Fourier space of 100×100 and 400×400, respectively.

5.3.5 The Effect of Sample Rate

The image normalization factor, ξ, was found to be constant with frequency for γ_κ, R, and γ_ρ imaging. In testing this, all three types of reconstructions were performed for an isolated scatter point located at the origin. In each simulation, γ_κ and γ_ρ were equal to 0.04 and 0.0909, respectively. A Ricker wavelet with ω_0 equal to 20 MHz was used with a subsequent 9.0 MHz lowpass filter. Data were truncated in Fourier space at 11.3 MHz to boost the pixel size. 100 views of data were simulated for each reconstruction, and simulations were performed at several frequencies between 30 and 75 MHz. In order to properly compare the images with different sampling frequencies, they were all normalized to a sampling frequency of 75 MHz. Recall that this normalization was discussed in Section 5.3, and that it involves multiplying each image by a factor of $(\frac{f_{s1}}{75})^2$, where f_{s1} is the data sampling frequency corresponding to the image under consideration.

Figure 5.13.A illustrates ξ as a function of frequency for the non-normalized γ_κ, γ_ρ, and R images. The average values of ξ are as follows:

$$\begin{aligned} \xi_{\gamma_\kappa} &= 7.87 \pm 0.01 \\ \xi_{\gamma_\rho} &= 15.78 \pm 0.04 \\ \xi_R &= 12.29 \pm 0.03 \end{aligned} \tag{5.39}$$

Evidently, upon proper normalization, ξ is constant for every type of imaging.

5.3.6 The Effect of Dispersion

As discussed in Section 1.6, the speed of sound in water and tissue is dependent upon frequency. Although the change in acoustic velocity is less than 0.5% over 1-20 MHz, analysis indicates that this results in significant changes in the shape of the pulse and the corresponding Fourier spectrum [43]. Figures 5.14.A and 5.14.B illustrate the effect of dispersion on the shape of the pulse scattered from a point at the origin, when the source and detector are located at a distance of 60 mm and 200 mm from the origin,

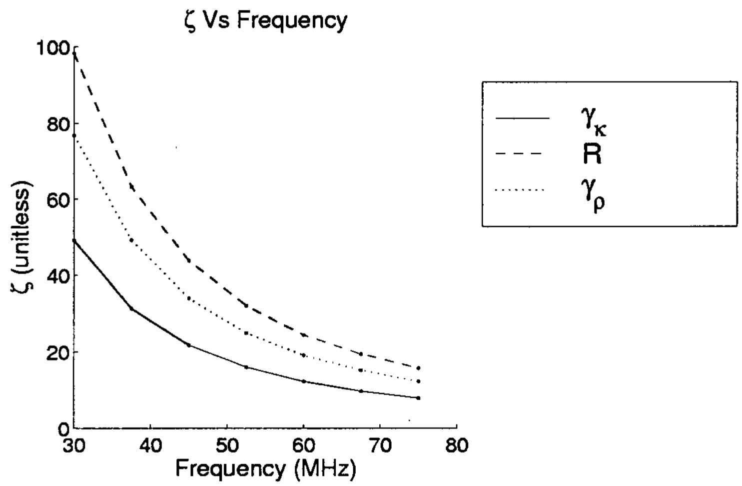

(A)

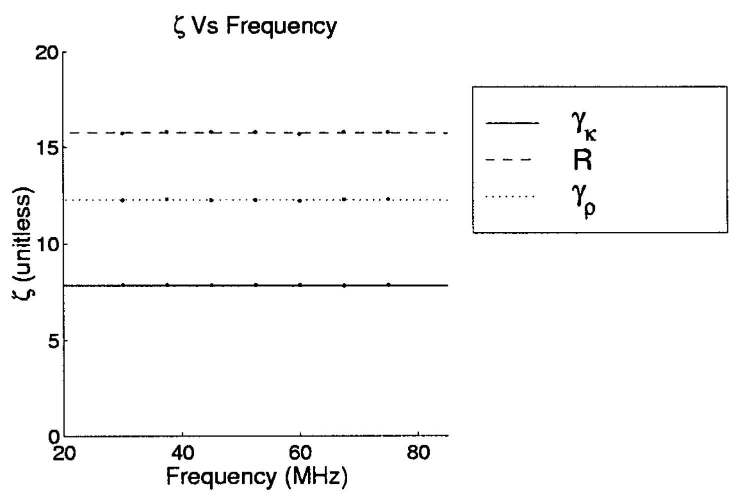

(B)

Figure 5.13: Figure A plots the frequency dependence of ξ for the non-normalized γ_κ, R, and γ_ρ images, while Figure B illustrates the same results for images which have been normalized to a common sampling frequency of 75 MHz.

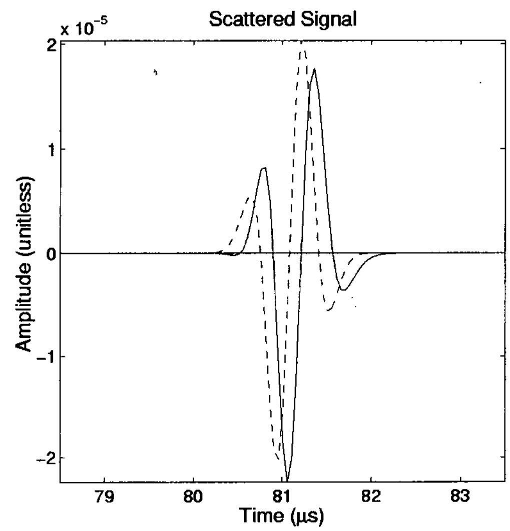

(A)

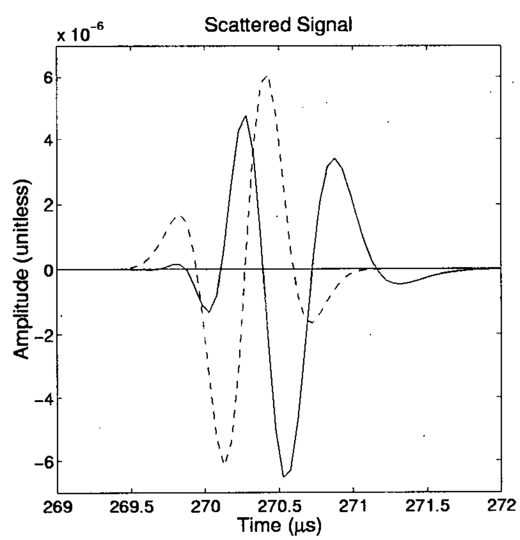

(B)

Figure 5.14: Figures A and B illustrate the effect of 1% dispersion over the frequency range of 1-20 MHz on the shape of a pulse scattered from a point at the origin. In A and B the source and detector were situated at a distance of 60 mm and 200 mm from the origin, respectively. The solid and dashed lines illustrate the pulses in the absence and presence of dispersion, respectively.

respectively. Evidently, the effect worsens as the propagation distance increases.

If dispersion is not corrected for in the reconstruction algorithm, it has the effect of creating dramatic halos and interference patterns due to the misplacement of ultrasound energy during the image reconstruction process. Figure 5.15 illustrates this effect. Figure A shows the PSF in the absence of dispersion for a point located at (3, 3) mm with γ_κ equal to 0.04. Data were sampled at 67.5 MHz, and a low $N_v = 50$ was chosen, which explains the poor shape of the PSF. However, since the halo effect is likely unavoidable at larger distances with this algorithm even for N_v on the order of a few hundred, useful information can be gained by starting with a PSF of this shape. Figure 5.15.B illustrates the effect in the presence of 1% dispersion over 1-20 MHz, with an f^2 dependence. This dependence was chosen for educational purposes only, on the premise that more complicated functions of frequency may be more difficult to correct for. Little has been done to date towards the experimental characterization of ultrasound dispersion in water and tissue. The halo and interference pattern effect is extreme and completely destroys the PSF. Sound energy that was in the PSF is spread along curved rays throughout the image. This is due to the destruction of valid phase information in the modelling of the scattered ultrasound field. Evidently then, even this small percentage dispersion can not be neglected in ultrasound computed tomography. Figure 5.15.C illustrates the γ_κ image based on the same dispersive data, although this time the dependence upon frequency was included in the tomography algorithm and thus corrected for. This approach restored the point-spread-function to a reasonably good extent, with very little change in the shape of the function. The minimum and maximum values in the image did change in going from the case of no dispersion to that of dispersion correction, with minima of -0.017 and -0.022, respectively, and maxima of 0.053 and 0.055, respectively. As such, the percentage changes in the reconstructed γ_κ minimum, maximum and range were 26%, 4% and 9%, respectively. It thus appears that UCT data can be corrected to yield useful reconstructions if the functional dependence of acoustic velocity upon frequency

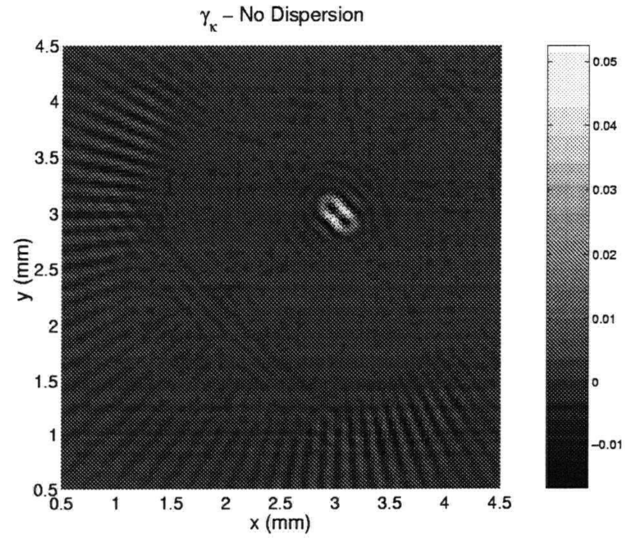

(A)

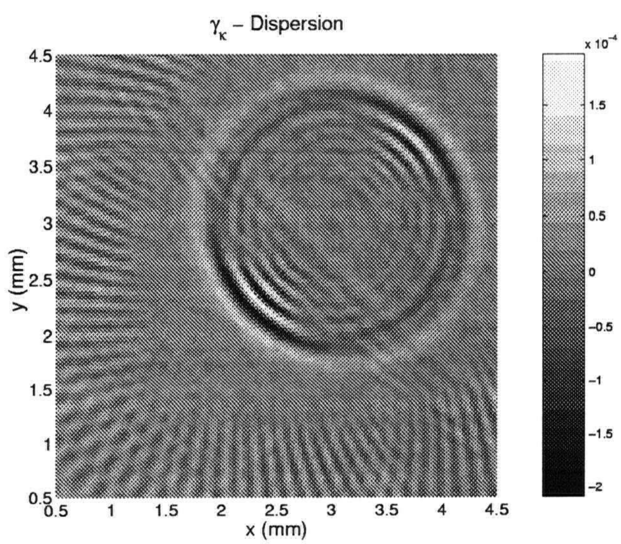

(B)

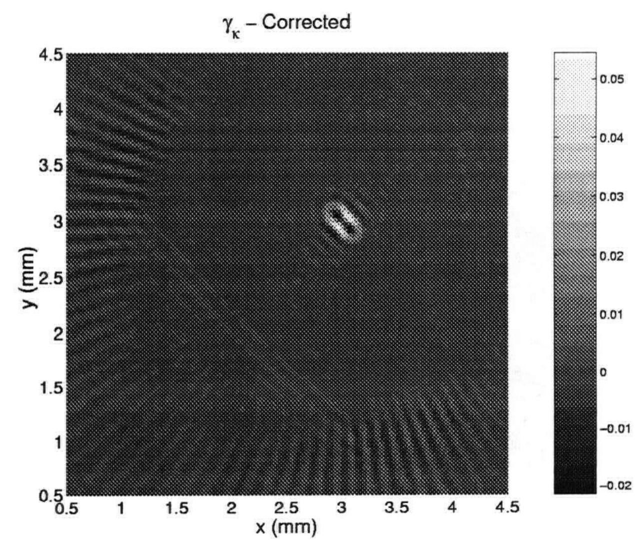

(C)

Figure 5.15: Figures A and B illustrate the γ_κ reconstructions for the scattering object given the absence and presence of dispersion, respectively, while Figure C illustrates the same reconstruction based on corrected data.

is known. The power sum residual comparing the two images is 22%.

5.3.7 Reconstruction of a Square Block

Thus far reconstructions of γ_κ and γ_ρ have been shown only for points that are infinitesimal with respect to the wavelengths in the insonifying ultrasound pulse. This section presents results for the reconstruction of γ_κ and γ_ρ for a square block in order to further examine the capabilities and limitations of the algorithm by Blackledge *et al*, subject to its underlying assumptions. The block had a width of 1.85 mm, a uniform γ_κ equal to 0.04, and a uniform γ_ρ equal to 0.0909. Insonification was simulated with a Ricker wavelet that had ω_0 equal to 6 MHz. A LPF was applied with a cutoff frequency of 2.6 MHz, and Fourier data were truncated at 3.4 MHz to boost the pixel size. These images were based on 100 views of data sampled at 30 MHz. This sampling frequency would preclude a point spacing of 0.05 mm in the scatter simulation procedure, but to reduce the computation time, this was increased to 0.074 mm. Figures 5.16.A and 5.16.B illustrate the reconstructed γ_κ image and its corresponding x-axis profile, while Figures 5.17.A and 5.17.B illustrate the same for γ_ρ. Note that the profiles have been normalized and are plotted with the normalized profiles of the original object. The square block is reasonably well defined in all dimensions in both the γ_κ and γ_ρ images. Aside from a higher amplitude edge, the pixels on the top of the block are relatively uniform. Those within a radius of 0.9 mm have an average amplitude of 1.4 ± 0.1 in the γ_κ image, while the corresponding pixels in the γ_ρ image have an average amplitude of 3.1 ± 0.2. Beyond the object past a radius of 1.3 mm, γ_κ oscillates with an average value of -0.03 ± 0.04, while γ_ρ oscillates with an average value of -0.06 ± 0.06. The FWHM measured at heights in the range of 0.5-0.55 on the normalized γ_κ profile is 1.85 ± 0.01 mm, which is the width of the original object. Similarly, the FWHM measured at heights in the range of 0.5-0.53 on the normalized γ_ρ profile is again 1.85 ± 0.01 mm. Note that the maximum amplitudes in the reconstructions are quite high relative to previous examples

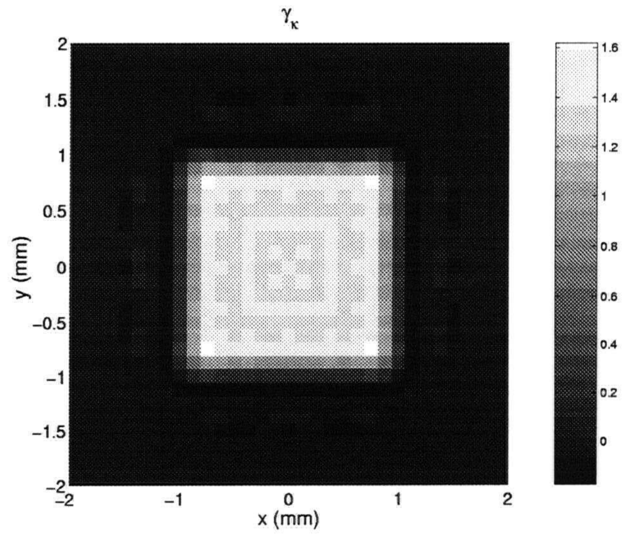

(A)

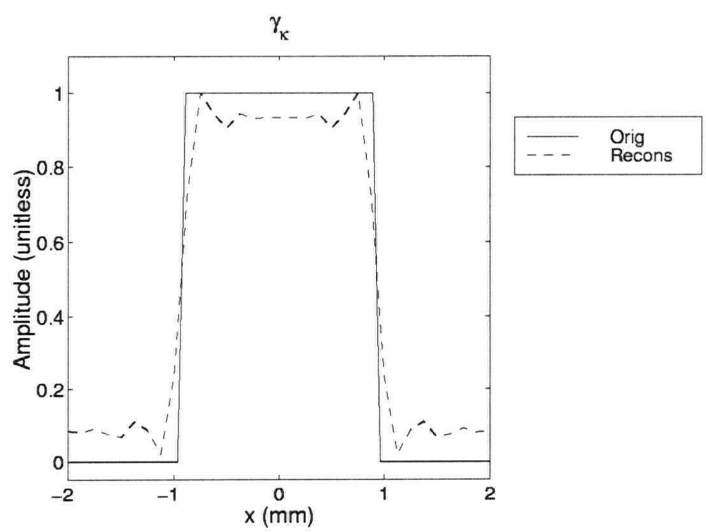

(B)

Figure 5.16: Figures A and B illustrate the resulting γ_κ image and x-axis profile, respectively, of a square block. Note that the profile has been normalized and is plotted with the normalized profile of the original object.

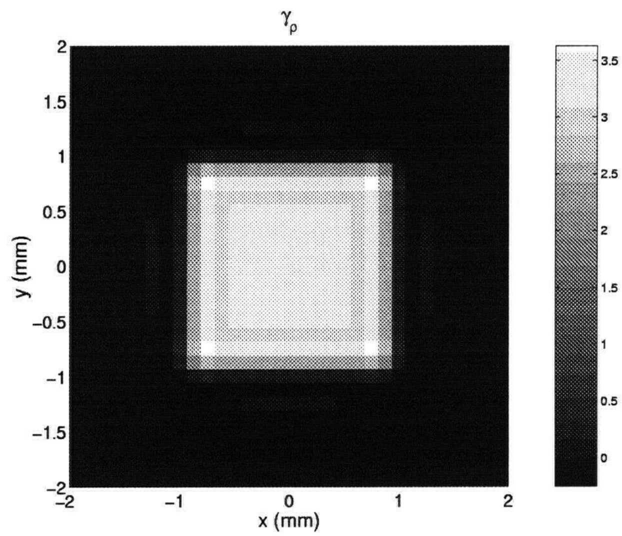

(A)

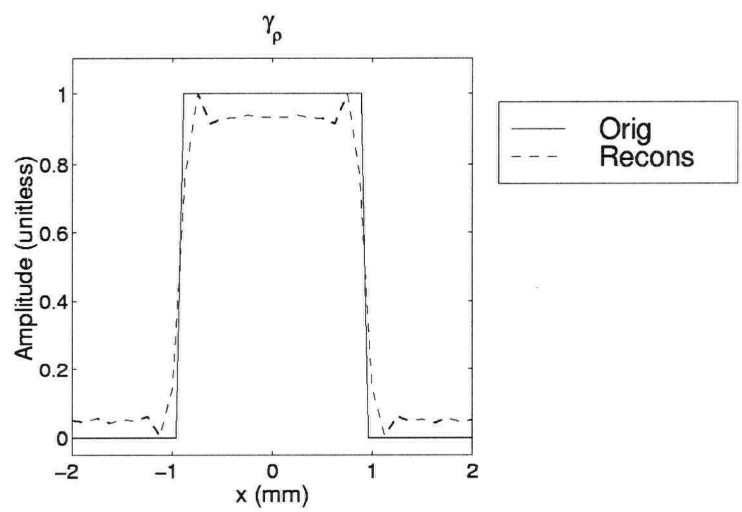

(B)

Figure 5.17: Figures A and B illustrate the resulting γ_ρ image and x-axis profile, respectively, of a square block. Note that the profile has been normalized and is plotted with the normalized profile of the original object.

due to the relatively large size of the element of area associated with each scatter point. If the images were normalized to a sampling frequency of 75 MHz, the maximum pixel amplitudes for γ_κ and γ_ρ would become 0.11 and 0.25, respectively, which is on the order of previous grid results.

5.4 Effect of Attenuation and the Approximate Correction

Figure 5.18 illustrates the effect of attenuation on the reconstruction of γ_κ for a single point located at (0, 0) mm in a cylindrical tissue. The point was characterized by γ_κ equal to 0.04, and it was centered inside a tissue with a radius of 20 mm. The source and detector were located at a distance of 100 mm from the origin. The Ricker wavelet had ω_0 equal to 20 MHz, and the sampling frequency was 67.5 MHz. The data were processed with a Butterworth LPF of order 20 with a cutoff of 9 MHz, and there were 80 views. Data were truncated at 11.3 MHz in order to boost the pixel size. As such, the image resolution was expected to be 0.08 mm. Figure 5.18 plots the γ_κ profile along the x-axis both in the absence and presence of attenuation in tissue and water. The profile along the y-axis was identical. As expected, attenuation reduced the amplitude of the point-spread-function significantly by 32%. The FWHM was 0.078 ± 0.002 mm and 0.098 ± 0.002 mm in the absence and presence of attenuation, respectively. Also, note that the ratio of the FWHM height to width is ~8:1 in the absence of attenuation and ~2:1 in the presence of attenuation. This pattern can be explained by the "beam hardening" that occurs due to attenuation. Water and tissue attenuate ultrasound in a stronger manner as frequency increases, shifting the insonifying pulse spectrum such that there is relatively more energy in the lower frequency range. This in turn translates into a "rounding" of the point-spread-function.

In analyzing the effect of attenuation, real world objects must be modeled. The reconstruction algorithm must be tested in simulation on tissues made of scatterers that experience widely different effects, depending upon the source and detector locations. As

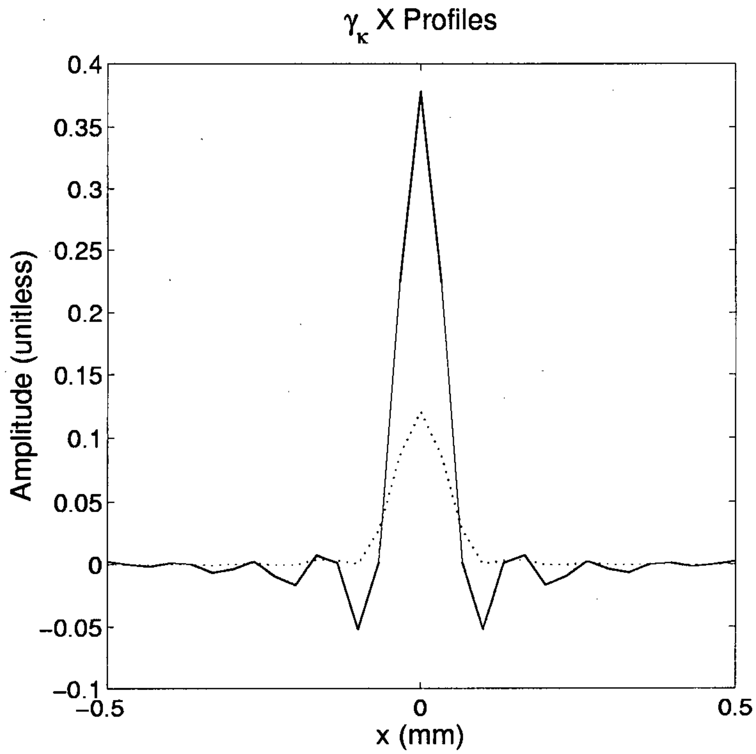

Figure 5.18: This figure illustrates the effect of attenuation in tissue and water on the reconstruction of γ_κ for a single scatter point located at (0, 0) mm. Shown are the x-axis profiles for γ_κ in both the absence (solid line) and presence (dotted line) of attenuation.

such, tissues with widths on the order of 60-80 mm must be reconstructed. This could potentially be accomplished if the Nyquist frequency is reduced to $\sim$2 MHz through the truncation of data in Fourier space, and if additionally the Cartesian grid has on the order of 900$\times$900 points. However, the number of views would necessarily be on the order of several hundred to ensure that the PSF energy for points with large $|\mathbf{r}|$ is not spread out along rays throughout the image. The computing required for this type of reconstruction is presently not available in the prototype scanner. In addition, points with large $|\mathbf{r}|$ would exhibit a halo effect, and the influence of attenuation on PSF shape would be difficult to discern.

To facilitate testing for the effect of attenuation as well as the capabilities of the approximate attenuation correction described in Section 4.1, an upward scaling in attenuation magnitude was applied to the scattering system. In this manner, distances in the image can be kept to a minimum for ease of reconstruction, and the expected point-spread-functions are Gaussian-like in shape for ease of analysis. As such, the magnitude of attenuation in tissue was scaled up by a factor of 1000; attenuation in water was not scaled. As in Section 4.1, a test was done to determine the optimal form of the approximate attenuation correction for this situation. Errors in the scatter amplitudes for small tissue sizes on the order of 1 mm were found to be minimized with an approximate attenuation correction coefficient given by $1/C$, where

$$C = 10^{-(1000\,\chi_t)\,(0.45\,\overline{d}_t)\,k} \times 10^{-\chi_w\,(6\,\overline{d}_w)\,k^2} \tag{5.40}$$

χ_t and χ_w are defined according to Equations 2.64 and 2.66 in Section 2.4, and χ_t has a multiplier of 1000 due to the upward scaling of attenuation in tissue. The $\overline{d}_t$ and $\overline{d}_w$ multipliers have the same order of magnitude as those for the case of realistic attenuation in tissue.

Figure 5.19 illustrates the reconstructed γ_κ image in the absence of attenuation for a grid of 9 closely spaced but isolated points of equal amplitude. The number of views was 50, the sampling frequency was 60, and there was no truncation of data in Fourier space. The data were processed with a Butterworth LPF of order 20 with a cutoff of 9 MHz. Note that the point-spread-functions are all well-defined with FWHM's of ~ 0.07 mm, whereas the expected image resolution is 0.08 mm for data with a band limit frequency of ~ 9 MHz. Figure 5.20.A illustrates the same grid of points reconstructed in the presence of the scaled attenuation. The effect is dramatic, with all but 4 outside points disappearing from the image. In addition, the remaining points no longer have cylindrically symmetric PSF's, but the FWHM values of these PSF's changed very little. The amplitudes of these remaining PSF's were reduced to one half their original value. Figure

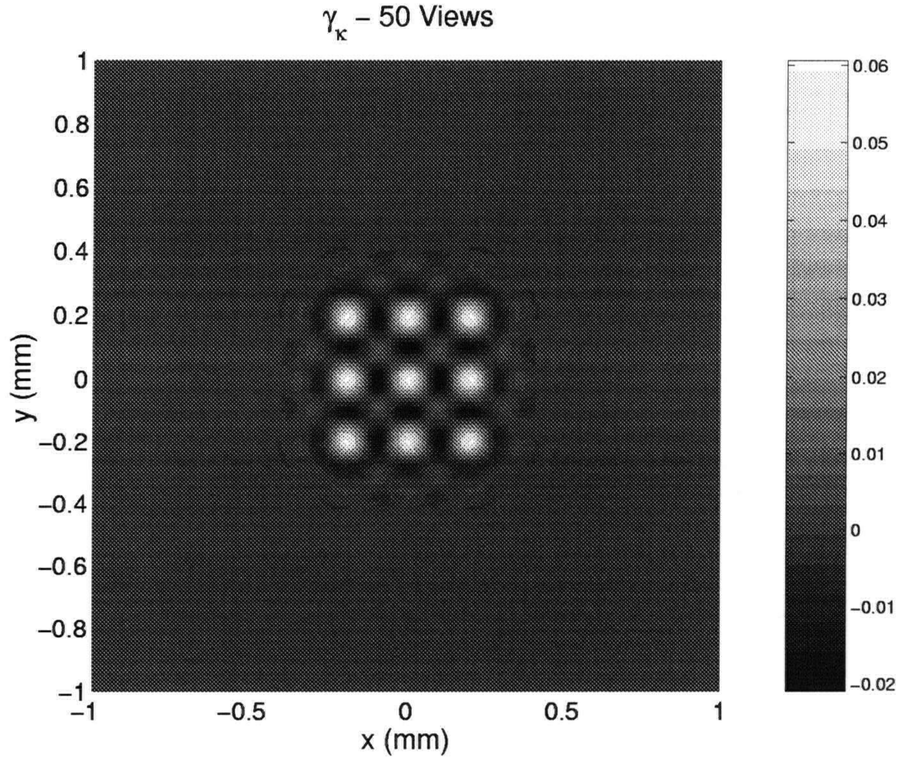

Figure 5.19: This figure illustrates the original grid of points for which γ_κ was reconstructed in the absence of attenuation.

5.20.B illustrates the same grid of points reconstructed with data corrected according to Equation 5.40. Unfortunately the missing points did not reappear. Instead, a distinctive interference pattern appeared, and the remaining points were severely overcompensated to over 40 times their original value. Their FWHM values were also reduced. Evidently, then, it appears as though the approximate attenuation correction can not be applied to ultrasound computed tomography.

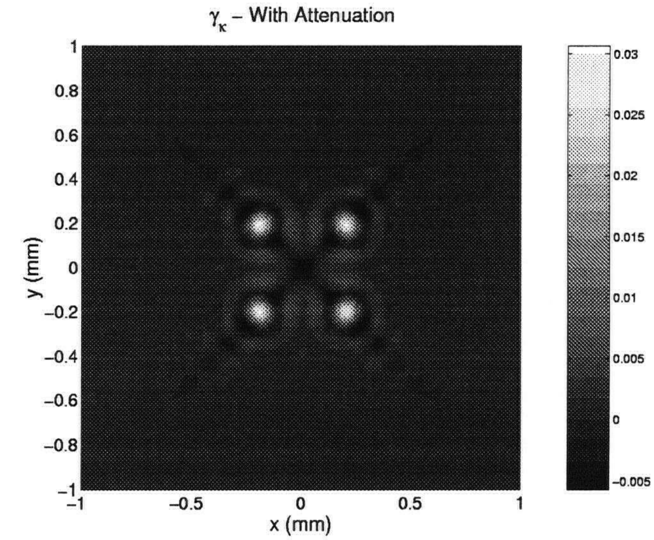

(A)

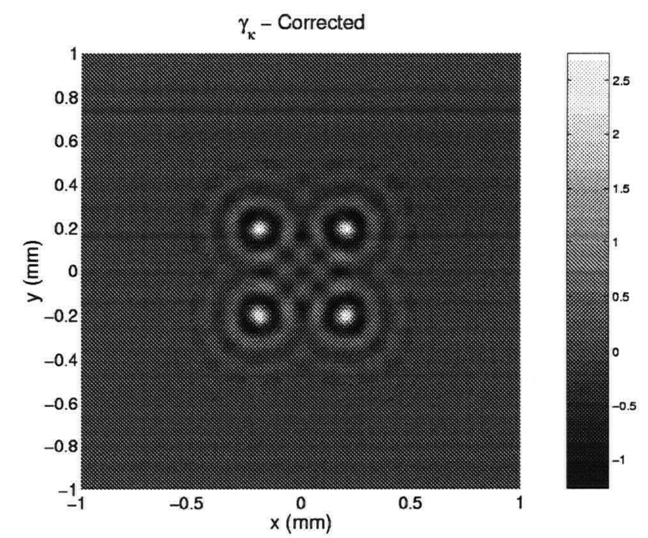

(B)

Figure 5.20: Figure A illustrates the effect of scaled attenuation in tissue and realistic attenuation in water on the reconstruction of γ_κ for the grid of points in Figure 5.19. Figure B illustrates the image for the grid based on scatter data that have been corrected for attenuation in tissue and water using the approximate attenuation coefficient defined in Equation 5.40.

5.5 Comparison of Fourier and Wavelet Denoising Methods

Preliminary tests of the moving average filter and several wavelet denoising methods have been done in simulation. Recall that the nature of the noise in pulsed UCT data was analyzed in Section 4.3.1. The unprocessed signal was shown to have primarily zero-mean Gaussian white noise, which lends itself to removal via wavelet denoising techniques. It was also shown that data which have been lowpass filtered beyond the source spectrum is often also zero-mean Gaussian and white for the most part. In cases where a low frequency band clutters the signal, subsequent high pass filtering was shown to render a signal with zero-mean Gaussian white noise. As such, wavelet processing can be applied at any stage of signal processing. In order to test both Fourier based and wavelet based denoising techniques, a data signal was simulated that represented scatter from an infinitesimal point located at (0, 0) mm. The insonifying Ricker wavelet had ω_0 equal to 20 MHz, and the sampling frequency was always 75 MHz. There were 100 views of data. Using the "randn" function in the Matlab^{TM} programming environment, Gaussian white noise was added to the data such that the SNR was equal to 35 db. A different noise vector was added to each view so that noise was not correlated. Figure 5.21 illustrates a closeup of the pulse region in the noiseless signal and a noisy signal from one angle, respectively.

As discussed in Section 4.5.3, this study adopted the relatively smooth Symlet 8 and Daubechies 9 mother wavelets, which were illustrated in Figure 4.10. Note that the Ricker wavelet was not used as a mother wavelet because this would have involved the custom creation of a wavelet family, which was beyond the scope of this thesis. Soft thresholding was always used, and results presented here are for the "huersure" threshold selection rule, which yielded slightly better results than the other methods. All three noise rescaling models (options "one", "sln" and "mln") were tested, and there was no discernible difference in the results. The denoised signal for a given mother wavelet was identical for resolution levels 1, 2 and 3. The denoised pulse result for level 4,

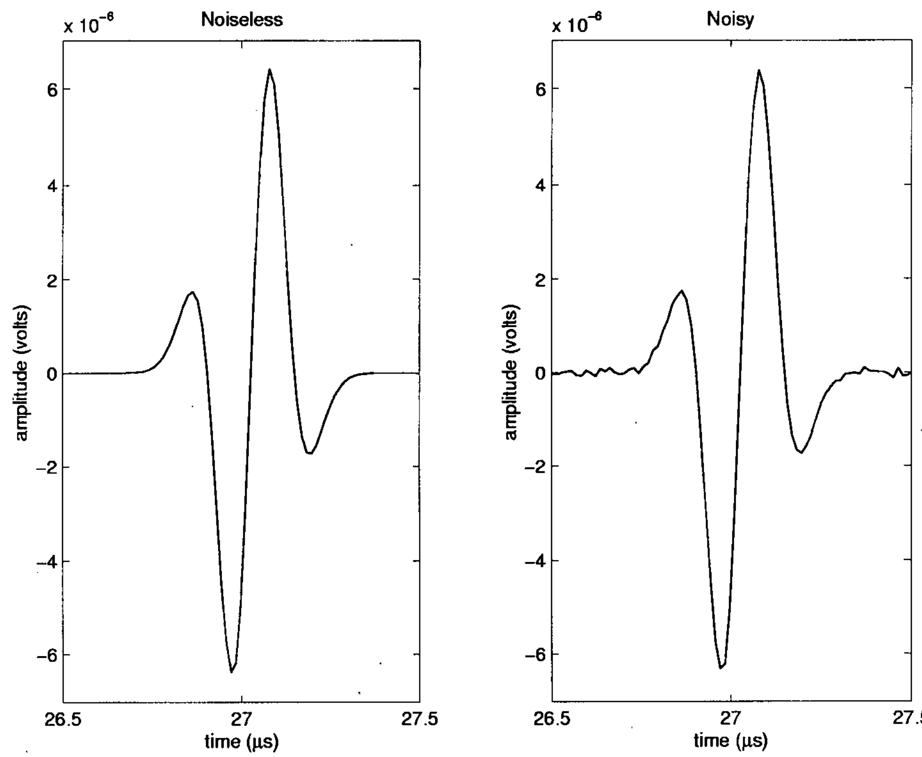

Figure 5.21: This figure zooms in on the region around the data pulse in the noiseless and noisy signals, respectively.

however, had an amplitude that was only about 25% that in the original data. Results for resolution level 1 are presented in this thesis. The denoised signal using the Symlet 8 wavelet family is illustrated in Figure 5.22. Evidently, the result is somewhat choppy even though smooth mother wavelets were chosen. Also shown is the wavelet denoised signal after it has been smoothed with a 5 point moving average filter. The result is very similar to the noiseless data. The following subsections will illustrate when this smoothing operation is necessary. The difference between the denoised signals for the Daubechies 9 and Symlet 8 families is very subtle, and in fact there is often a zero residual between the results of the two approaches for a given view. As such, the Daubechies 9

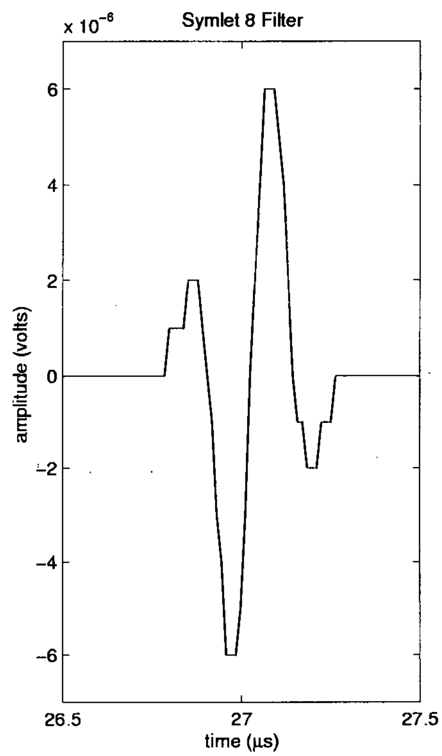

Figure 5.22: Figures A and B illustrate the denoised signal given filtering with the Symlet 8 and Daubechies 9 families, respectively, both with (right) and without (left) subsequent smoothing.

denoised signal is not shown.

5.5.1 Reconstruction with Noise-free and Noisy Data

Figure 5.23 illustrates the x-axis profiles for γ_κ reconstructions using both noise-free and noisy data. Figure A presents the noise-free case, while Figures B through C illustrate noisy reconstructions given lowpass filter cutoff frequencies of 9.0, 6.6 and 2.6 MHz, respectively. Recall that a LPF with f_0 = 9.0 MHz is nominal for the Ricker wavelet used in this simulation. Figure B indicates that nominal lowpass filtering is not

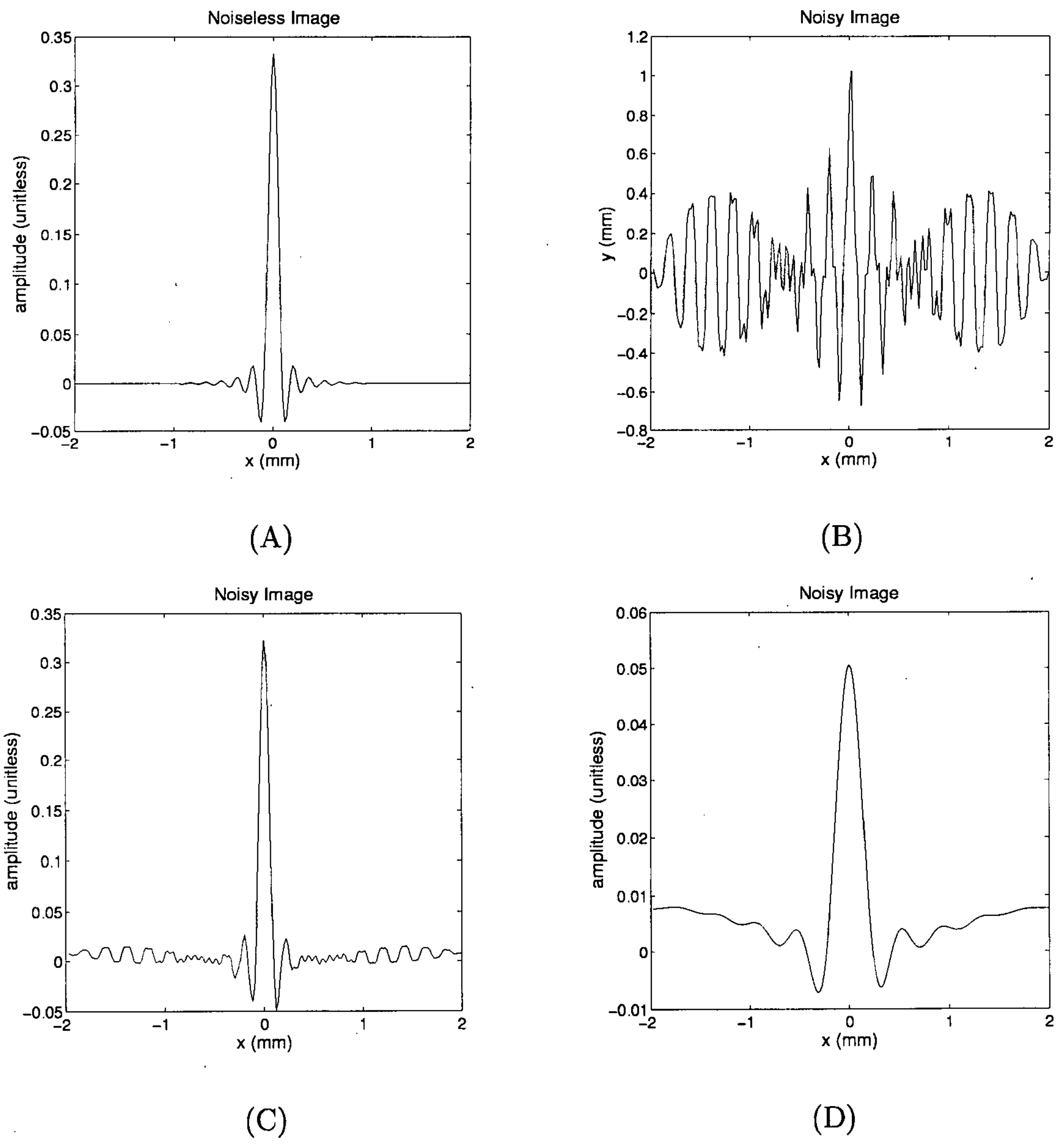

Figure 5.23: Figure A illustrates the x-axis profile of the γ_κ reconstruction in this simulation for noise-free data. Figures B through D present the x-axis profiles for noisy data with a SNR = 35 db, subject to lowpass filtering with f_0 = 9.0, 6.6 and 2.6 MHz, respectively.

feasible with noisy data. The reconstruction based on data with a slightly lower cutoff of 6.6 MHz was able to recover the shape and amplitude of the main peak, although the background is still very noisy. Filtering with a very low cutoff of 2.6 MHz broadened the peak as expected and increased the peak amplitude. It also produced a background amplitude that increases with distance from the origin, when in fact it should be relatively flat. Evidently then, even data that look reasonably good with a relatively low SNR of 35 db can not produce useful images regardless of the Butterworth filtering that is applied.

5.5.2 Preliminary Results of Noise Filtering

Narrower Bandwidth Data

Preliminary tests have been done to determine the effect of noise filtering on narrower bandwidth noisy UCT data. Data were denoised and then processed with a LPF with $f_0 = 2.6$ MHz, rather than the nominal 9.0 MHz. γ_κ image reconstruction was compared for data filtered with a 5 point moving average filter and the Daubechies 9 wavelet family. Filtering with the Symlet 8 wavelet has not been presented because the result overlaps with that of the Daubechies 9 family at this graph magnification. The images were normalized to the range 0-1, as was the image produced with noiseless data processed with the same LPF. The normalized x-axis profiles are illustrated in Figure 5.24. The result for the moving average filter is for all intents and purposes identical to that with no denoising at all, shown in Figure 5.23.D, with a corresponding power sum residual between the two images of only 0.005%. Thus the moving average filter does not afford any quality improvement. Image power sum residuals for various filtering tests (compared to images based on noiseless data) are tabulated in Table 5.4. Evidently, the Daubechies 9 wavelet family does an excellent job of denoising this low frequency data, even without prior smoothing. This indicates that the choppy features of the denoised data correspond to Fourier data above 2.6 MHz.

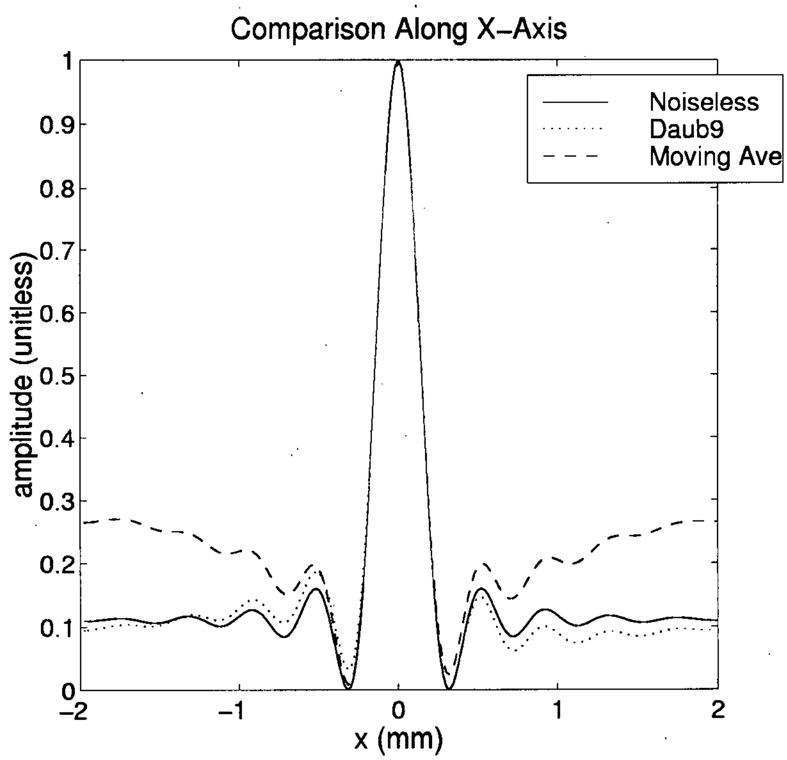

Figure 5.24: This figure compares the x-axis profiles for γ_κ reconstructions based on noise-free data as well as data filtered with the Daubechies 9 wavelet family and a 5 point moving average filter. In all cases a lowpass filter was applied with $f_0 = 2.6$ MHz, and the resulting images were normalized to the range of 0-1.

Wider Bandwidth Data

If the reconstruction of wavelet filtered data in the higher frequency range in desired, data smoothing is necessary due to the choppy features that result from the filtering process. This is illustrated in Figures 5.25.A-B and 5.25.C-D, in which lowpass filters were applied with f_0 equal to 6.6 and 9.0 MHz, respectively. Figures A and C present the non-normalized γ_κ x-axis profile for the non-smoothed data. Figures B and D compare the normalized profiles based on noise-free data and those which have been Symlet 8

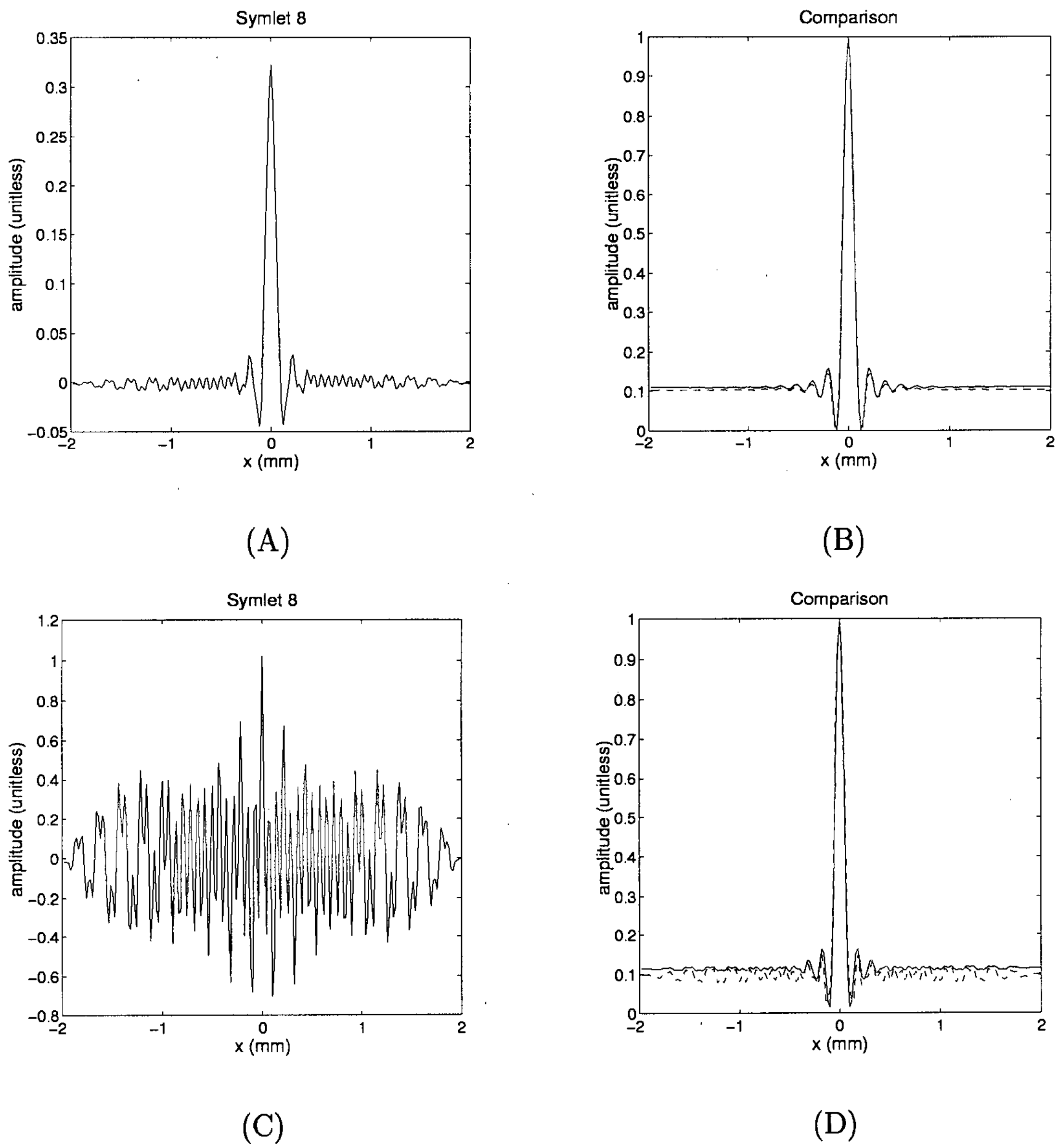

Figure 5.25: These figures illustrate the effect on γ_κ reconstruction that is afforded by smoothing Symlet 8 filtered data. Figures A and C illustrate the x-axis profile for non-smoothed data that have been lowpass filtered with $f_0 = 6.6$ and 9.0 MHz, respectively. Figures B and D compare the normalized profiles based on noise-free data (solid line) and those which have been wavelet filtered and smoothed with a moving average filter (dashed line). Again, a LPF has been applied, with $f_0 = 6.6$ and 9.0 MHz in Figures B and D, respectively.

Filter Applied	Image Power Sum Residual (%)
None - Noisy	22
5 Pt MoveAve	22
Symlet 8	3.7
Symlet 8 + 5 Pt MoveAve	3.8
Daubechies 9	0.9
Daubechies 9 + 5 Pt MoveAve	0.8

Table 5.4: The above data are the image power sum residuals for different filtering methods, together with the application of a LPF with $f_0 = 2.6$ MHz.

filtered as well as smoothed with a 5 point moving average filter. Evidently, the wavelet denoised data must be smoothed before the image reconstruction process. Similar results were noted in the case of Daubechies 9 wavelet filtering.

Several tests have been done with wider bandwidth data to compare the efficiency of the following three noise filtering approaches:

- Symlet 8 wavelet filtering followed by 5 point moving average filter (herein "Sym8").
- Daubechies 9 wavelet filtering followed by 5 point moving average filter (herein "Daub9").
- 5 point moving average filtering alone (herein "MoveAve").

These approaches were tested in combination with subsequent lowpass filtering during image reconstruction, with f_0 equal to both 6.6 and 9.0 MHz. The preliminary results are illustrated in Figure 5.26. Tables 5.5 and 5.6 present image power sum residuals for the various approaches, subject to lowpass filtering with f_0 equal to 6.6 and 9.0 MHz, respectively. Evidently, filtering with the Daubechies 9 wavelet family, followed by 5 point moving average filtering, results in the most accurate reconstruction of noisy data in this study. However, it appears as though the smoothing operation is essentially the limiting factor, since the Daub9 method affords absolute and relative decreases in the power sum residual of only 0.1% and $\sim$ 10%, respectively, in comparison to the MoveAve approach.

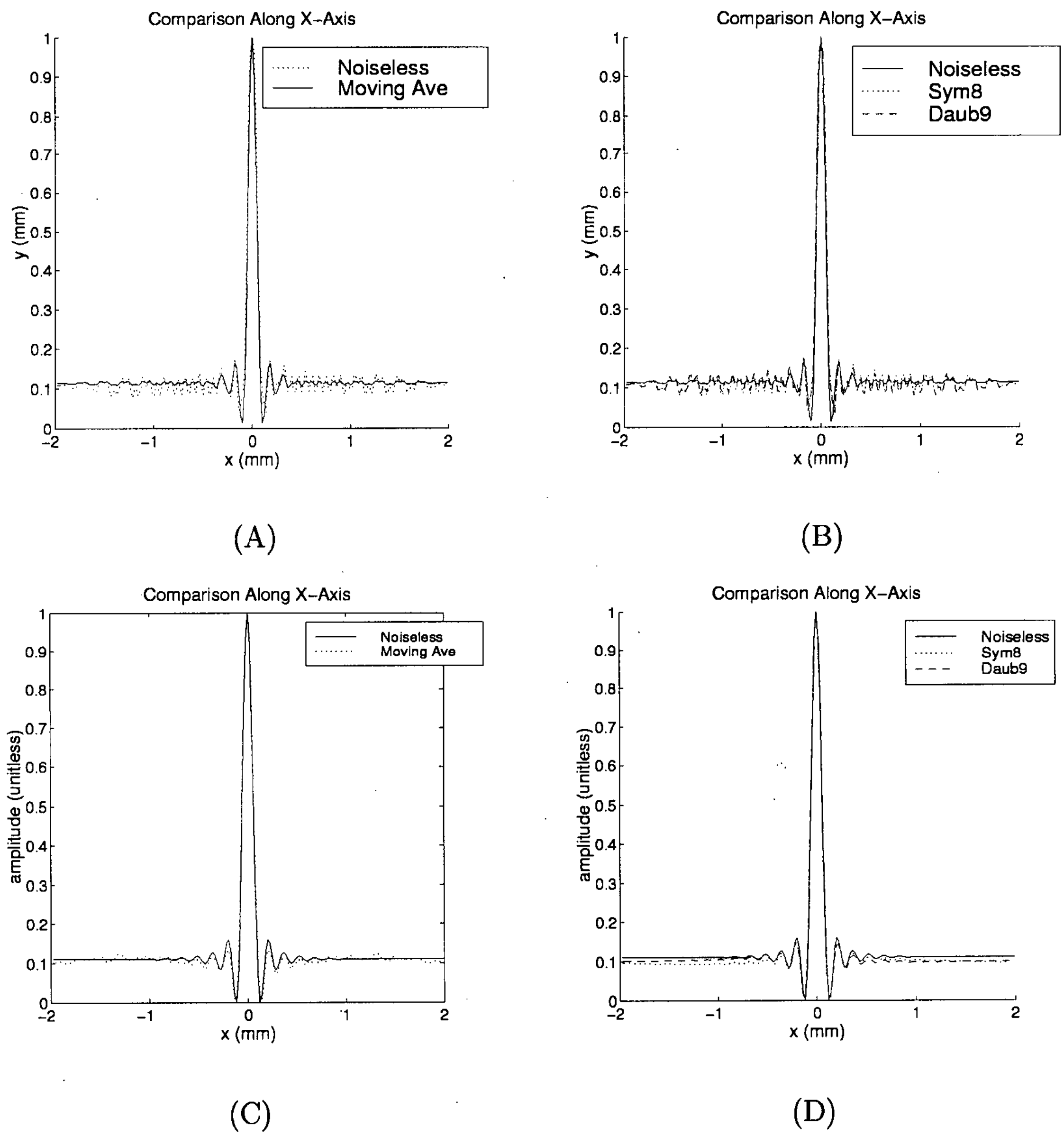

Figure 5.26: These figures compare the MoveAve, Sym8 and Daub9 noise filtering approaches. Normalized γ_κ x-axis profiles are shown. Figures A and B were based on data lowpass filtered with $f_0 = 6.6$ MHz, while data corresponding to Figures C and D were lowpass filtered with $f_0 = 9.0$ MHz.

Filter Applied	Image Power Sum Residual (%)
None - Noisy	113
MoveAve	0.8
Sym8	1.2
Daub9	0.7

Table 5.5: The above data present the image power sum residuals for the different filtering methods, together with the application of a LPF with $f_0 = 6.6$ MHz.

Filter Applied	Image Power Sum Residual (%)
None - Noisy	795
MoveAve	1.1
Sym8	1.1
Daub9	1.0

Table 5.6: This table presents image power sum residuals for the various filtering techniques, together with the application of a LPF with $f_0 = 9.0$ MHz.

Preliminary Conclusions Regarding Noise Filtering

The noise filtering results presented in this thesis hint that wavelet denoising alone has the potential to be superior to the conventional smoothing of pulsed ultrasound data. This was evident in the processing and reconstruction of narrower bandwidth data. The low frequency cutoff was able to remove the higher frequency choppy features introduced into the data by the wavelet denoising process. By extension, if a smooth mother wavelet can be custom-made to mimic the data, it is likely that the denoised signal would not exhibit high frequency choppy features. These data would not require subsequent smoothing with the moving average filter. In likelihood then, the custom wavelet filtered data would produce superior images, given that the behavior in the lower frequency region can be extrapolated to the higher frequencies.

5.6 Experimental Tests of the Method by Blackledge *et al*

5.6.1 Temperature Dependent Speed of Sound

Although the acoustic velocity, c_0, in water was set at 1.48 mm/μs in the simulations, the true speed of sound in the experimental setting varies with water temperature, T. As such, the following experimentally determined equation by Greenspan and Tschiegg was adopted to calculate c_0 [38]:

$$
\begin{aligned}
c_0 &= 1.402736\,\mathrm{mm}/\mu\mathrm{s} && (5.41)\\
\Delta &= 5.03358\,T - 0.0579506\,T^2 + 3.31636\times10^{-4}\,T^3 \\
&\qquad -1.45262\times10^{-6}\,T^4 + 3.0449\times10^{-9}\,T^5 \\
c_0 &= c_0 + \Delta\,\frac{\mathrm{mm}}{^{\mathrm{o}}\mathrm{C}\,\mu\mathrm{s}} && (5.42)
\end{aligned}
$$

In the above equation T is measured in degrees Celsius, and the resulting c_0 has an error of ±0.0001 mm/μs [38]. Figure 5.27 illustrates the resulting acoustic velocity as a function of water temperature. The method by Greenspan and Tschiegg provides an estimate of the speed of sound in the absence of dispersion at a pressure of 1 atmosphere, which is equal to 101.3 kPa. At the time of the following experiments, the air pressure at the lab location was 101.0 kPa, and hence this formula was considered accurate for this work. Furthermore, for the purpose of these experiments, the acoustic velocity in the fresh water in the water tank was assumed to be approximately the same as that in distilled water, described by Equation 5.41.

5.6.2 Introducing a General Source

Recall that the reconstruction method by Blackledge *et al* calls for a pulsed line source with a field that is dependent upon frequency and space according to the following equation:

$$p_0(\mathbf{r},\omega) = A(\omega)g(\mathbf{r}|\mathbf{r}_s,\omega) \qquad (5.43)$$

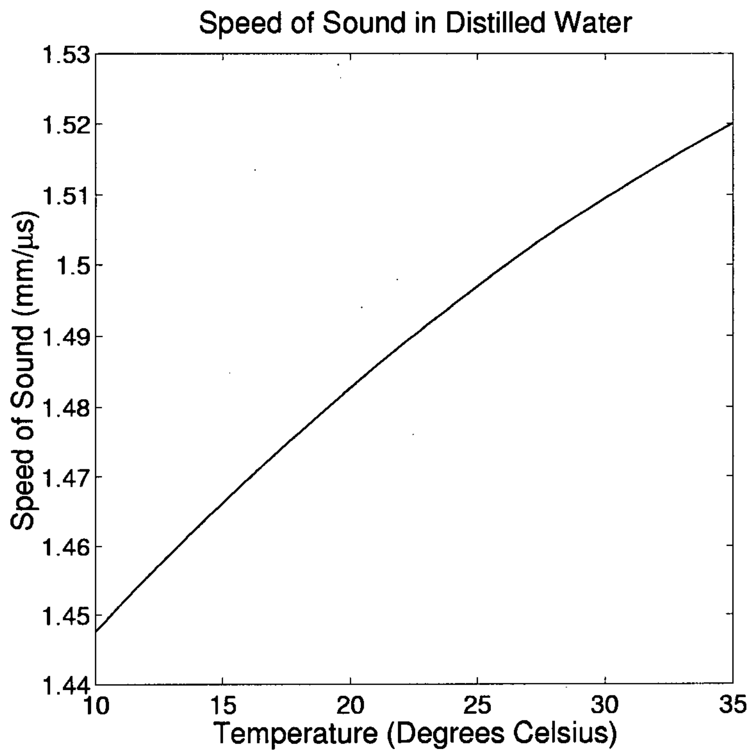

Figure 5.27: This figure illustrates the speed of sound in distilled water versus water temperature. The pressure is assumed to be 1 atmosphere and dispersion is not included.

where $g(\mathbf{r}|\mathbf{r}_s, \omega)$ is the 2D Green's function propagator and $A(\omega)$ is the amplitude spectrum of the source. As such, the desired source has zero phase at the source location (or alternatively at time zero), and its field spreads out cylindrically from $\mathbf{r}_s$. As discussed in Section 3.1, attempts were made to approximate this source field through the use of different transducers ranging from a line source for non-destructive evaluation to a custom-made concave source. However, the numerous difficulties described in the Apparatus Chapter limited the sources available for imaging experiments to only the Panametrics V326/5.0MHz/0.375". Use of this source introduced wrinkles into the experimental work in two aspects. First, the Panametrics field is beam-shaped rather than cylindrical. However, this feature simply limited the experimental work to the imaging of only small objects whose cross-section was entirely insonified by the laterally narrow ultrasound field. The second and most important wrinkle introduced by use of the Panametrics source is that the field does not have zero phase at the face of the transducer. This was determined by detecting the field at a particular location, $\mathbf{r}_d$, and backpropagating it to $\mathbf{r}_s$. Equation 5.43 models propagation, which mathematically is the act of operating on a source field by the Green's function. Backpropagation is simply the inverse operation of dividing a frequency dependent field in a point-by-point fashion by the frequency dependent Green's function. The backpropagated field at $\mathbf{r}_s$ for the signal detected at $\mathbf{r}_d$ is then described by

$$p_{bp}(\mathbf{r}_s, \omega) = p_0(\mathbf{r}_d, \omega)/g(\mathbf{r}_d|\mathbf{r}_s, \omega) \tag{5.44}$$

where p_0 is the detected source field. The pulsed field of the Panametrics transducer was recorded at a distance of 76.3 mm from the transducer face. This distance was measured accurately by using the Panametrics source to both insonify the hydrophone and measure the strong signal backscattered from the hydrophone. Knowledge of $\frac{1}{2}$ the time-of-flight of the backscatter signal, together with the calculation of the acoustic speed in water (27 $^{\circ}$C for this particular study) allowed for the accurate determination of the propagation distance. 500 signals were averaged in this experiment to reduce the noise in the data. The field was backpropagated to the source, and the result was not simply equal to the amplitude spectrum of the source, $A(\omega)$. Rather, the backpropagated field was equal to an initial field, p_{init}, with non-zero phase. It was then hypothesized that the correct model of the field from the Panametrics source is

$$p_0(\mathbf{r}, \omega) = p_{init}(\omega) g(\mathbf{r}|\mathbf{r}_s, \omega) \tag{5.45}$$

$p_{init}(\omega)$ is thus substituted for $A(\omega)$ in the reconstruction algorithm by Blackledge *et al*, and the functions F1 and F2, defined in Equation 2.27, become

$$\mathrm{F1} \;=\; \alpha\, p_{init}(\omega)\, \frac{\exp(2ika\, \cos(\frac{\theta}{2}))}{(2ika\, \cos(\frac{\theta}{2}))^{\frac{1}{2}}} \tag{5.46}$$

$$\text{F2} \;=\; \alpha^2\, p_{init}(\omega)\, k\, \frac{\exp(2ika)}{a}$$

The advantage of using the Panametrics beam source is that both backscatter and sidescatter signals are not contaminated by the background field that reaches the detector without first interacting with the scattering object. Thus according to Equation 2.26 the scattered field can simply be written as

$$\begin{aligned} p_s(\mathbf{r}_d, \mathbf{r}_s, \omega) &\approx \text{F2}\, \psi_\theta(\varphi_s, k) \\ &\approx \alpha^2\, p_{init}(\omega)\, k\, \frac{\exp(2ika)}{a} \psi_\theta(\varphi_s, k) \end{aligned} \tag{5.47}$$

This model was tested by comparing the results of Green's function operation on source fields measured at different distances from the Panametrics transducer. The key in this study is that the fields, p_A and p_B, measured at two Points A and B, respectively, can both be backpropagated to the source location to yield new complex Fourier spectra, $(p_{bp})_A$ and $(p_{bp})_B$, which should be similar. Furthermore, the re-propagation of $(p_{bp})_A$ to Point B should produce a new field, $p_{A\rightarrow src\rightarrow B}$, that is similar to p_B measured at Point B. The backpropagation and re-propagation of p_A is described by the following mathematics:

$$p_{A\rightarrow src\rightarrow B}(\mathbf{r}_B, \omega) = \frac{p_0(\mathbf{r}_A, \omega)}{g(\mathbf{r}_s|\mathbf{r}_A, \omega)}\, g(\mathbf{r}_B|\mathbf{r}_s, \omega) \tag{5.48}$$

Note that the field cannot simply be propagated from Point A to B due to the spatial dependency that is embodied in the Green's function. Operating on p_A with $g(\mathbf{r}_B|\mathbf{r}_A)$ would in effect model the scattering of ultrasound from Point A and the propagation of this secondary cylindrical source of sound from Point A to B. This is quite different than the situation at hand in which the source pulse simply travels from $\mathbf{r}_s$ past Point A to Point B.

Three pairs of points were investigated with distances equal to (33.1, 38.6) mm, (38.6, 54.1) mm, and (76.3, 88.1) mm. Again, the distances from the Panametrics transducer were accurately determined through detection of a backscatter signal from the hydrophone, and 500 signals were averaged to reduce noise in the data. $(p_{bp})_A$ and

$(p_{bp})_B$ were compared in a power sum residual calculation according to Equation 5.30, as were $p_{A\rightarrow src\rightarrow B}$ and p_B. Recall for example that the power sum residual of $p_{A\rightarrow src\rightarrow B}$ with respect to p_B is

$$Q = \frac{\Sigma|p_{A\rightarrow src\rightarrow B} - p_B|^2}{\Sigma|p_B|^2} \times 100\% \tag{5.49}$$

Given a non-dispersive speed of sound in water, the power sum residuals for all pairs of points were initially very large in the range of 40-160% for the comparison of $(p_{bp})_A$ and $(p_{bp})_B$ and in the range of 30-123% for the comparison of $p_{A\rightarrow src\rightarrow B}$ and p_B. Dispersion was then added in the following ad hoc manner in an attempt to improve the source model. A simple linear model of frequency dependent acoustic velocity was introduced in which the fractional range of dispersion over 0-20 MHz was chosen to be some value, f_1. Thus, the corresponding range over frequencies from 0 MHz to f_{Nyq} in the imaging experiment was calculated to be range_{disp}, given by:

$$\text{range}_{disp} = f_1 \times \frac{f_{Nyq}}{20\text{MHz}} \tag{5.50}$$

Recall from Section 5.3.6 that dispersion is on the order of 1% over the range of 1-20 MHz. As such, f_1 was varied from 0-0.01. The range of acoustic speed was then calculated to be

$$\text{range}_c = c_0 \times \text{range}_{disp} \tag{5.51}$$

where c_0 is the acoustic speed in the absence of dispersion. The minimum acoustic speed over the frequency range was not assumed to be c_0. Rather, it was calculated to be an initial value equal to c_{init}, given by

$$c_{init} = c_0 - f_2 \times \text{range}_c \tag{5.52}$$

in which f_2 was allowed to vary between -0.75 and 0.75. Finally, the acoustic speed as a function of frequency, f, was calculated by

$$c(f) = c_{init} + \text{range}_c \times \frac{\text{ABS}(f)}{f_{Nyq}} \tag{5.53}$$

Note that this model does not necessarily mimic physical reality. Rather, it was introduced for the sole purpose of reducing the difference between $(p_{bp})_A$ and $(p_{bp})_B$, as well as the difference between $p_{A\rightarrow src\rightarrow B}$ and p_B, thereby leading to a workable model of Panametrics source field propagation. Upon calculating the frequency dependent speed of sound, $p_{A\rightarrow src\rightarrow B}$ and p_B were recalculated based on the new corresponding frequency dependent wave numbers, $k(f)$. The best case scenario for the point sets equal to (33.1, 38.6) mm and (38.6, 54.1) mm was found to be $f_1 = 0.01$ and $f_2 = 0.5$, which resulted in power sum residuals in the range of 16-20% for the comparison of $(p_{bp})_A$ and $(p_{bp})_B$ and in the range of 14-15% for the comparison of $p_{A\rightarrow src\rightarrow B}$ and p_B. For the point set equal to (76.3, 88.1) mm, the optimal value of f_1 was smaller at 0.005. This resulted in a power sum residual of only 1% for the comparison of $(p_{bp})_A$ and $(p_{bp})_B$ and 2.5% for the comparison of $p_{A\rightarrow src\rightarrow B}$ and p_B. The corresponding dispersive speed of sound is plotted in Figure 5.28.A. Figure 5.28.B compares the pulses corresponding to $(p_{bp})_A$ and $(p_{bp})_B$ and those corresponding to $p_{A\rightarrow src\rightarrow B}$ and p_B, respectively, where $A = 76.3$ mm and $B = 88.1$ mm. There evidently is excellent agreement.

By virtue of the above experiment, the 2D Green's function was adopted as the propagator for the Panametrics source over the range of 30 to 60 mm subject to use of the dispersive speed of sound for which $f_1 = 0.01$ and $f_2 = 0.5$. Finally a source spectrum was determined as follows for use in the reconstruction algorithm. The reflectivity experiment (backscatter imaging) was performed with the Panametrics source/detector situated at $A_{bs} = 31.4$ mm. The source field for this reconstruction was determined by comparing the fields for Point Set 1, with $A = 33.1$ mm and $B = 38.6$ mm. The fields measured at Points A and B were both backpropagated to the source location to yield new fields, $(p_{bp})_A$ and $(p_{bp})_B$, respectively. The corresponding source spectrum, $(p_{init})_{bs}$ was chosen to be the average spectrum given by

$$(p_{init})_{bs} = \frac{(p_A)_{bp} + (p_B)_{bp}}{2} \tag{5.54}$$

The power sum residuals comparing $(p_{init})_{bs}$ to $(p_{bp})_A$ and $(p_{bp})_B$ were relatively low at

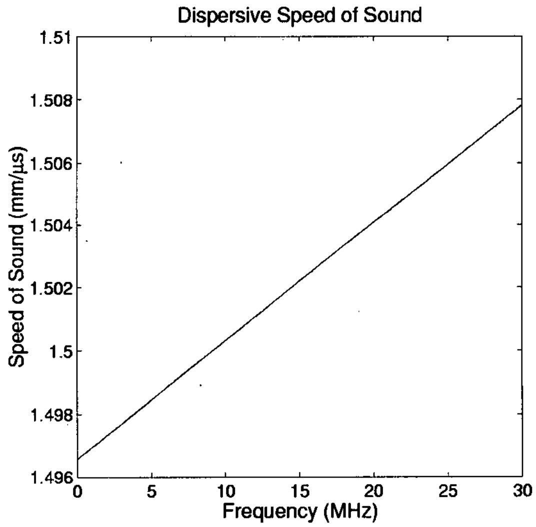

(A)

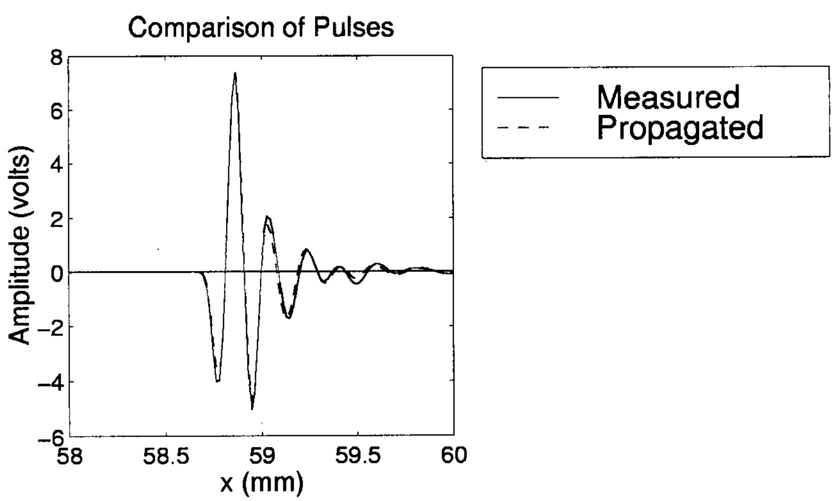

(B)

Figure 5.28: Figure A illustrates the dispersive speed of sound that yielded the least difference between $p_{A\rightarrow src\rightarrow B}$ and p_B, where $A = 76.3$ mm and $B = 88.1$ mm. Figure B compares the time dependent pulse corresponding to $p_{A\rightarrow src\rightarrow B}$ with the pulse measured at Point B.

3.3% and 2.4%, respectively. The γ_κ experiment (sidescatter imaging) was performed with the Panametrics source and the hydrophone situated at $A_{ss} = 51.4$ mm. Similarly, $(p_{init})_{ss}$ for this reconstruction was determined by comparing the fields for Point Set 2, with $A = 38.6$ mm and $B = 54.1$ mm. These fields were backpropagated to the source location to yield $(p_{bp})_A$ and $(p_{bp})_B$, and p_{init} was again chosen to be the average of these fields. The power sum residuals comparing $(p_{init})_{ss}$ to $(p_{bp})_A$ and $(p_{bp})_B$ were again low at 2.6% and 3.6%, respectively. As further verification of this exercise, Figures 5.29.A and 5.29.B compare the real and imaginary parts of $(p_{init})_{bs}$ and $(p_{init})_{ss}$ for Point Sets 1 and 2. Evidently, there is excellent agreement even though the distances of the points vary widely.

Of final note in this section is the fact that the source amplitude falls to 0.012% of its maximum frequency response at 12 MHz. Furthermore, only 0.02% of the power spectrum lies outside of the range from -12 to 12 MHz. As such, a low pass filter was applied to the corresponding experimental data with a cutoff frequency of $f_0 = 12$ MHz.

5.6.3 Experimental Work with Tissue Phantoms

Characterizing the Graphite/Gelatin Phantom

With the Panametrics source introduced into the reconstruction algorithm, the next step in the experimental work was the characterization of the graphite-gelatin tissue equivalent material (GG-TEM) described in Appendix D. This material was used due to its non-toxic nature. However, it is difficult to obtain consistent speed of sound results with different batches of this material [14]. Furthermore, the speed of sound of the material was not listed in the literature supplied with the formula obtained from another group. As such, the GG-TEM was characterized with the apparatus illustrated in Figure 5.30. The apparatus was made of a centrifuge tube with a diameter of $\frac{1}{2}$ inch. A 3 mm wide rod was placed through the tube, parallel to the rim of the tube. It was necessary to reduce the depth of the GG-TEM in the centrifuge tube to approximately 9 mm in order

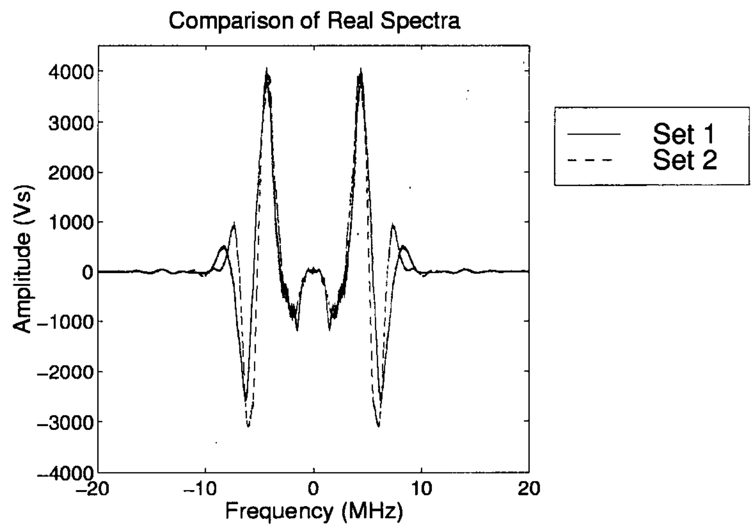

(A)

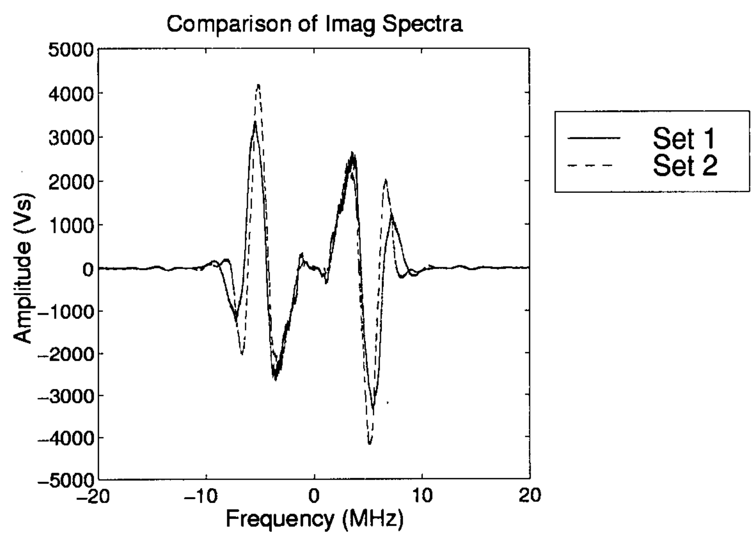

(B)

Figure 5.29: Figures A and B compare the real and imaginary parts, respectively, of $(p_{init})_{bs}$ and $(p_{init})_{ss}$ for Point Set 1 = (33.1, 38.6) mm and Point Set 2 = (38.6, 54.1) mm.

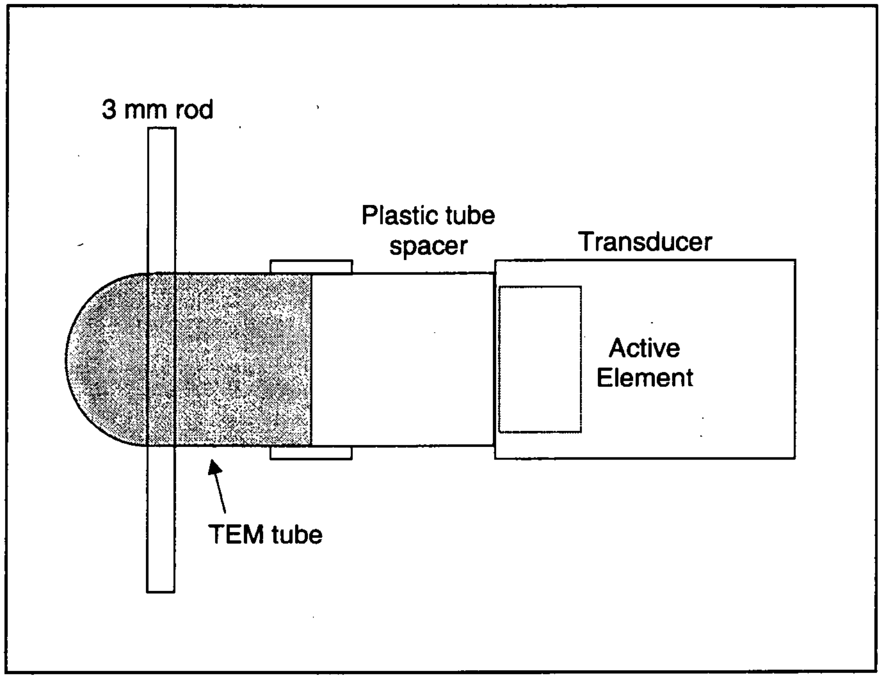

Figure 5.30: This figure illustrates the apparatus that was used to measure the speed of sound in the tissue equivalent material that the phantom was composed of.

to obtain a strong signal from the rod that was easily distinguished from the background of backscatter signals returning from the attenuating tissue equivalent material. It was also necessary to ensure that the tissue equivalent material was not touching the active element of the transducer, since this caused significant ringing of the transducer. This ringing was overcome by attaching an 11 mm deep spacer made of the top of a centrifuge tube of the same size to the tube containing the GG-TEM. The two tubes were attached with waterproof duct tape. Placing the spacer against the transducer did not have this effect because the tube was wider than the active element.

The speed of sound in the GG-TEM was determined in the following manner. First the empty apparatus was immersed in distilled water and insonified with the Panametrics source, which was placed against the centrifuge tube. The TOF of the backscatter signal from the rod was recorded. The temperature of the distilled water was 21°C, and hence the speed of sound in water was $c_0 = 1.4857 \pm 0.0001$ mm/μs (dispersion was ignored in this experiment). From the TOF of 26.75 ± 0.02 μs, the distance from the transducer face to the rod was calculated to be 19.87 ± 0.02 mm. The backscatter experiment was then repeated with the centrifuge tube filled with GG-TEM, and the plastic spacer again attached. The time-of-flight was 26.40 ± 0.02 μs. Accounting for the length of the spacer, the speed of sound in the tissue equivalent material was calculated to be

$$c_{TEM} = 1.530 \pm 0.002\,\mathrm{mm}/\mu\mathrm{s} \tag{5.55}$$

The density of the GG-TEM was also measured by comparing the mass of a centrifuge tube full of distilled water at 28°C to that of the same tube full of the tissue equivalent material. Figure 5.31 illustrates the density of water as a function of temperature according to 71st Edition of The Handbook of Chemistry and Physics [55]. At 28°C, the density of water is 0.99624 g/ml. Accounting for the mass of the tube, the ratio of the mass of a tube of distilled water at 28°C to that of a tube of GG-TEM was 0.91924, leading to a GG-TEM density of ρ_{TEM} equal to 1.084 ± 0.008 g/ml. From the speed of sound and density of the tissue equivalent material, the compressibility, κ_{tem}, can be calculated according to Equation 1.7:

$$\kappa_{TEM} = \frac{1}{c_{TEM}^2\,\rho_{TEM}} = (0.394 \pm 0.003) \times 10^{-3} \frac{\mathrm{g}}{\mu\mathrm{s}^2\mathrm{mm}^2} \tag{5.56}$$

With the GG-TEM characterized, γ_κ and γ_ρ can be calculated for any experiment involving the material.

Experimental Setup

A string phantom was made using the "candle method" described in Appendix D, in which string with a weight on the end is dipped into the graphite-gelatin tissue equivalent material several times, allowing 5 minutes in between for each layer to solidify. In this

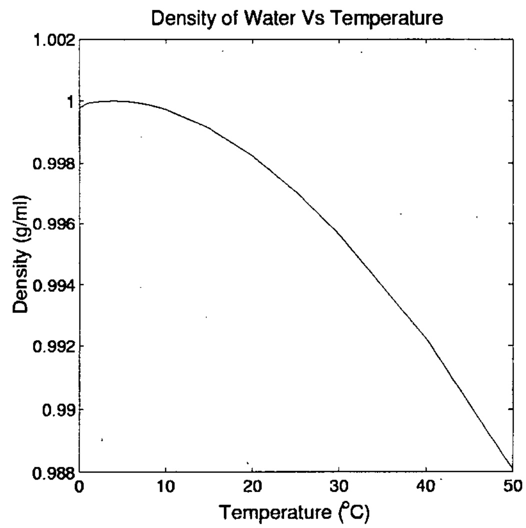

Figure 5.31: This plot illustrates the density of water as a function of temperature.

manner, a phantom with diameter equal to 3.0±0.3 mm was constructed. The large error in the diameter was due to the slightly undulating cylindrical surface of the phantom. The phantom was suspended in the middle of the tank with a plumb bob tied to its bottom to facilitate the centering of the phantom in the middle of the tank. For the reflectivity experiment, the source/detector transducer was situated at $(-31.41 \pm 0.03, 0)$ mm. For the γ_κ experiment, $|\mathbf{r}_s|$ and $|\mathbf{r}_d|$ were limited to a minimum of 50 mm due to the construction of the arm that holds the hydrophone. The source and detector positions were $(0, -51.35 \pm 0.05)$ mm and $(-51.41 \pm 0.05, 0)$ mm, and the value of $a = |\mathbf{r}_s| = |\mathbf{r}_d|$ in the reconstruction algorithm was chosen to be the average of the distances.

The Data and Associated Signal Processing

500 signals digitized at 60 MHz were averaged together to reduce the noise in the signal. Although it was desirable to collect data at many angles, it was found that the skin on the surface of the phantom did not prevent it from absorbing water and increasing

in diameter over time. As such, data were recorded at only one angle due to the several minutes required for the collection of a reasonable number of views by manually moving the apparatus (recall the internal corrosion of the traction drive). This view was copied for all other views, which was a valid approach for the cylindrically symmetric phantom. In fact, this approach has been published in the literature due to similar problems with graphite-gelatin tissue phantoms [32]. Figures 5.32.A and 5.32.B illustrate the data for backscatter and sidescatter, respectively. The signal-to-noise ratios for the backscatter and sidescatter signals in the absence of any filtering are 34 db and 10 db, respectively. The noise in the transmission data is identically a sawtooth of ± 0.5 mV, and there is a possibility that this is a digitization error of the Gagescope ADC board. However, given that the board is a 12 bit module, and that the voltage range was set at ± 100 mV, the digitization error was expected to be on the order of 0.05 mV. It is thus more likely that this sawtooth noise is an effect of either the hydrophone/preamp or the Panametrics receiver/amplifier.

Wavelet filtering was tested on these data. Initially the Daubechies 9 was adopted as the mother wavelet, in keeping with the best case simulation results presented in Section 5.5.2. The "huersure" threshold selection rule was tested with "mln" noise rescaling model for the most general approach in the event that the noise was not identically white and Gaussian. It is suggested in the Wavelet Toolbox Guide that level 5 is generally considered to be a good choice of denoised signal in wavelet filtering, so this was the basis of the following analysis [60]. Filtering the backscatter data with the Daubechies 9 family increased the SNR from 34 db to 39 db, but afforded very little improvement in the data. The power sum residual of the Fourier spectrum for the wavelet filtered data compared to that for the unfiltered data was only 0.6%. Furthermore, it was possible to obtain the same improvement by simply lowpass filtering the data with $f_0 = 12$ MHz. Upon applying the LPF to both the wavelet filtered data and the original data, there was no discernible difference between the two corresponding Fourier spectra, with a negligible

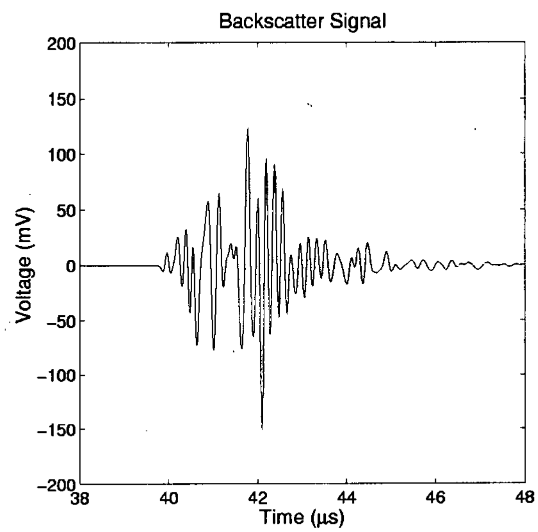

(A)

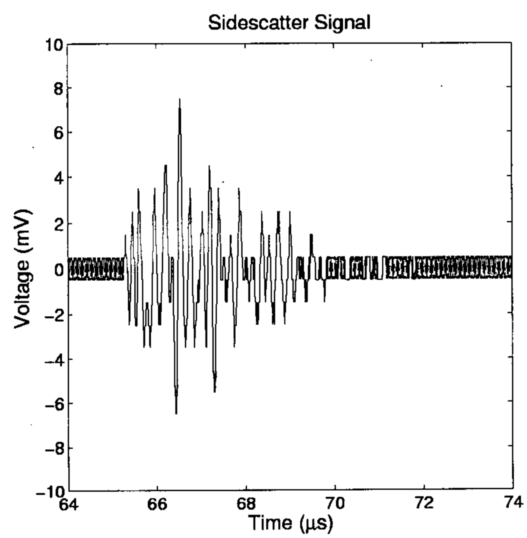

(B)

Figure 5.32: Figures A and B illustrate backscatter and sidescatter data for a graphite-gelatin tissue equivalent phantom.

power sum residual of 0.006%. It was noted that the data had features in common with the Daubechies 20 mother wavelet, illustrated in Figure 5.33.A. Filtering the backscatter data with this family produced identical results when compared to filtering with the Daubechies 9 family.

Filtering of the sidescatter data produced slightly different results. The power sum residual of the Fourier spectrum for the Daub20 filtered sidescatter signal relative to the original signal was 63%. Figure 5.33.B illustrates the filtered signal, wavelet decomposed at level 5. Figure 5.33.C illustrates a closeup of a noisy region of the signal, comparing the filtered and non-filtered versions. Evidently, there is a dramatic improvement in the noise level, and in fact the SNR was increased to 28 db, up from 10 db. However, it was again possible to obtain the same improvement by simply lowpass filtering the data with a cutoff frequency of $f_0 = 12$ MHz. Upon applying the LPF to both the wavelet filtered data and the original data, there was no discernible difference between the two corresponding Fourier spectra, with a negligible power sum residual of 0.06%. The same results were obtained when the sidescatter data were wavelet filtered with the Daubechies 9 family. Given the results of these preliminary tests on experimental data, wavelet filtering was not applied in the reconstructions to follow.

RESULTS FOR γ_κ AND REFLECTIVITY

The compressibility imaging was performed in water with a temperature of 25°C, with a speed of sound and density of approximately 1.497 mm/μs and 0.99705 g/ml, respectively. γ_κ is therefore -0.12 given the value of κ_{TEM} calculated in Section 5.6.3. The reflectivity experiment was performed in water with a temperature of 28°. The speed of sound and density of water for this temperature are 1.5047 mm/μs and 0.99624 g/ml. Given ρ_{TEM} determined in Section 5.6.3, γ_ρ is 0.09. The expected value of reflectivity is therefore $R = \gamma_\kappa - \gamma_\rho = -0.21$.

In calculating the data, $\psi_\theta(\varphi_s, k)$, in the 2D Fourier domain of the R or γ_κ cross-

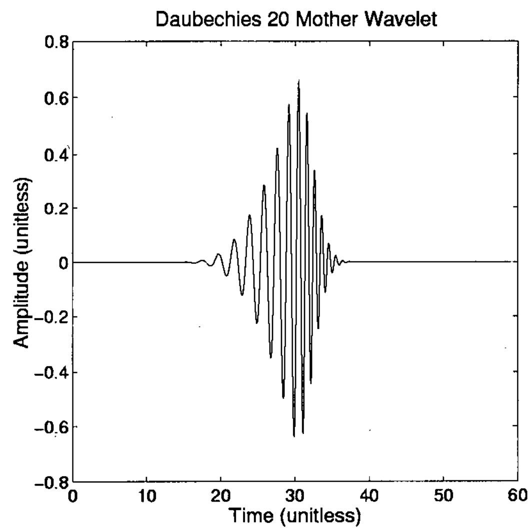

(A)

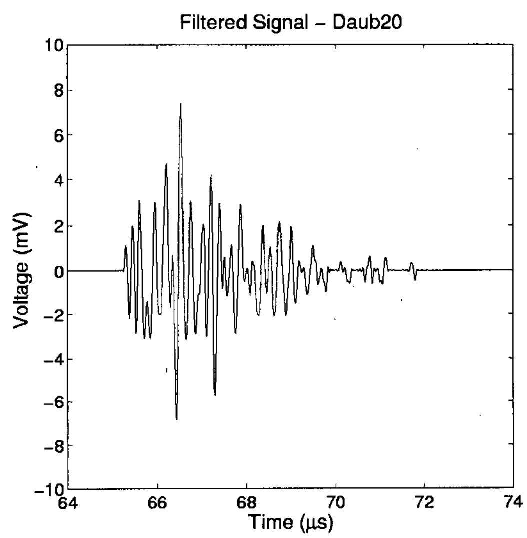

(B)

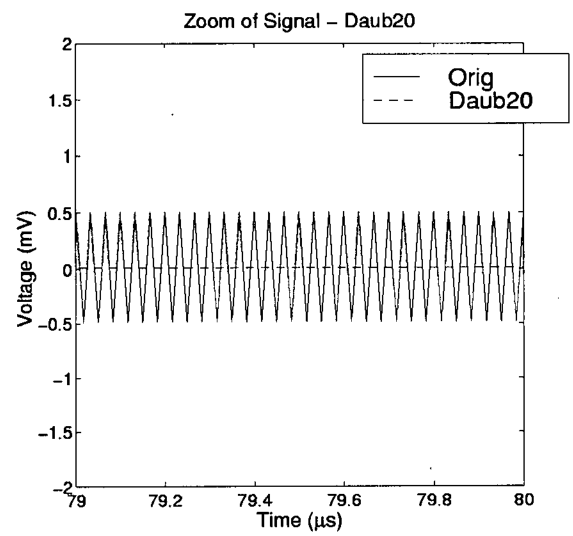

(C)

Figure 5.33: Figure A illustrates the Daubechies 20 mother wavelet. Figures B illustrates the sidescatter data for the phantom after it has been denoised with the Daubechies 20 family. Figure C compares a noisy region both before and after denoising. Note that the denoised line is identically equal to the x-axis.

section during image reconstruction, there is a deconvolution of the form

$$\psi_\theta(\varphi_s, k) \approx \frac{p_s(\mathbf{r}_d, \mathbf{r}_s, \omega)}{\alpha^2\, p_{init}(\omega)\, k\, \frac{\exp(2ika)}{a}} \tag{5.57}$$

Since both p_s and p_{init} are characterized by noise, the deconvolution is subject to error and results in ψ_θ data characterized by spikes. Even after lowpass filtering the data, the inherent noise was emphasized by the deconvolution and resulted in images with significant circle and streak artifacts that essentially destroyed the features of the image. The following smoothing approach was thus adopted in an initial attempt to overcome this problem. For a real valued image, only the real part of the corresponding 2D Fourier data has any effect on the resulting image upon inverse transforming. This is due to the existence of the following symmetry:

$$\mathrm{FT}(-u, -v) = \mathrm{FT}^{+}(u, v) \tag{5.58}$$

where u and v are the coordinates in Fourier space. The imaginary components of the 2D Fourier data therefore cancel out. As such, the real part of ψ_θ for the backscatter data along each radial line in Fourier space was smoothed twice with a moving average filter with a window size equal to 5. The real part of ψ_θ for the sidescatter data were similarly processed, but these data required 3 passes of the filter due to the relatively poor signal-to-noise ratio of 28 after lowpass filtering. In both experiments, the imaginary part of ψ_θ was left as is. Lastly it should be noted that the backscatter data were normalized by the amplitude spectrum of $(p_{init})_{bs}$ in order to remove any dependence upon the transducer response. Recall that the response of the hydrophone is relatively flat and as such this is not an issue with sidescatter data.

Upon smoothing the data, promising reflectivity and γ_κ images were obtained for the GG-TEM phantom. Figures 5.34.A and 5.34.B illustrate the reflectivity image and corresponding x-axis profile, while Figures 5.34.C and 5.34.D present the resulting γ_κ image and x-axis profile. These images were based on 100 views of data. Key points are as follows. First, the images indicate a negative R and γ_κ, as expected. Second, the

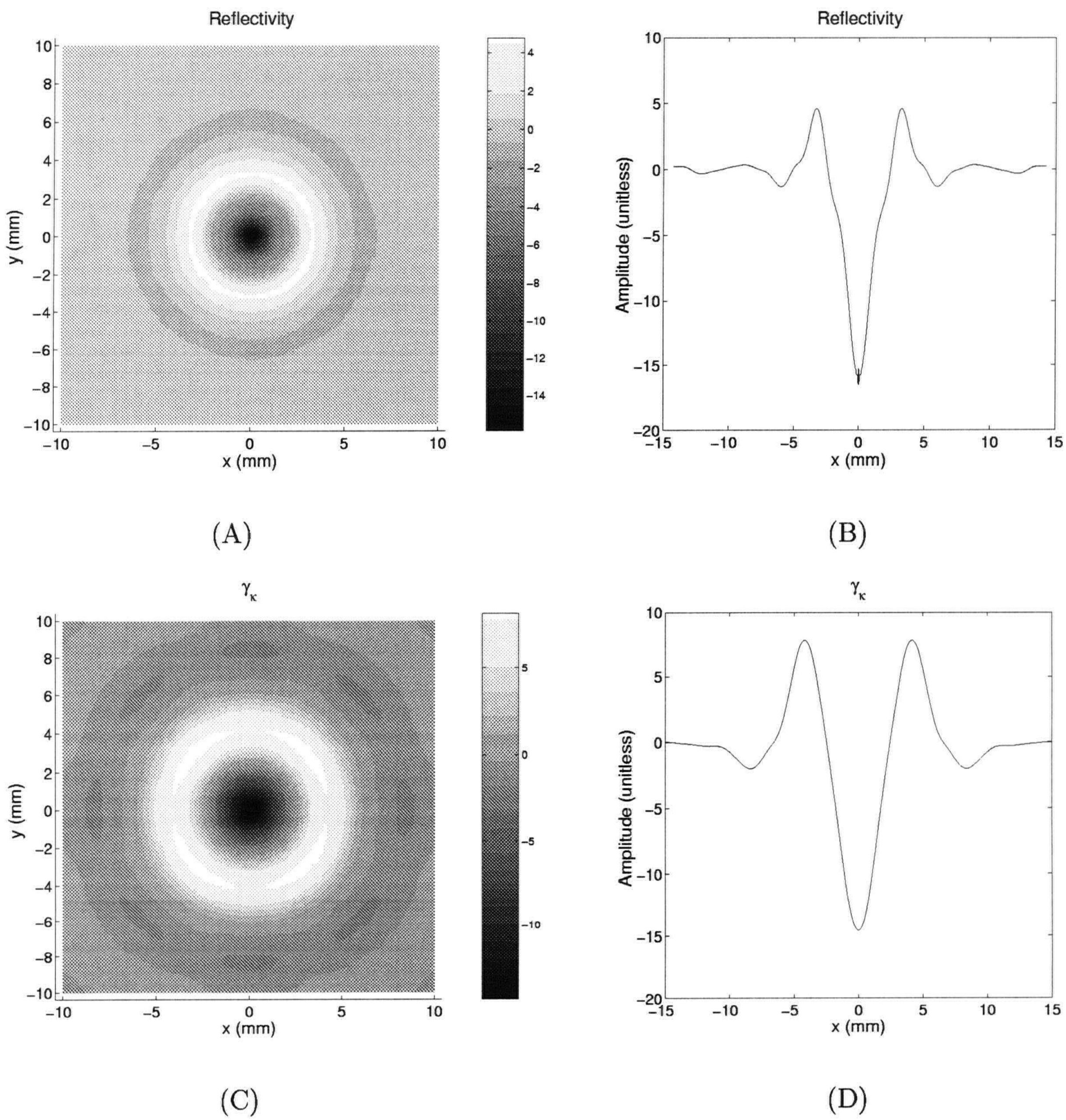

Figure 5.34: This composite presents imaging results for a 3 mm wide GG-TEM phantom based on 100 views of data. Figures A and B illustrate the reflectivity image and its corresponding x-axis profile, while Figures C and D present the γ_κ image and its corresponding x-axis profile.

full-width-half-max values are reasonable. Measured from zero amplitude, the FWHM of the x-axis profile of γ_κ is 2.94 ± 0.06 mm, which is in excellent agreement with the phantom width of 3.0 ± 0.3 mm. Measured from zero amplitude, the FWHM of the x-axis profile of R is very small at 1.94 ± 0.04 mm, which varies by 33% and 35% from the low and central values of the object diameter. As such, the agreement is not good, although the result is reasonable given the error in the source model, the necessary smoothing, and the application of the Born approximation in the development of the reconstruction algorithm. Both R and γ_κ have primarily negative profiles, as expected. The minimum values of R and γ_κ where the phantom is situated are $R_{min} = -16.5$ and $(\gamma_\kappa)_{min} = -14.6$, respectively. Normalization factors, ξ, are therefore required to obtain the actual values of γ_κ and R, as in the simulation tests. ξ_R and ξ_{γ_κ} are furthermore not the same, which was again seen in simulation. Due to the large shortfall in the FWHM of the R image, a valid cross-section for γ_ρ could not be calculated and is therefore not presented here.

It should be noted that the distance, a from the origin to the source or detector is a very important parameter in the reconstruction of experimental data. If this value is accurately known, the expected image will result, while errors in a can cause dramatic effects on the image. As an example, Figure 5.35 illustrates the effect on γ_κ when the parameter a is too large by 1% and 2%. An error of 1% leaves $(\gamma_\kappa)_{min}$ as is, but reduces the FWHM (measured from zero) to 2.00 ± 0.04 mm. An error of only 2% completely destroys the image. Note that an error in a was not the cause of the smaller FWHM for the reflectivity image presented in this section. a was varied to test this and 2.0 mm was the largest FWHM that was possible in the reconstruction of the data.

Final Remarks Regarding the Source

As discussed in Section 3.1, it was possible to detect a reasonable signal 3-5 cm directly in front of the line source. These data were used to determine if in fact the source model is able to properly describe the field from a broadband pulsed line source,

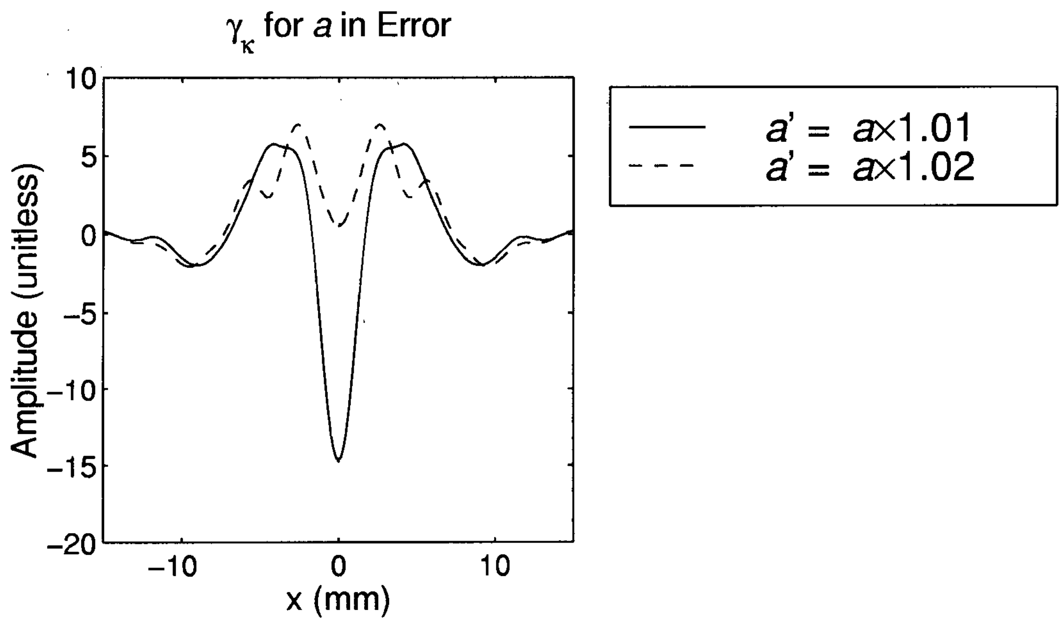

Figure 5.35: This figure illustrates the x-axis profile of the γ_κ image that results when a is increased in error by 1% and by 2%.

as expected. As with the Panametrics transducer, the pulsed field was measured at two points situated $A = 46.6$ mm and $B = 59.4$ mm from the line source. The fields p_A and p_B were backpropagated to the source location to yield $(p_{bp})_A$ and $(p_{bp})_B$, which were compared. $(p_{bp})_A$ was then re-propagated to Point B to yield a new field $p_{A\to src\to B}$, which was compared to the measured field p_B. Again it was necessary to add dispersion according to Equations 5.50 through 5.52 in order to reduce the power sum residuals, and values of f_1 and f_2 equal to 0.003 and -0.6, respectively, were found to be optimal. The resulting power sum residuals were 21% for the comparison of $(p_{bp})_A$ and $(p_{bp})_B$ and 23% for the comparison of $p_{A\to src\to B}$ and p_B. The results of this exercise are therefore slightly worse than for the study of the Panametrics source. Figure 5.36.A compares the pulses

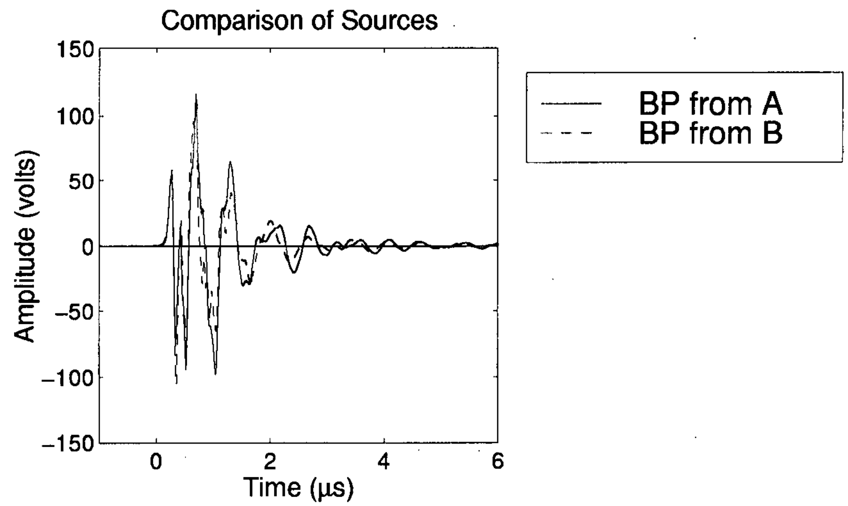

(A)

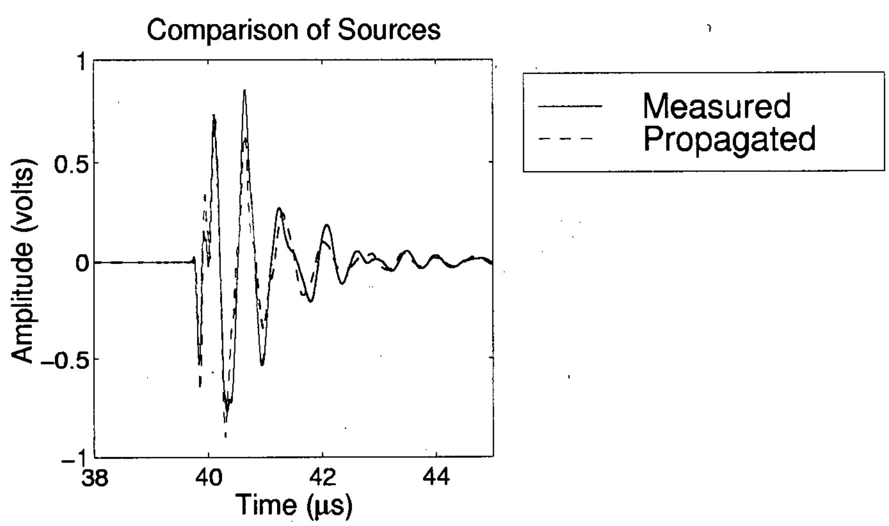

(B)

Figure 5.36: Figure A illustrates the dispersive speed of sound that yielded the least difference between $p_{A\rightarrow src\rightarrow B}$ and p_B, where $A = 46.6$ mm and $B = 59.4$ mm. Figure B compares the time dependent pulse corresponding to $p_{A\rightarrow src\rightarrow B}$ with the pulse measured at Point B.

corresponding to $(p_{bp})_A$ and $(p_{bp})_B$, while Figure 5.36.B compares those corresponding to $p_{A\rightarrow src\rightarrow B}$ and p_B. Although there is reasonable agreement, the power sum residuals indicate that the source model does not do a better job of describing the line source as compared to the Panametrics source. This is unfortunate given that the source terms in the reconstruction algorithm are aimed at a description of line sources.

5.7 Tests of the ART in Computer Simulation

Recall from Section 4.2.3 that images, I, equal to γ_κ or and γ_ρ can be obtained through the application of an algebraic reconstruction technique to the data. This algorithm solves the following system of equations:

$$\mathbf{b} = \mathbf{TI} \tag{5.59}$$

where

$$T_{ij} = A_i k_i^2\, \tilde{g}(\mathbf{r}_j|\mathbf{r}_s, k_i)\, I_j\, \tilde{g}(\mathbf{r}_j|\mathbf{r}_d, k_i)\, \Delta x \Delta y \tag{5.60}$$

and

$$\begin{aligned} \tilde{g}_j^i &= \tilde{g}(\mathbf{r}_j|\mathbf{r}_s, k_i)\, \tilde{g}(\mathbf{r}_j|\mathbf{r}_d, k_i) \\ b_i &= p_s(\mathbf{r}_d, \mathbf{r}_s, k_i) \\ A_i &= A(\omega_i) = A(k_i) \end{aligned} \tag{5.61}$$

In testing the ART, scatter data were simulated for 1 or more discrete points making up an object. These Fourier data were calculated for each view about the object as in Section 5.3 via Equation 5.27. Again, the width of the element of area associated with each scatter point was determined by the Nyquist frequency of the data. Evidently then, there is an element of area associated with both the left hand side and right hand side of Equation 5.59. As in the testing of the method by Blackledge *et al*, these elements of area, denoted by α_1 and α_2, are essentially factors that scale the resulting images. An increase in α_1 together with all other terms being kept constant will scale I upward. In contrast, an increase in α_2 alone will scale I downward. Care must therefore be taken when comparing different images. In the following tests, α_1 and α_2 were consistently made equal. This had the effect of cancelling these terms and allowing for the direct comparison of different images.

The full development and testing of an algorithm involving iterative techniques is generally regarded as an involved project in its own right. As such, the scope of this thesis allowed the inclusion of only a few investigations that were aimed at determining the potential capabilities and limitations of the method. The results of these preliminary tests will serve as a foundation for future work in this research project. Since the aim of this work was to evaluate the potential of the pulsed UCT methods at hand to provide quantitative images of tissue, the following key points were investigated in the ART approach:

- Image resolution.
- Ability to correct for frequency dependent attenuation.
- Ability to produce properly scaled images.
- Ability to reconstruct images for which $\frac{|\mathbf{r}|}{|\mathbf{r}_j|}$ is not $\ll 1$, where $\mathbf{r}_j$ is the position vector of either the source or detector.

In addition, since the ART involves iterative techniques, an over-riding factor is the ability of the reconstruction algorithm to converge on the correct image, I. In all the simulations performed, the convergence criterion was that the error was less than 1×10^{-7}.

In doing simulations to study these key points, it became clear that computing power, the speed of convergence, and the ability of the algorithm to converge were three major obstacles. For instance, the ART performed poorly in reconstructing larger images on the order of 30×30 or 20×20 pixels because the error was reduced very little in each iterative step. As such, convergence was almost nonexistent. Given that the scope of this thesis could not include an in-depth study into convergence methods and issues, these preliminary tests were necessarily limited to images with fewer than 20×20 pixels. This guideline was advantageous in that it limited the size of the propagator array, **A**, and therefore reduced the required computing time and memory. To further reduce the CPU time and memory requirements, the incident field Fourier spectrum was limited to less than 4000 discrete frequencies.

As with the implementation of the method by Blackledge *et al*, the number of frequencies in the Fourier data were further reduced by truncating the data set beyond a reasonable frequency. In the examples presented in the following sections, insonification was simulated with a Ricker wavelet that had ω_0 equal to 20 MHz. Recall from Section 5.3.1 that a lowpass filter with f_0 equal to 9.0 MHz can be applied to the corresponding scatter data without loss of valid information, and that the Fourier data can be subsequently truncated anywhere beyond 11.3 MHz. Therefore, the UCT data simulated in this section were processed with a lowpass Butterworth filter of order 20 with $f_0 = 9.0$ MHz, and data for both the γ_κ and R reconstructions were truncated at $(f_T)_{\gamma_\kappa}$ and $(f_T)_R$ equal to 14 MHz. Since the same (x, y) image grid is set up for γ_κ and R imaging before data processing begins, the truncation frequency can be the same for both image reconstructions. Recall that with the method by Blackledge *et al*, setting $(f_T)_{\gamma_\kappa}$ equal to $(f_T)_R$ resulted in different image sizes and pixel coordinates. The above truncation frequency was expected to have no effect on image reconstruction. For good measure though, this assumption was tested in simulation, and the power sum residual, given by Equation 5.30, was computed for the image based on truncated data relative to that based on the full original data set. The power sum residual was zero for all tests.

5.7.1 Choice of Iterative Method

Four methods were considered for the iterative solution of the linear system, $\mathbf{y} = \mathbf{A}\mathbf{x}$, in the ART. These were the Conjugate Gradient (CG) method, the Jacobi Iterative (JI) technique, the Gauss-Seidel (GS) method, and the Successive Under-Relaxation (SUR) technique, all of which are outlined in Appendix E. In this appendix it was indicated that the JI and GS methods require that **A** be diagonally dominant and that every diagonal element of **A** be nonzero. Given the nature of the propagator matrix, the condition of diagonal dominance is impossible to satisfy. In fact, the sum of the absolute value of all non-diagonal elements along a row in a typical propagator matrix is generally 2 orders of magnitude larger than the absolute value of the diagonal term. Therefore, the JI and GS methods can not be used.

The SUR and CG methods were tested to determine if they are able to converge upon an image solution in the ART reconstruction problem. Several simulations were done for a simple point scatterer located at the origin, with the source and detector located 100 mm from the origin. Values of ω ranging from 1×10^{-4} to 0.9 were tested, but convergence with the SUR method was not possible. In fact, for values of ω less than 1×10^{-3}, the method would diverge both immediately and rapidly. In contrast, the CG method converged in 98 iterations. Thus, the CG method is the only approach of the four that was available for use within the scope of this project.

5.7.2 Attenuation Correction and Choice of $\mathbf{x}^0$

This section presents the results of γ_κ and γ_ρ reconstruction for a 3×3 grid of isolated points. With this grid, the ability of the ART to reconstruct images in the presence of attenuation was studied. In addition, the effect of the choice of the initial image vector, $\mathbf{x}^0$, was also investigated. The grid was identical to that used in Section 5.3, with the exception that the x and y spacing between points was 0.26 mm instead of 1.5 mm. In other words, points in the nth column had γ_κ and γ_ρ equal to $0.04n$ and $0.0909n$, respectively. Data for 100 views were sampled at 45 MHz.

This test of attenuation correction is comparable to the study of the approximate correction, which was done in Section 5.4. For instance, the spacing of the points in the latter study was 0.20 mm in both the x and y dimensions, and the same Butterworth filter was used. Data were not truncated, though, so in effect a more complete data set was used in Section 5.4. As in the case of the method by Blackledge *et al*, it was not possible to perform an ART reconstruction of a grid of points with large x and y spacing due to computing power and memory restrictions. As well, convergence issues that were beyond the scope of this thesis limited the physical extent in the reconstructed images. As such, attenuation in tissue was scaled up by a factor of 1000 as in the testing of the approximate attenuation correction in Section 5.4 in order to facilitate the study of attenuation effects over smaller distances. Attenuation in water was left as is. Since the maximum distance between a scatter point and the origin was only 0.28 mm, the distance from the origin to the source or detector was set to a correspondingly small value of 2 mm.

An initial image vector, $\mathbf{x}^0$, must be selected to begin the iterative process. This was found to have an effect on the solution that the ART converged upon. Preliminary tests involving both the grid at hand as well as other scattering objects indicated that the matrix system involving propagators in the absence of attenuation does not have only one solution, but rather has several similar solutions that the ART converges upon given different initial estimates, $\mathbf{x}^0$, of the image. In contrast, when attenuation was considered in the system and a correction was applied, the image solution can vary widely given different initial estimates, $\mathbf{x}^0$, indicating a generally poorly behaved system.

Two approaches to selecting $\mathbf{x}^0$ were studied. In the first, $\mathbf{x}^0$ was set equal to [0.2 ... 0.2] for each view, regardless of whether γ_κ or γ_ρ was being imaged. It was found, however, that the reconstruction of γ_κ data for each detector angle converged upon a view with generally positive pixel amplitudes (since γ_κ was equal to equal to 0.04) with a maximum value of that was in the range of 0.3-0.35. Similarly, the reconstruction of reflectivity data for each detector angle converged upon a view with generally negative pixel amplitudes (since R was equal to -0.509, to yield a γ_ρ equal to 0.0909) with a minimum value that varied between -0.9 and -1. Thus, in a second reconstruction a custom $\mathbf{x}^0$ was determined for each view. For γ_κ imaging, data for the ith view were reconstructed, and the maximum pixel value, η^i, was calculated. $\mathbf{x}^0$ for the reconstruction of the next view was then chosen to be $[\eta^i ... \eta^i]$. Data for the first view was initially processed with $\mathbf{x}^0 = [0.1...0.1]$. The maximum pixel value, η, was determined, $\mathbf{x}^0$ was set equal to $\mathbf{x}^0 = [\eta ... \eta]$, and data for the first view were reprocessed. The case of γ_ρ imaging followed identically, except that instead determining the maximum pixel value for each view, the minimum pixel value was calculated and used as a basis for $\mathbf{x}^0$.

Figures 5.37.A and 5.37.B illustrate the γ_κ and γ_ρ image solutions in the absence of attenuation given the custom varied $\mathbf{x}^0$, while Figures 5.38.A and 5.38.B illustrate the same given a constant $\mathbf{x}^0$. Evidently, the choice of $\mathbf{x}^0$ can have a large effect on the maximum pixel amplitude in the absence of attenuation. Table 5.7 presents the maxi-

Image Type	$\mathbf{x}^0$ **Choice**	**Min (unitless)**	**Max (unitless)**
γ_κ	Constant	0	3.6
γ_κ	Custom Varied	0	43.7
γ_ρ	Constant	0	17.7
γ_ρ	Custom Varied	0	78.2

Table 5.7: The above data compare the maxima and minima for γ_κ and γ_ρ imaging of a grid of points in the absence of attenuation, given a $\mathbf{x}^0$ that is either constant or custom varied.

mum and minimum pixel values for the different images in the absence of attenuation. Although these images are not identical, they are in fact nearly scale versions of one another. To verify this, the images were normalized to one and the power sum residual was computed for the custom varied $\mathbf{x}^0$ image versus the constant $\mathbf{x}^0$ image. The power sum residuals for the γ_κ and γ_ρ images were 0.1% and 2.0%, respectively. As such, there is little difference in the absence of attenuation between the two methods of choosing $\mathbf{x}^0$ after the images are normalized.

The most noticeable effect of the custom varied $\mathbf{x}^0$ method, however, is that it produces very inferior images in the presence of attenuation. Figures 5.37.C and 5.37.D

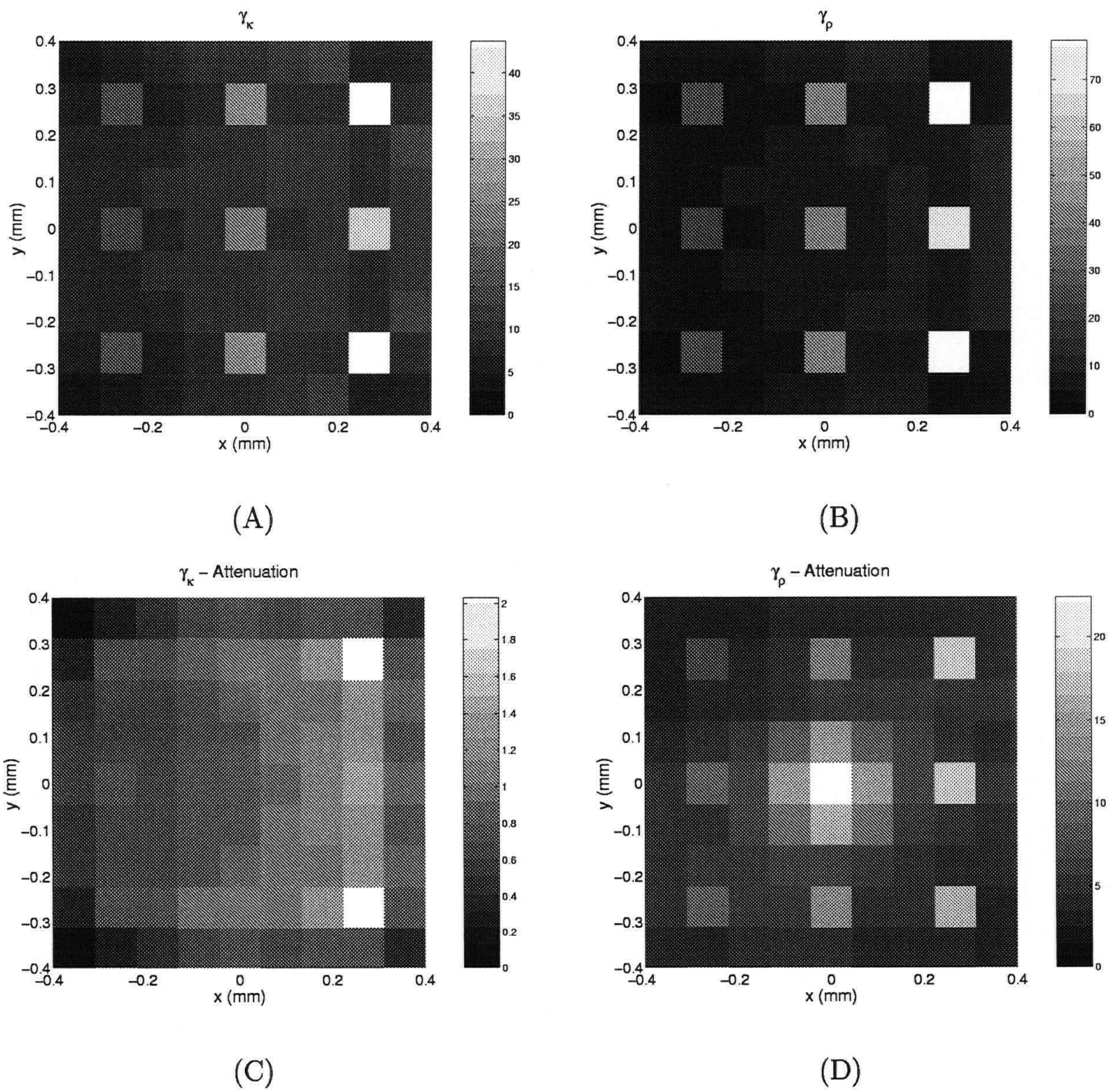

Figure 5.37: Figures A and B illustrate the γ_κ and γ_ρ image solutions for a 3×3 grid of isolated scatter points in the absence of attenuation given the custom varied $\mathbf{x}^0$. Figures C and D illustrate the same in the presence of attenuation.

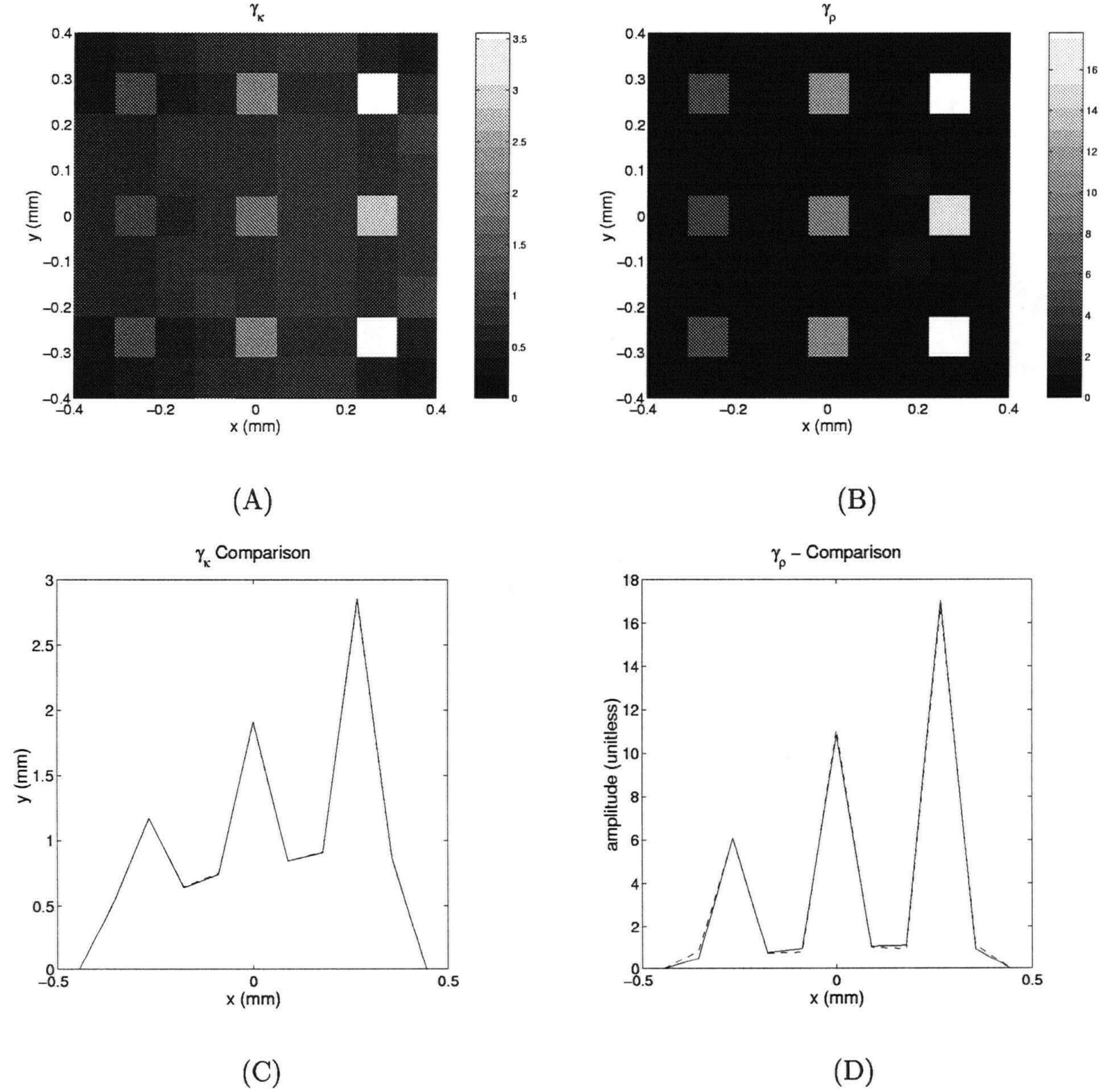

Figure 5.38: Figures A and B illustrate the γ_κ and γ_ρ image solutions for a 3×3 grid of isolated scatter points in the absence of attenuation, with a constant $\mathbf{x}^0$ equal to [0.1 ... 0.1]. Figure C and D compare the x-axis profiles for γ_κ and γ_ρ, respectively, in the presence (dashed line) and absence (solid line) of attenuation. Note that the dashed and solid lines in Figure C overlap identically.

illustrate γ_κ and γ_ρ for the grid in the presence of attenuation given the custom varied $\mathbf{x}^0$. Evidently, the method does not have the ability to correct for attenuation in this particular example. The reconstruction of a square block in Section 5.7.4, however, will illustrate an example in which the custom varied $\mathbf{x}^0$ worked quite well. These studies serve to illustrate that iterative methods do not always behave in an intuitive manner, and that their use requires an extensive understanding of convergence issues.

Returning to the method involving the constant $\mathbf{x}^0$ equal to [0.2 ... 0.2], these preliminary results indicate that the ART is able to reconstruct images well in the presence of attenuation given a $\mathbf{x}^0$ that promotes convergence to valid images. Figures 5.38.C and 5.38.D compare the x-axis profiles with (solid line) and without (dashed line) attenuation for the γ_κ and γ_ρ images, respectively. Note that the corresponding images have not been normalized or scaled in any way. The agreement is so good that the lines are nearly superimposed. In fact, the power sum residual is 0.004% and 0.009% for γ_κ and γ_ρ imaging, respectively.

An important final note regarding the quantitative imaging potential of the ART is that not all the pixels corresponding to water in Figure 5.38 are equal to zero as they should be. In addition, the heights of the peaks do not exhibit the same ratio along each row nor do they exhibit the 1:2:3 ratio exactly. The percentage ratio matrices of the normalized images relative to the actual scatter objects were

$$PR_{\gamma_\kappa} = \begin{bmatrix} 89 & 92 & 103 \\ 112 & 100 & 132 \\ 89 & 92 & 103 \end{bmatrix} \qquad PR_{\gamma_\rho} = \begin{bmatrix} 98 & 93 & 100 \\ 104 & 100 & 105 \\ 98 & 93 & 100 \end{bmatrix} \tag{5.62}$$

Evidently the γ_κ result is problematic in that the points on the positive x-axis has an error of 32%. However, although the ART is not fully quantitative, it behaves comparably with the method by Blackledge *et al.* The average over all entries for the percentage ratio matrices presented in Expression 5.37 (best case scenarios for Blackledge method) were $97 \pm 3\%$ and $95 \pm 4\%$ for γ_κ and γ_ρ, respectively. In comparison, the averages for this example are $100 \pm 14\%$ and $99 \pm 4\%$ for γ_κ and γ_ρ imaging, respectively. Thus, result for γ_κ is reasonable, while that for γ_ρ is better than the result for the method by Blackledge *et al.*

5.7.3 Reconstruction of Points

As in the tests of the method by Blackledge *et al*, imaging experiments were simulated for single isolated points to determine the image resolution capabilities of the ART. In addition, point reconstructions were able to test the ability of the ART to image objects with location $\mathbf{r}$ such that $\frac{|\mathbf{r}|}{|\mathbf{r}_j|}$ is not $\ll 1$, where $\mathbf{r}_j$ is the position vector of either the source or detector. The images were based on 40 views, and the iterative process for each view was begun with a constant $\mathbf{x}^0$ equal to [0.2 ... 0.2].

In the first test, reconstructions were done for a point at (0,0) mm in a non-attenuating background fluid with an acoustic velocity equal to that of water. The point was characterized by γ_κ and γ_ρ equal to 0.04 and 0.0909, respectively. The source and detector were located at a distance of 100 mm from the origin. The data were sampled at both 30 MHz and 45 MHz for comparison. Figures 5.39.A and 5.39.C illustrate the reconstructed PSF's for γ_κ and γ_ρ, respectively, given data sampled at 45 MHz. Figures 5.39.B and 5.39.D illustrate the PSF profiles along radial lines at the angles [0°, 22.5°, 45°, 67.5°]. A profile for 90° is not shown since it is identical to that for 0°. Also, note that the profiles for 22.5° and 67.5° overlap. The FWHM of the γ_κ PSF measured at 0.113 along both the x and y axes is 0.053 ± 0.001 mm. Note that this parameter was found to be equal along both the x and y axes, as was the case for all other cases presented in these sections. Since the cutoff frequency in the data is effectively 9 MHz after the application of the low pass filter, the expected image resolution is approximately 0.08 mm. As such, the ART is provides excellent results in this respect. The FWHM for the γ_ρ PSF measured at a height of 0.285 along both the x and y axes is 0.049 ± 0.001 mm.

Note that the γ_κ reconstruction looks noticeably wider than the γ_ρ reconstruction.

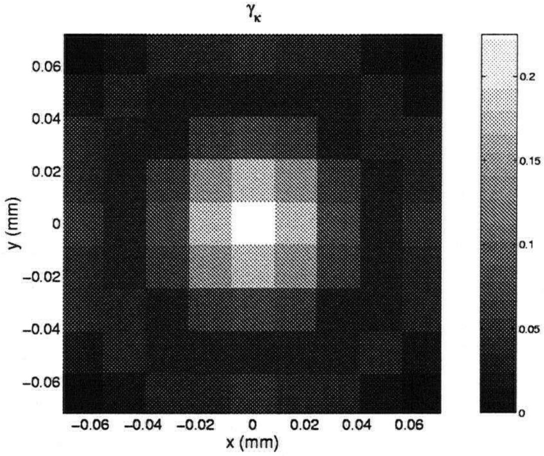

(A)

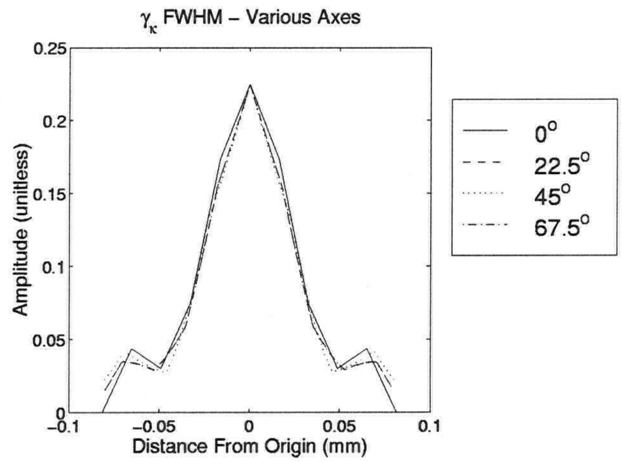

(B)

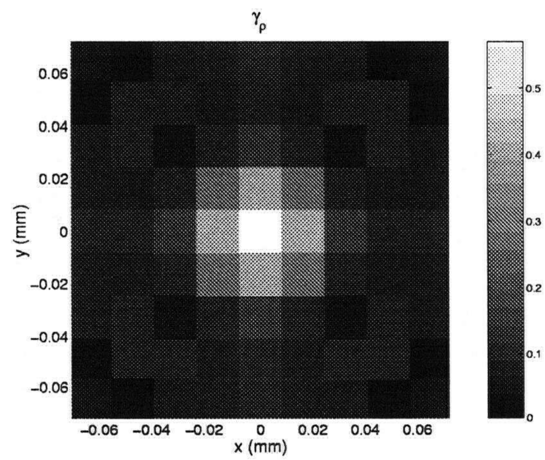

(C)

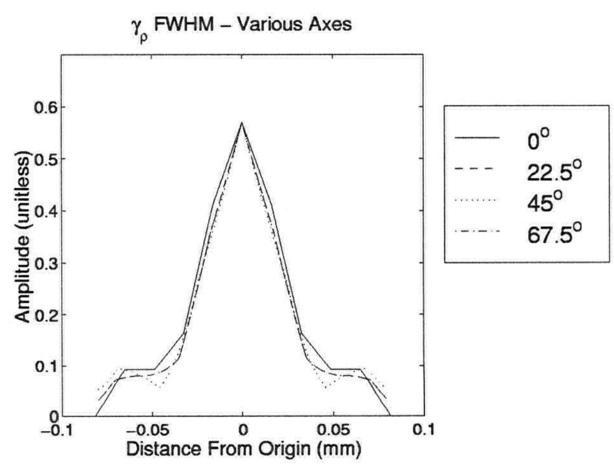

(D)

Figure 5.39: This figure illustrates the reconstructed PSF's for a point located at (0,0) mm with γ_κ and γ_ρ equal to 0.04 and 0.0909, respectively.

Image	Sampling Frequency (MHz)	Maximum (unitless)	ξ (unitless)	Background (unitless)
γ_κ	30	0.224	5.62	~ 0.04
γ_κ	45	0.225	5.61	~ 0.04
γ_ρ	30	0.570	6.27	~ 0.09
γ_ρ	45	0.569	6.25	~ 0.09

Table 5.8: The above data illustrate the maximum pixel values, rough background values and the image normalization factors, ξ, for the various reconstructions of a point at (0,0) mm.

This is simply an artifact of the Matlab^{TM} plotting routine and the image coarseness that results from the necessarily limited number of pixels. In reality, the reconstructions are cylindrically symmetric. This is illustrated in Figures 5.39.B and 5.39.D, which plot the PSF profiles along radial lines at various angles for the γ_κ and γ_ρ images, respectively. The average FWHM for the γ_κ image is 0.051 ± 0.001 mm, while that for the γ_ρ image is 0.048 ± 0.001 mm.

The FWHM along the x and y axes given data sampled at 30 MHz was again 0.053 ± 0.001 mm for γ_κ and 0.049 ± 0.001 mm for γ_ρ. The average FWHM over radial lines at angles of [0°, 22.5°, 45°, 67.5°] was 0.052 ± 0.001 mm for γ_κ and 0.047 ± 0.002 mm for γ_ρ. It should also be noted that as expected the PSF height scaled directly with the actual value of the corresponding γ_κ or γ_ρ. The PSF heights were nearly identical for the same image type with data sampled at 30 MHz and 45 MHz, and the nonzero background values were the same. Table 5.8 outlines the maximum pixel values, normalization factors (ξ) required to reproduce the original object, and the rough background values of the images.

The second set of simulations tested the ability of the ART to reconstruct images for a point for which $\frac{|\mathbf{r}|}{|\mathbf{r}_j|}$ was not much less than 1. Recall from Section 5.3.2 that the method by Blackledge *et al* had difficulty with this and produced halos rather than Gaussian PSF's as a result of the simplifying assumptions used in the derivation of the image reconstruction algorithm. Experimental parameters were identical to those in the previously reported simulation, except that the source and detector were a distance of 2 mm from the origin, the point was located at (-0.7,0) mm, and there were 100 views of data. Figures 5.40.A and 5.40.B illustrate the reconstructed PSF's for γ_κ and γ_ρ, respectively. For comparison, Figure 5.40.D presents the γ_κ PSF for image reconstruction using the method by Blackledge *et al*, given the same simulation conditions. Evidently, the ART produces a far superior well-defined Gaussian PSF based on far less data, as compared to the halo-shaped PSF in Figure 5.40.D. Figure 5.40.C illustrates the normalized x-axis profiles for the two ART produce images. Evidently, the γ_ρ profile is much neater in terms of shape and background than the γ_κ profile. Note that the FWHM values are wider than for the previously shown point at the origin. However, the point-spread-function FWHM for γ_κ and γ_ρ measured along both the x and y axes is 0.051 ± 0.001 mm and 0.048 ± 0.001 mm, respectively, which agree within error with the values for the point at the origin given 45 MHz data sampling. The average FWHM over radial lines at angles of [0°, 22.5°, 45°, 67.5°] was 0.051 ± 0.002 mm for γ_κ and 0.046 ± 0.002 mm for γ_ρ. Not only are the FWHM values comparable, but the heights of the point-spread-functions for the off center point are very close to those for the point at the origin. The maximum pixel values in the γ_κ and γ_ρ images for the off center point are 0.227 and 0.571, respectively, and these differ by only 0.9% and 0.4% from the values for the point at the origin. Given that $\frac{|\mathbf{r}|}{|\mathbf{r}_j|} = 0.35$ for this example, the algebraic reconstruction technique behaves very well and in a far superior manner when compared to the method by Blackledge *et al*. Recall from Section 5.3.2 that, for the latter method, the PSF for a point at (5,5) mm for which $\frac{|\mathbf{r}|}{|\mathbf{r}_j|} = 0.05$ had a halo shape and an amplitude that was reduced by 92% when compared to a point at the origin.

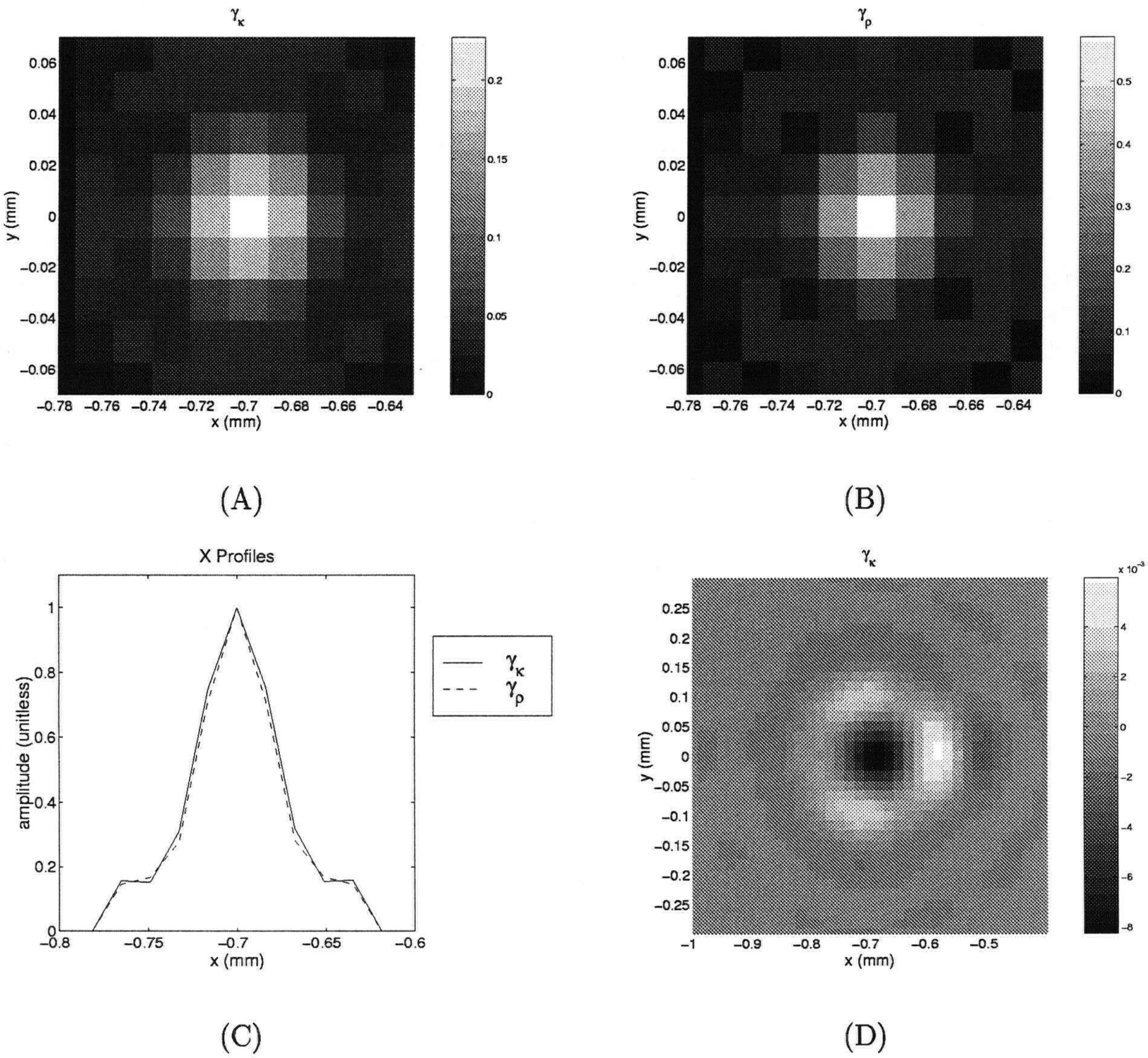

Figure 5.40: Figures A and B illustrate the reconstructed PSF's for a point located at (-0.7,0) mm with γ_κ and γ_ρ equal to 0.04 and 0.0909, respectively. Figure D presents the γ_κ PSF for the same point reconstructed under the same conditions using the method by Blackledge *et al*. Figure C presents the normalized x-axis profiles of the images produced via the ART.

Image	Attenuation	Pixel Average Over Disc (unitless)
γ_κ	N	2.01 ± 0.03
γ_κ	Y	1.96 ± 0.03
γ_ρ	N	6.7 ± 0.2
γ_ρ	Y	6.5 ± 0.1

Table 5.9: The above data present the average pixel value over a disc of radius 0.19 mm for the γ_κ and $\gamma_r ho$ of the square block using the ART.

5.7.4 Reconstruction of a Square Block

This section provides an idea of the ability of the ART to reconstruct objects that have a plateau region. Results are presented for a square block of width 0.38 mm with γ_κ and γ_ρ equal to 0.04 and 0.0909, respectively. The data were sampled at 45 MHz. Attenuation in tissue was again scaled up by a factor of 1000, and attenuation in water was left as is. The source and detector were again placed at a distance of 2 mm from the origin. $\mathbf{x}_0$ was varied for each angle of data based on the maximum value (for γ_κ) or minimum value (for R) of the reconstruction for the previous view.

Figures 5.41.A and 5.41.B illustrate the reconstructed γ_κ and γ_ρ images in the absence of attenuation, while Figures 5.41.C and 5.41.D compare the x-axis profiles for the original image and the reconstruction in both the presence and absence of attenuation for γ_κ and γ_ρ, respectively. Note that the image figures are not normalized, whereas the x-axis profiles all correspond to normalized images. The images reconstructions in the presence of attenuation were very similar in shape to their counterparts in the absence of attenuation. With normalization, the corresponding power sum residuals for γ_κ and γ_ρ imaging were 0.15% and 0.06%, respectively. It should be noted that the ART produced reconstructions with a definite plateau region, and Table 5.9 presents the average pixel value over a disc of radius 0.19 mm centered on the origin. Evidently, determining a custom $\mathbf{x}^0$ for each view worked well in this example, particularly in the case of γ_ρ reconstructions.

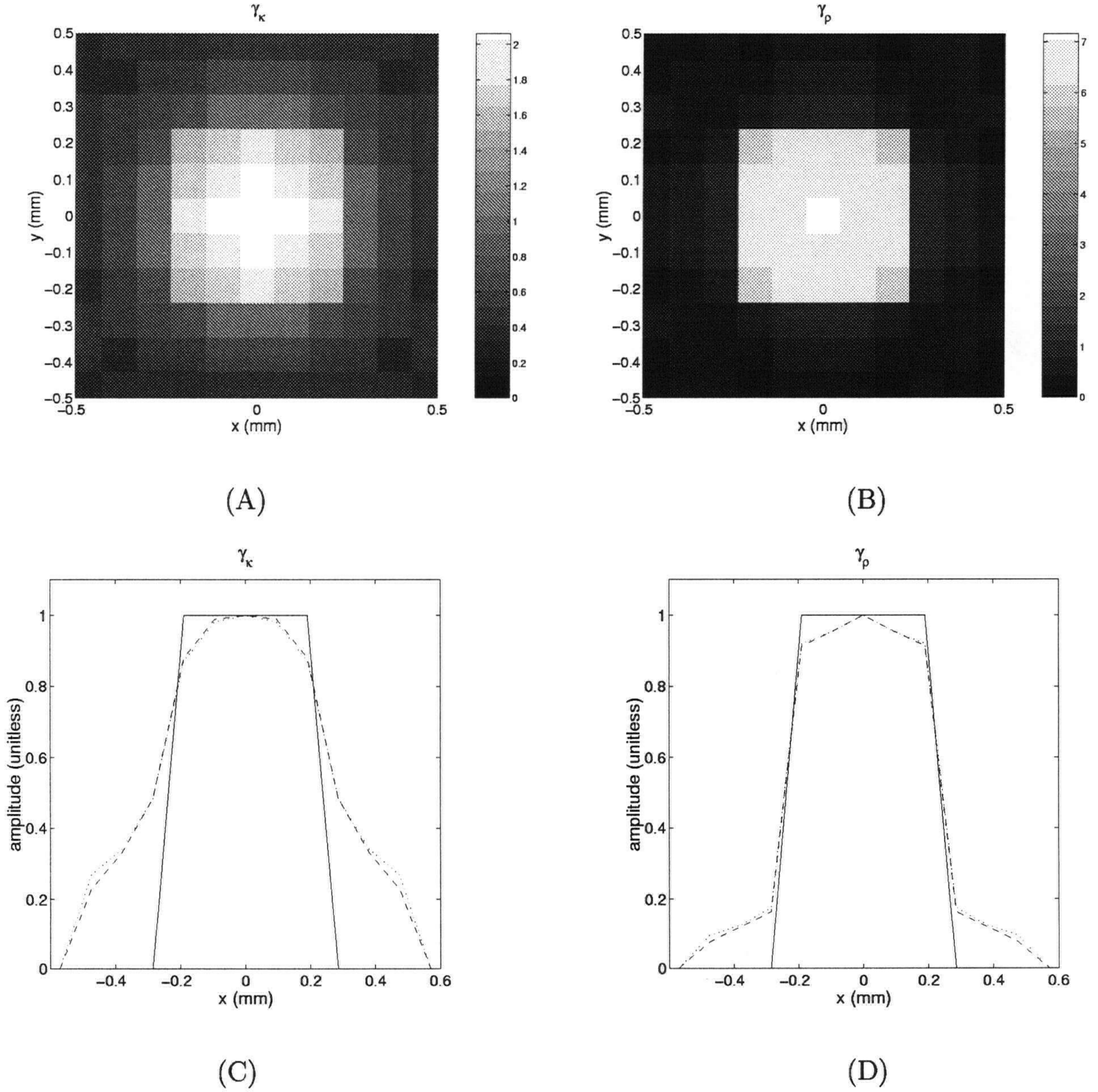

Figure 5.41: Figures A and B illustrate the γ_κ and γ_ρ reconstructions, respectively, in the absence of attenuation for a square block of width 0.38 mm and with γ_κ and γ_ρ equal to 0.04 and 0.0909, respectively. Figures C and D compare the normalized x-axis profiles for the original image (solid line), and the reconstructed γ_κ and γ_ρ in the presence (dotted line) and absence (dashed line) of attenuation.

Chapter 6
Conclusions and Future Work

6.1 General Remarks

This thesis entailed significant development and testing of a prototype scanner for pulsed ultrasound computed tomography that is aimed at reconstructing 2D cross-sections of spatially varying γ_κ and γ_ρ. In particular, compressibility beyond the palpable region can be investigated only through ultrasound imaging, and this information may be highly useful for tissue characterization. At the beginning of this work, it was hoped that a system could be developed that would lay the groundwork for a future scanner for use in the early detection of breast cancer. To this end, a direct Fourier method introduced by Blackledge *et al* was incorporated into the system, as well as an algebraic reconstruction technique involving attenuated propagators that was developed in this thesis. Both Fourier and wavelet based digital signal processing methods were also incorporated to remove noise from the data. A proof of concept study has been completed that has illuminated the capabilities and limitations of this first generation UCT scanner. Furthermore, a strong foundation has been laid for continued work in pulsed UCT, which is a new area of research in the Cancer Imaging Department of the BC Cancer Research Centre.

It was hypothesized that this system would be able to reconstruct quantitative images with resolution on the order of 1 mm, thereby providing a basis upon which to build a second generation system for use in the early detection of breast cancer. The major focus of this thesis was therefore the testing of the scanner in simulation. This provided a controlled environment in which to observe algorithm behavior under the best conditions.

The reconstruction algorithm by Blackledge *et al* has been thoroughly examined, and key preliminary studies of the ART have been conducted. In addition, the method by Blackledge *et al* has been tested in a tissue phantom experiment.

Contrary to the hypothesis, the method by Blackledge *et al* works well in only very limited cases. For instance, there is excellent image resolution of ~ 0.07 mm for points in the absence of attenuation for which $|\mathbf{r}| < 0.05|\mathbf{r}_j|$, where $\mathbf{r}_j$ is the distance from either the source or detector to the origin. Grids of such points were reconstructed in a quantitative fashion to within 5% of their actual values of γ_κ and γ_ρ. However, this method has far more limitations than capabilities due primarily to the lack of an available attenuation correction, an inherent TOF error, and lack of a model that can very accurately describe real-world transducers. These factors currently prevent the method from reconstructing quantitative images with useful resolution in most simulated and experimental settings.

The ART performed dramatically better. It consistently exhibited image resolution of ~ 0.05 mm for points with $|\mathbf{r}|$ equal to at least $0.3|\mathbf{r}_j|$ in both the absence and presence of attenuation. This method also reconstructed grids of such points in a quantitative manner to within 1% of their actual values. Most important, in simulation the ART was able to properly correct for attenuation to within an error of less than 0.2%. However, the algebraic reconstruction technique has difficulty converging on an image solution for γ_κ and γ_ρ cross-sections of more than 20×20 pixels, currently rendering it impractical. These theoretical results do indicate, though, that the method holds promise.

The non-periodic nature of the pulsed UCT data motivated the study of wavelet denoising methods, with appropriate wavelet families used in both the simulation environment and the experimental setting. Typical theoretical data required smoothing with a moving average filter after wavelet filtering in order to remove residual choppy features, and these data resulted in an image that had only 9% less error (relative to noiseless data) as compared to data processed solely with the moving average filter. In the experimental setting, wavelet analysis performed no better than lowpass Butterworth filtering with respect to noise removal.

The effect of dispersion on image reconstruction was studied for the method by Blackledge *et al* and shown to have a dramatic effect on algorithm performance. A typical value of 1% dispersion over 1-20 MHz had the effect of distorting Gaussian point-spread-functions into halo-shaped functions with amplitudes dramatically reduced by a factor of ~ 250. This was due to the destruction of valid phase information in the modelling of the scattered ultrasound field. A correction based on knowledge of the dispersive speed of sound was able to restore the PSF to within reasonable limits, with percentage errors of 26%, 4% and 9% in the minimum, maximum and range, respectively, of the corrected γ_κ cross-section. Although dispersion was not studied for the ART, it will indeed have a similar effect on the image reconstruction process since field phase information is equally important in this method. As such, precise knowledge of the dispersive nature of the speed of ultrasound in tissue and water is required in order to develop pulsed ultrasound computed tomography into a viable imaging technique.

This thesis has shed light on several areas that are in need of further research in order to develop a potentially viable imaging system. These areas involve the application of better digital signal processing techniques for noise removal, the modification of the scanner with respect to the stepper motor apparatus and the source, and the improvement of the reconstruction algorithms in terms of attenuation correction and isochrone warping in the method by Blackledge *et al*, and the problem of convergence in the algebraic reconstruction technique. These future directions are discussed in the following sections.

6.2 Key Future Work

6.2.1 Apparatus Improvements

Of primary importance to the success of the method by Blackledge *et al* is the incorporation of a pulsed cylindrical source whose field is identically described by the 2D Green's function propagator. This source model is necessary for the mathematics to reduce to a tractable method. Both the amplitude and Fourier phase characteristics of the field as a function of space and frequency must be modelled by the Green's function, and ideally the source would have zero phase at its face as well. It was expected that the Panametrics beam source would not necessarily be modelled identically by the 2D Green's function, but the line source theoretically should have been. However, it was found that the model varied from reality to a greater extent with the line source than with the Panametrics source. As such, it may not be possible to obtain a source that identically fits the model. The scientific literature currently does not offer an answer due to the lack of experimental studies in pulsed ultrasound computed tomography. It may ultimately be necessary to have a transducer custom-made to fit the model as closely as possible.

Due to the 3D nature of ultrasound propagation, it may be that even a custom made source will not be described by the 2D Green's function to within an acceptable error. An alternative may be to commission the surveying of the field from a suitable source at a continuum of points in space. From these data, a frequency dependent function of the source phase and amplitude characteristics could be built up throughout the imaging space. This would, of course, be an expensive option. Furthermore, this would require development of the algebraic reconstruction technique, since it is the only one of the two methods in which a general propagator can be incorporated. Essentially, a specialized propagator would be used to model the source field, and the 2D Green's function would be used initially to model scatter propagation. A 3D propagator could eventually be included for scatter. A discussion regarding development of the ART is included in Section 6.2.4.

The stepper motor apparatus must also be redesigned and rebuilt. It is suggested by this author that a gear mechanism be installed, with a separate gear controlling the movement of each of the source and detector transducer arms. This design will avoid the use of a bushing mechanism that is susceptible to corrosion. Although it will not be possible to attain the maximum possible theoretical resolution of $\lambda/2$, where λ is the maximum frequency in the source spectrum, the apparatus will work well and afford resolutions on the order of 1 mm, which is sufficient for the early detection of breast cancer [69].

6.2.2 Improved Digital Signal Processing

Both the theoretical and experimental tests of wavelet denoising suggest that this method may be limited in its ability to reduce noise in UCT data. In simulation, the moving average filter was equally effective for removing noise, and in experimental tests, wavelet filtering fared no better than lowpass Butterworth filtering. It is true that the success of wavelet denoising often depends on the creation of a custom wavelet family that mimics the ultrasound data features. However, the Daubechies 20 mother wavelet illustrated in Figure 5.33 indeed mimics the general features of the experimental data, yet wavelet denoising was no more effective than lowpass filtering. It is suggested that some effort be directed towards defining and testing a custom wavelet family based on the data features in order to obtain closure regarding this area of research.

6.2.3 Improvement of Method by Blackledge *et al*

Incorporation of Elliptical Projections

Section 5.1.3 illustrated that the elliptical data isochrones are "warped" into lines due to the simplifying assumption that $\frac{|\mathbf{r}|}{|\mathbf{r}_d|} = \frac{|\mathbf{r}|}{|\mathbf{r}_s|} << 1$, which is applied in the development of the reconstruction algorithm. In particular, this assumption leads to an approximate $S_{\mathbf{r}_j}$ function in the 2D propagator that overestimates the TOF of ultrasound from scatter points not located at the origin. The overestimation error increases with distance from the origin. The simplifying assumptions are necessary for tractable mathematics leading to the tomographic algorithm. The TOF errors had the effect of creating low amplitude halo-shaped point-spread-functions, rather than full height Gaussian PSF's, even for points with $\frac{|\mathbf{r}|}{|\mathbf{r}_d|}$ as small as 0.05. This effect is a significant result that seriously limits the capabilities of this reconstruction algorithm.

Section 2.3 illustrated that the isochrone "warping" manifests itself in each view through the reconstruction of a partial image of consecutive linear isochrones that are parallel to the line joining the source and detector. The intensity of each isochrone is directly proportional to the intensity of the point in the data signal with the TOF corresponding to the isochrone. It was shown that in the absence of time-of-flight error, these curves would be elliptical rather than linear. As such, a spatial correction must be developed that can be applied to each view in order to redistribute the image intensity into the proper pixels. The same correction can be applied to each view as it will depend only on the relative position of the source and detector, which defines the TOF information. The correction would follow from the geometrical description of the isochrones discussed in Section 2.3. Upon correcting the partial image for each view angle, the images can be summed to obtain an improved cross-section of γ_κ or reflectivity.

Incorporation of a Narrow-Beam Source

An important extension to the method by Blackledge *et al* would be the incorporation of a narrow beam pulsed field to replace the cylindrical field. The creation of a field with a width on the order of 1 mm is quite feasible with conventional phased array technology. This source would facilitate the application of a spatial mask to the partial image reconstructed for each view angle. The mask would be defined by the insonification region. Information would thus be dramatically more localized in each view, which should result in an improved cross-section of γ_κ or reflectivity upon the summation of the partial images.

The narrow beam source would also facilitate a frequency dependent attenuation correction. In the data region of the signal detected at each angle, the time samples could be corrected as follows. A group of 64 points, herein termed a signal portion, can be extracted with the time sample in question at the center. The TOF values in tissue of the samples in the signal portion differ by a maximum of $\sim 1.1\mu s$, and the corresponding attenuation in tissue varies over the small range of $\sim 0.01 - 0.6$ db (0.007-0.07% of field amplitude). The average TOF in tissue can be calculated for the time samples in the signal portion, and this can be used to determine a frequency dependent correction for the FFT of the signal portion. Given the small range of TOF values, this should not result in significant error over the points. The least amount of error will be associated with the point at the center of the signal portion. A correction can similarly be applied for attenuation in water. Upon correcting the FFT, the data can be inverse transformed to produce a corrected signal portion in the time domain. The time point at the middle can now be extracted to replace its corresponding point in the original signal. A first order image can be reconstructed with data that have been corrected by assuming an average attenuation coefficient throughout the tissue. The original data can then be corrected again using the attenuation characteristics determined by the first order image. A second and likely better image can be reconstructed using these data. This process can be repeated until there is little change in the image.

Again, the amplitude and Fourier phase characteristics of the field as a function of space and frequency must be modelled by the 2D propagator in order to incorporate a narrow beam source into the reconstruction algorithm by Blackledge *et al.* Combined with a spatial mask corresponding to the insonification region, this source model may be feasible. If, on the other hand, a specialized source propagator must be determined through an analysis of the field surveyed at a continuum of points in the insonification region, the narrow beam source can only be incorporated into the ART. Development of the method using a narrow beam field can be tested in a prototype using a specialized narrow beam source kindly provided by Mr. Jerry Posakony. This pulsed source has a field with FWHM values of 3-5 mm over the distance of 3-7 cm from the transducer. As such, it may be sufficient for use in a proof of concept study. Issues involved in the development of the algebraic reconstruction technique are discussed in the next Section.

6.2.4 Improvement of the Algebraic Reconstruction Technique

The ART must be substantially improved so that it can reconstruct images with dimensions greater than 20×20 pixels. An analysis of the condition number of the attenuated propagator matrix, $\mathbf{T}$, indicates that it is ill-conditioned. The condition number of the coefficient matrix $\mathbf{A}$ of a linear system, $\mathbf{y} = \mathbf{A}\mathbf{x}$, is a nonnegative number that estimates the amount by which small errors in either $\mathbf{y}$ or $\mathbf{A}$ can change the solution, $\mathbf{x}$. A small condition number suggests that the iterative solution of the system will not be sensitive to errors, while a large condition number indicates that small data or arithmetic errors may result in enormous errors in $\mathbf{x}$. The condition number for a matrix $\mathbf{A}$ is usually defined by

$$\text{Condition}(\mathbf{A}) = ||\mathbf{A}|| \cdot ||\mathbf{A}^{-1}|| \tag{6.1}$$

A condition number of infinity indicates that $\mathbf{A}$ is not invertible. For the various reconstructions attempted, the attenuated propagator matrix had a condition number that varied from a value on the order of 10^{20} to a value of infinity. This indicates that the systems were very ill-conditioned, which explains the difficulty in obtaining convergence. As such, in order to develop a viable reconstruction algorithm, research must be done to determine if the matrix system can be pre-conditioned using existing algorithms in mathematics.

It is suggested that the focus of this research be the method of singular value decomposition (SVD). This is a least squares approximation method that can be used to solve for $\mathbf{x}$ in the equation $\mathbf{y} = \mathbf{A}\mathbf{x}$, when $\mathbf{A}$ is singular and the system is ill-conditioned. In brief, when $\mathbf{A}$ is a matrix of dimension $M \times N$, where $M \geq N$, this method decomposes $\mathbf{A}$ into the following:

$$\mathbf{A} = \mathbf{U} \cdot \mathbf{W} \cdot \mathbf{V}^{\mathbf{T}} \tag{6.2}$$

$\mathbf{U}$ and $\mathbf{V}$ are both column-orthogonal matrices, with dimensions $M \times N$ and $N \times N$, respectively. The matrix $\mathbf{W}$ is a diagonal matrix with elements w_j greater than or equal to zero (the singular values) [74]. SVD then works with this decomposition of $\mathbf{A}$ to solve for $\mathbf{x}$ via a least squares approximation algorithm. An alternative and potentially better solution may also be possible through the application of thresholding to the $\mathbf{W}$ matrix. This is the standard process of zeroing small w_j's, which are responsible numerically for the ill-conditioning of $\mathbf{A}$.

The condition of the matrix system can also likely be improved if a narrow beam pulsed ultrasound field could be incorporated into the ART. The propagation matrix would thus become sparse due to the narrow insonification region. The matrix system may then reduce to a form that can be solved in a fast and feasible manner using iterative techniques. With the introduction of this source, the attenuation correction described in Section 6.2.3 would not be necessary since the propagators are attenuated. However, the concept of reconstructing successive images with an increasingly better characterization of attenuation should also be applied here. The first image can be obtained assuming an average attenuation. A second image can then be reconstructed using propagators that embody the attenuation information of the first image. This process can be repeated until there is little change in the image.

6.3 Additional Future Work

6.3.1 Tests with Better Phantoms

Extensive expansion of the experimental work is required to fully test the prototype UCT scanner. Upon improvement of the reconstruction algorithms, a CIRS$^{\text{TM}}$ 3D ultrasound calibration phantom should be acquired to test the system resolution. This phantom mimics average human tissue with inclusions similar to tumors with various sizes and attenuation coefficients. Additional tissue equivalent phantoms can also be constructed with inclusions to mimic inhomogeneities in tissue. A method should be devised for coating the phantoms with a substance that is relatively impervious to water.

6.3.2 Stacking of Planar Views to Create 3D Images

The present UCT prototype uses algorithms that include a 2D model of sound propagation to provide 2D planar cross-sections of γ_κ and reflectivity through the object. This is in keeping with the majority of UCT reconstruction algorithms [21, 32, 47, 53, 80]. The methods could be extended to combine consecutive, stacked planar images into a 3D composite image, properly accounting for overlapping pixels in neighbouring planes. Visualization software must also be written that can change the image orientation and scan through the different planes. The UCT scanner must also be modified to include the automated and accurate vertical movement of the transducers.

6.4 Final Remarks

In closing, extensive new results have been established regarding the potential viability of pulsed ultrasound computed tomography using both a direct Fourier method and an algebraic reconstruction technique. It has become evident in the course of this work that pulsed UCT is an involved and multifaceted problem that requires extensive research and development. With continued effort in the key areas discussed in the preceding sections, it is possible that pulsed UCT could become a viable imaging technique. Given the results and the potential for dramatic improvements in the ART through the application of conditioning algorithms such as SVD, it is possible that reasonably sized images of γ_κ and γ_ρ in attenuating media may be reconstructed with a second generation system. However, there is still a substantial amount of work to be done before this can potentially be achieved.

Bibliography

[1] American Cancer Society. **Breast Cancer Facts & Figures 1999-2000**. Atlanta: American Cancer Society (1999).

[2] American Institute of Ultrasound in Medicine. From the website "www.aium.org/stmts.htm#Safety in Training and Research," 1997.

[3] B.K. Alsberg, A.M. Woodward, M.K. Winson, J. Rowland, D.B. Kell, "Wavelet Denoising of Infrared Spectra," Online publication at "http://gepasi.dbs.aber.ac.uk/bka/articles/denoise/denoiana.htm," University of Wales, Institute of Biological Sciences (1997).

[4] B. Amini, M. Bjorklund, R. Dror, A. Nygren. **Tomographic Reconstruction of SPECT Data**. Web document, Rice University, 1997.

[5] ATL Ultrasound. **Fact Sheet on Breast Cancer**. Bottell, Washington: ATL Ultrasound.

[6] ATL Ultrasound. **White Paper on High Definition Imaging**. Bottell, Washington: ATL Ultrasound.

[7] L. W. Bassett, R.H. Gold, C. Kimme-Smith. **Hand-Held and Automated Breast Ultrasound**. New Jersey: Slack (1986)

[8] R.L. Bedi, A.R. Selfridge, "Acoustic Wave Sensor and Method of Making Same," United States Patent No. 5155708, October 13, 1992.

[9] B. Benoit. From the website "myweb.worldnet.net/~henrib/3Dpage3/3D_ultra3frame.html."

[10] J.M. Blackledge, R.E. Burge, K.I. Hopcraft, R.J. Wombell, "Quantitative Diffraction Tomography: I. Pulsed Acoustic Fields," **Journal of Physics D: Applied Physics**, **20**, No. 1, p. 1 (1987).

[11] D.T. Borup, S.A. Johnson, M.J. Berggren, "Nonperturbative Diffraction Tomography via Gauss-Newton Iteration Applied to the Scattering Integral Equation," **Ultrasound Imaging**, **14**, p. 69 (1992).

[12] E.O. Brigham. **The Fast Fourier Transform and Its Applications**. New Jersey: Prentice-Hall (1988).

[13] R.L. Burden, J.D. Faires. **Numerical Analysis**. Boston: PWS-Kent Publishing Company (1989).

[14] M.M. Burlew, E.L. Madsen, J.A. Zagzebski, R.A. Banjavic, S.W. Sum, "A New Ultrasound Tissue-Equivalent Material," **Radiology**, **134**, p. 517 (1980).

[15] P.H. Carter, "Unknown Transient Detection using Wavelets," **SPIE Proceedings: Wavelet Applications**, **2242**, p. 803 (1994)

[16] T.J. Cavicchi, "Matrix Solution of Transient High-order Ultrasonic Scattering," **The Acoustical Society of America**, **90**, No. 2, Part 1, p. 1085 (1991).

[17] T.J. Cavicchi, W.D. O'Brien, "Numerical Study of Higher-order Diffraction Tomography Via the Sinc Basis Moment Method," **Ultrasonic Imaging**, **11**, p. 42 (1989).

[18] I. Daubechies. **Ten Lectures on Wavelets**. In Volume 61 of the CBMS-NSF regional conference series in applied mathematics. Philadelphia: Society for Industrial and Applied Mathematics Press, p. 194 (1992).

[19] C.E. E. Davila, "Lecture Notes for EE5340 - Introduction to Biomedical Engineering," Electrical Engineering Department, Southern Methodist University, Dallas, TX, Copyright 1997.

[20] W.J. Davros, J.A. Zagzebski, E.L. Madsen, "Frequency-Dependent Angular Scattering of Ultrasound by Tissue-Mimicking Materials and Excised Tissues," **Journal of the Acoustical Society of America**, **80**, No. 1, pp. 229-237, 1986.

[21] A.J. Devaney, "A Filtered Backpropagation Algorithm for Diffraction Tomography," **Ultrasonic Imaging**, **4**, p. 336 (1982).

[22] A.J. Devaney, "Diffraction Tomographic Reconstruction from Intensity Data," **IEEE Transactions on Image Processing**, **1**, No. 2, p. 221 (1990).

[23] A.J. Devaney, "Inverse Source and Scattering Problems in Ultrasonics," **IEEE Transactions on Sonics and Ultrasonics**, **SU-30**, No. 6, p. 355 (1983).

[24] D.L. Donoho, "De-noising by soft-thresholding," **IEEE Transactions on Information Theory**, **41**, No. 3, p. 613 (1995).

[25] D. Donoho, "Nonlinear Wavelet Methods for Recovery of Signals, Densities, and Spectra from Indirect and Noisy Data," in **Different Perspectives on Wavelets: Proceedings of Symposia in Applied Mathematics, Vol. 47**. I. Daubechies ed. Providence, Rhode Island: American Mathematical Society, p. 173 (1993).

[26] D.W. Dudley. **Practical Gear Design**. New York: McGraw-Hill (1954).

[27] D.W. Dudely. **Dudley's Gear Handbook**. New York: McGraw-Hill (1991).

[28] R.L. Egan. **Breast Imaging: Diagnosis and Morphology of Breast Diseases**. Toronto: W.B. Saunders Company (1988).

[29] M. Fatemi, A.C. Kak, "Ultrasonic B-scan Imaging: Theory of Image Formation and Technique for Restoration," **Ultrasonic Imaging**, **2**, p. 1 (1980).

[30] S. Finette, "A Computer Model of Acoustic Wave Scattering in Soft Tissue," **IEEE Transactions on Biomedical Engineering**, **BME-34**, No. 5, p. 336 (1987).

[31] S.W. Fletcher, W. Black, R. Harris, "Report of the International Workshop on Screening for Breast Cancer," **Journal of the National Cancer Institute**, **85**, p. 1644 (1993).

[32] L.-J. Gelius, I. Johansen, N. Sponheim, J.J. Stamnes, "A Generalized Diffraction Tomography Algorithm," **Journal of the Acoustical Society of America**, **89**, No. 2, p. 523 (1991).

[33] S.A. Goss, R.L. Johnston, F. Dunn, "Compilation of Empirical Ultrasonic Properties of Mammalian Tissues," **Journal of the Acoustical Society of America**. **68**. p. 93 (1980).

[34] A.L. Graps, "An Introduction to Wavelets," **IEEE Computational Sciences and Engineering**, **2**, No. 2, p. 50 (1995).

[35] J.F. Greenleaf, R.C. Bahn, "Clinical Imaging with Transmissive Ultrasonic Computerized Tomography," bf IEEE Transactions on Biomedical Engineering, **BME-28**, No. 2, p. 177 (1981).

[36] J.F. Greenleaf, A. Chu, "Multifrequency Diffraction Tomography," **Acoustical Imaging**, **13**. New York: Plenum, p. 43 (1983).

[37] J.F. Greenleaf, S.A. Johnson, S.L. Lee, G.T. Herman, E.H. Wood, "Algebraic Reconstruction of Spatial Distributions of Acoustic Velocities in Tissue from their Time-of-Flight Profiles," **Acoustical Holography**, **6**. New York: Plenum, p. 71 (1975).

[38] M. Greenspan, C. Tschiegg, **Journal of the Acoustical Society of America**, **31**, p. 75 (1959).

[39] M. Hanke. **Conjugate Gradient Type Methods for Ill-posed Problems**. New York: Wiley (1995).

[40] C.D. Hodgeman, ed. **C.R.C. Standard Mathematical Tables**. Cleveland: Chemical Rubber Publishing Company, 12th Edition (1959).

[41] D.H. Howry, W.R. Bliss, "Visualization of the Soft Tissue Structures of the Body," **Journal of Laboratory and Clinical Medicine**, **40**, p. 579 (1952).

[42] D.H. Howry, D.A. Scott, W.R. Bliss, "The Ultrasonic Visualization of Carcinoma of the Breast and Other Soft Tissue Structures," **Cancer**, **7**, p. 354 (1954).

[43] D. Hykes, W.R. Hedrick, D.E. Starchman. **Ultrasound Physics and Instrumentation**. New York: Churchill Livingstone, 1985.

[44] K. Iwata, R. Nagata, "Calculation of Refractive Index Distribution from Interferograms using the Born and Rytov's [*sic*] Approximations," **Japan. J. Appl. Phys.**, **14**, p. 1921 (1975).

[45] J.A. Jensen. **Linear Description of Ultrasound Imaging Systems**. Copenhagen: Technical University of Denmark (1999).

[46] H.W. Jones, "Recent Activity in Ultrasonic Tomography," **Ultrasonics**, **31**, No. 5, p. 53 (1993)

[47] A.C. Kak, M. Slaney. **Principles of Computerized Tomographic Imaging**. New York: IEEE Press (1988).

[48] M. Kaveh, R.K. Muller, R.D. Iverson, "Ultrasonic Tomography Based on Perturbation Solutions of the Wave Equation," **Computer Graphics and Image Processing**, **9**, p. 105 (1979)

[49] M. Kaveh, M. Soumekh, "Unified Frequency-Domain Image Reconstruction," in **Mathematics in Signal Processing: Based on the Proceedings of a Conference Organized by the Institute of Mathematics and Its Applications on Mathematics in Signal Processing**, ed. by T.S. Durrani. Oxford: Clarendon Press, p. 333 (1987).

[50] L.E. Kinsler, A.E. Frey. **Fundamentals of Acoustics**. New York: John Wiley & Sons (1962).

[51] F.W. Kremkau. **Diagnostic Ultrasound: Principles, Instrumentation, and Exercises**. Montreal: Grune & Stratton (1984).

[52] C.C. Kuni. "Mammography in the 1990's: A plea for Objective Doctors and Informed Patients," **American Journal of Preventative Medicine**, **9**, p. 185 (1993).

[53] K.T. Ladas, A.J. Devaney, "Application of an ART Algorithm in an Experimental Study of Ultrasonic Diffraction Tomography," **Ultrasonic Imaging, 15**, p. 48 (1993).

[54] L.D. Landau, E.M. Lifshitz. **Theory of Elasticity**. New York: Pergamon Press (1970).

[55] D.R. Lide, ed. **CRC Handbook of Chemistry and Physics**. New York: CRC Press (1997).

[56] L.C. Ludeman. **Fundamentals of Digital Signal Processing**. New York: Harper & Row (1986).

[57] **A Wavelet Tour of Signal Processing, 2nd Edition**. New York: Academic Press, (1999).

[58] The Mathworks. **Matlab^{TM}: The Language of Technical Computing - Using Matlab Version 5**. Natick, MA: The Mathworks, Inc., (1997).

[59] A.B. Miller, R.D. Bulbrook, "UICC Multidisciplinary Project on Breast Cancer: The Epidemiology, Aetiology and Prevention of Breast Cancer," **International Jouranl of Cancer, 37**, p. 173 (1986).

[60] M. Misiti, Y. Misiti, G. Oppenheim, J.M. Poggi. **Wavelet Toolbox - For Use with Matlab^{TM}**. Natick, Massachusetts: The Mathworks (1996).

[61] G.W. Mitchell, L.W. Bassett (eds). **The Female Breast and Its Disorders**. Baltimore: Williams & Wilkins (1990).

[62] P.M. Morse, K.U. Ingard. **Theoretical Acoustics**. New Jersey: Princeton University Press (1968).

[63] National Cancer Institute, "Understanding Breast Changes - a Health Guide for All Women," leaflet publication. Bethesda, MD: National Cancer Institute (1998).

[64] National Cancer Institute, "Breast Cancer Facts," leaflet publication. Bethesda, MD: National Cancer Institute (1999).

[65] National Cancer Institute of Canada. **Canadian Cancer Statistics - 2000**. Toronto: Statistics Canada (2000).

[66] S.J. Norton, M. Linzer, "Ultrasonic Reflectivity Imaging in Three Dimensions: Exact Inverse Scattering Solutions for Plane, Cylindrical and Spherical Apertures," **IEEE Trans. Biomed. Eng., BME-28**, p. 202 (1981).

[67] D.M. Parkin, P. Pisani, J. Ferlay, "Estimates of the Worldwide Incidence of Eighteen Major Cancers in 1985," **International Journal of Cancer**, **54**, p. 590 (1993).

[68] Personal correspondence with Dr. J.M. Blackledge, October 1997.

[69] Personal correspondence with Dr. C. Bryce, Breast Cancer Oncologist with the BC Cancer Agency, September 1999.

[70] Personal correspondence with Mr. R. Luke, Ph.D. student, University of Washington, Department of Applied Mathematics.

[71] Personal correspondence with Mr. G. Posakony, June 1999.

[72] Personal correspondence with Mr. D. Reagan, owner of American Precision Gear Company, Incorporated May-June 1996.

[73] Personal correspondence with Dr. A. Selfridge, June 1997.

[74] W.H. Press, S.A. Teukolsky, W.T. Vetterling, B.P. Flannery. Numerical Recipes in C: The Art of Scientific Computing, Second Edition. Cambridge, MA: Cambridge University Press (1992).

[75] D.W. Rickey, P.A. Picot, D.A. Christopher, A. Fenster, "A Wall-Less Vessel Phantom for Doppler Ultrasound Studies," **Ultrasound in Medicine and Biology**, bf 21, No. 9, p. 1163 (1995).

[76] L.A.G. Ries, M.P. Eisner, C.L. Kosary, B.F. Hankey, L. Clegg, B.K. Edwards (eds). **SEER Cancer Statistics Review, 1873-1997**. Bethesda, MD: National Cancer Institute (2000).

[77] R. Rouzky, M. Batista, H. Longbothom, "An Application of Wavelets to Electromyographic Signals," **SPIE Proceedings: Wavelet Applications**, **2242**, p. 736 (1994).

[78] H.I. Schlaberg, M. Yang, B.S. Hoyle, M.S. Beck, C. Lenn, "Wide-Angle Transducers for Real-Time Ultrasonic Process Tomography Imaging Applications," **Ultrasonics**, **35**, p. 213 (1997).

[79] S.W. Smith. **The Scientist and Engineer's Guide to Digital Signal Processing**. San Diego: California Technical Publishing (1997).

[80] N. Sponheim, L.J. Gelius, I. Johansen, J.J. Stamnes, "Ultrasonic Tomography of Biological Tissue," **Ultrasonic Imaging**, **16**, p. 19 (1994).

[81] J.J. Stamnes. **Waves in Focal Regions**. Bristol: Hilger (1986).

[82] H. Stark, J.W. Woods, I. Paul, R. Hingorani, "Direct Fourier Reconstruction in Computer Tomography," **IEEE Transactions on Acoustics, Speech and Signal Processing, ASSP-29**, No. 2 (1981).

[83] N.A. Thacker and T.F. Cootes. **Vision Through Optimization.** Leeds: Computer Based Learning Unit, University of Leeds, Copyright 1994.

[84] J.J. Wild, D. Neal, "The Use of High Frequency Ulstrasonic Waves for Detecting Changes of Texture in Living Tissue," **Lancet**, **1**, p. 655 (1951).

[85] J.J. Wild, J.M. Reid, "Further Pilot Echographic studies on the Histologic Structure of the Living Intact Breast," **American Journal of Pathology**, **28**, p. 839 (1952).

[86] J.J. Wild, J.M. Reid, "Echographic Visualization of Lesions of the Living Intact Human Breast," **Cancer Reveiws**, **14**, p. 277 (1954).

[87] G. Wojcik, J. Mould, F. Lizzi, N. Abboud, M. Ostromogilsky, D. Vaughan, "Nonlinear Modeling of Therapeutic Ultrasound," 1995 IEEE Ultrasonics Symposium Proceedings, p. 1617 (1995).

[88] T. Yokoyama, K. Nagai, K. Mizutani, "Imaging Properties of Diffraction Tomography by Compound-Scanning Transmitter-Receiver Pair Transducers," **Japanese Journal of Applied Physics**, **32**, p. 2510 (1993).

[89] From the website "www.ynl.t.u-tokyo.ac.jp/publications/papers95/IEEE95/chung/node16.html."

[90] From the website "pipeline.keck.hawaii.edu:3636/realpublic/observing/interfacvinst/ktelgde-1.html."

[91] From the website "pcim.com/articles/1997/art0007/ell1.htm."

[92] From the University of Virginia Health System website "www.med.virginia.edu/medicine/clinical/pathology/educ/innes/text/wcd/myelo.html."

Appendix A
Detailed Derivation of Method by Blackledge *et al*

The reconstruction method of Blackledge *et al* was the starting point for the study involved in this thesis. This method is aimed at the reconstruction of images of compressibility and density for minimally attenuating objects. With this approach, the object being imaged is modelled as a nonhomogeneous fluid immersed in a uniform background fluid. The following pages outline the derivation in detail with references to three works: the paper by Blackledge *et al* [10], the paper by Norton and Linzer [66], and Section 6.2 of the book by Morse and Ingard [62]. In working through the math, minor errors were found in the work of Morse and Ingard, while several errors were found in the paper by Blackledge *et al*. To aid the reader in following the derivations, errors in the references have been noted.

A.1 The Wave Equation

The physics of the sound/fluid interaction is described by the Chernov Equation, which is a wave equation with the following form [10, 62, 66]:

$$\nabla \cdot (\frac{1}{\rho(\mathbf{r})}\nabla p(\mathbf{r},t)) = \kappa(\mathbf{r})\frac{\partial^2}{\partial t^2}p(\mathbf{r},t) \tag{A.1}$$

Note that this equation is expressed incorrectly in the paper by Blackledge *et al*, with a negative sign on the right hand side [62, 66]. In Equation A.1, $p(\mathbf{r},t)$ is the ultrasound pressure field at any time, t, during the measurement process and at any location, $\mathbf{r}$, in the measurement region. Since the 3D problem is difficult to solve, this model considers

2D pressure fields only. Thus, $\mathbf{r} = x\hat{\mathbf{x}} + y\hat{\mathbf{y}}$, where $\hat{\mathbf{x}}$ and $\hat{\mathbf{y}}$ are unit vectors in the xy-plane. $\rho(\mathbf{r})$ and $\kappa(\mathbf{r})$ are the spatially-varying density and compressibility in the image region.

The term

$$\kappa_0 \frac{\partial^2}{\partial t^2} p(\mathbf{r}, t) - \frac{1}{\rho_0} \nabla^2 p(\mathbf{r}, t) \tag{A.2}$$

is added to both sides of Equation A.1 [10, 62]. κ_0 and ρ_0 are the compressibility and density of the background fluid, which is typically water. Note that the step cited here in Reference [62] is incorrect in that the time derivative includes a factor of ρ and thus has improper units. Letting the time derivative terms on the left and right hand side be T1 and T2 respectively for simpler notation, the wave equation can be reduced as follows:

$$\begin{aligned} \nabla \cdot (\frac{1}{\rho} \nabla p) + \mathrm{T1} - \frac{1}{\rho_0} \nabla^2 p + \frac{1}{\rho_0} \nabla^2 p &= \mathrm{T2} \\ \{\nabla \cdot (\frac{1}{\rho} \nabla p) - \frac{1}{\rho_0} \nabla^2 p\} + \{\mathrm{T1} + \frac{1}{\rho_0} \nabla^2 p\} &= \mathrm{T2} \end{aligned} \tag{A.3}$$

The expression inside the first pair of curly brackets can be reduced further as follows:

$$\begin{aligned} \nabla \cdot (\frac{1}{\rho} \nabla p) - \frac{1}{\rho_0} \nabla^2 p &= \nabla \cdot (\frac{1}{\rho} \nabla p) - \nabla \cdot (\frac{1}{\rho_0} \nabla p) \\ &= \nabla \cdot \{(\frac{1}{\rho} - \frac{1}{\rho_0}) \nabla p\} \\ &= \nabla \cdot \{(\frac{\rho_0 - \rho}{\rho \rho_0}) \nabla p\} \\ &= -\frac{1}{\rho_0} \nabla \cdot \{(\frac{\rho - \rho_0}{\rho}) \nabla p\} \\ &= -\frac{1}{\rho_0} \nabla \cdot (\gamma_\rho \nabla p) \end{aligned} \tag{A.4}$$

where a $\gamma_\rho(\mathbf{r})$ function has now been defined as

$$\gamma_\rho(\mathbf{r}) = \frac{\rho(\mathrm{r}) - \rho_0(\mathrm{r})}{\rho(\mathrm{r})} \tag{A.5}$$

Substituting Equation A.4 into Equation A.3 yields

$$\begin{aligned} -\frac{1}{\rho_0} \nabla \cdot (\gamma_\rho \nabla p) + \mathrm{T1} + \frac{1}{\rho_0} \nabla^2 p &= \mathrm{T2} \\ \nabla^2 p + \rho_0 \, \mathrm{T1} &= \rho_0 \, \mathrm{T2} + \nabla \cdot (\gamma_\rho \nabla p) \end{aligned} \tag{A.6}$$

It is now necessary to reduce the time derivative terms in Equation A.6. For simpler notation, ∇ terms on the left and right hand side will be referred to as D1 and D2, respectively, and $\frac{\partial^2}{\partial t^2}p(\mathbf{r},t)$ will be written as $\ddot{p}$. Equation A.6 can then be rewritten as

$$\begin{aligned} \mathrm{D1} + \rho_0\kappa_0\,\ddot{p} &= \rho_0\kappa(\mathbf{r})\ddot{p} + \rho_0\kappa_0\,\ddot{p} + \mathrm{D2} \qquad (A.7)\\ \mathrm{D1} + \rho_0\,(\kappa_0 - \kappa(\mathbf{r}))\ddot{p} &= \rho_0\kappa_0\ddot{p} + \mathrm{D2} \end{aligned}$$

Noting that the speed of sound in the background fluid is $c_0 = \sqrt{\kappa_0\rho_0}$, the above equation can be further reduced:

$$\begin{aligned} \mathrm{D1} + \frac{1}{\kappa_0\,c_0^2}(\kappa_0 - \kappa(\mathbf{r}))\ddot{p} &= \rho_0\kappa_0\ddot{p} + \mathrm{D2} \qquad (A.8)\\ \mathrm{D1} - \frac{1}{c_0^2}\frac{\kappa_0 - \kappa(\mathbf{r})}{\kappa_0}\,\ddot{p} &= \rho_0\kappa_0\ddot{p} + \mathrm{D2}\\ \mathrm{D1} - \frac{1}{c_0^2}\,\gamma_\kappa(\mathbf{r})\ddot{p} &= \frac{1}{c_0^2}\,\ddot{p} + \mathrm{D2} \end{aligned}$$

where a $\gamma_\kappa(\mathbf{r})$ function has now been defined as

$$\gamma_\kappa(\mathbf{r}) = \frac{\kappa(\mathrm{r}) - \kappa_0(\mathrm{r})}{\kappa_0} \qquad (A.9)$$

Note that the $\gamma_\kappa(\mathbf{r})$ definition differs from that of $\gamma_\kappa(\mathbf{r})$ in that the background parameter, rather than the tissue parameter, is the denominator.

Substituting the ∇ terms back into Equation A.8 results in the final wave equation

$$\nabla^2 p(\mathbf{r},t) - \frac{1}{c_0^2}\frac{\partial^2}{\partial t^2}p(\mathbf{r},t) = \frac{\gamma_\kappa(\mathbf{r})}{c_0^2}\frac{\partial^2}{\partial t^2}p(\mathbf{r},t) + \nabla\cdot(\gamma_\rho\nabla p(\mathbf{r},t)) \qquad (A.10)$$

In the paper by Blackledge *et al*, this equation is quoted incorrectly with a factor of -1 in the time derivative on the right hand side. Equation A.10 is a time dependent wave equation with a forcing term that is a function of $\gamma_\kappa(\mathbf{r})$ and $\gamma_\rho(\mathbf{r})$. The forcing term gives rise to scatter due to inhomogeneities. For completeness, it is noted that if the tissue had been modelled as a medium that is solid, linear, isotropic and viscoelastic, the forcing function would take on a more complicated form involving tensor notation [47]. Interested readers are referred to the work by Iwata and Nagata done some years ago [44].

A.2 Fourier Domain and Born Approximation

The solution to Equation A.10 has time dependence embodied in an $\exp(iwt)$ term. Therefore

$$\frac{1}{c_0^2}\frac{\partial^2}{\partial t^2}p(\mathbf{r},t) = \frac{(iw)^2}{c_0^2}\,p(\mathbf{r},t) = -k^2 p(\mathbf{r},t) \tag{A.11}$$

where $k = \omega/c_0$ is the wave number in the background fluid. Substituting this expression for the $\ddot{p}$ terms into Equation A.10 and applying the Fourier Transform to both sides yields

$$\nabla^2 p(\mathbf{r},\omega) + k^2 p(\mathbf{r},\omega) = -k^2\gamma_\kappa(\mathbf{r})p(\mathbf{r},\omega) + \nabla\cdot(\gamma_\rho(\mathbf{r})\nabla p(\mathbf{r},\omega)) \tag{A.12}$$

Note that the expression quoted in the chapter by Morse and Ingard is incorrect in that the $\nabla\cdot(\gamma_\rho(\mathbf{r})\nabla p(\mathbf{r},\omega))$ term includes an extra negative sign. The solution to Equation A.12 at any detector location with position vector $\mathbf{r} = \mathbf{r}_d$ is given by

$$\begin{aligned} p(\mathbf{r}_d,\omega) &= p_0(\mathbf{r}_d,\omega) + k^2\int_{\Re^2} g(\mathbf{r}|\mathbf{r}_d,k)\gamma_\kappa(\mathbf{r})p(\mathbf{r},\omega)\,\mathrm{d}^2\mathbf{r} \\ &\quad - \int_{\Re^2} g(\mathbf{r}|\mathbf{r}_d,k)\nabla\cdot(\gamma_\rho(\mathbf{r})\nabla p(\mathbf{r},\omega))\,\mathrm{d}^2\mathbf{r} \end{aligned} \tag{A.13}$$

Note that the signs preceding the two integrals in the paper by Blackledge *et al* are both opposite to what they should be. In Equation A.13, $p_0(\mathbf{r}_s,\omega)$ is the incident ultrasound as a function of ω at any detector position $\mathbf{r}_d$, and $g(\mathbf{r}|\mathbf{r}_d,k)$ is the 2D Green's function that describes 2D wave propagation in the background fluid between any two locations described by $\mathbf{r}$ and $\mathbf{r}_d$. It is common knowledge that $g(\mathbf{r}|\mathbf{r}_d,k)$ is the solution to the following equation

$$(\nabla^2 + k^2)\,g(\mathbf{r}|\mathbf{r}_d,k) = -\delta^2(\mathbf{r}-\mathbf{r}_d) \tag{A.14}$$

which is given by

$$g(\mathbf{r}|\mathbf{r}_d,k) = -\frac{i}{4}H_0^1(k|\mathbf{r}-\mathbf{r}_d|) \tag{A.15}$$

where H_0^1 is the Hankel function of the first kind [81]. The Green's function is symmetric with respect to the interchange of $\mathbf{r}$ and $\mathbf{r}_d$. Note that the solution quoted in the reference by Blackledge *et al* is incorrect by a factor of -1, which results in the wrong pulse shape upon propagation of the incident field.

Equation A.13 is nonlinear in that the total field $p(\mathbf{r}_d, \omega)$ is not only being solved for, but it is also found within the integral. Thus, it is not possible to determine an exact analytical solution to this equation without linearizing it. In order to do this, the commonly used Born approximation is applied, in which the interacting sound field is assumed to be approximately equal to the incident field. In other words, the tissue is assumed to be a weak scatterer of sound. The application of the Born approach yields

$$\begin{aligned} p(\mathbf{r}_d, \omega) &= p_0(\mathbf{r}_s, \omega) + k^2 \int_{\Re^2} g(\mathbf{r}|\mathbf{r}_d, k)\gamma_\kappa(\mathbf{r})p_0(\mathbf{r}_s, \omega)\mathrm{d}^2\mathbf{r} - \\ & \int_{\Re^2} g(\mathbf{r}|\mathbf{r}_d, k)\nabla \cdot (\gamma_\rho(\mathbf{r})\nabla p_0(\mathbf{r}_s, \omega))\mathrm{d}^2\mathbf{r} \end{aligned} \tag{A.16}$$

Note again that the signs preceding the two integrals in the paper by Blackledge *et al* are both opposite to what they should be, which is the error carried over from Equation A.13.

A.3 Introducing the Pulsed Line Source

The 2D-based image reconstruction method assumes that the interrogating pulse derives from a line source, which is generally considered to be a field that is easily obtainable in the lab [10, 32]. The incident field at any given location, $\mathbf{r}$, due to a source with position vector, $\mathbf{r}_s$, is written

$$p_0(\mathbf{r}, \omega) = A(\omega)g(\mathbf{r}|\mathbf{r}_s, k) \tag{A.17}$$

and Equation A.17 can now be expressed as

$$\begin{aligned} p(\mathbf{r}_d, \mathbf{r}_s, \omega) &= A(\omega)g(\mathbf{r}_d|\mathbf{r}_s, k) + \\ & A(\omega)k^2 \int_{\Re^2} g(\mathbf{r}|\mathbf{r}_d, k)\gamma_\kappa(\mathbf{r})g(\mathbf{r}|\mathbf{r}_s, k)\,\mathrm{d}^2\mathbf{r} - \\ & A(\omega) \int_{\Re^2} g(\mathbf{r}|\mathbf{r}_d, k)\nabla \cdot (\gamma_\rho(\mathbf{r})\nabla g(\mathbf{r}|\mathbf{r}_s, k))\,\mathrm{d}^2\mathbf{r} \end{aligned} \tag{A.18}$$

Note again that the signs preceding the two integrals in the paper by Blackledge *et al* are the opposite of what they should be due to the error propagated through the derivation from Equation A.13. The incident pulse is furthermore assumed to be band limited with values of ω from Ω_1 to Ω_2 only. The source and detector are also assumed to be significantly far from any point of ultrasound scatter, located at $\mathbf{r}$ in the image space such that the following relation holds for $\mathbf{r}_j$ equal to $\mathbf{r}_s$ or $\mathbf{r}_d$:

$$|k||\mathbf{r}-\mathbf{r_j}| \gg \mathbf{1} \tag{A.19}$$

for every wave number that satisfies the expression

$$\frac{\Omega_1}{c_0} \leq |k| \leq \frac{\Omega_2}{c_0} \tag{A.20}$$

These assumptions allow the exact Green's Function to be approximated by a simpler function given by

$$\begin{aligned} g(\mathbf{r}|\mathbf{r}_j, k) &\approx \alpha S(k|\mathbf{r}-\mathbf{r}_j|) \\ S(k|\mathbf{r}-\mathbf{r}_j|) &= \frac{\exp(ik|\mathbf{r}-\mathbf{r_j}|)}{(k|\mathbf{r}-\mathbf{r_j}|)^{\frac{1}{2}}} \\ \alpha &= i\frac{\exp(3i\pi/4)}{2(2\pi)^{\frac{1}{2}}} \end{aligned} \tag{A.21}$$

Note that the value of α quoted in the paper by Blackledge *et al* is incorrect by a factor of i, resulting in the wrong phase information. By extension, $\nabla g \approx \nabla S$, which is derived in Appendix B to be

$$\begin{aligned} \nabla S &= ik\,\hat{\mathbf{n}}_j\,S \\ \hat{\mathbf{n}}_j &= \frac{(\mathbf{r}-\mathbf{r}_j)}{|\mathbf{r}-\mathbf{r}_j|} \end{aligned} \tag{A.22}$$

To simplify notation in the derivation to follow, $S_{\mathbf{r}_j}$ will be used to denote $S(k|\mathbf{r}-\mathbf{r}_j|)$. Substituting the approximate expressions for g and ∇g into Equation A.18 yields

$$\begin{aligned} p(\mathbf{r}_d, \mathbf{r}_s, \omega) \approx\; & \alpha A(\omega)(S(k|\mathbf{r}_d-\mathbf{r}_s|) + \alpha^2 A(\omega) k^2 \int_{\Re^2} S_{\mathbf{r}_d}\,\gamma_\kappa(\mathbf{r})\,S_{\mathbf{r}_s}\,\mathrm{d}^2\mathbf{r} - \\ & \alpha^2 A(\omega) \int_{\Re^2} S_{\mathbf{r}_d}\,\nabla\cdot(\gamma_\rho(\mathbf{r})\,\nabla S_{\mathbf{r}_s})\,\mathrm{d}^2\mathbf{r} \end{aligned} \tag{A.23}$$

Note again that the signs preceding the two integrals in the paper by Blackledge *et al* are both opposite to what they should be, since this error was carried over from Equation A.13.

A.4 Derivation of Equation 2.16

Several steps are involved in deriving Equation 2.16 in Section 2.2.1, given by

$$\begin{aligned} p(\mathbf{r}_d, \mathbf{r}_s, \omega) &\approx \alpha A(\omega) S(k|\mathbf{r}_d - \mathbf{r}_s|) + \alpha^2 A(\omega) k^2 I \\ I &= \int_{\Re^2} S_{\mathbf{r}_d} (\gamma_\kappa(\mathbf{r}) + \cos(\theta)\gamma_\rho(\mathbf{r})) S_{\mathbf{r}_s} \, \mathrm{d}^2\mathbf{r} \end{aligned} \tag{A.24}$$

from Equation A.23 in the preceding section. Most of the steps involve reducing the integral

$$\int_{\Re^2} S(k|\mathbf{r} - \mathbf{r}_d|) \nabla \cdot (\gamma_\rho(\mathbf{r}) \nabla S(k|\mathbf{r} - \mathbf{r}_s|)) \, \mathrm{d}^2\mathbf{r} \tag{A.25}$$

to the expression

$$k^2 \int_{\Re^2} S_{\mathbf{r}_d} \left(\hat{\mathbf{n}}_d \cdot \hat{\mathbf{n}}_s\right) \gamma_\rho(\mathbf{r}) S_{\mathbf{r}_s} \, \mathrm{d}^2\mathbf{r} \tag{A.26}$$

which will now be shown. By the Chain Rule,

$$\nabla \cdot (S_{\mathbf{r}_d} \gamma_\rho(\mathbf{r}) \nabla S_{\mathbf{r}_s}) = \nabla S_{\mathbf{r}_d} \cdot (\gamma_\rho(\mathbf{r}) \nabla S_{\mathbf{r}_s}) + S_{\mathbf{r}_d} \nabla \cdot (\gamma_\rho(\mathbf{r}) \nabla S_{\mathbf{r}_s}) \tag{A.27}$$

Therefore, the desired integral can be written as

$$\begin{aligned} \int_{\Re^2} S_{\mathbf{r}_d} \nabla \cdot (\gamma_\rho(\mathbf{r}) \nabla S_{\mathbf{r}_s}) \, \mathrm{d}^2\mathbf{r} &= \int_{\Re^2} \nabla \cdot (S_{\mathbf{r}_d} \gamma_\rho(\mathbf{r}) \nabla S_{\mathbf{r}_s}) \, \mathrm{d}^2\mathbf{r} \\ &\quad - \int_{\Re^2} \nabla S_{\mathbf{r}_d} \cdot (\gamma_\rho(\mathbf{r}) \nabla S_{\mathbf{r}_s}) \, \mathrm{d}^2\mathbf{r} \end{aligned} \tag{A.28}$$

By the Divergence Theorem,

$$\int_{\Re^2} \nabla \cdot \{S_{\mathbf{r}_d} \gamma_\rho(\mathbf{r}) \nabla S_{\mathbf{r}_s}\} = \oint_C \{S_{\mathbf{r}_d} \gamma_\rho(\mathbf{r}) \nabla S_{\mathbf{r}_s}\} \cdot dl \tag{A.29}$$

where C is a contour enclosing the extent of $\Re^2$ (the 2D image space), and dl is the infinitesimal vector line element that is always tangential to C. However, because the contour C lies inside the background fluid, $\gamma_\rho = 0$ everywhere on the contour and the integral in Equation A.29 is therefore zero. As such, Equation A.28 has now been reduced to

$$\int_{\Re^2} S_{\mathbf{r}_d} \nabla \cdot (\gamma_\rho(\mathbf{r}) \nabla S_{\mathbf{r}_s})\, \mathrm{d}^2\mathbf{r} \;=\; -\int_{\Re^2} \nabla S_{\mathbf{r}_d} \cdot (\gamma_\rho(\mathbf{r}) \nabla S_{\mathbf{r}_s})\, \mathrm{d}^2\mathbf{r} \tag{A.30}$$

Recalling again that $\nabla S_{\mathbf{r}_j} = ik\, \hat{\mathbf{n}}_j\, S_{\mathbf{r}_j}$ results in the expression

$$\begin{aligned}\int_{\Re^2} S_{\mathbf{r}_d} \nabla \cdot (\gamma_\rho(\mathbf{r}) \nabla S_{\mathbf{r}_s}) \mathrm{d}^2\mathbf{r} &= -\int_{\Re^2} (ik)^2 \hat{\mathbf{n}}_d\, S_{\mathbf{r}_d} \cdot \hat{\mathbf{n}}_s\, \gamma_\rho\, S_{\mathbf{r}_s}\, \mathrm{d}^2\mathbf{r} \\ &= k^2 \int_{\Re^2} S_{\mathbf{r}_d} \left(\hat{\mathbf{n}}_d \cdot \hat{\mathbf{n}}_s\right) \gamma_\rho(\mathbf{r}) S_{\mathbf{r}_s}\, \mathrm{d}^2\mathbf{r}\end{aligned} \tag{A.31}$$

which is the desired result in Equation A.26.

Lastly, an expression for $\hat{\mathbf{n}}_s \cdot \hat{\mathbf{n}}_d$ must be derived. In order to do this, an imaging geometry must be defined. Figure A.1 illustrates the experimental UCT setup in which a source transducer with position vector $\mathbf{r}_s$ insonifies an object located about the origin with a pulse that has an amplitude spectrum $A(t)$. The scattered field is detected by a second transducer with position vector $\mathbf{r}_d$. Both the source and detector are situated at a distance a from the origin, and at angles of φ_s and φ_d, respectively. Note that φ_s is always larger than φ_d. The unit vectors $\hat{\mathbf{n}}_s$ and $\hat{\mathbf{n}}_d$ can then be written as

$$\begin{aligned}\hat{\mathbf{n}}_s &= \cos(\varphi_s)\hat{\mathbf{x}} + \sin(\varphi_s)\hat{\mathbf{y}} \\ \hat{\mathbf{n}}_d &= \cos(\varphi_d)\hat{\mathbf{x}} + \sin(\varphi_d)\hat{\mathbf{y}}\end{aligned} \tag{A.32}$$

θ describes the angle between the pulse propagation direction and the detector angle, and it is defined in terms of the other angles by

$$\theta = \varphi_d - \varphi_s + \pi; \tag{A.33}$$

With these definitions,

$$\hat{\mathbf{n}}_s \cdot \hat{\mathbf{n}}_d = \cos(\varphi_d)\cos(\varphi_s) + \sin(\varphi_d)\sin(\varphi_s) \tag{A.34}$$

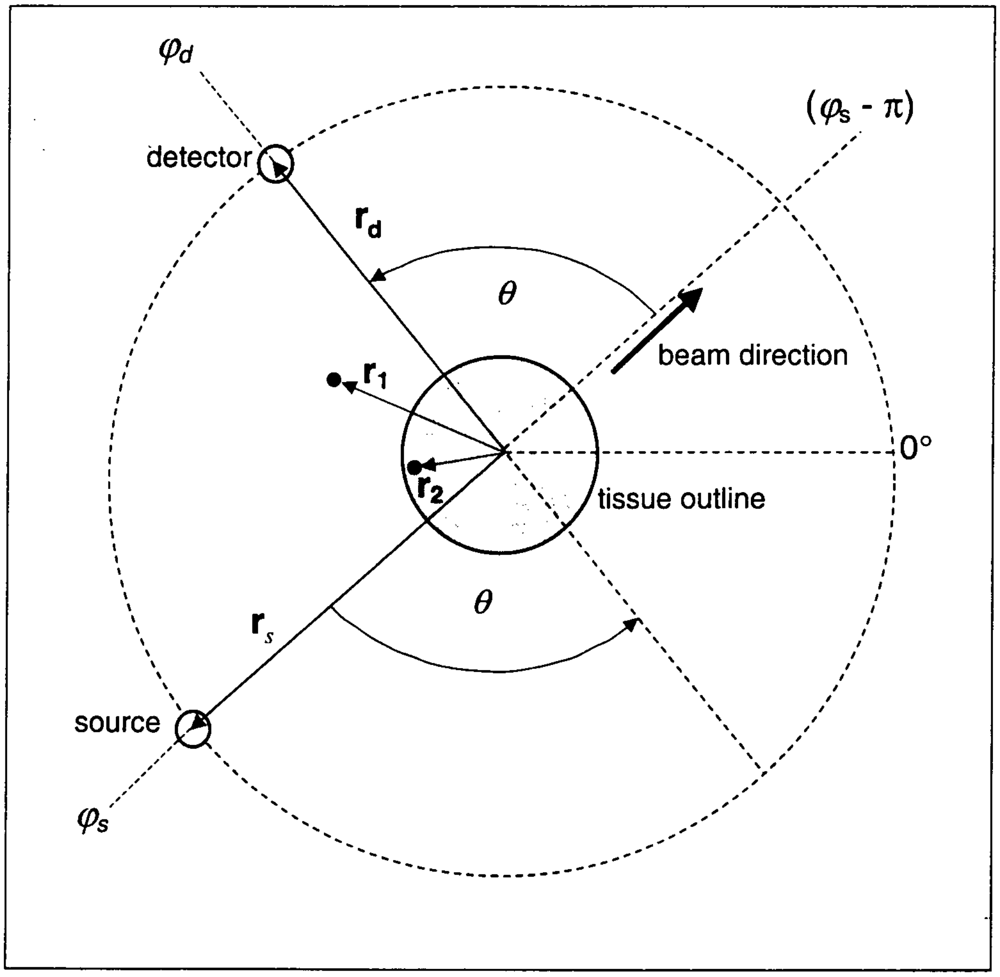

Figure A.1: This schematic illustrates the UCT experiment geometry upon which a reconstruction algorithm is developed. Vectors $\mathbf{r}_1$ and $\mathbf{r}_2$ are two examples of $\mathbf{r}$, which is the location vector of scatter points within the image.

A trigonometric identity states that

$$\cos(t_1 \pm t_2) = \cos(t_1)\cos(t_2) \mp \sin(t_1)\sin(t_2) \tag{A.35}$$

and thus

$$\hat{\mathbf{n}}_s \cdot \hat{\mathbf{n}}_d = \cos(\varphi_d - \varphi_s) = \cos(\theta - \pi) = -\cos(\theta) \tag{A.36}$$

Note that the paper by Blackledge *et al* quotes a value for this expression that is incorrect by a factor of -1. Substituting this expression for the dot product into Equation A.31 results in

$$\int_{\Re^2} S_{\mathbf{r}_d} \nabla \cdot (\gamma_\rho(\mathbf{r}) \nabla S_{\mathbf{r}_s}) \mathrm{d}^2\mathbf{r} \;=\; -k^2 \int_{\Re^2} S_{\mathbf{r}_d} \cos(\theta)\, \gamma_\rho(\mathbf{r}) S_{\mathbf{r}_s}\, \mathrm{d}^2\mathbf{r} \tag{A.37}$$

Replacing the second integral in Equation A.23 with this expression yields the following equation for the total field at detector position $\mathbf{r}_d$

$$\begin{aligned} p(\mathbf{r}_d, \mathbf{r}_s, \omega) \;&=\; \alpha A(\omega)(S(k|\mathbf{r}_d - \mathbf{r}_s|) + \alpha^2 A(\omega) k^2 \times \\ &\int_{\Re^2} S_{\mathbf{r}_d} \left(\gamma_\kappa(\mathbf{r}) + \cos(\theta)\gamma_\rho(\mathbf{r})\right) S_{\mathbf{r}_s}\, \mathrm{d}^2\mathbf{r} \end{aligned} \tag{A.38}$$

By extension, the scattered field is given by

$$p_s(\mathbf{r}_d, \mathbf{r}_s, \omega) \;\approx\; \alpha^2 A(\omega)\, k^2 \int_{\Re^2} S_{\mathbf{r}_d} \left(\gamma_\kappa(\mathbf{r}) + \cos(\theta)\gamma_\rho(\mathbf{r})\right) S_{\mathbf{r}_s}\, \mathrm{d}^2\mathbf{r} \tag{A.39}$$

A.5 Simplification of Equation A.38

The following steps involve the reduction of Equation A.38 to yield Equation 2.23 in Section 2.2. Recall that Equation 2.23 expresses the total field at any location as

$$\begin{aligned} p(\mathbf{r}_d, \mathbf{r}_s, \omega) \;&\approx\; \alpha A(\omega)(S(k|\mathbf{r}_d - \mathbf{r}_s|) + \alpha J) \\ J \;&=\; k \frac{\exp(ik(|\mathbf{r}_d| + |\mathbf{r}_s|))}{(|\mathbf{r}_d||\mathbf{r}_s|)^{\frac{1}{2}}} \int_{\Re^2} \chi\, \mathrm{d}^2\mathbf{r} \\ \chi \;&=\; \exp(ik\hat{\mathbf{n}}_d \cdot \mathbf{r})(\gamma_\kappa(\mathbf{r}) + \cos(\theta)\gamma_\rho(\mathbf{r})) \exp(ik\hat{\mathbf{n}}_s \cdot \mathbf{r}) \end{aligned} \tag{A.40}$$

Substituting the full expression for S into Equation A.38 leads to

$$\begin{aligned} p(\mathbf{r}_d, \mathbf{r}_s, \omega) \;\approx\; & \alpha A(\omega)(S(k|\mathbf{r}_d - \mathbf{r}_s|) + \alpha^2 A(\omega) k^2 \times \\ & \int_{\Re^2} \frac{\exp(ik|\mathbf{r}-\mathbf{r}_d|)}{(k|\mathbf{r}-\mathbf{r}_d|)^{\frac{1}{2}}} (\gamma_\kappa(\mathbf{r}) + \cos(\theta)\gamma_\rho(\mathbf{r})) \frac{\exp(ik|\mathbf{r}-\mathbf{r}_s|)}{(k|\mathbf{r}-\mathbf{r}_s|)^{\frac{1}{2}}} \,\mathrm{d}^2\mathbf{r} \end{aligned} \tag{A.41}$$

Comparing Equations A.40 and A.41, it is evident that the key step in the derivation is

to show that

$$\begin{aligned} \frac{\exp(ik|\mathbf{r}-\mathbf{r}_d|)}{|\mathbf{r}-\mathbf{r}_d|^{\frac{1}{2}}} \frac{\exp(ik|\mathbf{r}-\mathbf{r}_s|)}{|\mathbf{r}-\mathbf{r}_s|^{\frac{1}{2}}} = & \\ \frac{\exp(ik(|\mathbf{r}_d| + |\mathbf{r}_s|))}{(|\mathbf{r}_d||\mathbf{r}_s|)^{\frac{1}{2}}} & \exp(ik\hat{\mathbf{n}}_d \cdot \mathbf{r}) \exp(ik\hat{\mathbf{n}}_s \cdot \mathbf{r}) \end{aligned} \tag{A.42}$$

In order that the exponential terms on the left hand side of Equation A.42 reduce to those on the right hand side, it must be shown that

$$|\mathbf{r}-\mathbf{r}_j| = \hat{\mathbf{n}}_j \cdot \mathbf{r} + |\mathbf{r}_j| \tag{A.43}$$

where $\mathbf{r}_j$ is equal to $\mathbf{r}_s$ or $\mathbf{r}_d$. $|\mathbf{r}-\mathbf{r}_j|$ can be rewritten as

$$\begin{aligned} |\mathbf{r}-\mathbf{r}_j| &= \frac{|\mathbf{r}-\mathbf{r}_j|^2}{|\mathbf{r}-\mathbf{r}_j|} \\ &= \frac{(\mathbf{r}-\mathbf{r}_j)\cdot(\mathbf{r}-\mathbf{r}_j)}{|\mathbf{r}-\mathbf{r}_j|} \\ &= \frac{(\mathbf{r}-\mathbf{r}_j)\cdot\mathbf{r}}{|\mathbf{r}-\mathbf{r}_j|} - \frac{(\mathbf{r}-\mathbf{r}_j)\cdot\mathbf{r}_j}{|\mathbf{r}-\mathbf{r}_j|} \\ &= \mathrm{T1} - \mathrm{T2} \end{aligned} \tag{A.44}$$

Recalling that

$$\hat{\mathbf{n}}_j = \frac{(\mathbf{r}-\mathbf{r}_j)}{|\mathbf{r}-\mathbf{r}_j|} \tag{A.45}$$

it is evident that T1 is simply the first term of Equation A.43. Thus, all that remains is to show that T2 reduces to $-|\mathbf{r}_j|$. Analytically, T2 can be reduced mathematically by deriving a different expression for $(\mathbf{r}-\mathbf{r}_j)$ as follows:

$$\begin{aligned} \mathbf{r}-\mathbf{r}_j &= \mathbf{r}_j\mathbf{r}_j^{-1}(\mathbf{r}-\mathbf{r}_j) = \mathbf{r}_j(\mathbf{r}_j^{-1}\mathbf{r} - \mathbf{r}_j^{-1}\mathbf{r}_j) \\ &= \mathbf{r}_j(\mathbf{r}_j^{-1}\mathbf{r} - 1) \end{aligned} \tag{A.46}$$

The inverse of $\mathbf{r}_j$ is

$$\frac{1}{\mathbf{r}_j} = \frac{1}{a}\cos(\eta)\hat{\mathbf{x}} + \frac{1}{a}\sin(\eta)\hat{\mathbf{y}} \tag{A.47}$$

where η is the source or detector angle. Substituting this expression for $\mathbf{r}_j$ into Equation A.46 yields

$$\mathbf{r} - \mathbf{r}_j = \mathbf{r}_j\,(\frac{r_x}{a}\cos(\eta) + \frac{r_y}{a}\sin(\eta) - 1)$$

The physics model now assumes that the object is being insonified in the far field of the source, so that $|\mathbf{r}|/|\mathbf{r}_j|$ is always $\ll 1$. This means that

$$\begin{aligned} \frac{r_x}{a} &\ll 1 \\ \frac{r_y}{a} &\ll 1 \end{aligned} \tag{A.48}$$

and therefore

$$\mathbf{r} - \mathbf{r}_j = \mathbf{r}_j \times (\delta - 1) = -\mathbf{r}_j \tag{A.49}$$

where $\delta \approx 0$. Substituting the above expression into Equation A.44 allows T2 to be expressed as

$$\begin{aligned} \mathrm{T2} &\approx -\frac{\mathbf{r}_j \cdot \mathbf{r}_j}{|-\mathbf{r}_j|} \\ &= -|\mathbf{r}_j| \end{aligned} \tag{A.50}$$

and an alternate expression for $|\mathbf{r} - \mathbf{r}_j|$ has thus been shown to be

$$\begin{aligned} |\mathbf{r} - \mathbf{r}_j| &= \frac{(\mathbf{r} - \mathbf{r}_j) \cdot \mathbf{r}}{|\mathbf{r} - \mathbf{r}_j|} + |\mathbf{r}_j| \\ &= \hat{\mathbf{n}}_j \cdot \mathbf{r} + |\mathbf{r}_j| \end{aligned} \tag{A.51}$$

Substituting this expression into S and noting that, according to Equation A.49,

$$\frac{1}{|\mathbf{r} - \mathbf{r}_j|} \approx \frac{1}{|\mathbf{r}_j|} \tag{A.52}$$

yields the following result

$$\begin{aligned} S(k|\mathbf{r}-\mathbf{r}_j|) &= \frac{\exp(ik|\mathbf{r}-\mathbf{r}_j|)}{(k|\mathbf{r}-\mathbf{r}_j|)^{\frac{1}{2}}} \\ &\approx \frac{\exp(ik(\hat{\mathbf{n}}_j\cdot\mathbf{r}+|\mathbf{r}_j|))}{k^{\frac{1}{2}}|\mathbf{r}_j|^{\frac{1}{2}}} \end{aligned} \tag{A.53}$$

Note that this approximation results in a loss of phase information and ultimately is responsible for the relatively poor performance of the reconstruction algorithm. This will be discussed in more detail in Section 5.1.3

Equation A.38 finally reduces to

$$p(\mathbf{r}_d,\mathbf{r}_s,\omega) \approx \alpha A(\omega) S(k|\mathbf{r}_d-\mathbf{r}_s|) + \alpha^2 A(\omega)\, k\, \Upsilon \int_{\Re^2} \chi\, \mathrm{d}^2\mathbf{r} \tag{A.54}$$

where

$$\begin{aligned} \Upsilon &= \frac{\exp(ik(|\mathbf{r}_d|+|\mathbf{r}_s|))}{(|\mathbf{r}_d||\mathbf{r}_s|)^{\frac{1}{2}}} \\ \chi &= \exp(ik\hat{\mathbf{n}}_d\cdot\mathbf{r})(\gamma_\kappa(\mathbf{r})+\cos(\theta)\gamma_\rho(\mathbf{r}))\exp(ik\hat{\mathbf{n}}_s\cdot\mathbf{r}) \end{aligned} \tag{A.55}$$

Thus, Equation A.40 is derived.

A.6 Substitution for $\mathbf{r}_s$ and $\mathbf{r}_d$

The following will illustrate the final step in the derivation of the reconstruction algorithm by Blackledge *et al*, which involves the substitution of

$$\begin{aligned} \mathbf{r}_d &= a\hat{\mathbf{n}}_d = a\hat{\mathbf{x}}\cos(\varphi_d) + a\hat{\mathbf{y}}\sin(\varphi_d) \\ \mathbf{r}_s &= a\hat{\mathbf{n}}_s = a\hat{\mathbf{x}}\cos(\varphi_s) + a\hat{\mathbf{y}}\sin(\varphi_s) \end{aligned} \tag{A.56}$$

into Equation A.54. It will be shown that this process generates the final expression for the total ultrasound field measured at any point $\mathbf{r}$, which is given by:

$$\begin{aligned} p_\theta(\mathbf{r},\omega) &\approx \alpha A(\omega)\left\{\frac{\exp(2ika\cos(\frac{\theta}{2}))}{(2ka\cos(\frac{\theta}{2}))^{\frac{1}{2}}} + \frac{\alpha k\exp(2ika)}{a}\psi_\theta(\varphi_s,k)\right\} \\ \psi_\theta(\varphi_s,k) &= \int_{\Re^2}\exp(-i(ux+vy))(\gamma_\kappa(\mathbf{r})+\cos(\theta)\gamma_\rho(\mathbf{r}))\,\mathrm{dxdy} \end{aligned} \tag{A.57}$$

where u and v are defined by

$$\begin{aligned} u &= -2k\sin(\frac{\theta}{2}+\varphi_s)\sin(\frac{\theta}{2}) \\ v &= 2k\cos(\frac{\theta}{2}+\varphi_s)\sin(\frac{\theta}{2}) \end{aligned} \tag{A.58}$$

Note that the signs quoted for both u and v in the paper by Blackledge *et al* are opposite to what they should be.

This mathematical reduction depends on simplifying the term $|\mathbf{r}_d - \mathbf{r}_s|$, the square of which can be expressed as follows:

$$\begin{aligned} |\mathbf{r}_d - \mathbf{r}_s|^2 &= |\,a\,\{\cos(\varphi_d)-\cos(\varphi_s)\}\hat{\mathbf{x}} + a\,\{\sin(\varphi_d)-\sin(\varphi_s)\}\hat{\mathbf{y}}\,|^2 \\ &= a^2\,\{\cos(\varphi_d)-\cos(\varphi_s)\}^2 + a^2\{\sin(\varphi_d)-\sin(\varphi_s)\}^2\} \\ &= a^2\,\{\cos^2(\varphi_d)+\sin^2(\varphi_d)+\cos^2(\varphi_s)+\sin^2(\varphi_s)\} \\ &\qquad -a^2\,\{2\cos(\varphi_d)\cos(\varphi_s) - 2\sin(\varphi_d)\sin(\varphi_s)\} \\ &= 2a^2\{1-\cos(\varphi_d)\cos(\varphi_s)-\sin(\varphi_d)\sin(\varphi_s)\} \end{aligned} \tag{A.59}$$

Also, $\cos(\theta)$ must be expressed in terms of φ_d and φ_s through use of trigonometric identities as follows

$$\begin{aligned} \cos(\theta) &= \cos(\varphi_d - \varphi_s + \pi) \\ &= \cos(\varphi_d - \varphi_s)\,\cos(\pi) - \sin(\varphi_d-\varphi_s)\,\sin(\pi) \\ &= -\cos(\varphi_d-\varphi_s) \\ &= -\cos(\varphi_d)\cos(\varphi_s) - \sin(\varphi_d)\sin(\varphi_s) \end{aligned} \tag{A.60}$$

Substituting this expression for $\cos(\theta)$ into Equation A.59 yields

$$|\mathbf{r}_d - \mathbf{r}_s|^2 = 2a^2\{1+\cos(\theta)\} \tag{A.61}$$

According to a trigonometric identity

$$1+\cos(t) = 2\,\cos^2(\frac{t}{2}) \tag{A.62}$$

Thus,

$$
\begin{aligned}
|\mathbf{r}_d - \mathbf{r}_s| &= \{2a^2\{2\,\cos^2(\frac{\theta}{2})\}\}^{\frac{1}{2}} \\
&= 4a\,\cos(\frac{\theta}{2})
\end{aligned} \tag{A.63}
$$

This expression for the norm can now be substituted into Equation A.54, together with the relation $|\mathbf{r}_d| = a = |\mathbf{r}_s|$, to yield

$$
\begin{aligned}
p(\mathbf{r}_d, \mathbf{r}_s, \omega) &\approx \alpha\, A(\omega)\, \frac{\exp(2ika\,\cos(\frac{\theta}{2}))}{(2ika\,\cos(\frac{\theta}{2}))^{\frac{1}{2}}} + \alpha^2\, A(\omega)\, k\, \frac{\exp(2ika)}{a}\, \psi_\theta \\
\psi_\theta &= \int_{\Re^2} \exp(ik\hat{\mathbf{n}}_d \cdot \mathbf{r})(\gamma_\kappa(\mathbf{r}) + \cos(\theta)\gamma_\rho(\mathbf{r}))\exp(ik\hat{\mathbf{n}}_s \cdot \mathbf{r})\, \mathrm{d}^2\mathbf{r}
\end{aligned} \tag{A.64}
$$

The final step involves reducing the ψ_θ term by showing that

$$
\exp(ik(\hat{\mathbf{n}}_d \cdot \mathbf{r} + \hat{\mathbf{n}}_s \cdot \mathbf{r})) = \exp(-i(ux + vy)) \tag{A.65}
$$

where u and v are defined in Equation A.58. Expanding the exponent argument in Equation A.65 as follows

$$
\begin{aligned}
k\{\hat{\mathbf{n}}_d \cdot \mathbf{r} + \hat{\mathbf{n}}_s \cdot \mathbf{r}\} &= k\,(\cos(\varphi_d)\hat{\mathbf{x}} + \sin(\varphi_d)\hat{\mathbf{y}}) \cdot (x\hat{\mathbf{x}} + y\hat{\mathbf{y}}) + \\
&\qquad k\,(\cos(\varphi_s)\hat{\mathbf{x}} + \sin(\varphi_s)\hat{\mathbf{y}}) \cdot (x\hat{\mathbf{x}} + y\hat{\mathbf{y}}) \\
&= kx\,(\cos(\varphi_d) + \cos(\varphi_s)) + ky\,(\sin(\varphi_d) + \sin(\varphi_s))
\end{aligned} \tag{A.66}
$$

results in alternate expressions for u and v given by

$$
\begin{aligned}
u &= -k\,(\cos(\varphi_d) + \cos(\varphi_s)) \\
v &= -k\,(\sin(\varphi_d) + \sin(\varphi_s))
\end{aligned} \tag{A.67}
$$

Substituting $\theta = \varphi_d - \varphi_s + \pi$ and applying the following trigonometric identities

$$
\begin{aligned}
\sin^2(\frac{t}{2}) &= \frac{1}{2}\,(1 - \cos(t)) \\
\sin(t) &= 2\,\sin(\frac{t}{2})\cos(\frac{t}{2}) \\
\sin(t_1 + t_2) &= \sin(t_1)\cos(t_2) + \cos(t_1)\sin(t_2)
\end{aligned} \tag{A.68}
$$

allows the term $(\cos(\varphi_s) + \cos(\varphi_d))$ to be further reduced to arrive at

$$
\begin{aligned}
(\cos(\varphi_s) + \cos(\varphi_d)) &= \cos(\varphi_s) - \cos(\varphi_d + \pi) \\
&= \cos(\varphi_s) - \cos(\theta + \varphi_s) \\
&= \cos(\varphi_s) - \{\cos(\theta)\cos(\varphi_s) - \sin(\theta)\sin(\varphi_s)\} \\
&= \cos(\varphi_s)\,(1 - \cos(\theta)) + \sin(\theta)\sin(\varphi_s) \\
&= 2\,\cos(\varphi_s)\sin^2(\frac{\theta}{2}) + 2\,\sin(\frac{\theta}{2})\cos(\frac{\theta}{2})\sin(\varphi_s) \\
&= 2\,\sin(\frac{\theta}{2})\,\{\cos(\varphi_s)\sin(\frac{\theta}{2}) + \sin(\varphi_s)\cos(\frac{\theta}{2})\} \\
&= 2\,\sin(\frac{\theta}{2})\sin(\frac{\theta}{2} + \varphi_s)
\end{aligned}
\tag{A.69}
$$

Similarly, with the application of the following trigonometric identity

$$
\cos(t_1 \pm t_2) = \cos(t_1)\cos(t_2) \mp \sin(t_1)\sin(t_2) \tag{A.70}
$$

the term $(\sin(\varphi_s) + \sin(\varphi_d))$ can be reduced to yield

$$
\begin{aligned}
(\sin(\varphi_s) + \sin(\varphi_d)) &= \sin(\varphi_s) - \sin(\varphi_d + \pi) \\
&= \sin(\varphi_s) - \sin(\theta + \varphi_s) \\
&= \sin(\varphi_s) - \{\sin(\theta)\cos(\varphi_s) + \cos(\theta)\sin(\varphi_s)\} \\
&= \sin(\varphi_s)\,(1 - \cos(\theta)) - \sin(\theta)\cos(\varphi_s) \\
&= 2\,\sin(\varphi_s)\sin^2(\frac{\theta}{2}) - 2\,\sin(\frac{\theta}{2})\cos(\frac{\theta}{2})\cos(\varphi_s) \\
&= -2\,\sin(\frac{\theta}{2})\,\{\cos(\varphi_s)\cos(\frac{\theta}{2}) - \sin(\varphi_s)\sin(\frac{\theta}{2})\} \\
&= -2\,\sin(\frac{\theta}{2})\cos(\frac{\theta}{2} + \varphi_s)
\end{aligned}
\tag{A.71}
$$

Substituting these results into Equation A.67 yields

$$
\begin{aligned}
u &= -2k\,\sin(\frac{\theta}{2})\sin(\frac{\theta}{2} + \varphi_s)) \\
v &= 2k\,\sin(\frac{\theta}{2})\cos(\frac{\theta}{2} + \varphi_s)
\end{aligned}
\tag{A.72}
$$

Thus, the final equation for the total ultrasound field has been proven to be

$$\begin{aligned}
p(\mathbf{r}_d, \mathbf{r}_s, \omega) &\approx \mathrm{F1} + \mathrm{F2} \times \psi_\theta(\varphi_s, k) \\
\mathrm{F1} &= \alpha\, A(\omega)\, \frac{\exp(2ika\, \cos(\frac{\theta}{2}))}{(2ika\, \cos(\frac{\theta}{2}))^{\frac{1}{2}}} \\
\mathrm{F2} &= \alpha^2\, A(\omega)\, k\, \frac{\exp(2ika)}{a} \\
\psi_\theta(\varphi_s, k) &= \int_{\Re^2} \exp(-i(ux + vy))(\gamma_\kappa(\mathbf{r}) + \cos(\theta)\gamma_\rho(\mathbf{r}))\,\mathrm{d}x\,\mathrm{d}y \\
u &= -2k\, \sin(\frac{\theta}{2})\sin(\frac{\theta}{2} + \varphi_s)) \\
v &= 2k\, \sin(\frac{\theta}{2})\cos(\frac{\theta}{2} + \varphi_s)
\end{aligned} \tag{A.73}$$

The above equation provides the basis for the reconstruction algorithm by Blackledge *et al* described in detail in Section 2.2.2.

A closing note regards a quick dimensional analysis of both the intermediate and final solutions to the wave equation, given by Equations A.54 and A.73, respectively. Looking at the first term of Equation A.54, the dimensions are the same as that of $A(\omega)$, since both α and S are dimensionless. $A(\omega)$ is the Fourier Transform of the incident pulse amplitude as a function of time, which is given by some function $A(t)$. The units of $A(t)$ will generally be volts since this is what is measured by the detector transducer. Voltage is not involved in the Fourier Transform integral, so the final units of $A(\omega)$ are Vs. The units of the incident field are the same. The units of the second term in Equation A.54 are

$$\begin{aligned}
[\alpha^2 A(\omega) k \Upsilon \int_{\Re^2} \chi\, \mathrm{d}^2\mathbf{r}] &\equiv \mathrm{Vs}\, [\frac{1}{\mathrm{m}}]\, [\frac{1}{(|\mathbf{r}_d||\mathbf{r}_s|)^{\frac{1}{2}}}][\int_{\Re^2} \chi\, \mathrm{d}^2\mathbf{r}] \\
&\equiv \frac{\mathrm{Vs}}{\mathrm{m}^2}\, [\int_{\Re^2} \chi\, \mathrm{d}^2\mathbf{r}]
\end{aligned} \tag{A.74}$$

χ is unitless, so the dimensions of the 2D spatial integral are m^2, and the dimensions of the final expression are again Vs, which is consistent with the first term. An analysis of Equation A.73 yields the same results. The first term has dimensions

$$[\alpha\, A(\omega)\, \frac{\exp(2ika\, \cos(\frac{\theta}{2}))}{(2ika\, \cos(\frac{\theta}{2}))^{\frac{1}{2}}}] \equiv [A(\omega)] \equiv \mathrm{Vs} \tag{A.75}$$

while the second term has dimensions

$$[\alpha^2 \, A(\omega) \, k \, \frac{\exp(2ika)}{a} \, \psi_\theta(\varphi_s, k)] \equiv \frac{\mathrm{Vs}}{\mathrm{m}^2} \, [\psi_\theta(\varphi_s, k)] \tag{A.76}$$

ψ_θ is the 2D spatial integral of a unitless function, so its units are m^2, and the final dimensions of the second term are again Vs as expected.

Appendix B
Derivation of ∇S

In order to develop the reconstruction algorithms included in this thesis, knowledge of $\nabla S(k|\mathbf{r}-\mathbf{r}_j|)$ is required, where $\alpha S(k|\mathbf{r}-\mathbf{r}_j|)$ is an approximation to the 2D Green's function propagator that describes ultrasound propagation in the far field of the source. In this appendix, $\nabla S(k|\mathbf{r}-\mathbf{r}_j|)$ is derived for the situation without attenuation due to tissue and water included. This exercise results in a correction to the value quoted in Blackledge *et al* [10]. To simplify notation in the following derivation, $S_{\mathbf{r}_j}$ will denote $S(k|\mathbf{r}-\mathbf{r}_j|)$. It is also shown in this appendix that $\nabla S(k|\mathbf{r}-\mathbf{r}_j|)$ and $\nabla S(k|\mathbf{r}_j-\mathbf{r}|)$ are equal.

B.1 Derivation of $\nabla S(k|\mathbf{r}-\mathbf{r}_j|)$

The starting point of this calculation is the expression for the propagator term that neglects attenuation effects, which is given by

$$S_{\mathbf{r}_j} = \frac{\exp(ik|\mathbf{r}-\mathbf{r}_j|)}{(k|\mathbf{r}-\mathbf{r}_j|)^{\frac{1}{2}}} \tag{B.1}$$

Letting $f(x,y) = |\mathbf{r}-\mathbf{r}_j|$ for simplicity, Equation B.1 can be rewritten

$$S_{\mathbf{r}_j} = \frac{\exp(ikf(x,y))}{(kf(x,y))^{\frac{1}{2}}} \tag{B.2}$$

From this one can derive $\nabla S_{\mathbf{r}_j}$, where

$$\begin{aligned} \nabla S_{\mathbf{r}_j} &= \nabla\{\exp(ikf(x,y))\, k^{-\frac{1}{2}}\, f(x,y)^{-\frac{1}{2}}\} \\ &= k^{-\frac{1}{2}}\, f(x,y)^{-\frac{1}{2}}\, \nabla\{\exp(ikf(x,y))\} + \\ &\quad k^{-\frac{1}{2}}\, \exp(ikf(x,y))\, \nabla\{f(x,y)^{-\frac{1}{2}}\} \end{aligned} \tag{B.3}$$

Equation B.3 $\nabla \exp(ikf(x,y))$ can be expanded as

$$\nabla \exp(ikf(x,y)) = ik \exp(ikf(x,y)) \nabla f(x,y) \tag{B.4}$$

Equation B.4 and $\nabla f(x,y)$ can be expanded as follows:

$$\begin{aligned} \nabla f(x,y) &= \nabla \{ |(x-r_x)\hat{\mathbf{x}} + (y-r_y)\hat{\mathbf{y}}| \} \\ &= \nabla \{ \{(x-r_x)^2 + (y-r_y)^2\}^{\frac{1}{2}} \} \\ &= \frac{1}{2} \frac{1}{f(x,y)} \{2(x-r_x)\hat{\mathbf{x}} + 2(y-r_y)\hat{\mathbf{y}}\} \\ &= \frac{(x-r_x)}{|\mathbf{r}-\mathbf{r}_j|}\hat{\mathbf{x}} + \frac{(y-r_y)}{|\mathbf{r}-\mathbf{r}_j|}\hat{\mathbf{y}} \\ &= \frac{(\mathbf{r}-\mathbf{r}_j)}{|\mathbf{r}-\mathbf{r}_j|} \\ &= \hat{\mathbf{n}}_j \end{aligned} \tag{B.5}$$

From this result, the form of $\nabla f(x,y)^{-\frac{1}{2}}$ can be derived:

$$\begin{aligned} \nabla f(x,y)^{-\frac{1}{2}} &= -\frac{1}{2} f(x,y)^{-\frac{3}{2}} \nabla f(x,y) \\ &= -\frac{1}{2} \frac{\hat{\mathbf{n}}_j}{f(x,y)^{\frac{3}{2}}} \end{aligned} \tag{B.6}$$

Combining Equations B.6 and B.4, the result is

$$\begin{aligned} \nabla S_{\mathbf{r}_j} &= \hat{\mathbf{n}}_j \frac{\exp(i(k|\mathbf{r}-\mathbf{r}_j|)^{\frac{1}{2}})}{(k|\mathbf{r}-\mathbf{r}_j|)^{\frac{1}{2}}} \{ik - \frac{1}{2}\frac{1}{|\mathbf{r}-\mathbf{r}_j|}\} \\ &= \{ik\hat{\mathbf{n}}_j - \boldsymbol{\Delta}_{\mathbf{r_j}}\} S_{\mathbf{r}_j} \end{aligned} \tag{B.7}$$

where

$$\boldsymbol{\Delta}_{\mathbf{r_j}} = -\frac{1}{2}\frac{\hat{\mathbf{n}}_j}{|\mathbf{r}-\mathbf{r}_j|} \tag{B.8}$$

Equation B.7 differs from the result quoted in the paper by Blackledge *et al* in that the factor of $\frac{1}{2}$ is not found within the curly brackets [10]. Recalling from Section A.3 that the following assumption is applied:

$$k\,|\mathbf{r}-\mathbf{r}_j| \gg 1 \tag{B.9}$$

or equivalently that

$$\begin{aligned} k &\gg \frac{1}{|\mathbf{r}-\mathbf{r}_j|} \\ &\gg \frac{1}{2}\frac{1}{|\mathbf{r}-\mathbf{r}_j|} \end{aligned} \tag{B.10}$$

is assumed to hold in the derivation of the image reconstruction algorithms used herein, Equation B.7 reduces to

$$\nabla S_{\mathbf{r}_j} = ik\hat{\mathbf{n}}_j S_{\mathbf{r}_j} \tag{B.11}$$

This final result agrees with that quoted within the paper [10]. The reduction of Equation B.7 by dropping the real term is commonly found in the literature [10, 66]. However, it is important to note that this assumption implies that $\nabla S_{\mathbf{r}_j}$ does not impart a phase shift when operating on an ultrasound field. This effect of this assumption is studied in detail in Section 5.1.1. In support of this study, Appendix C shows the derivation of the scattered field, $p_s(\mathbf{r}_d, \mathbf{r}_s, \omega)$, for the case in which the full expression for $\nabla S_{\mathbf{r}_j}$ is used.

B.2 Derivation of $\nabla S(k|\mathbf{r}_j - \mathbf{r}|)$

In the derivation of the reconstruction algorithms, the propagator from the source to the scatter point, $S(k|\mathbf{r}_o - \mathbf{r}|)$, is equal to the propagator from the scatter point to the detector, $S(k|\mathbf{r} - \mathbf{r}_s|)$, by the Principle of Reciprocity. It will now be shown that $\nabla S(k|\mathbf{r}_j - \mathbf{r}|)$ and $\nabla S(k|\mathbf{r} - \mathbf{r}_j|)$ are also equal. Equations B.1 through B.4 hold, with the exception that now $f(x,y) = |\mathbf{r}_j - \mathbf{r}|$. The expression for $\nabla f(x,y)$ can be expanded as follows:

$$\begin{aligned} \nabla f(x,y) &= \nabla\{\,\{(r_x - x)^2 + (r_y - y)^2\}^{\frac{1}{2}}\,\} \\ &= \frac{1}{2}\frac{1}{f(x,y)}\{-2(r_x - x)\hat{\mathbf{x}} - 2(r_y - y)\hat{\mathbf{y}}\} \\ &= \frac{(x - r_x)}{|\mathbf{r}_j - \mathbf{r}|}\hat{\mathbf{x}} + \frac{(y - r_y)}{|\mathbf{r}_j - \mathbf{r}|}\hat{\mathbf{y}} \\ &= \frac{(\mathbf{r} - \mathbf{r}_j)}{|\mathbf{r} - \mathbf{r}_j|} \end{aligned}$$

$$= \hat{\mathbf{n}}_j$$

Thus, the result is the same as for $\nabla S(k|\mathbf{r}-\mathbf{r}_j|)$, and it therefore follows that

$$\nabla S(k|\mathbf{r}_j-\mathbf{r}|) = \nabla S(k|\mathbf{r}-\mathbf{r}_j|) \tag{B.12}$$

As such, the Principle of Reciprocity holds for the gradient of the propagator as expected.

Appendix C
Improved Derivation of P_s

Recall that in Sections B and 4.2.2, the gradient of $G(k|\mathbf{r}-\mathbf{r}_j|)$ (the nonconstant portion of the propagator) was determined, where $G = S$ in the case if of no attenuation, and $G = \tilde{S}$ when attenuation is considered. In both cases, $\nabla G(k|\mathbf{r}-\mathbf{r}_j|)$ takes the form:

$$\nabla G(k|\mathbf{r}-\mathbf{r}_j|) = G(k|\mathbf{r}-\mathbf{r}_j|)\,(ik\hat{\mathbf{n}}_j - \boldsymbol{\Delta}_{\mathbf{r_j}}) \tag{C.1}$$

In the above, j is equal to either s or 0 for propagation to the detector from any point or from the source to any point, respectively. An important assumption in both the original method by Blackledge *et al* and the ART developed in this thesis is that $\boldsymbol{\Delta}_{\mathbf{r_j}}$, is negligible. This appendix expands upon the derivation of the expression

$$\int_{\Re^2} G(k|\mathbf{r}-\mathbf{r}_d|)\nabla\cdot(\gamma_\rho(\mathbf{r})\nabla G(k|\mathbf{r}-\mathbf{r}_s|))\mathrm{d}^2\mathbf{r} \tag{C.2}$$

which is found in the development of both reconstruction algorithms used in this thesis. Specifically, the full expression for $\nabla G(k|\mathbf{r}-\mathbf{r}_j|)$ is retained, rather than applying the assumption that

$$\nabla G(k|\mathbf{r}-\mathbf{r}_j|) \approx ik\hat{\mathbf{n}}_j\, G(k|\mathbf{r}-\mathbf{r}_j|) \tag{C.3}$$

To simplify notation in the following derivation, $G_{\mathbf{r}_j}$ will denote $G(k|\mathbf{r}-\mathbf{r}_j|)$).

The first steps in the derivation are identical to those outlined in Equations A.23 through A.30, which involve only vector calculus, with the exception that $G_{\mathbf{r}_j}$ and $\nabla G_{\mathbf{r}_j}$ are substituted for $S_{\mathbf{r}_j}$ and $\nabla S_{\mathbf{r}_j}$, respectively. These steps result in the expression

$$\int_{\Re^2} G_{\mathbf{r}_d}\nabla\cdot(\gamma_\rho(\mathbf{r})\nabla G_{\mathbf{r}_s})\,\mathrm{d}^2\mathbf{r} \;=\; -\int_{\Re^2}\nabla G_{\mathbf{r}_d}\cdot(\gamma_\rho(\mathbf{r})\nabla G_{\mathbf{r}_s})\,\mathrm{d}^2\mathbf{r} \tag{C.4}$$

Recalling again that $\nabla G_{\mathbf{r}_j} = G_{\mathbf{r}_j}(ik\hat{\mathbf{n}}_j - \boldsymbol{\Delta}_{\mathbf{r_j}})$ results in the expression

$$\begin{aligned}\int_{\Re^2} G_{\mathbf{r}_d}\nabla\cdot(\gamma_\rho(\mathbf{r})\nabla G_{\mathbf{r}_s})\mathrm{d}^2\mathbf{r} &= -\int_{\Re^2}(ik)^2\hat{\mathbf{n}}_d G_{\mathbf{r}_d}\cdot\hat{\mathbf{n}}_s\gamma_\rho G_{\mathbf{r}_s}\,\mathrm{d}^2\mathbf{r} \\ &= -k^2\int_{\Re^2} G_{\mathbf{r}_d}\gamma_\rho G_{\mathbf{r}_s}(ik\hat{\mathbf{n}}_d - \boldsymbol{\Delta}_{\mathbf{r_d}})\cdot(ik\hat{\mathbf{n}}_s - \boldsymbol{\Delta}_{\mathbf{r_s}})\,\mathrm{d}^2\mathbf{r}\end{aligned} \tag{C.5}$$

Recalling from Equation A.36 that

$$\hat{\mathbf{n}}_s\cdot\hat{\mathbf{n}}_d = -\cos(\theta) \tag{C.6}$$

finally results in

$$\begin{aligned}&\int_{\Re^2} G(k|\mathbf{r}-\mathbf{r}_d|)\nabla\cdot(\gamma_\rho(\mathbf{r})\nabla G(k|\mathbf{r}-\mathbf{r}_s|))\mathrm{d}^2\mathbf{r} \\ &\quad = -k^2\int_{\Re^2} G(k|\mathbf{r}-\mathbf{r}_d|)\,\Phi(\varphi_s,\varphi_d,\theta)\,\gamma_\rho(\mathbf{r})\,G(k|\mathbf{r}-\mathbf{r}_s|)\,\mathrm{d}^2\mathbf{r}\end{aligned} \tag{C.7}$$

where

$$\Phi = \cos(\theta) - \frac{i}{k}(\boldsymbol{\Delta}_{\mathbf{r_d}}\cdot\hat{\mathbf{n}}_s + \boldsymbol{\Delta}_{\mathbf{r_s}}\cdot\hat{\mathbf{n}}_d) + \frac{1}{k^2}\boldsymbol{\Delta}_{\mathbf{r_d}}\cdot\boldsymbol{\Delta}_{\mathbf{r_s}} \tag{C.8}$$

In the case of both attenuated and nonattenuated propagators, Φ simply equals $\cos(\theta)$ upon the application of Assumption C.3. Therefore, the only change from the case in which $\boldsymbol{\Delta}_{\mathbf{r_j}}$ is ignored is that $\gamma_\rho(\mathbf{r})$ is multiplied by a factor of Φ rather than simply $\cos(\theta)$. As per Equations A.39 and 4.25, the new expression for the scattered field is

$$\begin{aligned}p_s(\mathbf{r}_d,\mathbf{r}_s,\omega) &= \alpha^2 A(\omega)\,k^2\times \\ &\quad \int_{\Re^2} G(k|\mathbf{r}-\mathbf{r}_d|)\,(\gamma_\kappa(\mathbf{r})+\Phi\gamma_\rho(\mathbf{r}))\,G(k|\mathbf{r}-\mathbf{r}_s|)\,\mathrm{d}^2\mathbf{r}\end{aligned} \tag{C.9}$$

C.1 Nonattenuated Propagators Revisited

For the nonattenuated 2D Green's function propagator, $\alpha S(k|\mathbf{r}-\mathbf{r}_j|)$, recall from Equation B.8 that

$$\boldsymbol{\Delta}_{\mathbf{r_j}} = \frac{1}{2}\frac{\hat{\mathbf{n}}_j}{|\mathbf{r}-\mathbf{r}_j|} \tag{C.10}$$

Typically $|\mathbf{r}-\mathbf{r}_j|$ will be kept to greater than $0.8|\mathbf{r}_j|$, where $|\mathbf{r}_j|$ is the distance of the source or detector from the origin. Furthermore, $|\mathbf{r}_j|$ will typically be on the order of

100-200 mm. A worst case scenario might be characterized by the outermost regions of tissue having $|\mathbf{r} - \mathbf{r}_j| \approx 0.7|\mathbf{r}_j|$ and $|\mathbf{r}_j| = 100$ mm. This leads to

$$\mathbf{\Delta}_{\mathbf{r_j}} <\approx 0.00714\,\mathrm{mm}^{-1}\,\hat{\mathbf{n}}_j \tag{C.11}$$

Substituting this expression into Equation C.7 and recalling that $\hat{\mathbf{n}}_s \cdot \hat{\mathbf{n}}_d = -\cos(\theta)$ yields

$$\Phi = \cos(\theta)(1 + \frac{0.01428i\,\mathrm{mm}^{-1}}{k} - \frac{1}{k^2}\,0.00714^2\,\mathrm{mm}^{-2}) \tag{C.12}$$

and thus according to Equation C.9,

$$\begin{aligned} p_s(\mathbf{r}_d, \mathbf{r}_s, \omega) &= \alpha^2 A(\omega)\, k^2 \times \\ & \int_{\Re^2} S(k|\mathbf{r} - \mathbf{r}_s|)\,(\gamma_\kappa(\mathbf{r}) + \Phi\gamma_\rho(\mathbf{r}))\, S(k|\mathbf{r} - \mathbf{r}_d|)\,\mathrm{d}^2\mathbf{r} \end{aligned} \tag{C.13}$$

C.2 Attenuated Propagators Revisited

For the attenuated 2D Green's function propagator, $\alpha\tilde{S}(k|\mathbf{r} - \mathbf{r}_j|)$, recall from Equation 4.23 that

$$\begin{aligned} \mathbf{\Delta}_{\mathbf{r_j}} &= (k^2\,1.4053 \times 10^{-5}\,\mathrm{mm} + 1.2255 \times 10^{-2}\,k)(\hat{\mathbf{x}} + \hat{\mathbf{y}}) \\ &= (Bk^2 + Ck)(\hat{\mathbf{x}} + \hat{\mathbf{y}}) \end{aligned} \tag{C.14}$$

This expression can be substituted into Equation C.7, and the following relations regarding the unit vectors, $\hat{\mathbf{n}}_s$ and $\hat{\mathbf{n}}_d$, can be applied:

$$\begin{aligned} \hat{\mathbf{n}}_d &= \hat{\mathbf{x}}\cos(\varphi_d) + \hat{\mathbf{y}}\sin(\varphi_d) \\ \hat{\mathbf{n}}_s &= \hat{\mathbf{x}}\cos(\varphi_s) + \hat{\mathbf{y}}\sin(\varphi_s) \end{aligned} \tag{C.15}$$

Recall that φ_s and φ_d are the angles of the source and detector, respectively. The result for Φ is thus

$$\begin{aligned} \Phi &= \cos(\theta) + \frac{1}{k^2}(Bk^2 + Ck)^2|\hat{\mathbf{x}} + \hat{\mathbf{y}}|^2 \\ & -\frac{i}{k}\,(Bk^2 + Ck)\,\{\cos(\varphi_s) + \cos(\varphi_d) + \sin(\varphi_s) + \sin(\varphi_d)\} \end{aligned} \tag{C.16}$$

and according to Equation 4.25, the new expression for the scattered field is

$$\begin{aligned} p_s(\mathbf{r}_d, \mathbf{r}_s, \omega) &= \alpha^2 A(\omega)\, k^2 \times \\ & \int_{\Re^2} \tilde{S}(k|\mathbf{r} - \mathbf{r}_s|)\, (\gamma_\kappa(\mathbf{r}) + \Phi\gamma_\rho(\mathbf{r}))\, \tilde{S}(k|\mathbf{r} - \mathbf{r}_d|)\, \mathrm{d}^2\mathbf{r} \end{aligned} \tag{C.17}$$

Appendix D
Phantom Construction

The following formula for a tissue equivalent material was provided by Mr. Authur Worthington of the Ultrasound Imaging Group at the Ontario Cancer Institute. It uses powdered graphite to achieve the desired attenuation, which mimics that in soft tissue. The formula is meant to produce a phantom with a speed of sound of 1.54 mm/μs at 22°C and an attenuation coefficient of -1.1 $\frac{\mathrm{db}}{\mathrm{MHz\cdot cm}}$. This attenuation is achieved through use of fine powdered graphite with a granule size rating of at most 325 mesh. Note that mesh sizes are the standard method of measuring graphite granules, and this rating is simply the size of the holes in the finest wire mesh that can pass all the graphite granules in a sample. The attenuation coefficient can be changed by varying the coarseness of graphite. Materials such as metal or wooden rods and ball bearings can be placed in the phantom as it hardens to test the imaging of non-uniform objects.

This formula is for a cylindrical phantom that is 10 cm deep and 2 cm in radius. The volume is therefore 125 cm^3, and this is approximately equal to the volume of water that is used to create the phantom. Hence, the amount of water used is 125.7 cm^3, with a weight, w of 125.7 g. Given that W is the total weight of the phantom, the formula requires that

$$\frac{w}{W} = 0.741 \tag{D.1}$$

Thus, the total weight of the phantom is 169.6 g. The following formula completes the phantom:

- 5% gelatin powder by weight, 8.5 g
- 0.9% NaCl by weight, 1.5 g
- 20% graphite powder (325 mesh) by weight, 33.9 g

The instructions for constructing the phantom are as follows:

- Degas water by boiling.
- Add NaCl and gelatin. Stir well and wait until solution clarifies.
- Add graphite a bit at a time and stir well.
- Let cool to about 40-50°C.
- Pour into mold.
- Rotate mold periodically as phantom solidifies to keep graphite from settling.

An alternate method of constructing cylindrically symmetric phantoms that works very well is the "candle method." Essentially, a "wick" made of string is successively dipped into the phantom mixture, allowing 2-3 minutes in between for quick drying. A weight is tied to the end of the wick so that it can be easily plunged into the mixture. In this manner, cylindrical phantoms of length 6-10 cm and with diameters of ~2-6 mm can be easily constructed. The phantom construction can also be varied by changing the mixture to one with a different speed of sound and/or attenuation coefficient after a certain diameter is reached.

APPENDIX E
ITERATIVE METHODS

In applying the reconstruction algorithm that includes attenuated propagators, one must solve a system of linear algebraic equations, given by $\mathbf{y} = \mathbf{A}\mathbf{x}$, for $\mathbf{x}$. This has been done iteratively, and several methods were studied in this effort: the conjugate gradient (CG) method, the Jacobi Iterative (JI) method, the Gauss-Seidel (GS) method, and the Successive Under-Relaxation (SUR) method. The algorithms for each are described below, and results of their use are presented in Section 5.7.1.

E.1 CONJUGATE GRADIENT METHOD

The conjugate gradient method solves the matrix system by minimization of a residual error function. It is furthermore a Krylov Subspace solver, which means the following. The iterated $\mathbf{x}$ is an evolving function of both the initial guess $\mathbf{x}_0$ as well as the residual vector and the matrix $\mathbf{A}$. Functions of this sort belong to Krylov Subspace. The conjugate gradient method finds an $\mathbf{x}$ by systematically searching through Krylov Subspace for the $\mathbf{x}$ that minimizes the residual. The minimization of the residual produces a sequence of coefficients, $t^{(i)}$, and vectors, $\mathbf{p}^{(i)}$, upon which the iterated $\mathbf{x}$ is built.

The CG method minimizes the residual of the matrix equation along a set of conjugate directions [39, 83]. This is defined as a set of directions such that a line minimization along any direction in the set does not interfere with any other previous minimizations that were done along any other directions in the set. In other words, having performed a line minimization along a direction u, a new direction, v must be chosen for the next minimization step such that minimizing along v will not "spoil" the minimization along u.

Minimization along conjugate directions is an efficient approach to the iterative solution of a linear system.

The following illustrates the algorithm for the conjugate gradient method, when an array equation

$$\mathbf{y} = \mathbf{A}\mathbf{x} \tag{E.1}$$

must be solved for $\mathbf{x}$ given knowledge of $\mathbf{A}$ and $\mathbf{y}$. The matrix $\mathbf{A}$ can be square or overdetermined. The algorithm begins by calculating the initial residual, $\mathbf{r}^{(0)}$, and a measure of error, $e^{(0)}$, given by

$$\begin{aligned} \mathbf{r}^{(0)} &= \mathbf{A}\mathbf{x}^{(0)} - \mathbf{y} \\ e^{(0)} &= \frac{\sum_{j=1}^{N} r_j^2}{\sum_{j=1}^{N} y_j^2} \times 100\% \end{aligned} \tag{E.2}$$

where N is the length of $\mathbf{x}$, or equivalently the number of pixels in the image. Also, the first conjugate vector, $\mathbf{p}^{(0)}$, is calculated by

$$\mathbf{p}^{(0)} = -\mathbf{A}'\mathbf{r}^{(0)} \tag{E.3}$$

While $e^{(i)}$ is greater than a very small limit, η, which in practice was chosen to be 1×10^{-7}, the following set of commands is executed [39]:

$$\begin{aligned} s^{(i)} &= |\mathbf{A}'\mathbf{r}^{(i-1)}| \qquad u^{(i)} = |\mathbf{A}\mathbf{p}^{(i-1)}| \qquad t^{(i)} = \frac{(s^{(i)})^2}{(u^{(i)})^2} \\ \mathbf{x}^{(i)} &= \mathbf{x}^{(i-1)} + t^{(i)}\mathbf{p}^{(i-1)} \\ \mathbf{r}^{(i)} &= \mathbf{r}^{(i-1)} + t^{(i)}\mathbf{A}\mathbf{p}^{(i-1)} \\ v^{(i)} &= |\mathbf{A}'\mathbf{r}^{(i)}| \qquad q^{(i)} = \frac{(v^{(i)})^2}{(s^{(i)})^2} \\ \mathbf{p}^{(i)} &= q^{(i)}\mathbf{p}^{(i-1)} - \mathbf{A}'t^{(i)} \end{aligned} \tag{E.4}$$

In practice when using this algorithm in the reconstruction of attenuating objects as described in Section 4.2, it was necessary to apply a simple boundary condition in order to achieve convergence. Under this condition, it was assumed that the image was sufficiently larger in width than the object such that the pixels in the outermost border corresponded to water and hence had values of zero. Hence, the boundary condition manifests itself as a vector mask of 1's and 0's. This mask is multiplied point-by-point with the vector $\mathbf{x}$ during each iteration in order to apply the boundary conditions at each step. The error given by Equation E.2 is recalculated, and when it becomes less than η, the algorithm is assumed to have converged upon a good solution, $\mathbf{x}$, that satisfies Equation E.1.

E.2 Jacobi Iterative Technique

The Jacobi iterative method is a technique to solve Equation E.1 iteratively for $\mathbf{x}$ when $\mathbf{A}$ is square. The technique converts the system $\mathbf{y} = \mathbf{A}\mathbf{x}$ into an equivalent system of the form $\mathbf{x} = T\mathbf{x} + \mathbf{c}$, where T is some $n \times n$ matrix and $\mathbf{c}$ is some vector [13]. Upon selecting an initial guess, $\mathbf{x}_0$, at the solution, the vector $\mathbf{x}$ is iterated by computing

$$\mathbf{x}^{(i)} = T\,\mathbf{x}^{(i-1)} + \mathbf{c} \tag{E.5}$$

To convert $\mathbf{y} = \mathbf{A}\mathbf{x}$ into the form $\mathbf{x} = T\mathbf{x} + \mathbf{c}$, one solves each successive equation in the system for successive elements of $\mathbf{x}$. As an example, equations 1 and 2 in the system are rearranged to solve for x_1 and x_2, respectively. The procedure is quite simple as follows. The kth equation can be written as

$$\begin{aligned} y_k &= \sum_{j=1}^{n} A_{kj}\,x_j \qquad\qquad (E.6) \\ &= \sum_{j=1,\,j\neq k}^{n} A_{kj}\,x_j + A_{kk}\,x_k \end{aligned}$$

which can be rearranged to yield

$$\begin{aligned} x_k &= \sum_{j=1,\,j\neq k}^{n} \frac{-A_{kj}}{A_{kk}}\,x_j + \frac{y_k}{A_{kk}} \qquad\qquad (E.7) \\ &= \{\sum_{j=1,\,j\neq k}^{n} \frac{-A_{kj}}{A_{kk}}\,x_j + 0\cdot x_k\} + \frac{y_k}{A_{kk}} \end{aligned}$$

Combining the equations for all elements, x_k, of $\mathbf{x}$ yields a matrix equation of the form $\mathbf{x} = T\mathbf{x} + \mathbf{c}$, where

$$T_{kj} = \begin{cases} \frac{-A_{kj}}{A_{kk}}, & k \neq j \\ 0, & k = j \end{cases}$$

and

$$c_k = \frac{y_k}{A_{kk}} \tag{E.8}$$

As such, the elements x_k of the iterated solution can finally be calculated as follows:

$$x_k^{(i)} = \sum_{j=1, j\neq k}^{n} \frac{-A_{kj}}{A_{kk}} x_j^{(i-1)} + \frac{y_k}{A_{kk}} \tag{E.9}$$

As in the case of the CG method, a mask vector of 1's and 0's to distinguish pixels in tissues from those in water can be multiplied point-by-point with $\mathbf{x}$ in order to apply boundary conditions during each iteration. At the end of each iteration, a residual vector $\mathbf{r}^{(i)} = \mathbf{A}\mathbf{x}^{(i)} - \mathbf{y}$ is determined, and from this the error given by Equation E.2 is calculated. The iteration continues until the error becomes less than some limit η. Evidently, this algorithm requires that all diagonal elements of $\mathbf{A}$ be nonzero. Furthermore, the algorithm has difficulty converging and often can not converge unless the matrix is diagonally dominant. In a diagonally dominant matrix,

$$|A_{kk}| >= \sum_j |A_{kj}| \text{ for } j = 1, 2, ..., k-1, k+1, ..., n \tag{E.10}$$

Again, a boundary condition was applied in which the pixels in the outermost border were assumed to correspond to water and hence have values of zero.

E.3 Gauss-Seidel Iterative Technique

The Gauss-Seidel is an improved version of the Jacobi Iterative method. The JI method successively calculates the k elements of the current ith iterated solution using only the previous solution, $x^{(i-1)}$. Since the new solution is assumed to be a better approximation to the desired $\mathbf{x}$, it would seem useful to compute the kth element of $x^{(i)}$ with the (k-1) newly calculated elements of $x^{(i)}$ together with elements (k+1) through n of the previous solution, $x^{(i-1)}$. The Gauss-Seidel algorithm makes use of this variation and thus calculates the elements x_k of the iterated solution as follows [13]:

$$x_k^{(i)} = \frac{-\sum_{j=1}^{k-1} A_{kj} x_j^{(i)} - \sum_{j=k+1}^{n} A_{kj} x_j^{(i-1)} + y_k}{A_{kk}} \tag{E.11}$$

Again, all diagonal elements of $\mathbf{A}$ must be nonzero, and the method has difficulty converging when $\mathbf{A}$ is not diagonally dominant. As per the previous two methods, a boundary condition was applied in which the pixels in the outermost border were set to zero.

E.4 SUR Iterative Technique

This method is a modification of the Gauss-Seidel iterative algorithm that results in convergence of some systems that would otherwise not converge with the GS method. The SUR method calculates the elements x_k of the iterated solution by the following equation [13]:

$$x_k^{(i)} = (1-\omega)\, x_k^{(i-1)} + \omega\, \frac{-\sum_{j=1}^{k-1} A_{kj} x_j^{(i)} - \sum_{j=k+1}^{n} A_{kj} x_j^{(i-1)} + y_k}{A_{kk}} \tag{E.12}$$

ω is some positive fraction that is less than 1, and the proper selection of this parameter can facilitate the solution of systems that fail to converge with the GS method. Unfortunately, though, ω must be chosen in what is best described as a "hit and miss" manner [13]. Due to the division by A_{kk}, all diagonal elements of $\mathbf{A}$ must be nonzero. Note that if ω is chosen to be some positive value greater than 1, the method is referred to as the Successive Over-Relaxation algorithm, which is used to accelerate the solution of systems that do in fact converge with the Gauss-Seidel method [13]. A boundary condition was again applied in which the pixels in the outermost border were set to zero.